Doktorarbeit

Conjugated porous polymers for heterogeneous visible light photocatalysis

Zur Erlangung des Grades

„Doktor der Naturwissenschaften“

im Promotionsfach Chemie

dem Fachbereich Chemie, Pharmazie und Geowissenschaften

der Johannes Gutenberg-Universität Mainz.

Cyrine Ayed

Geboren in Tunis, Tunesien

Mainz, 2020

Dekan:

Prodekan:

Gutacher 1:

Gutacher 2:

Tag der mündlichen Prüfung:

Affidavit

I hereby confirm that I have completed the present dissertation independently and without inadmissible external support. I have not used any sources or tools other than those indicated and have identified literal and analogous quotations.

Furthermore, I confirm that this thesis has not yet been submitted as part of another examination process neither in identical nor in similar form.

Place, date: **Signature:**

Abstract

The main target of this thesis is set on the design of conjugated porous polymers (CPPs), in particular, conjugated microporous polymers (CMPs) and covalent triazine frameworks (CTFs), for visible light photocatalysis in green reaction media. Visible light-driven conversion of basic, abundant and cheap chemicals into high value compounds is explored in depth. The emphasis is paid to the employment of mild and environmentally benign reaction conditions as using visible light as irradiation source, molecular oxygen as green oxidant, and aqueous solvents as reaction media. The chemical features of the designed materials, their band structures, and their textural, morphological and optoelectronic properties are also discussed in details**.**

First, a series of CMPs, with different electron donor/acceptor combination, are designed for the visible light-promoted oxidative cleavage of the C=C bonds of styrenes. The CMP (BBT), with specific phenyl/ benzothiazole as donor/acceptor combination, could cleave highly efficiently the C=C of styrene in aqueous system (water/acetonitrile: 24/1), owning to the most efficient charge separation among the polymer series. High conversion (ca. 91%) and high selectivity (ca. 86%) toward benzaldehyde are achieved.

To further expand the catalytic applications in pure water, a structural design strategy of CTFs, combing different electron donor/acceptor building blocks using hydrophilic mesoporous silica (SBA-15) as support, is presented. The CTFs, with excellent dispersibility, are examined for the visible light photocatalytic epoxidation of styrene in pure water. The CTF, with the most extended π-conjugated benzothiazole/phenyl/triazine and therefore the most enhanced intermolecular electron delocalization, exhibited the highest styrene oxide selectivity (> 50%), with the byproduct being benzaldehyde with a selectivity of ~ 46%. The mechanistic study, based on advanced analytical tools, is conducted, revealing that sodium bicarbonate as well as the reactive oxygen species are responsible for the epoxidation process.

Furthermore, a thiophene-containing CTF directly synthesized on SBA-15 (CTF-Th@SBA-15) is prepared and tested for the photocatalytic partial oxidation of biomass-derived 5-hydroxymethylfurfural (HMF) to 2,5-diformylfuran (DFF) in pure water. The use of thiophene units as building block into the polymer backbone imparts the CTF with broad visible light absorbance and extremely high oxidation potential. This latter together with the accessible mesopores contribute to the efficient conversion of HMF to DFF with high selectivity (> 99%). The photocatalytic performance of CTF-Th@SBA-15 is further investigated through the visible-light promoted degradation of organic contaminants in aqueous media. CTF-Th@SBA-15 demonstrates excellent adsorption capacity toward the organic dye molecules in water, owning to the high surface area and the added hydrophilic properties induced by the presence of SBA-15. Moreover, this leads not only to high photodegradation performance of the dyes in water, but also for efficient photocatalysis in solvent-free medium.

At last, a CPP photocatalyst with immobilized TiO_2 nanoparticles (wt. 20%) displays efficient photocatalytic performances for the oxidative coupling reaction of amines and the selective oxidation of organic sulfides, leading to high reaction conversions and selectivity. The enhanced efficiency of the formed heterojunction, in comparison to those of the pristine single photocatalytic systems; either CPP or TiO_2; can be attributed to the improved photo-induced charge separation and thus to the suppressed electron-hole recombination.

Zusammenfassung

Das Hauptziel dieser Arbeit ist das Design von konjugierten porösen Polymeren (CPPs) wie konjugierte mikroporöse Polymere (CMPs) und kovalente Triazin-Netzwerke (CTFs) für Photokatalyse in grünen Reaktionsmedien. Die lichtinduzierte Konversion von günstigen Basischemikalien in hochwertige Verbindungen wurde eingehend erforscht. Der Schwerpunkt lag an dem Einsatz von milden und umweltschonenden Reaktionsbedingungen, dabei wurden sichtbares Licht als Bestrahlungsquelle, molekularer Sauerstoff als grünes Oxidationsmittel und wässrige Lösungsmitteln als Reaktionsmedien verwendet. Der Einfluss von weiteren chemischen und physikalischen Eigenschaften auf die katalytische Effizienz wie z. B. Morphologie, Bandstrukturen und andere opto-elektronischen Eigenschaften wurden ebenfalls eingehend erforscht.

Zunächst wurde eine Reihe von CMPs mit verschiedenen Elektronendonator-Akzeptor-(D-A) Kombinationen für die photokatalytische oxidative Spaltung der C=C-Bindung von Styrolderivaten synthetisiert und verwendet. In einer Mischung von Acetonitril/Wasser (1:24), konnten die C=C-Bindungen durch die CMPs erfolgreich gespalten werden, wobei das CMP (BBT) mit Phenylbenzothiazol als D-A-Kombination war der effizienteste Photokatalysator. Das ließ sich auf die höchste Ladungsseparationseffizienz zurückführen. Sehr hohe Umsetzungen bis ca. 91% und Selektivitäten bis ca. 86% für Benzaldehyd als Produkt konnten erzielt werden.

Um die Einsatzbarkeit der CPPs im reinen Wasser zu ermöglichen, wurden verschiedene CTFs direkt auf mesoporösem Siliciumdioxid (SBA-15) synthetisiert. Durch die zusätzlich gewonnene Hydrophilie durch SBA-15 waren die CTFs in Wasser sehr gut dispergierbar. Die photokatalytische Epoxidierung von Styrol konnte unter sichtbarem Licht in reinem Wasser mit einer Selektivität > 50% erreicht werden. Benzaldehyd wurde als Hauptnebenprodukt identifiziert mit einer Selektivität von ~46%. Die mechanistische Studie zeigte die entscheidenden Rollen von reaktiven Sauerstoffspezies und Natriumhydrogencarbonat für die Epoxidierungsreaktion, die während der Katalyse erzeugt wurde.

Darüber hinaus wurde ein thiophenhaltiges CTF auf SBA-15 hergestellt und für die photokatalytische partielle Oxidation von 5-Hydroxymethylfurfural (HMF) zu 2,5-Diformylfuran (DFF) in reinem Wasser getestet. Der Einbau von Thiopheneinheiten ins Polymergerüst verleiht dem CTF eine breite Absorption im sichtbaren Bereich und ein extrem hohes Oxidationspotential. Letzteres trägt zusammen mit den zugänglichen Mesoporen zur effizienten Umwandlung von HMF in DFF mit hoher Selektivität (> 99%) bei.

Des Weiteren wurde CTF-Th@SBA-15 für den photokatalytischen Abbau von organischen Schadstoffen in wässrigen Medien eingesetzt. CTF-Th@SBA-15 zeigte ein ausgezeichnetes Adsorptionsvermögen von organischen Farbstoffmolekülen im Wasser, was auf die große Oberfläche und die zusätzlichen hydrophilen Eigenschaften zurückzuführen war. Dies führte nicht nur zu einer hohen Photoabbausrate der Farbstoffe in Wasser, sondern auch zu einer effizienten Katalyse im lösungsmittelfreien Zustand.

Schließlich wurde eine Studie über den Einfluss der Ladungsseparation auf die photokatalytische Effizienz der CPPs durchgeführt. Hier wurde das Konzept des Heteroübergangs genutzt, indem TiO_2-Nanopartikel (wt. 20%) auf die Oberfläche von CMPs immobilisiert wurden. Durch die Kombination von TiO_2 und CMP konnte der Elektronentransfer zwischen beiden Materialien erzeugt und damit die Rekombination der Exzitonen verzögert werden. Im Vergleich zum reinen CMP zeigte das Hybridmaterial eine wesentlich erhöhte katalytische Aktivität für die oxidative Kopplungsreaktion von Aminen und die selektive Oxidation organischer Sulfide.

Table of Contents

List of figures

List of tables

List of schemes

List of acronyms

A	Acceptor moiety
AcO	Acetophenone
AO	Ammonium oxalate
$APbX_n$	Lead-halide perovskite
B	External magnetic field.
BET	Brunauer Emmett Teller method
Bi_2O_3	Bismuth(iii) oxide
$BiVO_4$	Bismuth vanadate
BJH	Barrett, Joyner and Halenda method
BQ	Benzoquinone
BT	Benzothiodiazole unit
BzA	Benzaldehyde
BzOH	Benzoic acid
C	Concentration of the solution
c	Speed of light
CB	Conduction band
CdS	Cadmium sulfide
CdSe	Cadmium selenide
CMP	Conjugated microporous polymer
COF	Covalent organic framework
CP-MAS	Cross polarization magic angle spinning
CPP	Conjugated porous polymers
CPs	π-conjugated polymers
CV	Cyclic voltammetry
D	Donor moiety
d	Thickness of the measurement cell
DCM	Dichloromethane
DCT	2,5- dicyanothiophene

DFF	2,5-diformylfuran
DFT	Density functional theory
DMF	N,N-dimethylformamide
DMF	Dimethylformamide
DMPO	5,5-dimethyl-1-pyrroline *N*-oxide
DMSO	Dimethyl sulfoxide
DRS	Diffuse reflectance spectra
e^-	Photogenerated electron
Eg	Optical band gap
E_{ox}	Oxidative potential
EPR	Electron paramagnetic resonance spectroscopy
E_{red}	Reductive potential
EtOAc	Ethylacetate
FFCA	5-formylfuran-2-carboxylic acid
FDCA	Furan-2,5-dicarboxylic acid
FTIR	Fourier transform infrared spectroscopy
g	g-factor
GC-MS	Gas chromatography-mass spectrometry
g-CN	Graphitic carbon nitrides
h	Planck constanth Planck's constant
h^+	Photogenerated holes
HMF	5-hydroxymethylfurfural
HMFCA	5-(hydroxymethyl)furan-2-carboxylic acid
HOMO	Highest occupied molecular orbital
HR-TEM	High resolution- transmission electron microscopy
I, I_0	Intensity of incident monochromatic radiation
ICP-MS	Inductively coupled plasma mass spectrometry
ISC	Intersystem crossing
IsPr	Isopropanol
IUPAC	International Union of Pure and Applied Chemistry

K	Adsorption equilibrium
KI	Potassium iodide
LED	Light emitting diode
L-H	Langmuir-Hinshelwood model
LUMO	Lowest unoccupied molecular orbital
MB	Methylene blue
MeCN	Acetonitrile
$MeNO_2$	Nitromethane
Mes-Acr^+	9-mesityl-10-methylacridinium
NaN_3	Sodium azide
Nb_2O_5	Niobium pentoxide
NLDFT	Nonlinear density functional theory
NMR	Nuclear magnetic resonance
OrG	Orange G
P_2O_5	Phosphorus pentoxide
PBN	N-tert-butyl-α-phenylnitrone
PC	Photocatalyst
PhAcA	Phenylacetaldehyde
PolyHIPEs	Polymerized High internal phase emulsions
POPs	Porous organic polymers
POMs	Polyoxometalates conjugated polymers
XRD	Powder X-ray diffraction
QSDFT	Quenched solid density functional theory
r	Reaction rate
Rh6G	Rhodamine derivative
RhB	Rhodamine B
ROS	Reactive oxygen species
S	Substrate
SBA-15	Mesoporous silica (Santa Barbara Amorphous type material)
SCE	Saturated calomel electrode

SEM	Scanning electron microscopy
SET	Single electron transfer
SO	Styrene oxide
Sty	Styrene
t	Triplet state
TEM	Transmission electron microscopy
TEMP	2,2,6,6-tetramethylpiperidine
TEMPO	2,2,6,6-Tetramethylpiperidine 1-oxyl
TfOH /CF_3SO_3H	Trifluorosulfonic acid
TGA	Thermalgravimetric analysis
Th	Thiophene unit
THF	Tetrahydrofuran
TiO2	Titanium dioxide
TiO_2 P25	Degussa Titanium dioxide
UV	Ultraviolet
UV-Vis DRS	Ultraviolett-Visible Diffuse Reflectance Spectroscopy
VB	Valence band
VOCs	Volatile organic compounds
WO_3	Tungsten trioxide
$ZnCl_2$	Zinc chloride
ZnO	Zinc oxide
ε	Extinction coefficient,
θ	Water contact angle
λ	Wavelength of light
v	Frequency of light
ΔG	Free Gibbs energy
μ_B	Bohr magneton

1. Introduction

Nowadays, the steadily rising energy consumption caused by the industrial development and the population growth rely on an intensive exploitation of non-renewable sources such as the combustion of fossil fuels. This led to serious environmental concerns (greenhouse effect and air pollution), and therefore urge to develop new renewable energy production technologies. The main source of energy on earth is the solar irradiation, which is natural, abundant and sustainable resource. Measurements show that only 0.1‰ of the energy reaching the earth from the sun can be sufficient to cover all or most of the current and future energy needs worldwide.[1, 2] Consequently, the question of how to invest into the solar energy has become an emerging field of research ever since.

The use of sunlight was never new to life on earth and humankind as photosynthesis is one of its best illustrations. Indeed, during the process of photosynthesis, green plants and certain other organisms harness energy from sunlight and convert into chemical energy to produce carbohydrates and oxygen. Inspired by that, the first active use of photochemistry antedated to the 14^{th} century, in which ancient Egyptian and Indian curer treated a leukoderma (skin disease) by exposing plants extracts or seeds to sunlight, known as heliotherapy.[3] Later in 1912, Giacomo Cimincian, recognized as the father or pioneer of photochemistry, introduced the concept of modern photochemistry.[4] Since then, tremendous progress in photochemistry has been made covering wide fields of application, i.e., chemical synthesis, photomedicine, electronics, printing technology and photography, environment and energy.[5, 6] Particularly, the field of photocatalysis, notably visible-light photocatalysis, has been the subject of extensive research over the past decade, most of which were amenable for commercial exploitation. Indeed, a look to the recent literature reveals a steadily flux of more than 5000 international patents in this field for various applications over the last 20 years (compared to few hundreds throughout the 20^{th} century).

Among various photocatalytic systems with visible-light activity, inorganic semiconductors such as TiO_2 and transition metals complexes such as $Ru(bpy)_3Cl_2$ and fac-$Ir(ppy)_3$ were widely and commonly used as photocatalysts in a large range of applications from water splitting, solar energy storage, pollutants removal to photovoltaics and organic redox transformation reactions.[7-11] Nevertheless, there are still intrinsic drawbacks associated with these rather homogeneous metal complex systems, or the traditional metal oxide semiconductors, for example, high cost, toxicity of the rare metals, and limited availability in nature. To overcome this issue, some organic dyes, such as cyanoarenes, xanthenes and acridiniums, have been designed and used as metal-free alternative.[12-16] Nevertheless, there are also limited in term of application as they suffer from photo-bleaching in addition to their limited photoredox capacity.

Metal-free photocatalytic systems have attracted much more attention recently. Among those, polymeric carbon nitrides, have been widely employed as metal-free photocatalysts due to their promising electronic and optical properties.[17] However, they still lack of the broad use for organic photoredox reactions due to the limitation of the fine tunability of their energy band positions.

One intriguing and pure organic candidate, conjugated porous polymers (CPPs), have emerged as a new promising class of efficient, stable and metal-free photocatalysts due to the flexible tunability of their semiconductor properties via a variety of the donor–acceptor combination on the molecular level, and the ability of precise tuning of their band position, band gap, and p/n characters.[18, 19] The CPPs combine unique photoactive π-conjugated skeletons with favorable porous properties. They possess a three-dimensional network, offering also a unique spatial design possibility, which is usually unavailable for conventional conjugated polymers.[18, 20] Over the last decade, several kinds of porous conjugated polymers(CPPs), i.e., conjugated microporous polymers (CMPs), and covalent triazine-based frameworks (CTFs), have been investigated and demonstrated great potential in visible light photocatalysis,[21-23] with potential applications including photocatalytic water splitting,[24-29] antibacterial treatment,[30, 31] photodegradation of organic pollutants,[32-35] as well as photocatalytic organic synthesis.[36-47] Notably, the production of value-added industrial chemicals via light-driven organic transformations, has emerged as a very interesting and sustainable alternative to the conventional organic synthesis routes, which relies on benign synthetic strategies, limiting the use of harsh conditions and toxic substances, minimizing the generation of byproducts and hazardous waste and improving even the selectivity toward the target products. Consequently, enormous efforts have been devoted to further explore greener and more sustainable approaches such as the use of alternative feedstock preferably from renewable materials, or basic abundant and cheap substrates as well as the employment of mild reaction conditions.

In particular, special attention has been drawn to the choice of the reaction media in the chemical processes. Indeed, the chemical community worldwide has been lately considering the solvent's nature as a key component of sustainable chemistry and, hence, moving from the classical volatile organic solvents toward "much greener " counterparts has become more challenging for today's chemists. Ideally, a "green" solvent should have low volatility, non-toxicity, ability to dissolve a wide range of compounds, low-cost, and easy processability and recyclability. Particularly, water seems to be an appealing candidate since it suits the most aforementioned considerations.[48, 49] So far, only a few research reports have been described the use of CPPs in aqueous media.[36, 50, 51] Therefore, the development of further CPPs as photoactive materials to promote challenging photocatalytic reactions under much milder reaction conditions, i.e., use of water as solvent, would be highly desirable.

2. Aim of work

The main target of this thesis is set on the development of conjugated porous polymers (CPPs) as organic and heterogeneous visible light active photocatalysts for challenging photocatalytic reactions in green reaction media. This thesis consists of the following main parts:

1- Molecular design strategy of CPPs with special focus on conjugated microporous polymers (CMPs) and covalent triazine frameworks (CTFs), and their use mainly for visible light-driven conversion of basic, abundant and cheap chemicals into high value compounds.

2- Employment of green reaction conditions, e.g. the use of benign oxidants such as molecular oxygen and aqueous solvents as green reaction media (biphasic or pure water), and exploration of new organic transformations which can be catalyzed over the designed materials.

3- Elucidation of structure and property relation of the designed CPPs: several parameters have been investigated such as (i) morphology, (ii) porosity, (iii) functional groups, (iv) energy band structures, (v) charge separation efficiency; and (vi) charge transport/transfer within the polymer backbone.

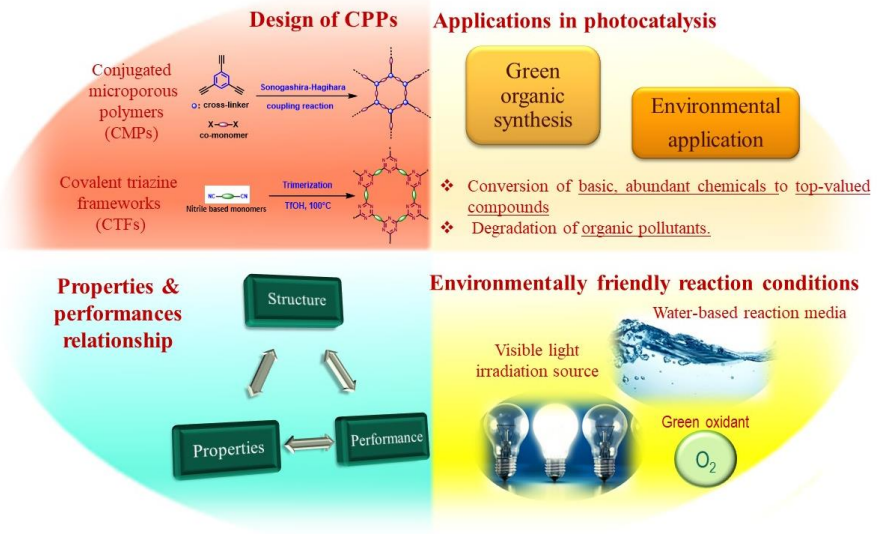

In order to facilitate a comprehensive study, this work is divided into five chapters: The first chapters, chapter 1 and 2, cover the theory and aim of work, then the 3rd chapter gives an overview of the current state of art and presents the fundamental aspects of photocatalysis, visible light photocatalysis, conjugated porous polymers and green chemistry concept. Chapter 4 describes briefly the main characterization methods employed in this work. Chapter 5 reports and interprets thoroughly the results acquired in this work. The experimental details are provided in chapter 6.

3. State of art

3.1. Photocatalysis: history and fundamentals

3.1.1. History

Back in 1901, Giacomo Ciamician was one of the first chemists to investigate the effect of "light and light alone" in enabling chemical reactions, as he highlighted in various talks the potential of photochemistry in future industrial processes.[4] Later in 1911, the term "photocatalysis" firstly appeared in scientific publications, reporting the Prussian blue bleaching over illuminated ZnO particles.[52] Inspired by that, scientists have explored further reactions by using ZnO as photocatalyst under light irradiation. One example was the photoreduction of Ag^+ to Ag over ZnO under light irradiation reported in 1924.[53] Later in 1932, the photoreduction of $AgNO_3$ to Ag and $AuCl_3$ to Au have been also examined employing TiO_2 and Nb_2O_5 as photocatalysts.[54] Around 1938, the photobleaching effect of dyes over TiO_2 has been demonstrated in presence of molecular oxygen.[55] Despite this remarkable progress, the field of photocatalysis remained in its infancy due to the lack of practical implementation. It wasn´t until 1970s, when Fujishima and Honda discovered the splitting of water into hydrogen and oxygen over a TiO_2 electrode under UV light irradiation.[56] At the same time, Frank and Bard first evoked the use of various inorganic semiconductors for pollutants degradation in water streams. Illuminated TiO_2, ZnO, and CdS demonstrated their efficiency in oxidizing cyanide (CN) to cyanate (CNO^-) and sulfite $SO3_2^-$ to $S_2O_3^{2-}$ toward less harmful forms.[57] Later in 1979, Fujishima *et al.*, also used inorganic semiconductors for the photo-reduction of CO_2 under light irradiation.[58] Since then, significant efforts have been devoted to understand the fundamental principles of photocatalysis, enhance the photocatalytic efficiency, explore new and more sophisticated photocatalysts, and expand the scope of the reactions.

3.1.2. Fundamentals

The term "photocatalysis" or "photocatalytic reaction" consists of a chemical reaction initiated by photoabsorption of a "photocatalyst", which participates in the reaction but remains chemically unaltered during and after the reaction. This explanation concords well with the definition given in the International Union of Pure and Applied Chemistry IUPAC (Glossary of terms used in photochemistry-3rd edition), which stipulates photocatalysis as *"change in the rate of a chemical reaction or its initiation under the action of ultraviolet, visible or infrared radiation in the presence of a substance—the photocatalyst—that absorbs light and is involved in the chemical transformation of the reaction partners"*. A photocatalyst, in turn, is best described as *"a catalyst able to produce, upon absorption of light, chemical transformations of the reaction partners. The excited state of the photocatalyst repeatedly interacts with the reaction partners forming reaction intermediates and regenerates itself after each cycle of such interactions"* according to the same glossary.[59]

The principle of photocatalysis can be explained through the electronic structure of semiconducting materials, as shown in **Figure 1.**

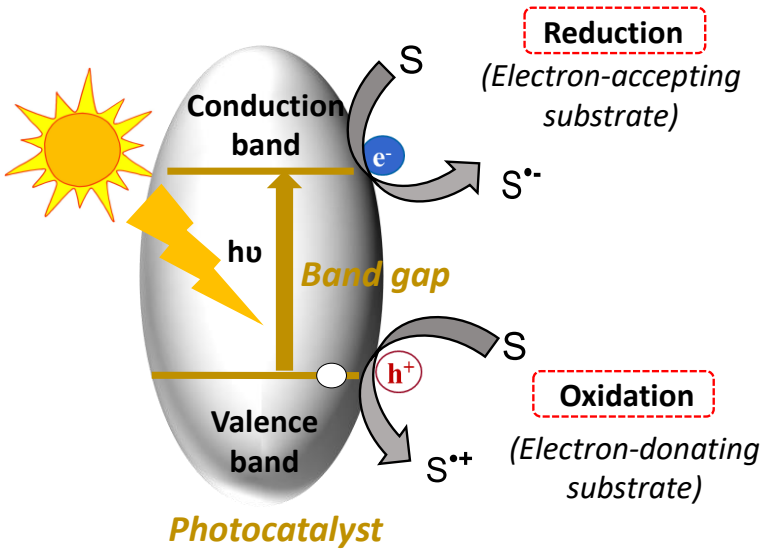

Figure 1. Schematic illustration of the formation of photogenerated electron-hole pairs upon absorption of light. S: substrate.

Once subjected to photons radiation of energy ($h\upsilon$) equal or higher than that of the band gap, an electron can transit from the valence band (VB) into a vacant conduction band (CB), leaving behind a positive hole in the VB. The photogenerated electrons/holes can migrate to the surface of the semiconductor and interact with eventual adsorbed substrates: the photoexcited can reduce an electron acceptor substrate whereas, the positive holes can trap an electron from a donor substrate, causing its oxidation. Therefore, both oxidative and reductive cycles for distinct substrates can be performed, which expand the repertoire of photoredox reactions. Nevertheless, it is worth mentioning that some of the generated charge carriers could not react with the adsorbed substrates and could recombine within the bulk/surface of the semiconductor engendering the release of heat. The charge carriers' recombination is then deleterious for the photocatalytic activity and must be considered. [60-62]

Following the preceding explanation, change in Gibbs free energy (ΔG) is frequently discussed to predict whether a given photocatalytic reaction is thermodynamically feasible. Reactions with a negative ΔG indicates that they can occur spontaneously with release of free energy and are called exergonic reactions (**Figure 2a**). In contrast, reactions with a positive ΔG ($\Delta G > 0$) require an input of energy (i.e photons) to occur and are known, as endergonic reactions (**Figure 2b**). Herein lies the most significant difference between conventional catalysis and photocatalysis; during a catalytic process, the reaction rate is increased by reducing the activation energy of the intermediate states, leading to negative Gibbs energy change. This limits catalysis to only thermodynamically possible reactions.

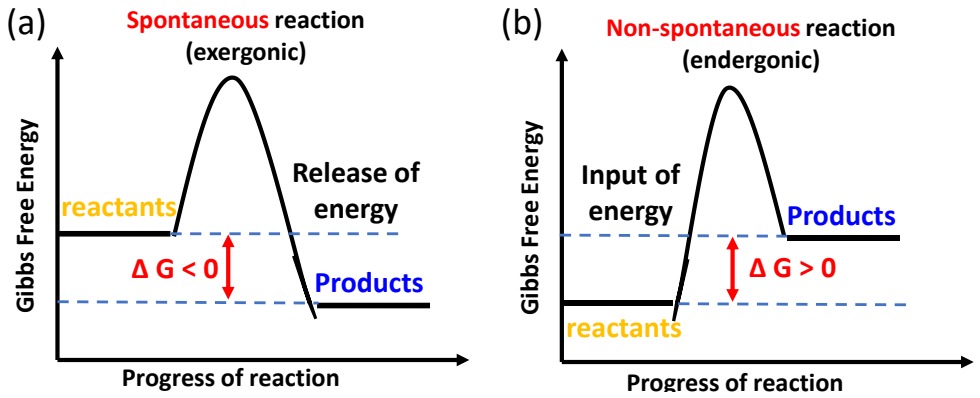

Figure 2. Changes in free Gibbs energy in case of (a) exergonic and (b) endergonic reactions.

However, photocatalysis is able to drive thermodynamically reactions with overall negative and positive ΔG, with respect to the redox potentials. A photocatalytic reaction requires the standard electrode potential of a substrate to be reduced ($E_{red.}$) to be lower (more anodic), than the CB bottom ($\Delta G_e < 0$) and the redox potential of a substrate to be oxidized (Pox) to be higher (more cathodic), than the VB top ($\Delta G_h < 0$). The overall ΔG corresponds to the difference between $E_{red.}$ and $E_{ox.}$and can then be either positive or negative depending on whether $E_{red.}$ is higher or lower than $E_{ox.}$, respectively.[60, 61, 63] A noteworthy example is the photocatalytic water splitting reaction into molecular hydrogen and oxygen, which can be achieved despite its large positive ΔG of 237 KJ mol^{-1}.[64, 65]

Once the thermodynamic requirements for a given (photo) catalytic process are satisfied, the focus would be next on how fast does a reaction proceed. Reaction rates can be generally predicted by kinetics. Kinetics of reactions occurring on a solid surface, i.e., photocatalysis, are different to those occurring in homogenous phase (solutions or in gas phase). Indeed, the latter exhibits often a first order reaction rate (r), with the concentration (or molar amount) of a substrate or a product ([A]) being directly proportional to the reaction time (t).[60]

$$r = -\left(\frac{d[A]}{dt}\right) = k\,[A]$$

Regarding photocatalytic processes, first order kinetics are also observed with two possible reaction models; “diffusion-controlled” or “surface reaction-limited” models. For the diffusion-controlled process, the surface reactions and the following desorption process take place very quickly and engender a very low concentration of adsorbed molecules on the surface. This results in an overall rate corresponding to the rate of adsorption of substrate molecules. It is noteworthy to mention here that, the rate constant k reflects the diffusion constant and the effective surface area of a substrate and does not involve the photocatalyst reactivity. For surface-reaction limited process, the overall rate corresponds to the rate of the surficial reaction (surface adsorption in equilibrium during the reaction) and is not

proportional to the substrate concentration, i.e., the reaction of the photogenerated e^-/h^+ with the eventual surface adsorbed substrates. Although these models obey to first order rate law, this is still not comparable to the first-order kinetic of monomolecular reactions discussed above and Langmuir-Hinshelwood model has been then suggested to discuss the photocatalytic reaction's mechanism in suspensions. The L-H mechanism implies a linear reciprocal relation between the photocatalytic reaction rate and the concentration of reaction substrate in a solution and defines the reaction rate as:

$$r = \frac{ks*KC}{KC - 1};$$

where *r*, *C*, *k*, *K*, and *S* are rate of the reaction, concentration of a substrate, rate constant, adsorption equilibrium constant, and saturated amount of adsorption, respectively. Needless to say, as mentioned previously, that the recombination process, which may occur within the bulk /surface of the photocatalyst, would affect the overall photocatalytic reaction rate.[60, 61, 66]

3.2. Visible light photocatalysis

Visible light constitutes the largest fraction of the solar spectrum and artificial illumination sources (44%). Visible-light photocatalysis has drawn much attention due to its potential applications in environmental remediation and organic transformations. Several visible light responsive photocatalysts with efficient solar utilization have been developed over the last decade and tested for a wide range of photoredox reactions such as transition metal complexes,[7, 9, 67] organic dyes,[13, 68-72] metal sulfides,[73] metal oxides,[74-76] graphitic carbon nitride,[77, 78] and metal/organic composites.[79-82] They can be classified either as homogeneous or heterogeneous photocatalysts, as described in **Figure 3** and the following paragraphs.

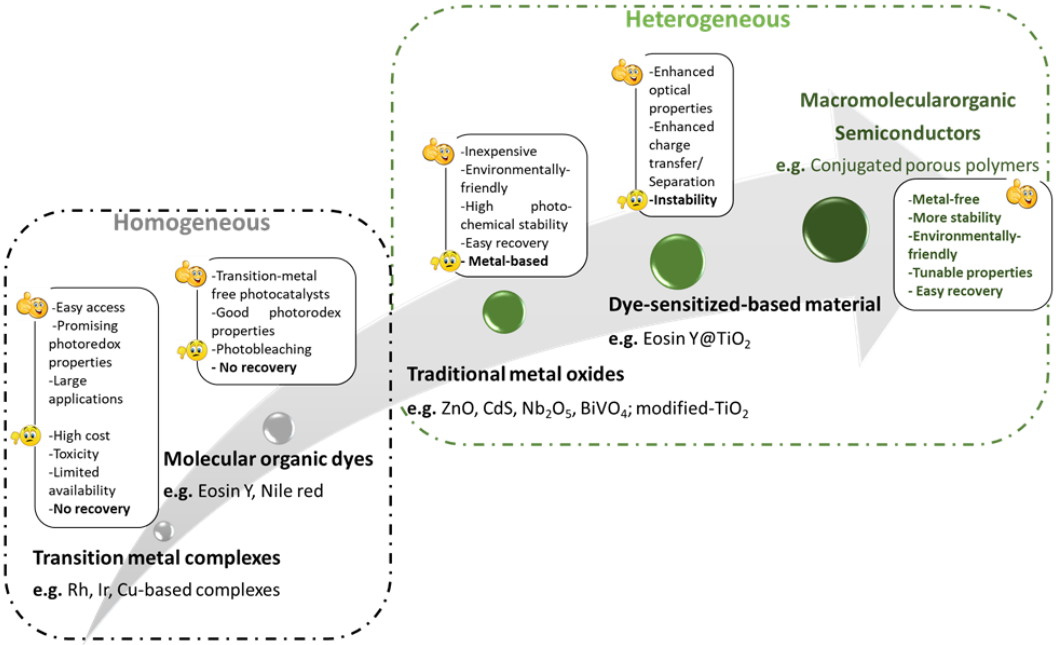

Figure 3. Most common visible-light homogeneous and heterogeneous photocatalysts with specific properties.

3.2.1. Homogeneous photocatalysis

Homogeneous photocatalysis implies that the photocatalyst and the substrates are in the same solvent phase. When a photocatalyst is irradiated by visible light, an electron transits from the ground state to the excited state forming (PC*). The excited photocatalyst (PC*) can then undergo a reductive quenching cycle via accepting an electron from a donor, returning to the ground state in reduced form ($PC^{\cdot-}$). On the other hand, it can undergo an oxidative quenching cycle via donating an electron to an acceptor, coming back to the ground state in the oxidized form ($PC^{\cdot+}$). Both oxidative and reductive quenching cycles enable the photoredox reactions. Moreover, the resulting excited photocatalyst can further undergo a second single electron oxidation/reduction, and returns to its original oxidation state (**Figure 4**).[68, 83, 84]

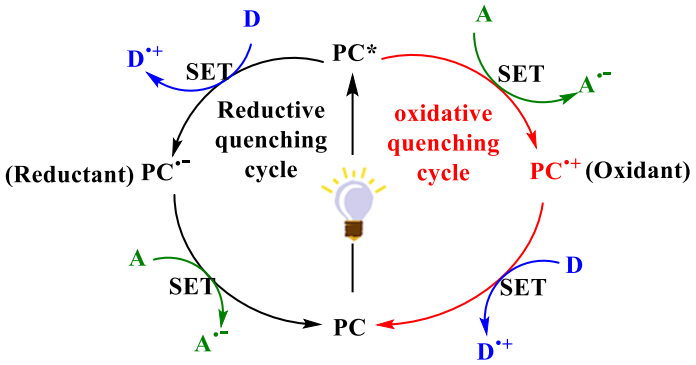

Figure 4. Homogeneous photoredox catalysis, A: Acceptor; D: Donor; PC: photocatalyst, SET: Single electron transfer. Adapted from [85].

Ruthenium and iridium-based transition metal complexes are the most studied homogeneous photoredox catalysts due to their outstanding photophysical and chemical properties, such as their good absorption of visible light, long excited state lifetime, reversible redox properties and tunable optical properties by variation of ligands (**Figure 5a**).[7, 84, 86-88] However, their high costs, their limited availability in Nature, their instability (sensitivity) under oxygen or a moisture and the high toxicity of ruthenium and iridium salts restrict their utilization in industrial applications.[89] More recently, other metal-based coordination compounds based on chromium (III), iron (II), nickel (0), zirconium (IV), cerium (III), molybdenum (0), cobalt (III), uranium (VI) and copper (I) have attracted much attention as cost effective alternative to the Ru and Ir-counterparts.[8, 90, 91] Among them, copper complexes are gaining attention due of their distinctive coordination chemistry and various redox chemistry behaviors, leading to broad applications in diverse catalytic fields, i.e.; water splitting,[92] and CO_2 reduction,[93, 94] Nevertheless, these materials are still subject to challenges related to the environmental impact of metals. Therefore, the need to develop new-eco-friendly metal-free homogeneous photocatalysts became imminent. Later, photo-organo-catalysts (POCs), or small-molecule organic photocatalysts, such as organic dyes have been widely investigated as efficient, metal-free, visible-light alternative photocatalysts for several photochemical and photosynthetic applications (**Figure 5b**).[13, 68, 71, 72] As example, xanthene dyes, i.e; Rose Bengal, Eosin Y, Rhodamine B (RhB), rhodamine derivative (Rh6G), and acridiniuims dyes, i.e; 9-mesityl-10-methylacridinium (Mes-Acr+), have been extensively used in several visible light-driven organic transformations with performances, analogue or greater than that of $[Ru(bpy)_3]^{2+}$.[13] For example, methylene blue was found more efficient than $[Ru(bpy)_3]^{2+}$[95] at catalyzing the aryl boronic acid oxidation, leading to high yield of phenol adducts.[96]

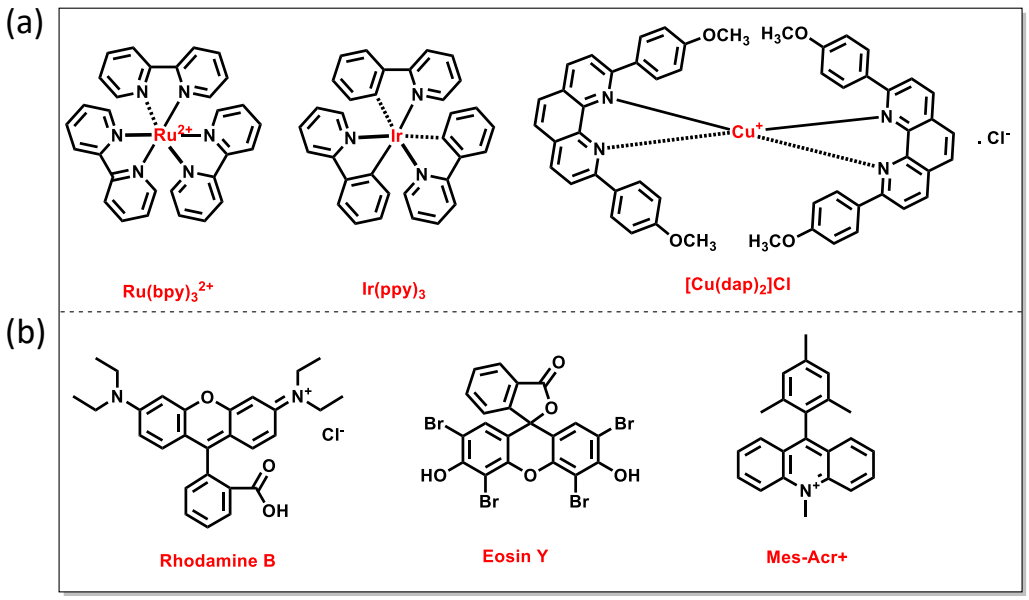

Figure 5. Chemical structures of (a) ruthenium, iridium and copper complexes and (b) some organic dyes.

Despite the achievements, these systems exhibit still distinctive drawbacks, notably the poor photostability (photobleaching), thermal instability, and issues in recycling processes, which limits further development in scaling up strategies as well as the long-term commercial implementation. Thus, an increase focus has been aimed on the development of heterogeneous photocatalytic systems, which could overcome these issues.

3.2.2. Heterogeneous visible-light photocatalysis

Heterogeneous photocatalysis implies that the photocatalyst and the substrates are in different phases. The process involves mainly electron and energy transfers, similarly to homogeneous photocatalysis (**Figure 6**): upon illumination, electrons are excited from the valence band (VB) of the photocatalyst to its conduction band (CB), creating simultaneously an oxidizing and a reducing entities on a single particle. The photogenerated holes/electrons pairs can then oxidize and reduce electron donor/acceptor substrates via single-electron transfer.[85, 97, 98] Intense research efforts have been devoted to develop efficient heterogeneous photocatalysts for synthetic and environmental applications, including metal-based (e.g.: inorganic semiconductors: metal oxides, metal sulfides, modified metal oxides (doping, surface modification, dye sensitization) and non-metal based; (e.g.: organic semiconductors: carbon nitride, such as graphene, reduced graphene oxide, g-C_3N_4, and polyoxometalates (POMs) conjugated polymers).[73-76, 78-81]

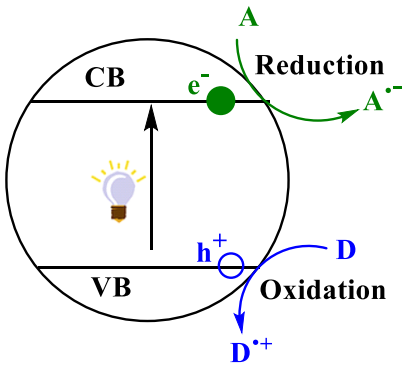

Figure 6. Heterogeneous photoredox catalysis. A: Acceptor; D: Donor, (e^-,h^+): photogenerated electrons and holes. Adapted from [85].

3.2.2.1. Metal-based heterogeneous photocatalysts

Titanium dioxide (TiO_2) is a naturally occurring mineral found in the earth's crust, which after processing, can be used in a range of industrial and consumer products, including paints, coatings, adhesives, paper, printing inks, textiles, as well as ceramics, floor and wall coverings, roofing tiles, cosmetics, pharmaceuticals and food colorants. More recently, TiO_2 is gaining popularity in the field of photocatalysis and became the most frequently used heterogeneous semiconductor for water purification,

energy conversion and in organic synthesis.[99-102] Nevertheless, due to its wide band gap, TiO_2 is only photoactive under ultraviolet irradiation (λ < 380 nm), which limits often their practical applications. Therefore, several approaches have been implemented to extend its absorption range into the visible region. For instance, Rueping and co-workers have reported the employment of TiO_2 P25 as efficient photocatalyst for the visible-light driven Meerwein-arylation of heteroaromatic compounds in presence of aryldiazonium salts.[103] Indeed, the authors revealed that the surface complexation between TiO_2 and the reagent is responsible of visible-light absorption; i.e.; the aryldiazonium salts, in contact with TiO_2 P25, forms a TiO_2-diazoether complex, establishing of a new electron donor level above the VB of the metal oxide, narrowing then the band gap.[103] Other researchers have largely focused on the so-called "dye-sensitization technique" as more efficient strategy to improve the TiO_2 absorption into broader visible light range.[104] The principle consists of anchoring a dye molecule at the surface of TiO_2 semiconductor. Once illuminated, the dye sensitizer gets excited and an electron jumps from its HOMO to its LUMO. Then, the photogenerated electron can be injected into the unoccupied TiO_2 states (CB). Another possibility is that the electron is directly excited from the HOMO of the sensitizer level to the CB of TiO_2.[105] In both cases, the presence of the dye sensitizer narrows the energy band gap and leads to visible light responsivity. As example, Li Ren and co-workers have used Eosin Y as a dye sensitizer and the combined system (Eosin Y@TiO_2) has demonstrated its efficiency in selectively oxidizing benzyl ethers to the corresponding benzoate esters under blue light irradiation.[106] Last but not least, scientists revealed that doping TiO_2 surface with metals or non-metals could be an efficient strategy to improve the visible light absorption, enhance charge separation, as well as reduce electron-hole recombination rates.[85, 107, 108] Shen and co-workers have shown that the doped nickel (II) oxide on TiO_2 (NiO@TiO_2) can catalyze the cascade radical carbon-carbon bond formation/cyclization of N,N-dimethylanilines with N-phenylmaleimides under blue light irradiation.[109] Other than TiO_2 based photocatalysts, several metal oxide semiconductors have been developed as efficient heterogeneous photocatalysts in promoting important organic transformations,[100] including zinc oxide (ZnO),[110-112] Niobium pentoxide (Nb_2O_5),[113, 114] tungsten trioxide (WO_3),[115-117] Bismuth(iii) oxide (Bi_2O_3),[118-121] and Bismuth vanadate ($BiVO_4$).[122] For example, Shinya Furukawa and co-workers showed the ability of Nb_2O_5 in oxidizing primary, secondary, and cyclic amines under visible light irradiation.[114] Cadmium-based photocatalysts such as cadmium sulfide (CdS) and cadmium selenide (CdSe) have been also used in various visible-light organic transformations.[123-126] One of the main advantage of these materials is the ability to tune their optical properties by modifying the nanoparticle size.[127] As example, CdS nanosheets demonstrated their efficiency in the photocatalytic oxidative coupling of benzyl amines to imines under visible light.[124] Interestingly, lead-halide perovskite

($APbX_n$), have emerged as promising materials with tunable optical properties for application in organic synthesis.[128] The photocatalytic formation of symmetrical and unsymmetrical disulfides from thiols has been achieved, for example, using $CsPbBr_3$ in air and under blue light irradiation.[129] Despite their successful application in light-mediated organic transformations, the high cost and limited availability of precious metals have hindered the use of metal-based visible light photocatalysts in large-scale and commercial application. Thus, based on the aforementioned drawbacks, the development of new metal-free based visible light photocatalysts is highly desired.

3.2.2.2. Non-metal based heterogeneous photocatalysts: Carbon nitrides

Graphitic carbon nitrides (g-CN) are a class of metal-free conjugated polymers, containing mainly two earth-abundant elements – carbon, nitrogen and hydrogen impurities (**Figure 7**). They have been intensively studied over the last years for heterogeneous photocatalysis.[130, 131] They possess a band gap of ca. 2.7 eV and allow reactions under visible light irradiation. The materials are advantageous due to the potentials of their valence and conduction bands, which are suitable for the oxidation and reduction of the most common organic compounds.[78, 85, 130] From the design perspective, g-CN based polymers could be easily synthesized from readily available, cheap and nitrogen-rich precursors such as urea, cyanamide, dicyandiamide, or melamine. Interestingly, their properties can be tailored via the synthetic approach, the precursors' nature and the polymerization conditions.[131] For instance, the optical and electronic properties can be modified by only varying the C/N ratio, or the experimental conditions or the polymerization degree.[132] The addition of either a molecular doping agent (anchoring organic groups to the precursors)[133, 134] or an elemental doping agent (insertion of metal or non-metal into the CN framework),[135] can affect significantly the band gap, the VB and CV positions and influence then the photocatalytic performance. Their textural and structural properties, i.e. surface area, pore size, pore size distribution, morphology and crystallinity, are also important for photocatalysis and can be adjusted through surface engineering technique (e.g. use of template).[136] In addition, g-CN materials are chemically and thermally stable, inexpensive, recyclable and reusable, which is crucial for potential industrial scale-up.[137] Therefore, tremendous research efforts have been devoted to investigate the use of g-C_3N_4 based materials as efficient metal-free visible light photocatalyst for various photocatalytic applications such solar fuel production,[138, 139] (e.g. CO_2 reduction,[140] water splitting,[141])environmental remediation (e.g., degradation of organic pollutants),[130, 142-144] and organic synthesis. Herein are some reported organic transformations catalyzed over g-C_3N_4 based systems: selective oxidation of alcohols,[145-147] amines,[148, 149] sulfides,[150] hydrogenation of benzene,[151] photocatalytic Diels-Alder cyclization,[152] etc.

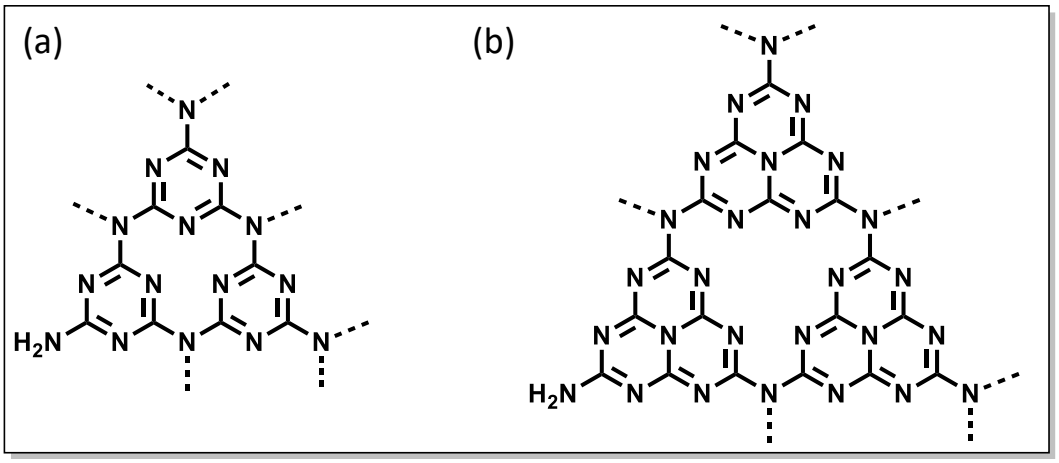

Figure 7. Structure of carbon nitrides consisting of (a) triazine (b) and heptazine.

Despite the aforementioned advantages and the broad field of applications, the usage of g-C_3N_4 as an efficient photocatalyst is still restricted by the limited chemical diversity due to the limited building blocks available (triazine and heptazine). Moreover, they suffer from the fast recombination of charge carriers,[137] the low surface area in absence of a template agent [153] and the necessity of structure modification to achieve the desired conversions.[146, 148, 149, 151]

3.3. Conjugated polymers (CPs)

π-conjugated polymers (CPs) have emerged as promising alternatives to the traditional inorganic semiconductors for photocatalysis. They are metal-free, organic semiconductor materials, consisting of fully π-conjugated systems with delocalized electrons along the polymer backbone. Their molecular structures can be finely-tuned to improve their visible light absorption. In addition, they exhibit excellent chemical stability and robustness. They also possess unique electronic and optical properties, enabling efficient charge separation and transfer, which is critical to trigger photoredox reactions. All these interesting features make CPs an attractive platform for visible-light driven photocatalytic applications.[25]

Conjugated porous polymers (CPPs) are a sub-class of conjugated polymers, containing fully cross-linked and fully π-conjugated network (**Figure 8**). The cross-linking structure, endows the CPPs with permanent intrinsic (nano) porosity, which, in addition to the fully π -conjugation, makes them more unique among the porous materials.[154, 155] Since the discovery of the first CPPs in 2007,[156] tremendous attempts have been made toward the design and synthesis of CPPs as versatile platforms for applications ranging from gas separation and storage, optoelectronic devices and energy storage,[157, 158] chemical sensors,[159-161] and photocatalysis.[154, 162, 163] The efficiency of these materials towards the above-described applications has been found to be highly dependent on the choice of the molecular building blocks and synthetic conditions, revealing the structure-property relationship of

CPPs.[155] In general, the design strategy consists of connecting π-conjugated organic building blocks and their spatial construction. In this regard, several conjugated bond formation reactions were reported, including Suzuki–Miyuara,[164] Sonogashira–Hagihara,[156, 165] Yamamoto,[166] Glaser, Heck,[167] Negishi,[168] or Kumada,[169] coupling reactions, direct arylation,[170, 171] as well as Friedel–Crafts reaction,[172] Schiff-base reaction,[173-175] etc. Moreover, various templating effects can be used to control the morphology. Post-synthetic modifications can be also considered to adjust the structure or function. Due to the strong covalent bonding within the network, CPPs possess superior chemical stability, even in presence of organic solvents, hydrofluoric acid, and high intensity-radiation.[165, 176] In addition, the key-feature of CPPs is the large variety of differentially functionalized monomers, which can be incorporated within their backbones. Therefore, by careful selection of the building blocks, the textural, morphological (porosity, specific surface area) and optoelectronic properties can be customized to suit their targeted application.[18]

Recently, several sub-classes of CPPs, such as conjugated microporous polymers (CMPs),[18] covalent triazine-based frameworks (CTFs),[177] or π- conjugated polyHIPEs (polymerized high internal phase emulsions)[21] have been developed and displayed great potential in visible light photocatalysis. Herein, the light will be shed on the CMPs and CTFs based materials since they are the main photocatalysts studied in this thesis.

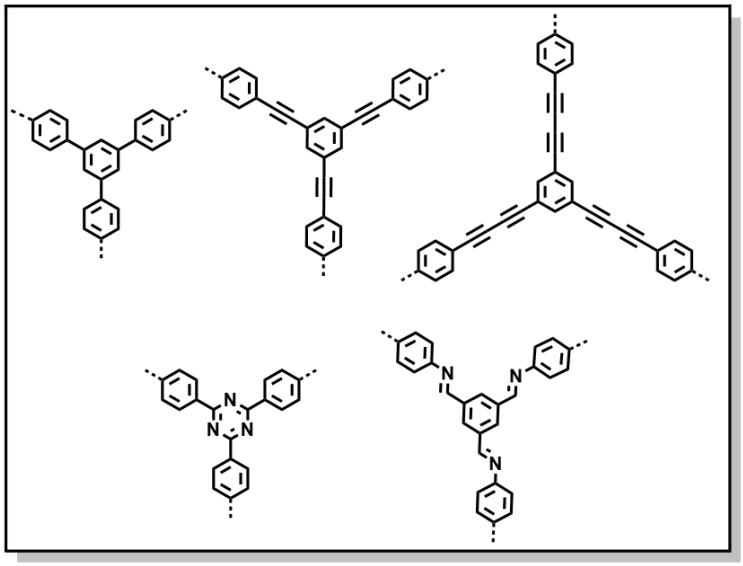

Figure 8. Some examples of conjugated porous polymers.

3.3.1. Conjugated microporous polymers (CMPs): synthesis and applications in photocatalysis

CMPs are a class of amorphous three-dimensional (3D) semiconducting polymers, combining extended conjugation and permanent microporosity. Indeed, they contain rigid aromatic groups, which are linked either directly to each other's or via establishing double or triple bonds, leading to the π-

conjugated microporous network. The alternation between single and double-/triple-bonds along the extended skeleton, imparts the CMPs with important electronic properties, which expand their range of applications. Moreover, they possess a broad structural diversity due to the variety of the molecular building blocks, which allows the control of functionalities and structure in CMPs. One other feature of these materials is the high surface area and the microporosity, which contribute in the reactivity and an enhancement in the light harvesting properties. Since the discovery of the first CMP by Cooper in 2007,[156] much attention has been given to the development of CMPs with unique properties and practical applications.[18, 178, 179]

3.3.1.1. Synthesis

CMPs can be obtained, either through a homocoupling of a unique monomer or via reaction of two or more monomers. Their porosity, morphology and optoelectronic properties are mainly governed by the monomer geometries.[156, 178, 179] The incorporation of different heteroatoms or metals in the monomers or post-synthetic modifications in CMPs can also affect these properties.[180, 181] Various reactive coupling groups has been used to prepare CMPs, including halogens, boronic acids, alkynes, alkenes, nitriles, amine, and aldehydes substituted aromatic monomers. A diverse pool of synthetic routes has been reported in the literature,[18, 178] and the most common approaches are summarized in **Figure 9**.

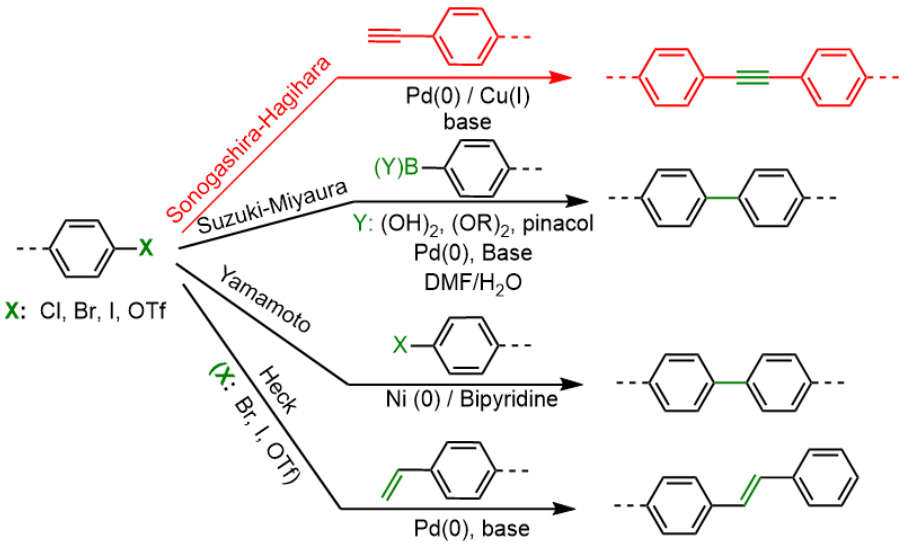

Figure 9. Most common synthetic routes of CMPs.

In this work, Sonogashira-Hagihara coupling reactions have been employed as effective synthetic route of the CMPs. In fact, this approach, firstly reported by Sonogashira, Tohda and Hagihara in 1975 [182], has been also used to prepare the first CMPs and consists of coupling an aryl-/vinyl halide or triflates with an alkyne-containing monomer using a palladium catalyst (e.g.,

tetrakis(triphenylphosphine)palladium) and a copper cocatalyst (e.g., copper(I) iodide), in the presence of an amine base.[182] It is noteworthy to mention that copper-free Sonogashira-Hagihara reactions have been used to make CMPs [183, 184] but the presence of a Cu co-catalyst in the coupling reaction has shown an improved reactivity with higher yield of product.[185, 186] This has been attributed to the fact that copper (I) salt and amines led to the generation of alkynylcopper species from terminal alkynes, as important intermediate for transmetalation process.[182] In addition, these reactions have been tested initially in fours solvents: N,N-dimethylformamide (DMF), 1,4-dioxane, tetrahydrofuran (THF), and toluene. However, the CMPs formed in DMF exhibited the highest surface areas and levels of microporosity.[187] Importantly, the Sonogashira-Hagihara reaction requires anaerobic and anhydrous reactions conditions as the alkyne-containing monomers may homocouple under oxygen atmosphere.[186, 188] In general, this synthetic approach is easy to implement and is compatible with different types of functional groups, without the need to protect the groups or the use of strong bases. Moreover, it leads to high yield products and selectivity under mild operation conditions, and has therefore gained importance in organic synthetic schemes of the pharmaceutical and agrochemical industries.[189-191] More recently, this reaction can even be extended to green solvents such as water,[192] making it much more attractive for industrial applications.

The Sonogashira-Hagihara coupling reaction involves two related catalytic cycles, namely the Pd-cycle and the Cu-cycle (**Figure 10**). It follows the general oxidative addition-reductive elimination pathway. The “palladium” cycle is analogues to other C-C coupling reactions, while the “copper” cycle is still under debate.[189] First, Pd(0) active species (Pd^0L_2) can be generated either from (Pd^0L_4) via dissociation of two neutral phosphine ligands or from the reduction of different Pd(II) pre-catalysts by reductive reagents present in the reaction mixture (e.g., the alkyne substrate or an added phosphine ligand). Then, an oxidative insertion of the active Pd(0) to the substrate R1-X (R1= aryl, hetaryl, vinyl; X= I, Br, Cl, OTf) takes place. The resulted Pd(II) complex reacts with the terminal acetylene via a transient copper(I) acetylide species, which are generated in the “copper cycle”. This results in the formation of an alkynylpalladium(II) intermediate ($R_1Pd(-C{\equiv}CR_2)L_2$). At the end, a trans/cis isomerization of the intermediate followed by reductive elimination give rise to the cross-coupled product and regenerate the active Pd(0) species for the next catalysis run.

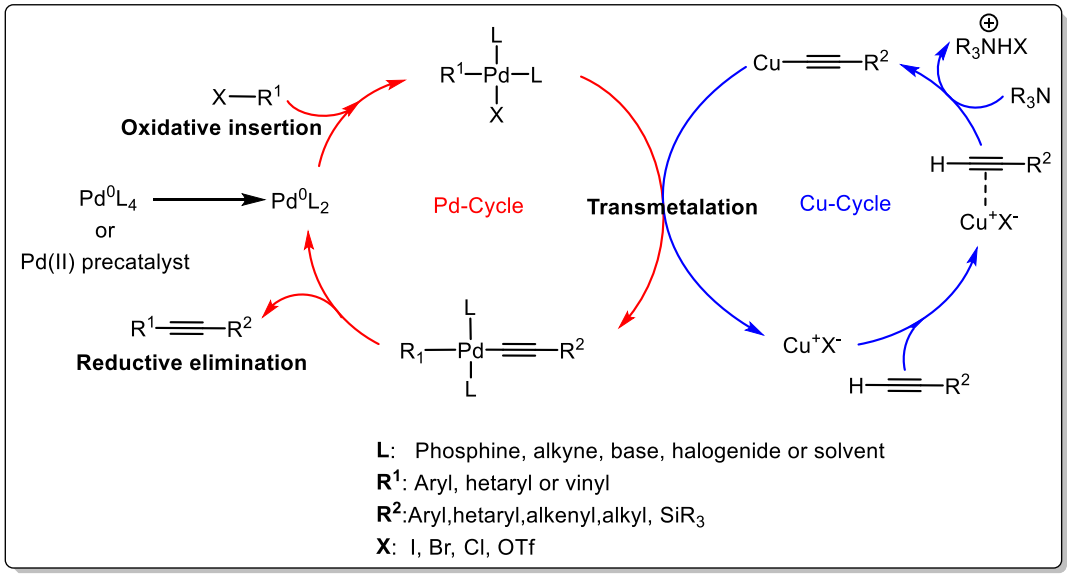

Figure 10. General mechanism for the Pd/Cu catalyzed Sonogashira cross-coupling reaction.

3.3.1.2. Applications in photocatalysis

Due to their extended conjugation, high porosity, tunable optoelectronic properties and often-outstanding chemical and thermal stabilities, CMPs have been used in a wide range of applications such as gas storage and separations,[172, 193-197] encapsulation of chemicals,[198, 199] heterogeneous catalysis,[200-202] photocatalysis,[43, 82, 165, 203-206] light emittance,[207-211] chemosensing,[160, 161, 212, 213] and energy storage.[214-217] In the following paragraphs, the use of CMPs in the photocatalysis field is highlighted.

The earliest report about CMPs-based photocatalyst was released by Vilela and co-workers in 2013.[165] They reported the use of a benzothiadiazole-based CMP as metal-free photocatalyst for photocatalytic oxygen activation under visible-light irradiation. The CMP photocatalyst has demonstrated its efficiency in oxidizing α-terpinene into ascaridole in 96% conversion with 420 nm irradiation. Since then, series of CMPs materials have been intensively explored as heterogeneous photocatalysts for a vast number of visible light-induced catalytic applications. For example, Son and co-workers have investigated the use of benzodifuran-containing CMPs as efficient photocatalyst for photocatalytic oxidation of primary amines into imines under blue LED irradiation, achieving conversions up to 98%.[41] Maji and co-workers have presented a structural design strategy of CMPs, using an electron donor (tetraphenylethylene (TPE)) and various ratios of an electron-acceptor (9-fluorenone (F)), and have demonstrated their excellent photocatalytic activities towards hydrogen generation under visible-light irradiation.[218] The CMP with optimal band gap of 2.3 eV achieved the highest H_2 evolution of 660 μmol h^{-1} g^{-1}, probably due to the most efficient charge transfer.

Our research group has also designed a series of CMPs nanoparticles containing thiophene (Th) moiety as electron-donor unit and benzothiadiazole (BT) moiety as electron-withdrawing unit in various ratios and have assessed their performances for the photo-inactivation of Escherichia coli K-12 and B. subtilis.[219] It was shown that the pure benzothiadiazole containing CMPs (Th-BT-100), exhibited the best light-induced antimicrobial activity due to the strongest singlet oxygen generation, playing a crucial role in the photo-inactivation process. Enhanced efficiencies with increased BT unit have been also observed. Another research study revealed the use of an encapsulated-photoactive CMP within a giant polymer vesicle as efficient and robust metal-free minireactor for the regeneration of nicotinamide adenine dinucleotide (NAD^+) cofactor from the non-enzymatic visible-light driven photocatalytic oxidation of NADH.[220] Recently, broader range of photocatalytic applications over CMPs has been covered[178, 179, 221], including water splitting,[222-224] CO_2 reduction,[225, 226] photocatalytic dyes degradation,[163, 227] and organic transformations,[204] e.g., Suzuki coupling reactions,[82] Stille-type coupling reactions,[228] photooxidative hydrogenation of arylboronic acids,[42] and [2+2] cylcloaddition of styrene derivatives.[229]

Besides the wide range of applications, scientists have been seeking for new strategies to improve better the photocatalytic performance of CMPs. To do so, CMPs can be finely tuned involving their molecular structure (conjugation extension, appropriate selection of building blocks (e-donor/acceptor combinations, functional components introduction, etc.), their morphology (large accessible surface area, porosity, etc.) and their optical and electronic properties (band gap engineering, HOMO and LUMO adjustment, etc.).[179] Recent reports have also shown that the incorporation of different functional nanomaterials, such as transition metal elements or other semiconductors materials,[227, 228, 230, 231] into the CMP networks enhance the photocatalytic performances due to the synergistic effects of the components.

3.3.2. Covalent triazine frameworks (CTFs): synthesis and applications in photocatalysis

Covalent triazine frameworks (CTFs) are seen either a sub-class of COFs due to their ordered backbone structure, or as conjugated porous polymers given their conjugated nature and porosity. They are fully π-conjugated networks, which are comprised of triazine units with strong aromatic C=N linkages and possess permanent porosity (**Figure 11**).The conjugation as well as the strong covalent bonds endow CTFs with unique optical and semiconducting properties and high chemical stability.[177, 232]

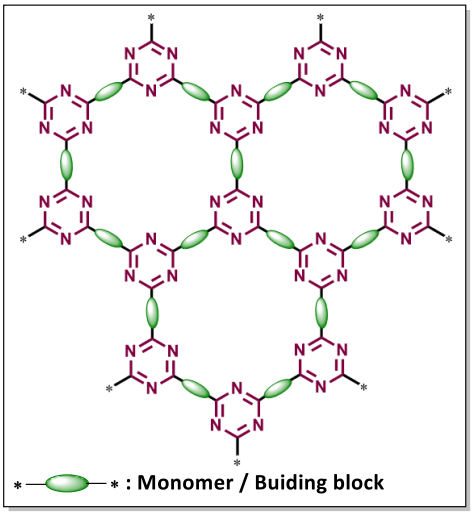

Figure 11. Schematic representation of covalent triazine frameworks.

CTFs are highly stable even in presence of strong acids and bases,[233] giving them a great potential over the other porous polymers to be used for future applications. Note that the presence of strong irreversible covalent bonds usually hinders the formation of ordered structures and lead often to amorphous materials. Although most of the reported CTFs were amorphous (or semi-crystalline), highly crystalline CTFs can still be obtained.[234-236] Another feature of CTFs is their chemical tunability: apart from the high intrinsic nitrogen content, additional nitrogen groups can be introduced within CTFs' network by adding nitrogen-rich functional groups in the monomer structure, e.g., pyridine, pyrimidine, dimethylpyridine (lutidine), bipyridine and phenylene-bispyridine.[237-240] The increase in nitrogen content can be advantageous for several practical applications, e.g., CO_2 reduction. An enhanced performance of CTFs has been attributed to enhanced interactions between nitrogen atoms and CO_2 molecules. Moreover, CTF's surface can be modified via incorporation of functional heteroatoms, which allows further the control and tunability of the features above.[193, 241, 242] All these properties make CTFs a versatile platform for various applications, such as separation and storage of gases, energy storage, environment remediation and dye degradation, photocatalysis and heterogeneous catalysis.[177, 232, 233]

3.3.2.1. Synthesis

The first synthetic route of CTFs has been reported by Thomas *et al.*, who have employed nitrile monomers and zinc chloride ($ZnCl_2$) as Lewis acid under ionothermal conditions.[243] They have used high temperature (> 400 °C), under which molten $ZnCl_2$ has been obtained and has catalyzed the trimerization of the nitrile-based monomers into triazine units. Most of the synthesized CTFs using this method have been either amorphous or semi-crystalline, except of CTF-0,[235] CTF-1,[243] and CTF-2.[236] This has been attributed to the planarity of the applied monomers as well as the reaction conditions.

A planar monomer (e.g., 2,6-dicyanonaphthalene) generates highly crystalline CTFs, while a contorted structure (e.g., 2,5-dicyanothiophene) forms amorphous CTFs (**Figure 12a**). On the other hands, the use of high temperature often lead to material's carbonization, unwanted side reactions, nitrile groups' cleavage, deficient pore enlargement, pore wall collapse and therefore loss of crystallinity.[243, 244] Moreover, these very harsh conditions limit the large-scale synthesis.

Then, Cooper *et al.* have sought for milder alternative and have developed the so-called "superacid method", in which the polymerization of nitrile monomers has occurred in presence of trifluorosulfonic acid as catalyst under both room temperature and microwave-assisted conditions.[245] In this case, all CTFs were obtained as amorphous and this method is advantageous because it avoids undesired decomposition, chemical bonds' cleavage and material's carbonization under low temperatures.[245] However, the synthesized CTFs have shown a limited degree of long-range order. To overcome this issue, Xu *et al.* have modified the superacid method by employing interfacial conditions and have designed successfully layered and crystalline CTFs.[246] Indeed, CH_2Cl_2 has been used as a solvent because it can dissolve a wide range of monomers. Moreover, CH_2Cl_2 is immiscible with CF_3SO_3H, the mixture of which leads to abundant dynamic CH_2Cl_2/CF_3SO_3H interfaces under vigorous stirring. This dynamic interface plays a crucial role in the preparation of crystalline CTFs. Nevertheless, this method requires large solvent consumption, which limits its industrial implementation. Note that the aforementioned methods have used nitrile monomers as building blocks. Few methods using other monomers' types (e.g, aldehyde, amidine, amide etc.) have been also exploited, i.e., phosphorus pentoxide (P_2O_5) catalyzed method,[247] amidine based polycondensation methods,[248, 249] and a Friedel–Crafts reaction method.[250] For instance, Jin and Tan and co-workers reported the preparation of CTFs via the polycondensation of amidines and aldehydes monomers under relatively mild conditions; using dimethyl sulfoxide (DMSO) as solvent and cesium carbonate (Cs_2CO_3) as base, at 120 °C (**Figure 12b**).[249] The obtained CTFs were amorphous. The same authors were further able to synthesize ordered crystalline CTFs by using alcohols monomers instead of aldehydes. Indeed, a controlled in-situ oxidation reaction, which consisted of gradually oxidizing the alcohols monomers to aldehydes in presence of DMSO, air and base, was found to be the key step in slowing down the nucleation rate in initial stage and promoting the crystal growth in the polymerization stage, leading therefore to highly crystalline CTFs **(Figure 12b)**.[248]

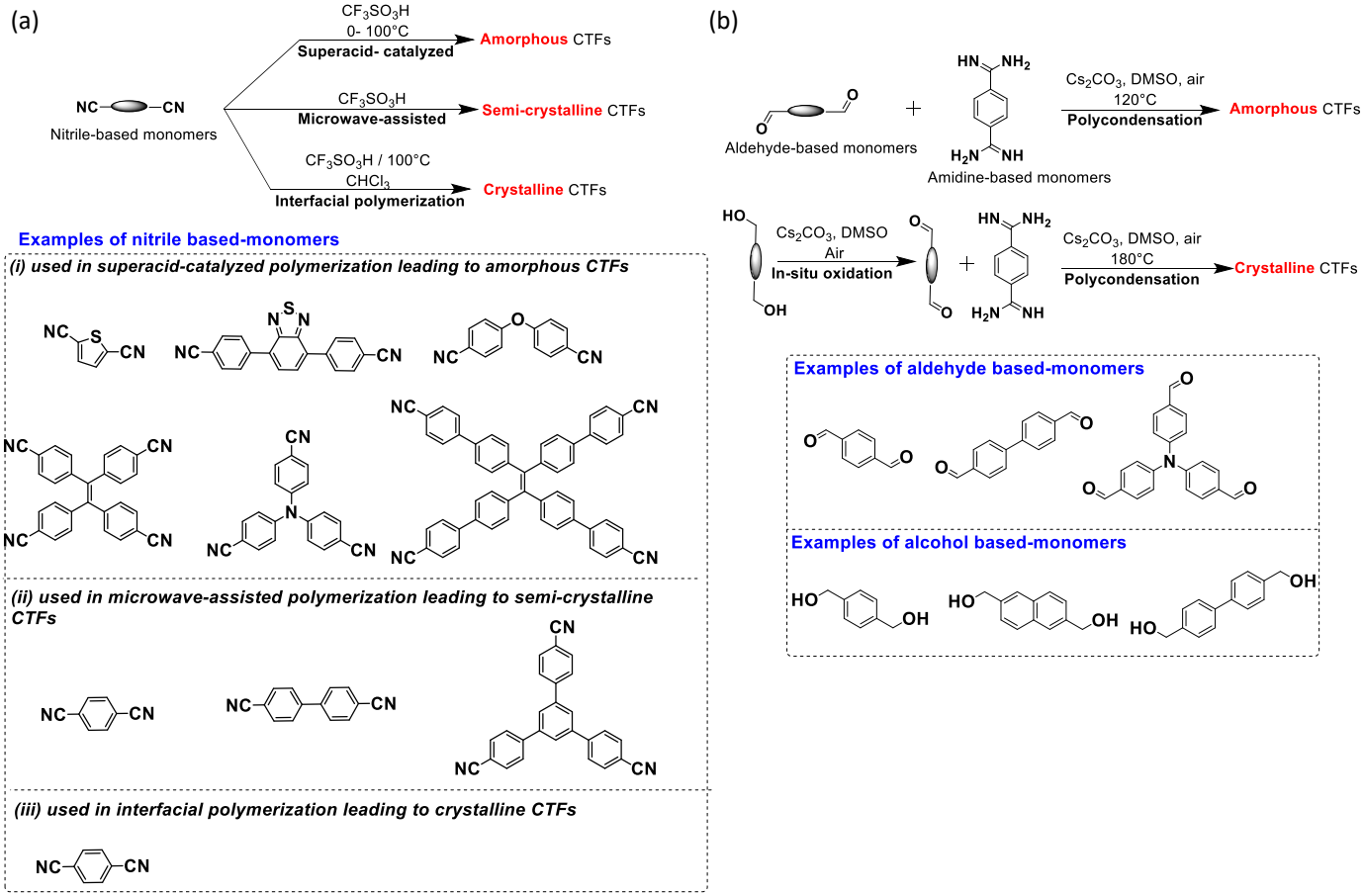

Figure 12. Synthetic routes to prepare CTFs using (a) nitrile and (b) aldehyde based monomers.

More recently, our research group has taken inspiration from these synthetic protocols together with their associated drawbacks and have developed a novel, facile, solvent-free synthesis route of CTFs under relatively mild conditions (**Figure 13**).[46] In principle, CTFs are polymerized through trimerization of nitrile-functionalized aromatic units under trifluorosulfonic acid' vapors at 100 °C. The as-designed CTFs exhibited defined morphological, textural, optical and electronic properties. In this work, a slight modification of the previously described procedure has been adopted to construct the CTFs materials.

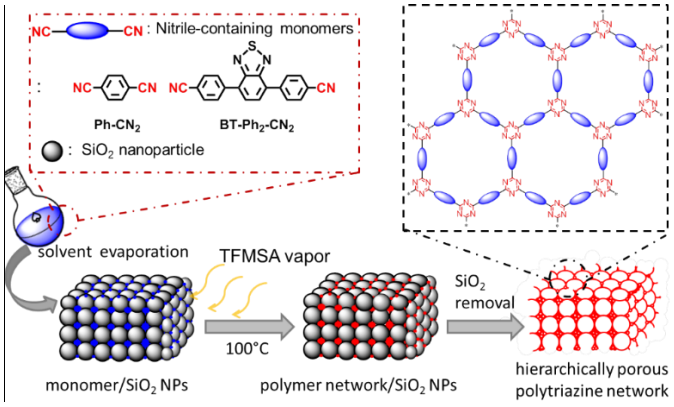

Figure 13. Schematic of solid vapor synthesis of CTF based materials.[251]

3.3.2.2. Applications in photocatalysis

Owning to their structural diversity, high BET surface areas, chemical and thermal stabilities, CTFs have been employed in various photocatalytic applications including photodegradation of organic pollutants, photocatalytic organic transformations, photocatalytic water splitting, photoreduction of CO_2, etc.[177, 232, 233] For example, Bi and co-workers have designed CTF based- materials with a graphene-like layered morphology and have shown their excellent photocatalytic activity for water splitting under visible light irradiation.[252] Wang and co-workers have demonstrated the efficiency of a benzothiadiazole-based CTF in promoting the photocatalytic reduction of CO_2 to CO, with a CO formation rate of 18.2 μmol h^{-1} and a high selectivity of 81.6%.[226] Song and co-workers have reported the use of a highly crystalline CTF as efficient photocatalyst for the degradation of methylene blue under visible light illumination.[35] More recently, Zhang and co-workers have investigated the application of CTFs in few light-driven organic transformations, i.e., selective oxidation of alcohols and saturated hydrocarbons,[46] photocatalytic synthesis of benzophosphole oxide,[253] and photocatalytic reduction of 4-nitrophenol (4-NP) to 4-aminophenol.[251]

3.4. Green chemistry

Nowadays, it has become widely admitted that there is an increasing need for more environmentally friendly processes in the chemical industry. This trend towards the so-called "Green Chemistry" or "Sustainable Processes" requires to shed more light on the economic and environmental effects of processes, together with their efficiencies. Green Chemistry can be defined as *"the utilization of a set of principles that reduces or eliminates the use or generation of hazardous substances in the design, manufacture, and application of chemical product"*.[254]

In this context, the choice of solvents is of great importance as the use of "inappropriate" ones can lead to high toxicity, risks, atmospheric pollution, waste management issues as well as health problems. For example, a waste charged with highly volatile solvents (e.g. chlorinated hydrocarbon-based), leads inevitably to pollution and health issues, as it is commonly removed by evaporation or distillation and it exposes workers to volatile organic compounds (VOCs). The use of polar aprotic solvents (e.g. dimethylformamide and dimethyl sulfoxide) results also in various environmental problems due to their high boiling, which hinder their removal by distillation. Due to their miscibility with water, they are often separated by washing with water, which give rise unavoidably to contaminated aqueous effluent.[48, 49, 255, 256] To overcome these issues, the best would be to run the reactions without any solvent. However, the latter is often essential to enable mass and heat transfers, affect solubility, stability and reaction rates and allow for thermodynamic and kinetic control over a given chemical process. A "good" solvent should

be relatively nontoxic and relatively nonhazardous, not inflammable or corrosive. Consequently, many efforts have been devoted to find sustainable reaction media for chemical reactions and notably the use of water as solvent has attracted recently much attention. Indeed, the use of water is very advantageous owning to its low-cost, abundant availability, non-toxicity, benignity, and non-flammability, which make it very attractive from both an economical and an environmental point of view. However, most of organic compounds are poorly soluble in water, and running organic transformations in water seemed to be detrimental at first glance. In contrast, water has been found to enhance the reactivities and selectivities due to its high polarity (i.e., hydrogen bonding, hydrophilicity, etc.) and unique physicochemical properties. Moreover, it eases the workup procedures, and enable the catalyst recovery, allowing organic reactions under mild reaction conditions.[48, 49, 255, 256]

The employment of conjugated porous polymers as photocatalysts in water has barely been studied. So far, there are only a few research reports about the use of CPPs in aqueous media or the synthesis of water compatible CMPs for photocatalytic reactions under visible light irradiation.[50, 51, 163] Recently, Zhang and co-workers have synthesized water-compatible azulen-based CMPs via post-protonation of azulene units within the CMP network. This system has served as efficient and recyclable photocatalyst for photoreduction of toxic heavy metal ions, e.g. photoreduction of aqueous chromium (VI), in water and under visible light irradiation.[51] Later, they have reported the design of stable and well dispersible conjugated microporous polymer nanoparticles by direct miniemulsion polymerization method. These CMPs have shown efficient photocatalytic activity in the degradation of rhodamine B and photooxidation of N,N,N′,N′-tetramethyl-pphenylenediamine under visible light irradiation.[163]

In the following thesis, we aim to design CPPs for a variety of photocatalytic applications in aqueous media under visible light irradiation.

4. Characterization techniques

4.1. UV-Vis spectroscopy (UV-Vis)

UV-vis spectroscopy is a unique technique, which allows qualitative and quantitative analysis of chemical compounds. It is based on the absorption of ultraviolet and visible light by a liquid sample. When the latter absorbs light with suitable energy photon, the constituent atoms and molecules undergo electronic transitions from a ground state (valence band) to an excited state (conduction band), resulting in distinct spectrum. The absorption intensity (A) follows the Lambert-Beer law and is proportional to the intensity of the incident monochromatic radiation before and after passing the measurement cell (I_0 and I).

$$A = \log\left(\frac{I_0}{I}\right) = \varepsilon * c * d$$

Where: ε, d and C are extinction coefficient, thickness of the measurement cell and concentration of the solution (C), respectively.

In addition, the optical band gap (E_g) could be deduced from the onset absorption in UV-Vis spectra following this equation:

$$E_{photon} = E_g$$

$$E_g\ (eV) = h * \nu = \frac{h * c}{\lambda} = \frac{1238\ (eV * nm)}{\lambda\ (nm)}$$

Where: h, ν, c and λ are Planck's constant, frequency of light, speed of light, wavelength of light, respectively.

In this work UV-Vis spectroscopy have been used to monitor the reaction kinetics by colorimetric methods.

4.2. UV-Vis diffuse reflectance spectroscopy (UV-Vis DRS)

Standard liquid UV-Vis spectroscopy is not suitable for insoluble solid samples (e.g. powder). UV-Vis diffuse reflectance spectroscopy (DRS) is an alternative to measure the absorption of opaque solid samples, which can be associated to the relative change in the amount of light reflected from the surface. Indeed, there is two different types of reflection: either regular or specular reflection usually related to the reflection from smooth surfaces (e.g. mirrors) and diffuse reflection related to the reflection from mat/dull surfaces (e.g. densely packed powders)(**Figure 14**). For example, considering an illuminated white wall (dull surface) by sunlight, the latter reflects the incident light at angles independent of the angle of incidence, whereas an illuminated mirror by sunlight reflects the incident light at angle of

reflection equal to the angle of incidence. When a solid sample (dull surface) is irradiated, the impinging light can undergo a reflection, a refraction and a diffraction over the sample surface.[257] Moreover, various factors can influence the diffuse reflectance spectra of a solid sample including particle size, packing density, shape and refractive power. An increase in the particle size cause an increase in the light penetration depth and attenuated scattering.[257, 258]

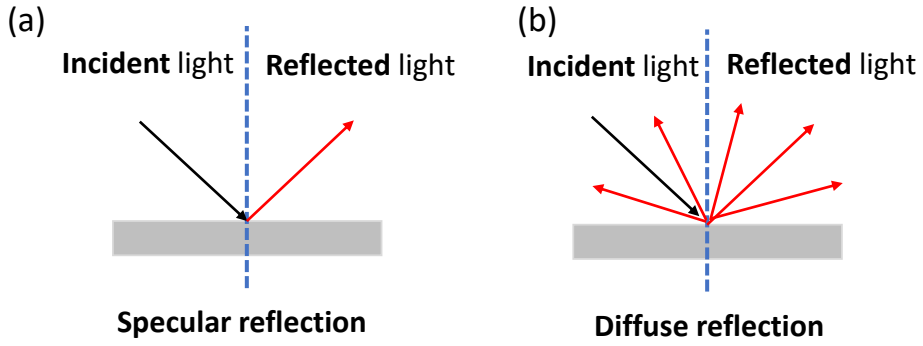

Figure 14. Two modes of light reflection: specular versus diffuse reflection.

In this work, UV-Vis DRS measurements were conducted to evaluate the absorption properties as well as the band gap energy of the synthesized photocatalysts.

4.3. Fourier transform infrared spectroscopy (FT-IR)

Infrared spectroscopy is an important characterization technique to elucidate the structure of matter at the molecular scale. It gives an insight into the chemical composition and the bonding arrangement of constituents within a material. The IR spectrum is obtained by Fourier transformation of the signal from an interferometer with a moving mirror to produce an optical transform of the infrared signal and gives a relation between intensity and frequency. Indeed, a molecule absorbs infrared radiation at specific frequencies, which are characteristic of its vibration modes (stretching, bending, rocking, etc.). Therefore, the pattern of vibrations provides a fingerprint of molecular structure and allow the identification of specific components or groups of atoms.[259] In this thesis, FT-IR was used as an important technique to identify the specific functional groups in the synthesized conjugated polymers.

4.4. Electron microscopy

The difference between electron microscopy and light microscopy lies on the use of an electron beam instead of light beam. Due to the shorter wavelengths of electrons in comparison to that of visible light source, electron microscopes give rise to higher-resolution images than standard light microscopes, with more reliable surface characterization and topology. Moreover, they have higher resolving power and can therefore detect even too small structures.

4.4.1. Scanning electron microscopy

Scanning electron microscopy (SEM) provides topographical, morphological and compositional information of a given sample. It can scan surfaces from a few nanometers to micrometers scale. Two main part in SEM are distinguished: the electron column and the electronics console. The electron column contains an electron gun, which generates and speed up electrons to an energy of 0.1-30 keV.[260] Consequently, a high-energy electrons beam is formed, whose energy dissipates, in contact with the sample surface, giving rise to various signals, notably secondary electrons, backscattered electrons, diffracted backscattered electron, etc. These signals are then collected and detected by a positively charged detector, creating a final image. The secondary and backscattered electrons reveal the topography and element contrast between areas with different chemical compositions within the sample. Scanning electron microscopy (SEM) is carried out to evaluate the morphological properties of the synthesized polymers.

4.4.2. Transmission electron microscopy

Transmission electron microscopy (TEM) is a microscopy technique, which allows the observation of internal structures of a given sample. The SETUP is similar to that of scanning electron microscope, with the difference that the electron beam is transmitted through an ultra-thin specimen, instead of hitting the surface. The specimen can be an ultrathin section of thickness less than 100 nm thick or can be suspended on a grid. Because of the much lower wavelength of electrons, TEM is capable of generating images with resolution close to a few Ångström. These images result from the interaction of the electron beam with the specimen, while passing through it. Indeed, some of the incident electrons are scattered and disappear from the beam, while the unscattered electrons give rise to a “shadow image” with varied darkness according to the compositional density of the specimen.[261] In this work, TEM was used to capture very fine details of the internal structures of the synthesized conjugated polymers.

4.5. Gas adsorption surface area analysis according to the BET-theory

The Brunauer, Emmett, and Teller (BET) theory, developed in 1938,[262] serves as the basis for the measurement of specific surface area of materials. It is based on multilayer physical adsorptions of inert gases (adsorbent) on solid surfaces (adsorbate). The most common used inert gas is nitrogen owning to its availability, high purity and its ability to interact with most solids. The amount of gas adsorbed relies on the exposed surface, the interaction between the solid and gas, the gas pressure and the temperature. This method permits also the assessment of pore sizes ranging from micropores (size < 2 nm), mesopores ([2 nm, 50 nm]), and macropores (size > 50 nm). Therefore, different types of isotherms

can be derived depending on the physicochemical conditions and solid porous texture.[263] According to IUPAC definition, six types can be distinguished as shown in **Figure 15.**

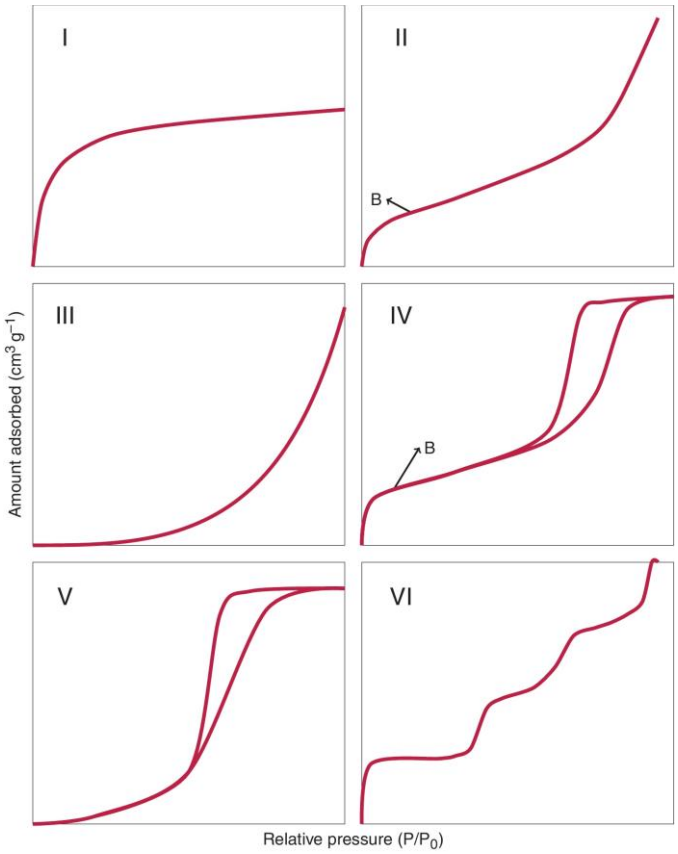

Figure 15. Sorption isotherms according to IUPAC classification.[264]

Type I isotherms are characteristic for microporous materials, and the gas molecules adsorb just as a monolayer at very low relative pressures. Type II corresponds to non-porous or macroporous materials. In this case, the available sites could be filled as monolayer at relative low pressure until complete coverage (indicated by the inflection point B). At high relative pressure, more layers are adsorbed on the previously formed multilayer leading to a continuous increase in the adsorbate thickness. Type III fits to low adsorption capacity of solids, revealed by an increase of the isotherm at higher relative pressures. Type IV isotherms are obtained for mesoporous materials with characteristic hysteresis loop and a saturation plateau at p/p_0 = 0.6 - 0.95. Type V isotherms corresponds to porous materials with pore size range similar to that of type IV isotherms. However, its initial part indicates a low adsorption capacity between the adsorbent and adsorbate. Type VI isotherms or “steppe” isotherms show a stepwise multilayer formation on a highly uniform non-porous surface. The sharpness of the steps is related to the system and the temperature and the step heights depend on the capacity of the monolayer to adsorb the next layer.[263, 265] In this thesis, the BET gas adsorption was used to assess the surface area and pore size distribution of the synthesized porous polymers.

4.6. Cyclic voltammetry

Cyclic voltammetry (CV) is a powerful electrochemical method, which measures current as a function of cyclic potential changes. It results in alternated oxidation and reduction of analyzed species via electron transfer processes. The typical CV setup (**Figure 16a**) consists of a measurement cell, holding three electrodes (working electrode, counter electrode, reference electrode). Electrolytes solutions (i.e. aqueous or in organic solvents) are often needed to ensure conductivity enhancement. The most common used electrodes are glassy carbon or gold electrodes as working electrode, platinum wires as counter electrode, and standard calomel electrode (SCE) or Ag/AgCl as reference electrodes. A typical CV measurement consists of applying a periodic potential between the working and the reference electrode and recording the responsive current between the working and the counter electrode. This latter ensures that current does not run through the reference electrode, which may affect the reference electrodes potential. During the measurement, the analyzed sample undergoes oxidation and reduction at the working electrode, which will then displayed in a cyclic voltammogram (**Figure 16b**).[266, 267]

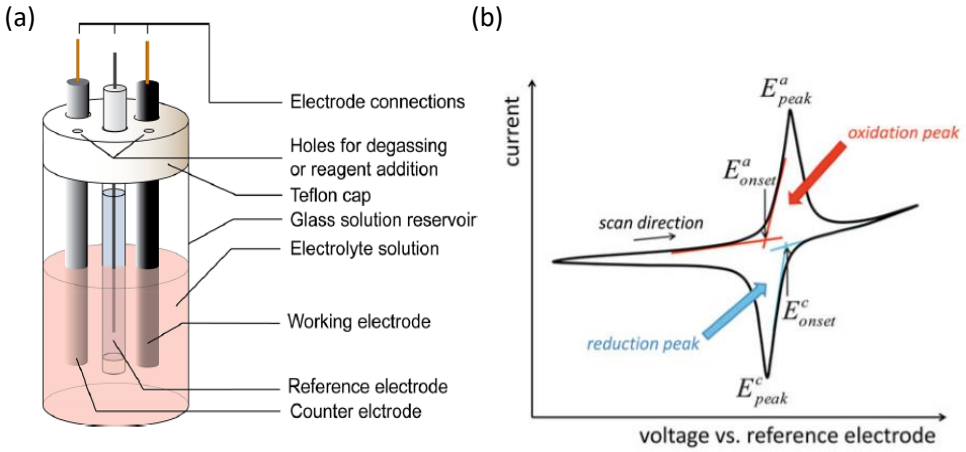

Figure 16. Schematic illustration of (a) an electrochemical cell and (b) a typical result from CV measurements. Adapted from [266, 267] respectively.

In this work, CV measurements were used for experimental determination of the highest occupied molecular orbital (HOMO) and the lowest unoccupied molecular orbital (LUMO) levels of the conjugated porous polymers as well as the redox potentials of some substrates.

4.7. Electron paramagnetic resonance

The electron paramagnetic resonance (EPR) spectroscopy or electron spin resonance (ESR) is a technique commonly employed for the detection and identification of chemical species with unpaired electrons. The basic concepts are similar to those of nuclear magnetic resonance (NMR), but it involves the excitation of electron spins rather than the spins of atomic nuclei. It has been applied to reveal the mechanism of formation of highly reactive radical intermediates during reaction processes. An EPR

spectroscope contains an external magnet, a microwave generator, a detector and a resonator with sample holder. Under exposure of external magnetic field, the eventual unpaired electron of the analyzed sample give two possible energy states following the Zeeman splitting equations: a lower energy state with spin parallel to magnetic field and a higher energy state with spin antiparallel the magnetic field:

$$E_{+\frac{1}{2}} = \frac{1}{2} * g * \mu_B * B$$

$$E_{-\frac{1}{2}} = -\frac{1}{2} * g * \mu_B * B$$

Where g, μ_B and B are g-factor, Bohr magneton, and external magnetic field, respectively.

The energy difference between the two energy states in a single unpaired electron can be defined as follow:

$$\Delta E = \boldsymbol{h\nu} = g * \mu_B * B$$

With the increase of the intensity of the applied magnetic field, the energy difference between the energy levels broadens until it matches with the microwave radiation, resulting in the absorption of energy, detectable by EPR.[268, 269] In this work, the EPR spectroscopy was used for the detection and characterization of radicals and some reactive intermediates during the photocatalytic processes.

4.8. Gas chromatography-mass spectrometry (GC-MS)

The gas chromatography-mass spectrometry (GC-MS) is an analytical tool, which combines a gas chromatography (GC) and a mass spectrometry (MS). It permits the separation of different compounds of a mixture and their identification according to their molecular weights. The separation is based on the volatility of the pure compounds, which are carried through a fixed stationary phased in the column by the flow of an insert gaseous mobile phase, e.g. helium, nitrogen, carbon dioxide, and hydrogen. Once separated by the GC, they are transported directly into the mass detector (MS), in which they are ionized and fragmented under a stream of electron beam. The mass-to-charge ratio (*m/z*) of each positive ionic fragment is then recorded and can be identified by comparison with a sample library or standards.[270] In this work, GC-MS was used to monitor photocatalytic reactions and kinetics, to identify eventual intermediates and to confirm the structure of final products.

5. Results and discussions

In the following chapter, the focus was set on the design and characterization of conjugated porous polymers (CPPs) for challenging photocatalytic applications under visible light irradiation. The emphasis was laid on the employment of mild and environmentally benign reaction conditions as using molecular oxygen as green oxidant, and aqueous solvents as reaction media.

First, a series of conjugated microporous polymers (CMPs), with different electron-donor/acceptor combinations, were designed and examined for the visible light-promoted oxidation of styrene into benzaldehyde in an acetonitrile–water mixture (1:24 (v/v)) (**section 5.1**). The presence of acetonitrile traces was necessary to enhance the dispersibility of the hydrophobic CMPs into the reaction media. To expand the catalytic applications in pure water, a structural design strategy of covalent triazine frameworks (CTFs), combing different electron donor/acceptor building blocks and using hydrophilic mesoporous silica (SBA-15) as support, was presented. The CTFs, with excellent dispersibility, were examined for the visible light promoted oxidation of styrene in pure water (**section 5.2**). Beside the catalyst design, more valuable products, i.e., styrene oxide, via the so-called styrene epoxidation was obtained.

Next, a thiophene-containing CTF, with high oxidation potential, was directly synthesized on SBA-15 (CTF-Th@SBA-15) and tested for the photocatalytic partial oxidation of biomass-derived 5-hydroxymethylfurfural (HMF) to 2,5-diformylfuran (DFF) in pure water (**section 5.3**). The photocatalytic performance of CTF-Th@SBA-15 was further investigated through the visible-light promoted degradation of organic contaminants in aqueous media and in solid-state (**section 5.4**).

Beside the general applicability of CPPs for photocatalysis in aqueous media, a particular attention was drawn to the factors, which can affect strongly the photocatalytic efficiency. The incorporation of functional nanomaterials with different band structures into the CPP network (heterojunction) was found to be a promising strategy for the enhancement of the photocatalytic performance by enhancing the photo-induced charge separation. Thus, an heterojunction of CPP photocatalyst with immobilized TiO_2 nanoparticles (wt. 20%) was prepared and employed as heterogeneous photocatalyst for visible light oxidative coupling reaction of amines and the selective oxidation of organic sulfides (**section 5.5**). Their photocatalytic performances were then compared to those of the single photocatalytic systems either only consisting of the CMPs or TiO_2.

5.1. Designing conjugated microporous polymers for visible light-promoted photocatalytic carbon-carbon double bond cleavage in aqueous medium

This subchapter is based on the published article "Designing conjugated microporous polymers for visible light-promoted photocatalytic carbon-carbon double bond cleavage in aqueous medium".[1] Cyrine Ayed designed and performed the experiments, analyzed the data and drafted the manuscript. Dr. Lucas Caire da Silva performed the ^{13}C solid-state NMR measurements. Dr. Di Wang performed the EPR measurements. Cyrine Ayed, and Prof. Dr. Kai Zhang contributed to the final version of the manuscript. Prof. Dr. Kai Zhang supervised the project.

Herein, a structural design strategy of conjugated microporous polymers (CMPs) as a class of metal-free, heterogeneous, stable and reusable photocatalyst for visible light-promoted C=C bond cleavage reaction of styrene is presented. Via different electron donor and acceptor combinations in the CMP backbone structure, we systematically investigated the structure influence of the CMPs on their optical and electrochemical properties, and thereby revealing the structure and performance relation in the photocatalytic C=C double bond cleavage reaction. As result, the CMP with the specific electron donor acceptor combination containing benzothiazole as strong electron withdrawing and phenyl as weak electron donating unit was the most efficient photocatalyst. The C=C bond in various alkenes, mostly styrene derivatives could be successfully cleaved, and forming aldehydes as product with high conversion and moderate to high selectivity. The green aspect of the work is demonstrated by the utilization of visible-light, molecular oxygen as cheap oxidant and water-based reaction medium.

5.1.1. Motivation

The synthesis of valuable carbonyl compounds such as aldehyde, acetic acid, acetaldehyde and ketones derivatives via the carbon-carbon double (C=C) bond cleavage from alkenes is a highly important reaction in chemical and pharmaceutical industries. These products have wide applications as important molecular building blocks and intermediates for the manufactures of perfumes, dyestuff, agrochemicals and pharmaceuticals.[271-275] Various studies have reported the thermal catalytic oxidation of alkenes, notably styrene, for the desired carbonyl products. An important example of the metal catalysts are iron-based systems such as Iron (II) chloride,[276] $Fe(NO_3)•9H_2O$, etc.[277, 278] Alternatively, Feng *et al.* have employed water-soluble palladium (II) complex for the selective aerobic oxidation of styrene in water obtaining benzaldehyde with high selectivity.[279] Zhang *et al.* have also observed the C=C bond cleavage and the formation of acetophenone with moderated selectivity over ZrO_2-supported palladium

[1]Ayed, C., Caire da Silva, L., Wang, D., Zhang, K. A. I., *J. Mater. Chem. A, 2018,6, 22145-22151*- Published by The Royal Society of Chemistry (RSC). Reproduced with permission.

nanoparticles.[280] Recently, Liu *et al.* have reported the use of gold nanoparticles mobilized carbon as catalyst for the selective oxidation of styrene.[272] The researchers pointed out that the strong Au-Carbon interaction could enhance the catalytic efficiency.

In comparison to the traditional thermal reaction conditions, photocatalysis offers an environmentally friendly and sustainable synthetic strategy. Nevertheless, there are only few photochemical reports on the photo-oxidative cleavage of C=C bonds of styrene. For instance, Guo *et al.* have reported the use of Au-Ti-decorated mesoporous silica for the photo-epoxidation reaction of styrene with moderated selectivity.[281] More recently, Shen *et al.* have developed a chiral manganese catalyst to trigger photocatalytic enantioselective epoxidation of terminal olefins, using water as an oxygen source and yielding epoxides with relatively high enantioselectivities.[282] So far, the photocatalytic systems reported were mainly based on transition metals. Very few molecular organic photocatalysts have been developed, such as eosin Y, which was used as an organophotoredox to mediate the oxidative cleavage of C=C bond.[283] However, despite the progress made so far in this field, considerable drawbacks are still associated to those metal based or organic molecular systems. For example, the toxicity of heavy metals, the instability and the lack of the reusability of the molecular photocatalysts lead to the need of the development of a more stable, reusable, metal-free and heterogeneous photocatalytic system.

Conjugated microporous polymers (CMPs), combining visible light-active π-backbone and microporous properties, have recently emerged as a new class of efficient, stable and heterogeneous photocatalysts for chemical transformations.[50, 284-286] Recent research activities demonstrated their wide application range in various photocatalytic reactions such as molecular oxygen activation,[284] selective oxidation of organic sulfides,[287] C-C or C-N bond formation,[203, 288, 289] dehalogenation,[290, 291] oxidative hydroxylation of arylboronic acids,[292] visible light-initiated free radical and cationic polymerization,[293, 294] cycloaddition,[295] sunlight driven oxidative homocoupling of amines,[296] visible light-driven C-3 functionalization of indoles,[297] and hydrogen evolution.[222, 224, 298] So far, the photocatalytic oxidative cleavage C=C bond over conjugated microporous polymers has not been reported.

In this chapter, we report the design of CMPs bearing different electron donor and acceptor-building blocks as heterogeneous photocatalysts for the C=C bond cleavage of alkenes, mostly styrene derivatives. We investigated the structure influence of the CMPs on their photocatalytic efficiency. It was shown that the photocatalytic reaction could be conducted with almost quantitative conversion and selectivity using the CMP containing benzothiazole as a strong electron withdrawing unit, together with phenyl group as electron donating unit in the polymer backbone. Additionally, the use of aqueous reaction

medium demonstrated its green and sustainable reaction nature. The mechanistic insight of the photoredox reaction was also investigated.

5.1.2. Synthesis and characterization of CMP-based photocatalysts

For the structural design of the CMPs, we choose different building blocks according to their electron affinity. As displayed in **Scheme 1**, thiophene (Th) as strong electron donor and benzothiodiazole (BT) as strong electron acceptor were polymerized via the palladium-catalyzed Sonogashira cross-coupling reaction[299] with triethynylbenzene (B) in the corresponding CMP backbone structures, referring to BTh and BBT, respectively. A mixed CMP was also synthesized containing 50% of BT unit and 50% of Th unit in the same manner, referring to BThBT.

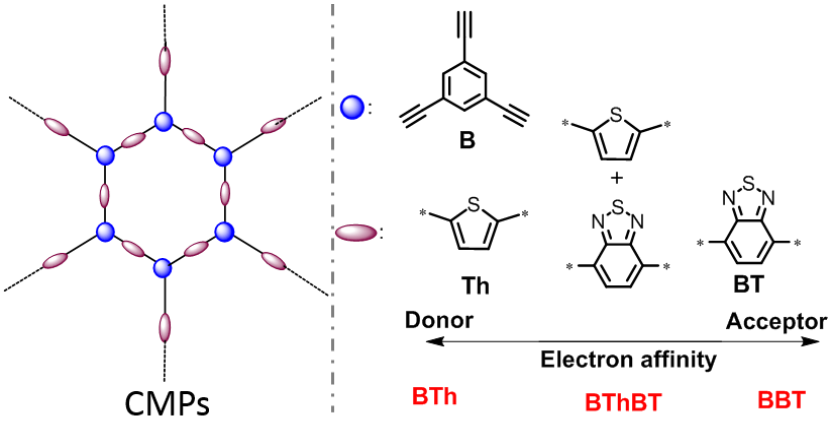

Scheme 1. Structural design of a series of conjugated microporous polymers (CMPs) via combination of different electron donor and acceptor building blocks.

The CMPs were obtained as amorphous solids as shown by the X-ray diffraction patterns (**Figure 17**). The detailed synthetic pathway with detailed characterization methods of the polymers are described in the Experimental Section **6.1.3**.

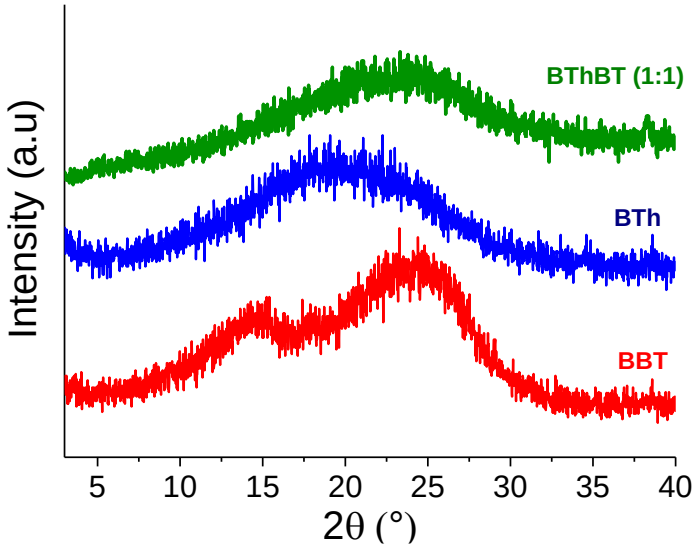

Figure 17. X-ray diffraction pattern of the prepared CMPs.

As displayed in **Figure 18**, the scanning electron microscopy (SEM) images of the CMPs showed a variety of shapes. BTh was obtained as irregularly shaped particles with a size ranging between 40 and 180 nm, whereas, BBT showed a fibrous structure with a diameter of ca. 200 nm. BThBT appeared as fused large particles and fibers.

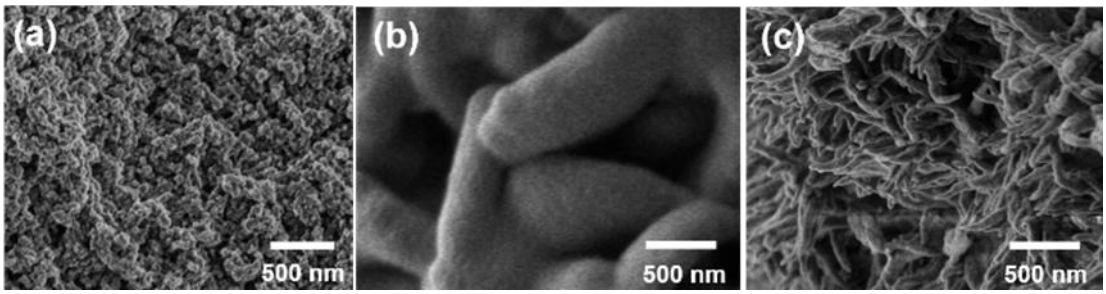

Figure 18. SEM images of (a) BTh, (b) BThBT and (c) BBT.

The Brunauer-Emmett-Teller (BET) surface areas of BTh, BThBT and BBT were measured to be 806 $m^2 g^{-1}$, 445 $m^2 g^{-1}$ and 129 $m^2 g^{-1}$, with pore sizes of 1.7 nm, 1.41 nm and 1.7 nm, respectively. The nitrogen gas sorption isotherms and pore size distributions are displayed in **Figure 19**.

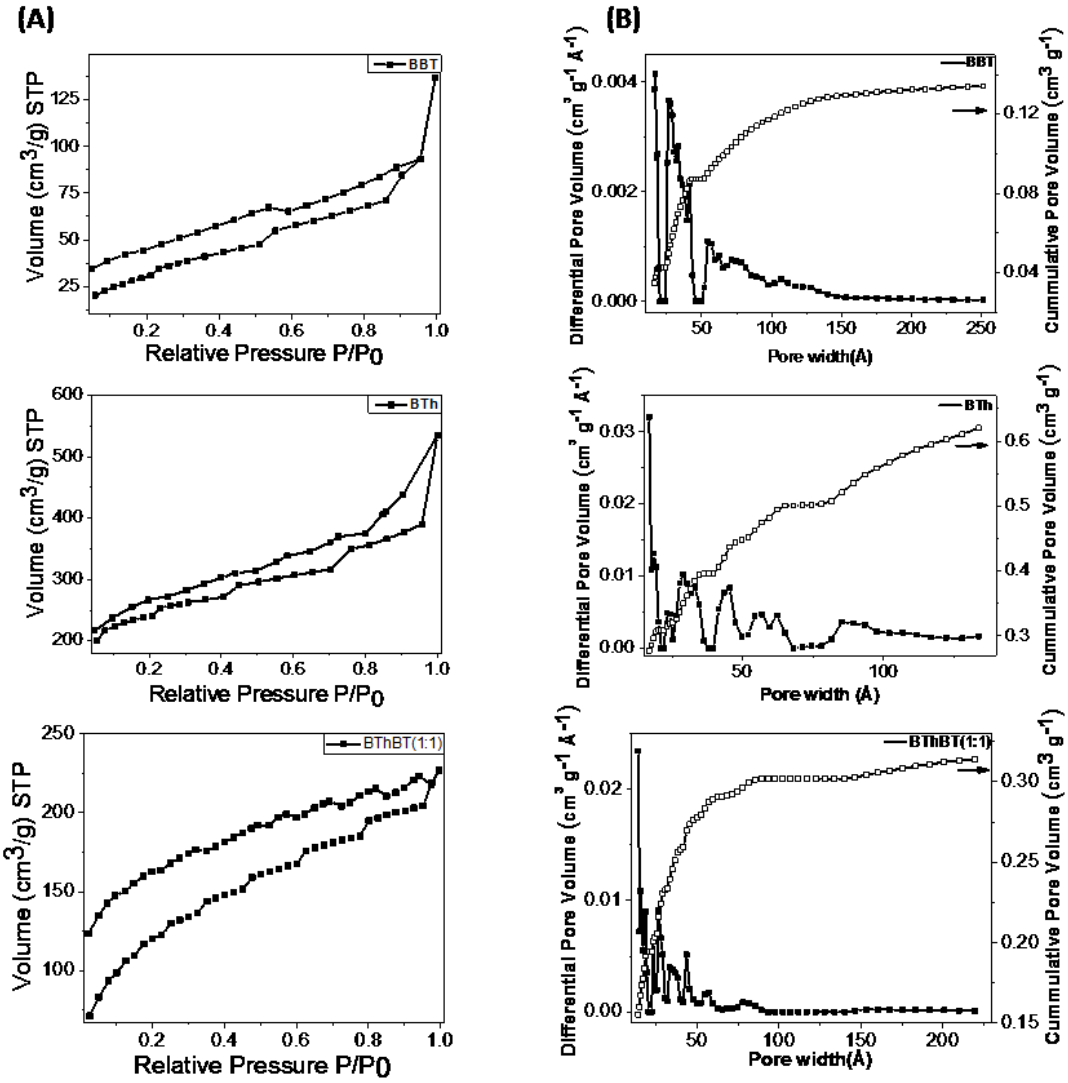

Figure 19. (A) Nitrogen sorption and desorption isotherms and (B) Pore size distributions of the as synthesized materials.

Their physical properties are listed in **Table 1.**

Table 1. Physical Properties of the designed CMPs.

CMP	S_{BET} (m^2 g^{-1})	Pore volume (cm^3 g^{-1})	Pore size (nm)	Band gap (eV)
BTh	806	0.620	1.7	2.36
BThBT	445	0.314	1.41	2.00
BBT	129	0.136	1.7	2.12

The solid state ^{13}C CP/MAS NMR spectra of all CMPs are displayed in **Figure 20**. The typical chemical shifts between 110 and 150 ppm shown for all CMPs, can be assigned to the aromatic rings in the polymer backbone. The signals from 80 to 100 ppm can be assigned to the carbon of the triple bond.

The resonance peak at 155 ppm could be observed, which can be assigned to the adjacent carbon next to nitrogen in the BT unit. The thiophene (Th) unit can be characterized by the signal at about 124 ppm, which is assigned to the =C-S single bond.[163, 219, 229]

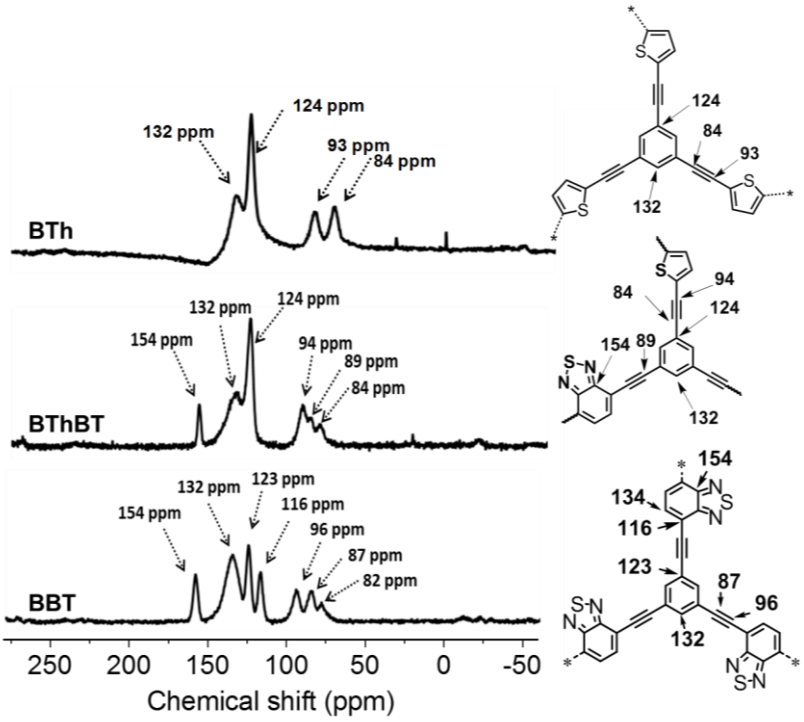

Figure 20. Solid state ^{13}C CP/MAS NMR spectra of the CMPs.

The Fourier transform infrared (FTIR) spectra **(Figure 21a)** showed typical signal at 2300 cm^{-1} which could be assigned to the -C≡C- stretching mode.[38] The signals at 1570 cm^{-1}, 1480 cm^{-1} are characteristic for the =N-S- , the -C=N- stretching modes in the benzothiadiazole moiety.[299] The vibrational peak at 790 cm^{-1} is attributed to the thiophene unit in BTh network.[163] The BThBT spectra contains both signals corresponding to the BT and Th units.[300] Thermogravimetric analysis (TGA) indicated that BBT was thermally the most stable up to 300 °C, whereas BTh and BThBT showed lower initial decomposition temperatures with BTh exhibiting the lowest weight loss among all of the CMPs (**Figure 21b**).

Figure 21c illustrates the UV/vis diffuse reflectance (DR) spectra of the CMPs. All three polymers showed similar absorption range with maximal absorption between 300 and 450 nm and gradually levelling off until ca. 800 nm. Additionally, a clear extension effect of the absorption range of the BT unit was revealed. The strong donor-based CMP, i.e BTh, absorbs mainly in the blue light range. In comparison, the spectra of BThBT as well as that of BBT, exhibited gradually a bathochromic shift up to ca. 60 nm.

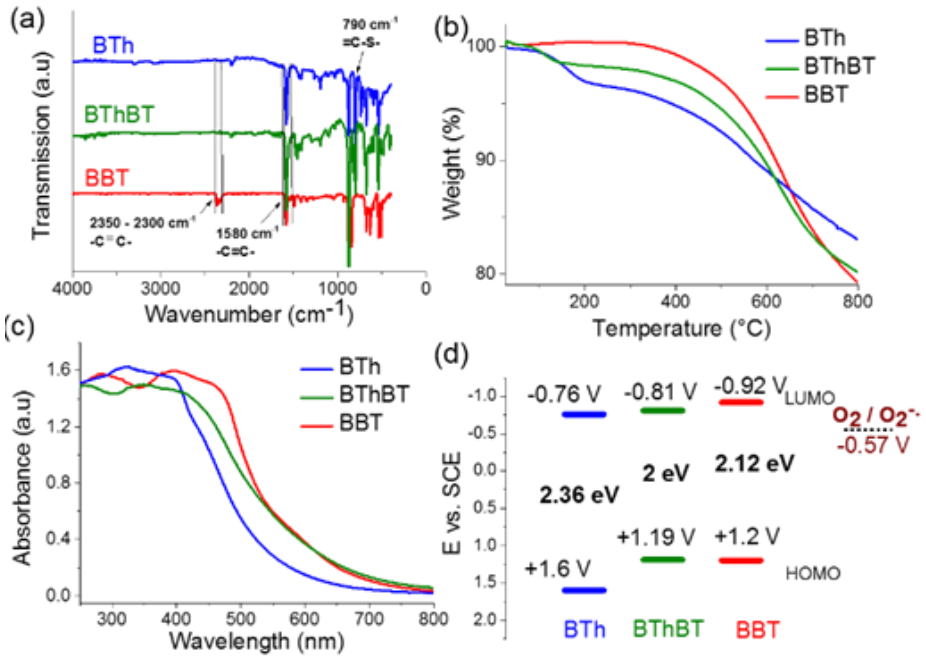

Figure 21. (a) FTIR, (b) TGA spectra of the materials under N_2 atmosphere with a heating rate of 10 ^oC/min, (c) UV/vis DR spectra, and (d) energy band structures of the as synthesized CMPs and the $O_2/O_2^{\bullet-}$ couple.

To gain further insight into the electronic properties, cyclic voltammetry (CV) measurements were conducted to reveal the energy band structure of the designed materials (**Figure 22**).

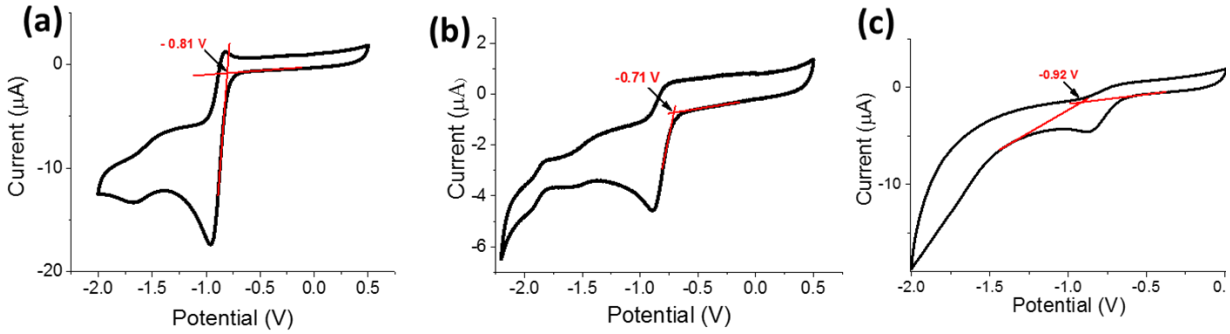

Figure 22. Cyclic voltammograms of (a) BTh, (b) BThBT and (c) BBT.

The electronic band positions of the CMPs are displayed in **Figure 21d**. BBT exhibited the highest LUMO level at – 0.92 V vs SCE among the CMPs, indicating its strong activation ability of molecular oxygen into its active states such as superoxide oxygen and singlet oxygen. The reduction potential of the $O_2/ O_2^{\bullet-}$ lies at −0.57 V vs SCE.[301, 302] The results strongly suggests the possible superior photocatalytic activity of BBT for oxidative reactions.

5.1.3. Visible light-promoted photocatalytic carbon-carbon double bond cleavage in aqueous medium

To investigate the photocatalytic performance of the designed CMPs, we tested the oxidative cleavage of C=C bond using styrene as model substrate under visible light irradiation. The experiments were first carried out at room temperature using BBT as the photocatalyst due to its highest reduction potential and molecular oxygen as an oxidant in various solvents. The results are listed in **Table 2**. The conversion of styrene catalyzed by BBT was found to be strongly dependent on the solvent polarity (**Figure 23Figure *25***).

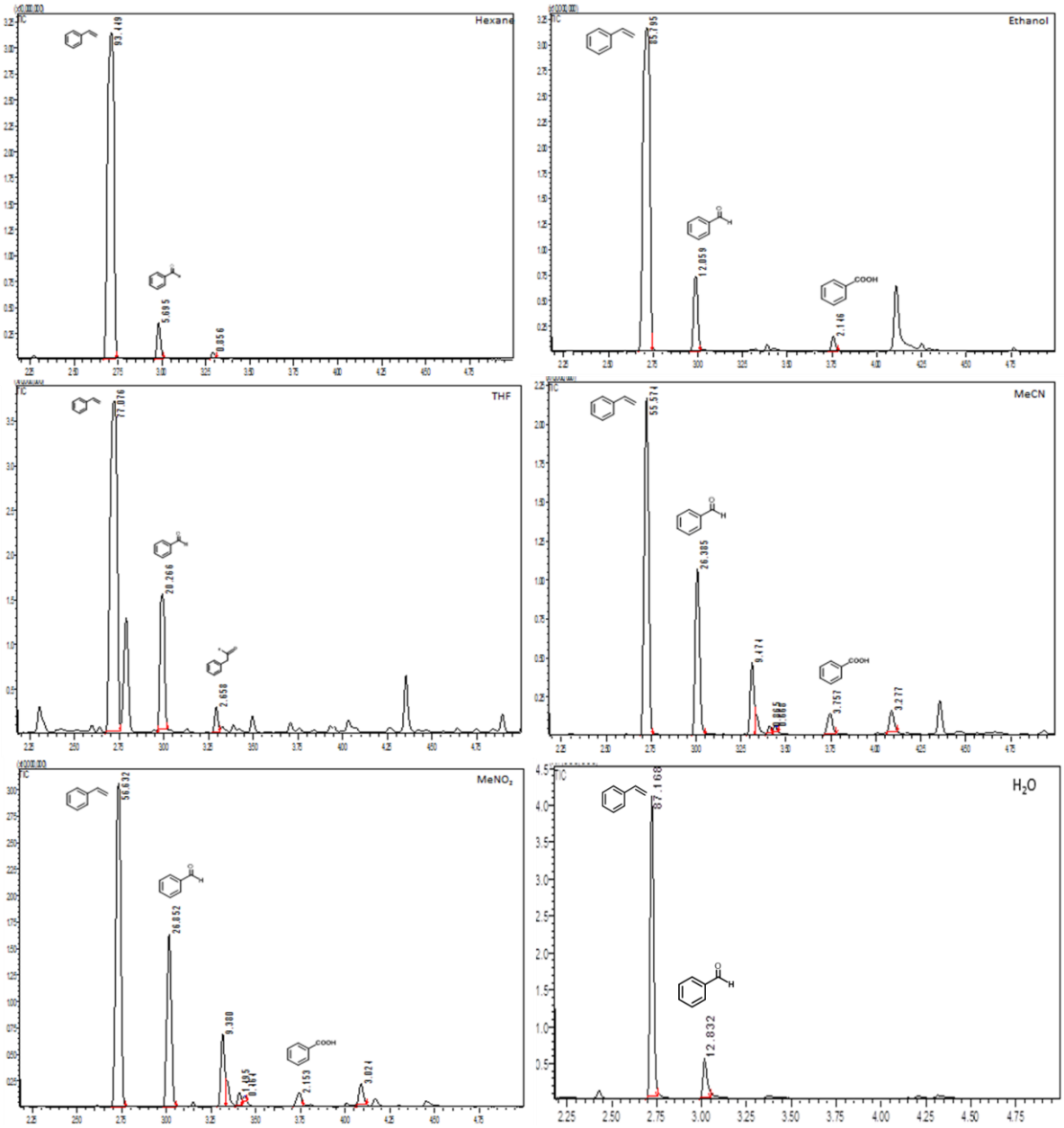

Figure 23. Chromatograms of the photooxidation of styrene, in various solvents, under blue light irradiation and using BBT.

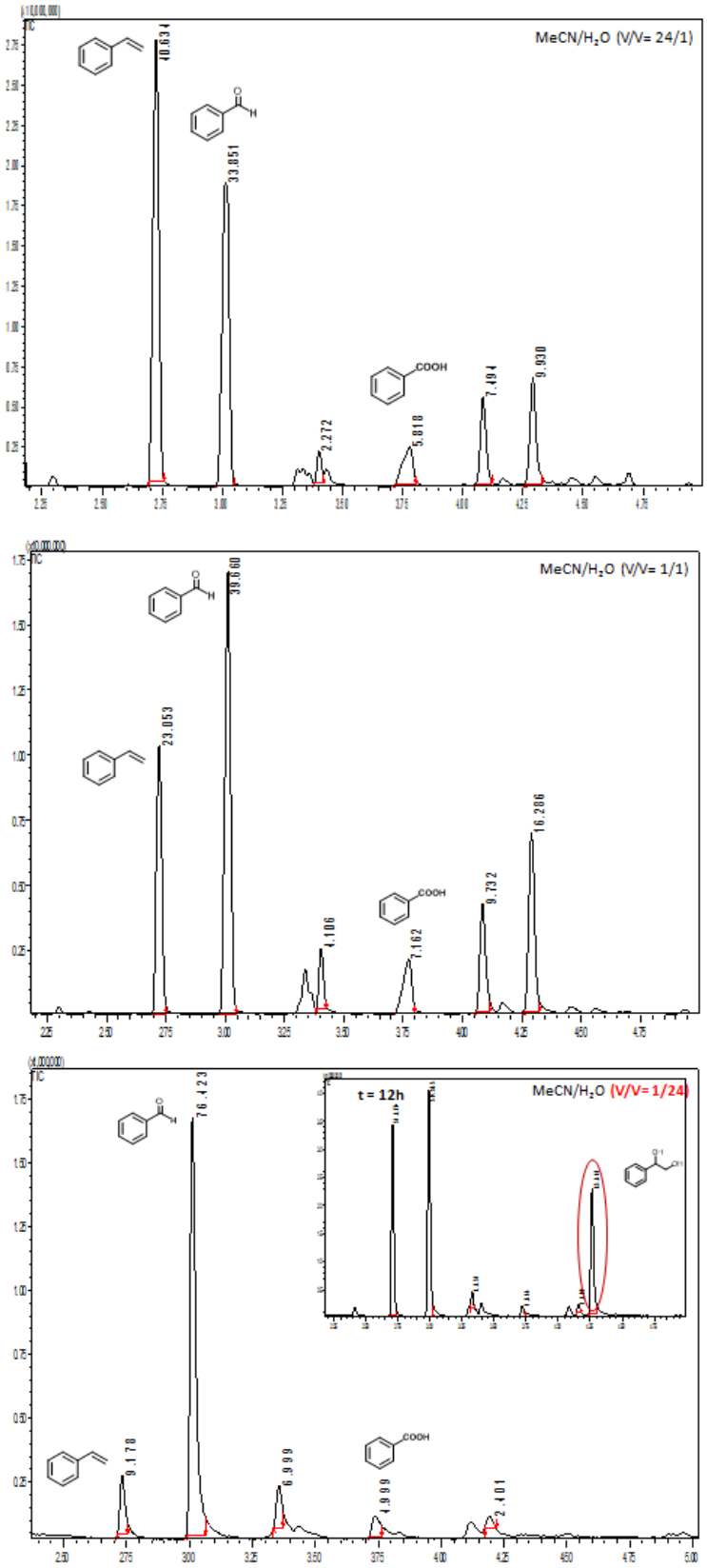

Figure 24. Photooxidation of styrene, in water-based biphasic system (various ratios), under blue light irradiation and using different BBT.

Mainly benzaldehyde was observed in various solvents, with relatively high selectivity (entries 1 to 9 in **Table 2** and **Figure 25**).

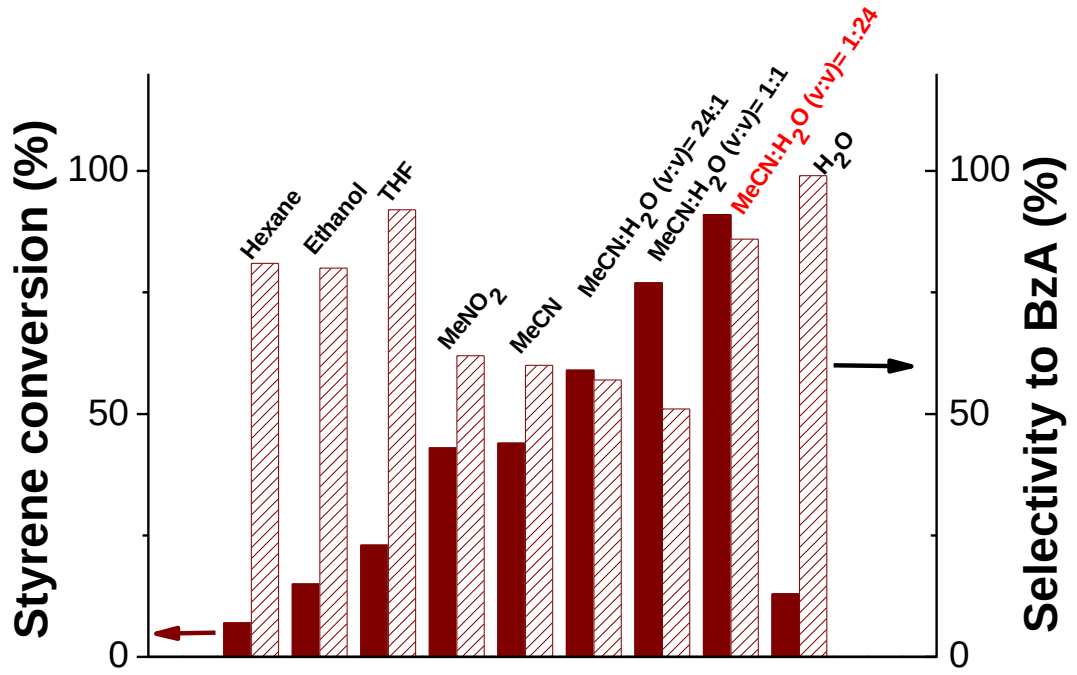

Figure 25. Solvent polarity dependent conversion, Evaluation of the solvent effect on the photoxodation of styrene, using 10 mg of BBT as photocatalyst, under the irradiation of a blue LED lamp (460 nm, 0.065W cm^{-2}), 1 atm. O_2, room temperature, 18h.

For instance, in an apolar solvent such as hexane (entry 1 in **Table 2**), a high selectivity of around 81% to benzaldehyde with a total styrene conversion of 7% was observed after 18 h. Increasing the polarity of the solvent (ethanol, THF, nitromethane and acetonitrile) led to an increase of the conversion of styrene up to 44% with benzaldehyde yields ranging from 61% to 92% (entries 2, 3, 4 and 5 in **Table 2**). When further increasing the solvent polarity by mixing water into acetonitrile, it was found that the photooxidation of styrene was noticeably enhanced upon addition of H_2O into acetonitrile under blue light irradiation (entries 6, 7 and 8 in **Table 2**). For example, the styrene conversion was increased by more than 2-fold from 44% to 91%, with high benzaldehyde yield of about 86%, when an optimized amount of water to acetonitrile (v/v =1/24) was added (entry 8 in **Table 2**). These results shed lights on the solvent-polarity-dependent-conversion in one hand and the effect of the water on the acceleration of the photooxygenation of styrene by O_2 in the other hand.[303]

The involvement of water in this reaction was further confirmed by the detection of 1-phenyl-1,2-ethanediol by GC-MS during the reaction, which is possibly due to the attack of water on the intermediate in the reaction process **(Figure 24).** However, it is noteworthy to mention that the reaction gave a poor conversion of 13% in pure water (entry 9 in **Table 2**), which is probably due to the hydrophobic nature of BBT, being weakly dispersible in water.

Table 2. Photocatalytic C=C bond cleavage using various CMPs with various reaction conditions.

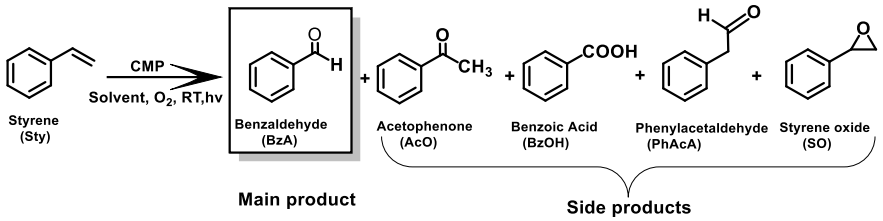

Entry[a]	photocatalyst	Solvent	O_2	Light	Additives	Conversion (%)[b]	Selectivity of BzA (%)[b]
1	BBT	Hexane	+	+	-	7	81
2	BBT	Ethanol	+	+	-	15	85
3	BBT	THF	+	+	-	23	92
4	BBT	$MeNO_2$	+	+	-	43	62
5	BBT	MeCN	+	+	-	44	60
6	BBT	MeCN/H_2O (V/V= 24/1)	+	+	-	59	57
7	BBT	MeCN/H_2O (V/V= 1/1)	+	+	-	77	51
8	BBT	MeCN/H_2O (V/V= 1/24)	+	+	-	91	85
9	BBT	H_2O	+	+	-	13	>99
10	BTh	MeCN/H_2O (V/V= 1/24)	+	+	-	16	69
11	BThBT	MeCN/H_2O (V/V= 1/24)	+	+	-	58	43
12[c]	BBT	MeCN/H_2O (V/V= 1/24)	+	-	-	n.d	n.d
13[d]	BBT	MeCN/H_2O (V/V= 1/24)	-	+	-	n.d	n.d
14[e]	-	MeCN/H_2O (V/V= 1/24)	+	+	-	48	79
15[f]	-	MeCN	+	+	-	30	85
16[g]	BBT	MeCN/H_2O (V/V= 1/24)	+	+	KI as hole scavenger	2	100
17[h]	BBT	MeCN/H_2O (V/V= 1/24)	+	+	NaN_3 as singlet oxygen scavenger	17	69
18[i]	BBT	MeCN/H_2O (V/V= 1/24)	+	+	Isopropanol as hydroxyl radical scavenger	88	45
19[j]	BBT	MeCN/H_2O (V/V= 1/24)	+	+	Benzoquinone as superoxide scavenger	1	100

[a)]Standard reaction conditions: 0.1 mmol of styrene, 10 mg of CMP in 1.5 mL of solvent under the irradiation of a blue LED lamp (460 nm, 0.16 W cm^{-2}), 1 atm. O_2, room temperature, 18h.[b)]Conversion determined by GC-MS, [c)] BBT, no light,1atm O_2, MeCN/H_2O: V/V= 1/24 [d)]with BBT, under light, no O_2, MeCN/H_2O: V/V= 1/24. [e)] without catalyst, under light,1atm O_2, MeCN/H_2O V/V= 1/24. [f)] without catalyst, under light, 1atm O_2, acetonitrile [g)]KI as a hole scavenger. [h)]NaN_3 as singlet oxygen scavenger, [i)] Isopropanol as Hydroxyl radical scavenger, [j)]Benzoquinone (BQ) as superoxide scavenger.

Taken into consideration the optimized reaction conditions above, the photocatalytic performance of the other designed CMPs was investigated under the same conditions using water-based-biphasic systems (MeCN/H_2O: v/v =1/24). As listed in **Table 2**, **Figure 26** and **Figure 97** in Experimental Section **6.1.5**, the reaction catalyzed by the BThBT reached lower conversion of about 58% with only 43% yield to benzaldehyde, whereas BTh was not efficient for this reaction exhibiting only 16% of conversion with forming benzaldehyde as the main product (entries 10 and 11).

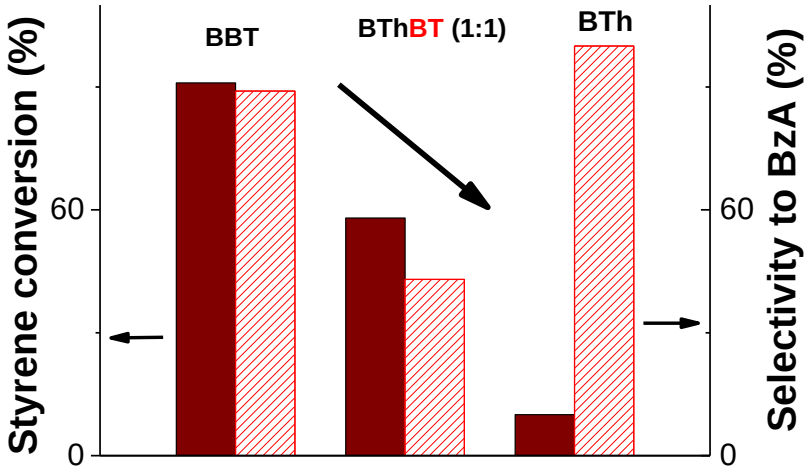

Figure 26. Photooxidation of styrene over different CMPs. Reaction conditions: 0.1 mmol of styrene (without inhibitor), 1.5 mL MeCN: H_2O = (V/V) = 1 : 24, O_2, 10 mg catalyst, Blue Led 0.065 W.Cm^{-2}, 18h.

The higher photocatalytic efficiencies of the BT-containing CMPs, BBT and BThBT, could be explained by a more efficient photogenerated charge separation within the polymer networks due to the donor- acceptor combinations. In comparison, BTh only contains electron donor units, which inhibits an efficient charge separation and transfer inside the CMP.

Indeed, **Figure 27a** reveals the most intense photocurrent signal of BBT among the three CMPs under visible light, indicating that the photogenerated charge separation in BBT is more efficient than BThBT, followed by the BTh as the most insufficient photocatalyst.

To further investigate the reaction mechanism and reveal the specific role of the photogenerated electron hole pairs during the photocatalytic process, we conducted a number of control experiments, using BBT as photocatalyst. The results are also listed in **Table 2** and summarized in **Figure 28**. In the absence of light, molecular oxygen, no reaction conversion was determined (entries 12 and 13 in **Table 2**). Without using photocatalyst, only conversion of 30% - 42% was determined (entries 14 and 15 in **Table 2**). The results indicate that all three components are indispensable.

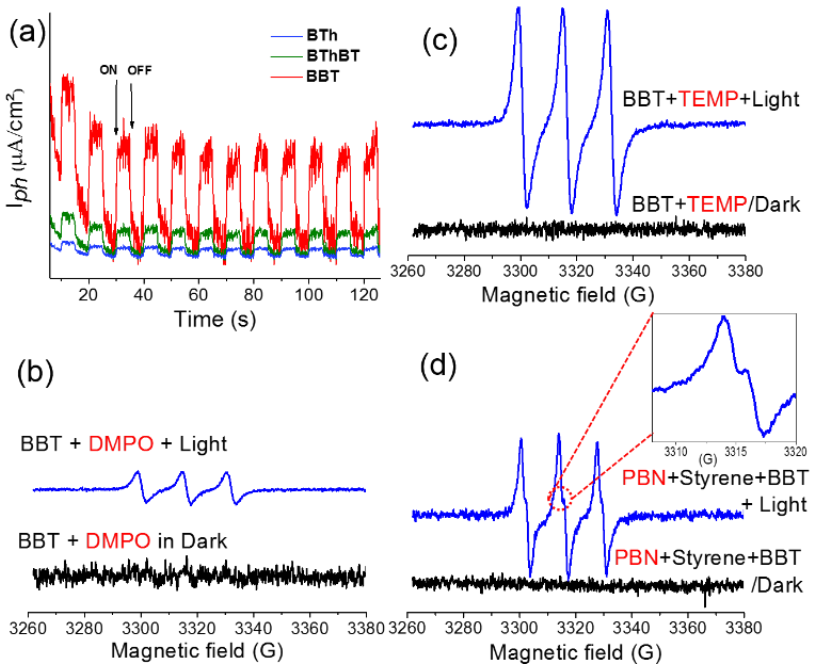

Figure 27. (a) Photocurrent responses of the CMPs under the illumination of visible light with wavelength ≥420 nm with a light ON/OFF model. EPR spectra of (b) DMPO-$O_2^{\bullet-}$ (g = 2.00639) and (c) TEMP-$^1O_2$ adducts (g = 2.00645) using BBT as photocatalyst in dark and under light irradiation (λ = 460 nm, 0.065 W/cm^2). (d) EPR spectra using PBN as a radical trapping agent for the radical intermediate of styrene, with BBT, under O_2 and light irradiation (g = 2.00667).

The effect of specific scavengers were also studied (**Figure 28**-**Figure *29***). A conversion of 2% was obtained in the presence of KI as a hole scavenger (entry 16 in **Table 2**). A conversion of 17% was reached in the presence of NaN_3 as a singlet oxygen scavenger (entry 17 in **Table 2**). Using isopropanol as hydroxyl scavenger led to a conversion of 88% (entry 18 in **Table 2**). Significantly, a conversion of only 1% was determined in the presence of benzoquinone as superoxide scavenger (entry 19 in **Table 2**).

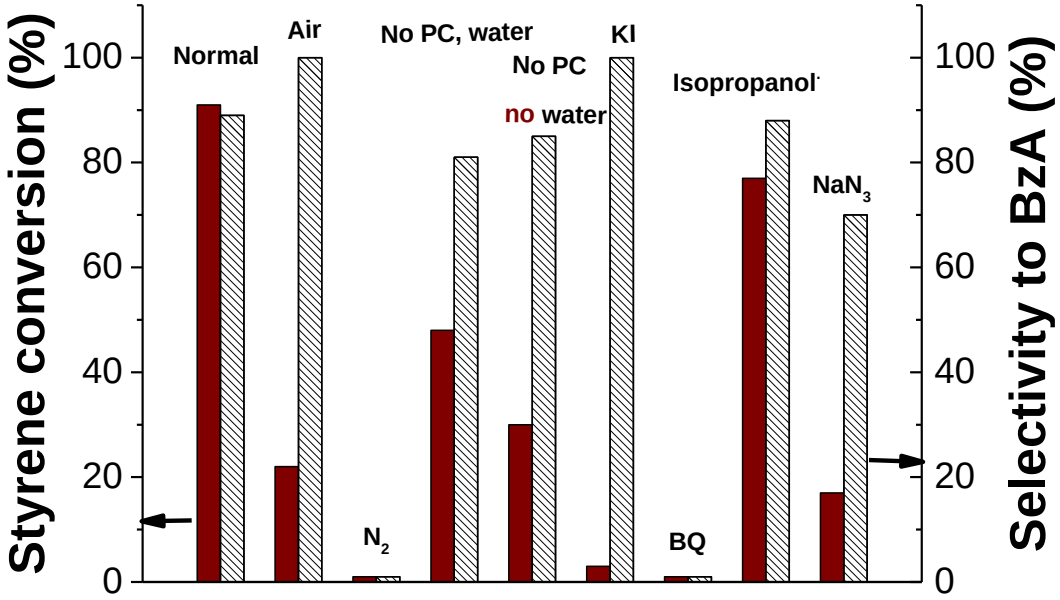

Figure 28. Control experiments using 10 mg of BBT as photocatalyst, under the irradiation of a blue LED lamp (460 nm, 0.065W cm^{-2}), 1 atm. O_2, room temperature, 18h.

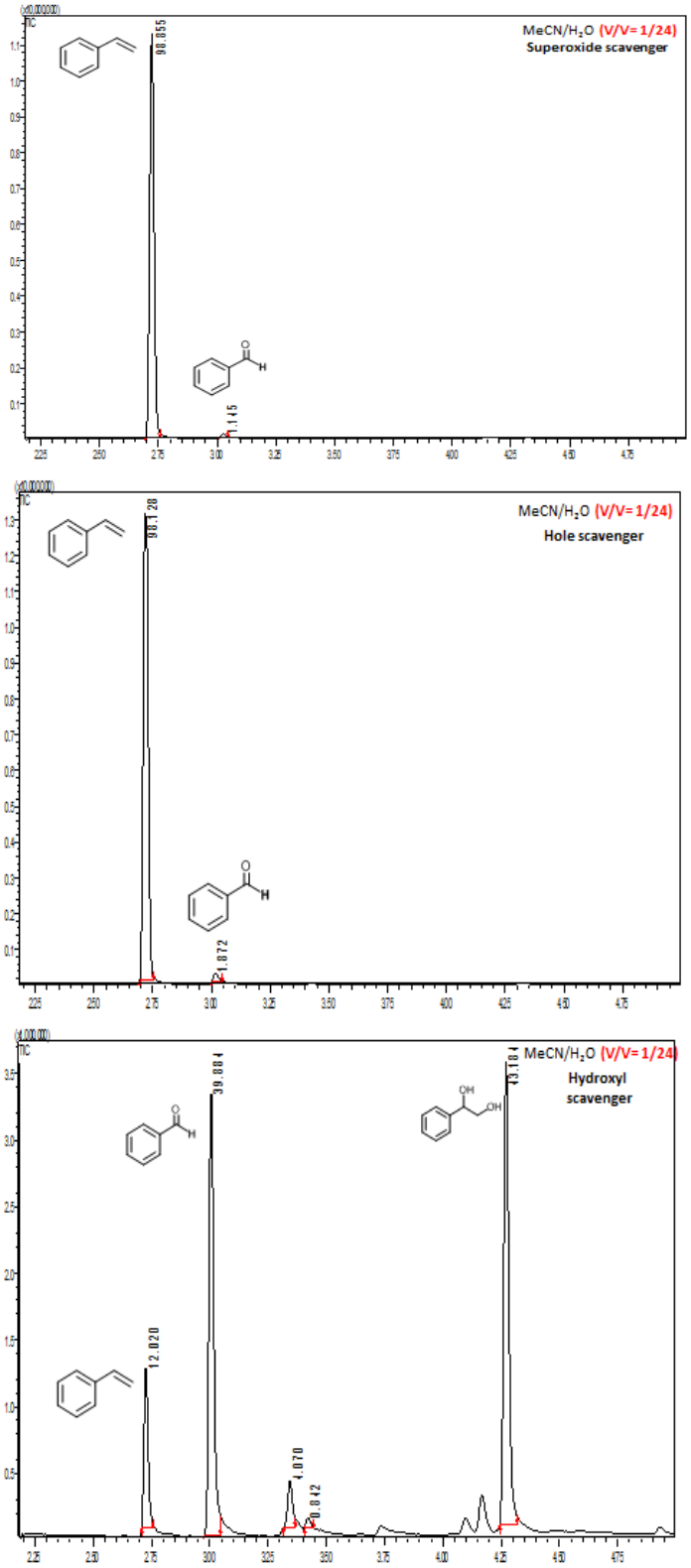

Figure 29. control experiments using 10 mg of BBT as photocatalyst, in presence of specific scavengers under the irradiation of a blue LED lamp (460 nm, 0.065W cm^{-2}), 1 atm. O^2, room temperature, 18h.

These results indicate that the activated oxygen species (superoxide and singlet oxygen), and photogenerated hole all participate during the oxidative C=C bond cleavage reaction. To precisely analyze the possible active oxygen species (superoxide and singlet oxygen) and their exact contribution during the photocatalytic reaction, we further conducted electron spin resonance (EPR) experiments using 5,5-dimethyl-1-pyrroline N-oxide (DMPO) and 2,2,6,6- tetramethylpiperidine (TEMP) as superoxide and singlet oxygen trapping agents, respectively. As shown in **Figure 27b** and **Figure 27c**, both active oxygen species could be determined, confirming their active roles for the reaction.

Based on the observations drawn from the experiments described above, we suggest a modified reaction mechanism for the oxidative C=C bond cleavage and aldehyde formation inspired from the literature (**Figure 30**).[283, 303] Under visible light irradiation, the charge separation occurs within the CMP based photocatalyst. The photogenerated hole of BBT oxidizes styrene **(1)** into its cationic radical intermediate **(1a)**. Further proof of the formation of the radical intermediate could be observed using N-tert-butyl-α-phenylnitrone (PNB) as a radical trapping agent (**Figure 27d**). A typical pattern for PBN trapped radical with g value equal to 2.00667 has been recorded. In the same time, the electron from the LUMO of the CMP assisted the reductive activation of molecular oxygen into superoxide ($O_2^{\bullet-}$), which undergoes [2+2] cycloaddition with the cationic radical of styrene to generate the 3-phenyl-1,2-dioxetane **(2)**. To note, singlet oxygen ($^1O_2$) also took part of the oxidation step. 1-phenyl-1,2-ethanediol **(3)** is then formed due to the attack of the water on the dioxetane intermediate, which ultimately is cleaved into benzaldehyde **(4)**, releasing formaldehyde as the possible side product.

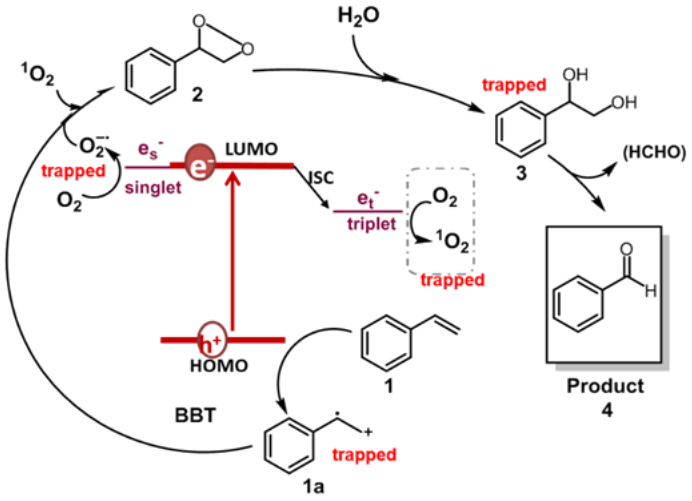

Figure 30. Suggested reaction mechanism for the aerobic C=C double bond cleavage of styrene using BBT as photocatalyst.

However, the high-performance liquid chromatography (HPLC) did not give a confirmation of the existence of formaldehyde. Nevertheless, the ^{1}H NMR spectra showed traces of possible formaldehyde formation (see Experimental Section **6.1.5**). The results indicate that the formed formaldehyde as the side product could be directly oxidized. Additionally, the overoxidation of the aldehyde may result in the formation of carboxylic acids, depending on the nature of the substrate (see the scope of substrates below).To further demonstrate the general applicability of BBT as photocatalyst, the screening experiments with various styrene derivatives have been carried out under the same conditions and the results are listed illustrated in **Figure 31** and **Figure 98** in Experimental section **6.1.5**. High conversion was obtained in most cases under the same conditions. However, both electron-withdrawing substitution groups on the phenyl rings of the substrates such –F **(5a)** or –Cl **(5b)** or –Br **(5c, 5d)** and electron-donating substitution such as methyl **(5e, 5f),** methoxy **(5j)**, led to lower benzaldehyde yield than the model reaction. Nevertheless, it appears that the variation of the position of the substituent on the phenyl ring does not have considerable effect on the conversion, and on the yield of the corresponding aldehyde, neither.

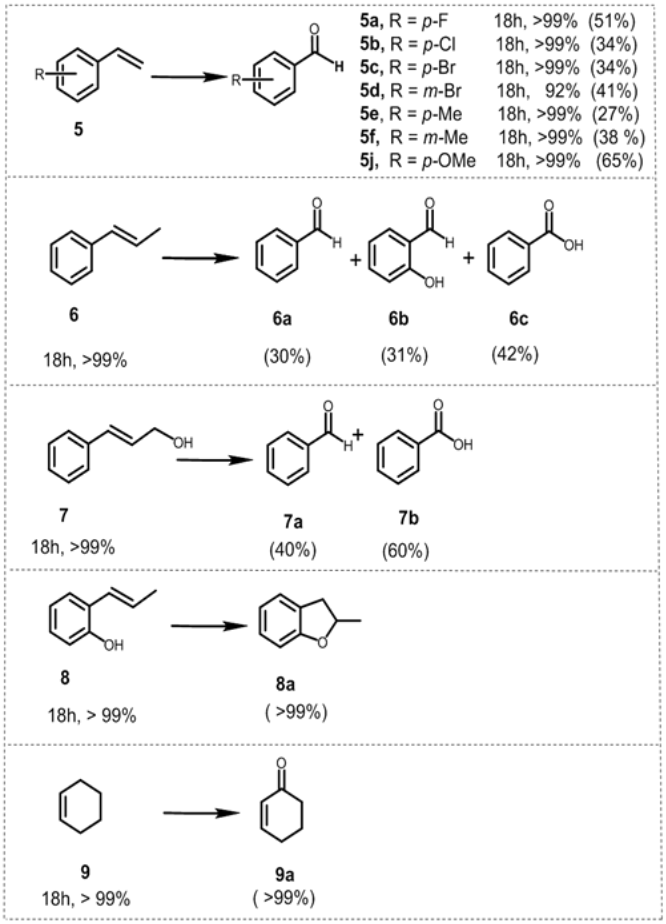

Figure 31. Scope of alkenes for the photocatalytic C=C bond cleavage using BBT as photocatalyst.

Following the same procedure, trans-β-methyl styrene **6** and cynnamyl alcohol **(7)** were utilized as substrates to test secondary olefins under identical conditions. Both **(6)** and **(7)** were oxidized to the corresponding carbonyl compounds, offering benzoic acids as the main product with a yield of 40% **(6c)** and 60% **(7b)** respectively, which implied that BBT was also suitable for the secondary olefins. Additionally, BBT could be efficiently used for the synthesis of benzofuran **(8a)** from 2-allylphenols **(8)** and 2-cyclohexen-1-one **(9a)** from cyclohexene **(9)**, both in excellent yields.

The stability and reusability of BBT were investigated via 5 additional repeat experiments under the same reaction conditions. As shown in **Figure 32Figure *33***, BBT could catalyse the reaction for 5 additional cycles without significantly affecting its catalytic efficiency. However, the yield to benzaldehyde decreased in favour of the formation of 1-phenyl-1,2-ethanediol, assuming a slow-down of the photocatalytic reaction after five cycles of use.

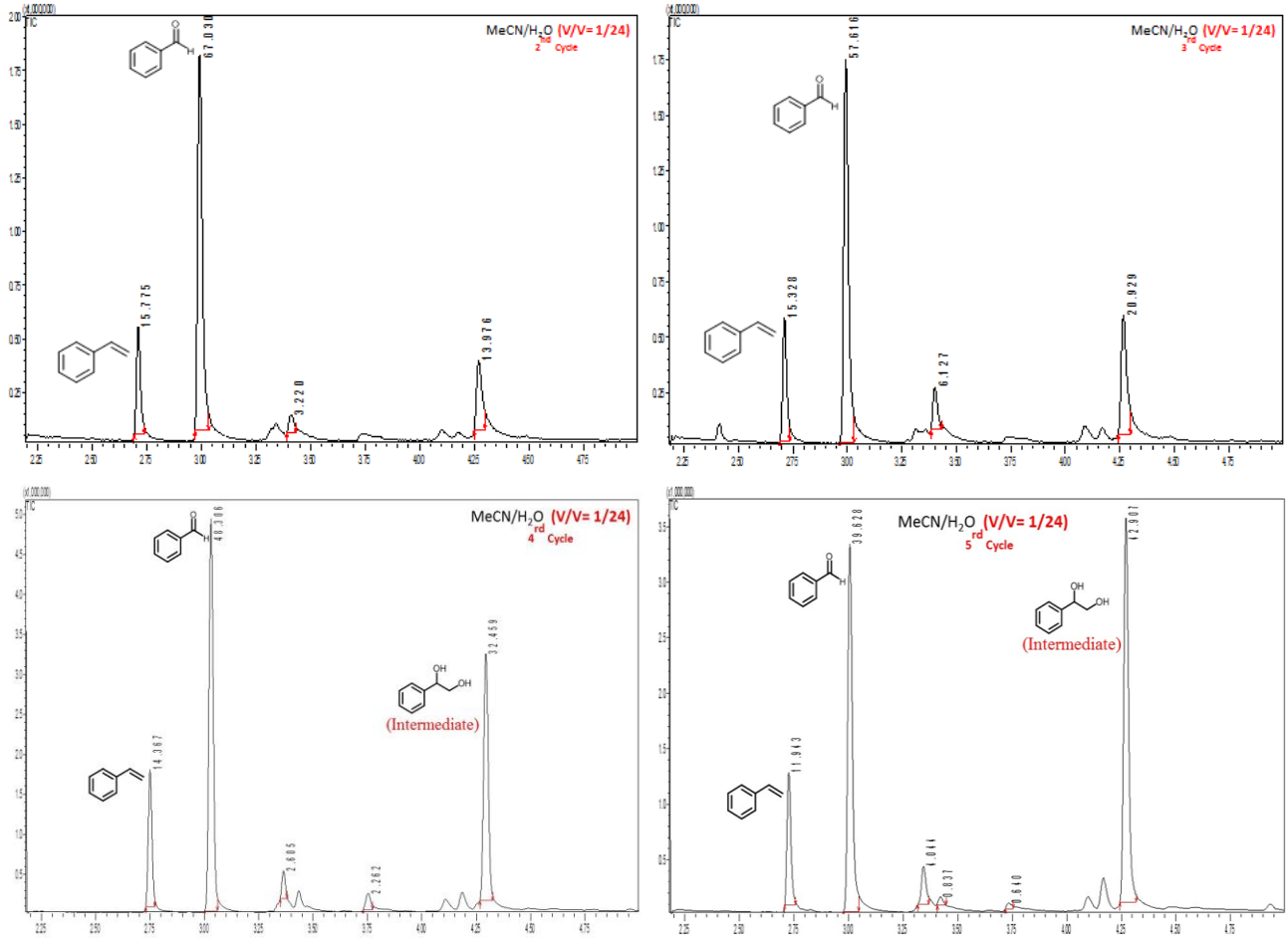

Figure 32. Repeating experiments of the photooxidative cleavage of styrene using BBT as photocatalyst.

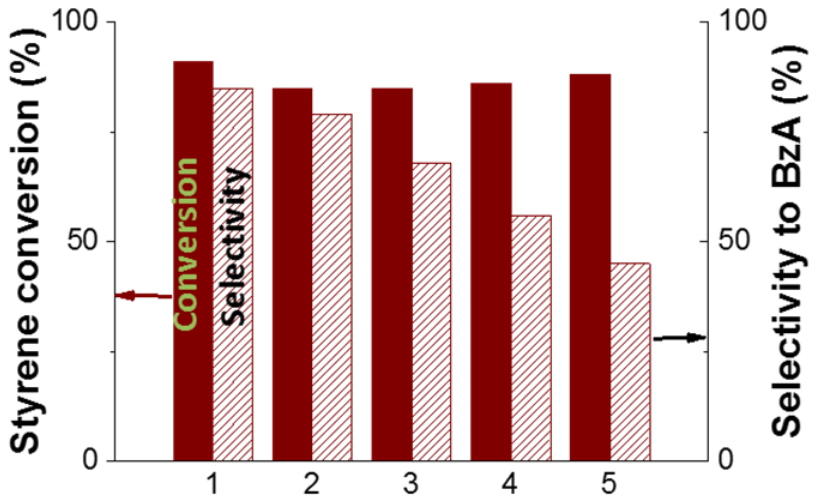

Figure 33. Repeating experiments of the photooxidative cleavage of styrene using BBT as photocatalyst.

FT-IR and UV/div spectra **(Figure 34)** remain unchanged after the repeating experiments, which further confirm the high stability of the photocatalyst.

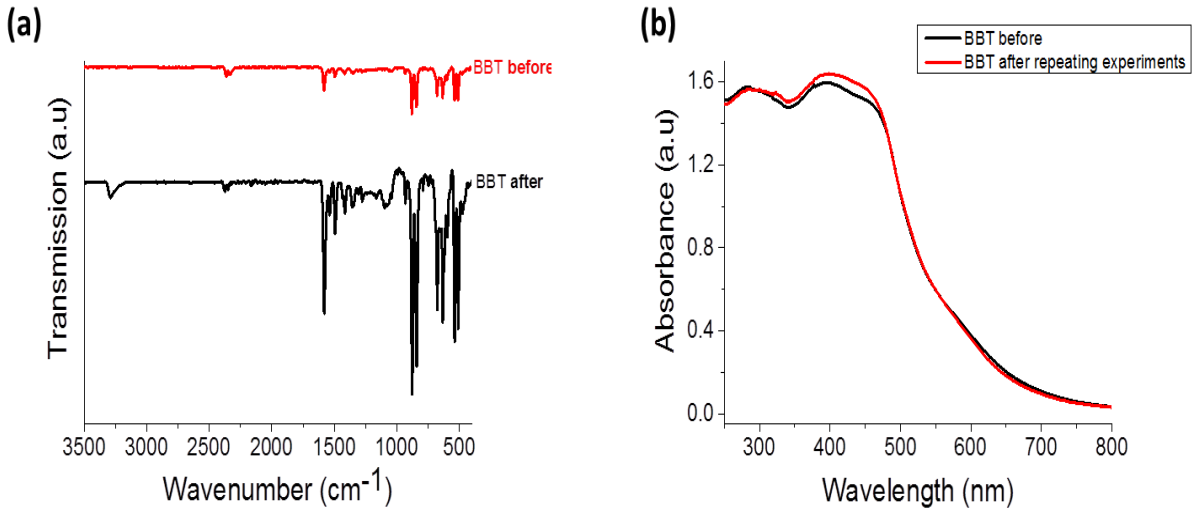

Figure 34. FTIR and UV/vis DR spectra of BBT before and after the repeating experiments.

5.1.4. Conclusion and outlook

In summary, we demonstrated the design strategy of conjugated microporous polymers (CMPs) as heterogeneous, visible-light active and stable photocatalysts for the photocatalytic C=C bond cleavage reaction of alkenes. By combining specific electron donor and acceptor building blocks with the CMP backbone structure, we found out that the CMP containing benzothiodiazole as a strong electron acceptor and phenyl as weak electron donor was the most efficient photocatalyst. The photocatalytic cleavage reaction of the C=C bond was found to be strongly dependent on the solvent polarity, with the aqueous

reaction mixture being the ideal reaction medium with benzaldehyde as main products with high efficiency and selectivity.

5.2. Designing covalent triazine framework for photocatalytic epoxidation of styrene with *in-situ* generated hydrogen peroxide in aqueous medium

This subchapter is based on the unpublished article "Designing covalent triazine framework for photocatalytic epoxidation of styrene with in-situ generated hydrogen peroxide in aqueous medium". Cyrine Ayed designed and performed the experiments, analyzed the data and drafted the manuscript. Dr. Lucas Caire da Silva performed the ^{13}C solid state NMR measurements. Cyrine Ayed, Prof. Dr. Kai Zhang and Prof. Dr. Katharina Landfester contributed to the final version of the manuscript. Prof. Dr. Kai Zhang and Prof. Dr. Katharina Landfester supervised the project.

In the previous chapter, conjugated microporous polymers, with specific electron donor-acceptor, has been designed and has demonstrated its efficiency for the photocatalytic oxidation of styrene under visible light irradiation. Benzaldehyde was obtained as main product in water based reaction medium with high conversion and selectivity. Indeed, the reaction could not be carried out in pure water due to the hydrophobic nature of the CMPs. Therefore, developing a CPP, whose structure can favor reactions in aqueous environment is indeed more desirable. Beside the catalyst design, gaining more valuable products from the styrene oxidation, in particular, styrene oxide via the so-called styrene epoxidation is of considerable high interest due to the versatile utilization of styrene oxide in the further productions of petrochemicals, pharmaceuticals and fine chemicals. Herein, we report a design strategy of covalent triazine frameworks (CTFs) as heterogeneous, metal-free, stable and recyclable photocatalysts for visible light-driven epoxidation of styrene in water, using $NaHCO_3$ as promoter and oxygen as oxidant. Different electron donor-acceptor combinations in the CTF core were investigated to correlate between the structural, optical and photocatalytic properties. The CTF bearing benzothiazole as electron acceptor, phenyl as electron donor and triazine as electron acceptor exhibited the highest styrene oxide selectivity among the polymer series. The reaction involves an *in-situ* photogeneration of hydrogen peroxide from water and reactive oxygen species, which in presence of $NaHCO_3$, gives rise to peroxymonocarbonate, serving as the actual epoxidizing agent.

5.2.1. Motivation

The epoxidation of alkenes, notably styrene, has received increasing attention and a research interest, as it is a key reaction for the production of styrene oxide.[304] The latter is an important organic intermediate in the synthesis of petrochemicals, pharmaceuticals and fine chemicals. The conventional styrene epoxidation reaction involves organic peracides as oxidizers.[305-307] However, this route led to poor styrene oxide selectivity with a high generation of byproducts.[307] consequently, several attempts have been made to substitute this conventional route with the use of environmentally friendly photocatalytic systems. Mainly metal-based photocatalysts have been used including $[Ru(bpy)_3]Cl_2 \cdot 6$

H_2O,[308] copper nanoparticles supported on titanium nitride (Cu@TiN),[309] TiO_2 dispersed on SiO_2,[310] Calcium modified V_2O_5@SiO_2[311] and WO_3-TiO_2 mixed metal oxides,[312] in organic solvents together with H_2O_2 or O_2 as oxidizing agents. Under these conditions, the selectivity to styrene oxide ranged from 18% to 90%. A few studies have reported later the use of metal-based g-C_3N_4 as photocatalysts at high temperature (> 60 °C).[313, 314] Nevertheless, none reported the photocatalytic epoxidation of styrene over pure organic, metal-free CPP so far. There is therefore need for the development of CPP-based photocatalytic systems with high stability and good reusability.

Moreover, the desire for sustainability surpasses nowadays the catalyst design itself and converges toward the exploration of greener reaction media, notably the use of water, because of its availability, its low cost, its non-toxicity and non-corrosivity. The previously synthesized CMP presented relatively poor catalytic performance for the photocatalytic oxidation of styrene in pure water. Thus, developing another class of CPPs, who can promote photocatalytic reactions in aqueous medium is advantageous.

Herein, a series of covalent triazine frameworks (CTFs) bearing different electron donor-acceptor building blocks are designed as heterogeneous photocatalysts for the epoxidation of styrene under visible light irradiation in aqueous medium. Molecular oxygen was also used as oxidizing agent at atmospheric pressure. Then, the structural influence of the as-designed CTFs on their photocatalytic efficiency is investigated. It was shown that the photocatalytic reaction could be conducted with almost quantitative conversion with all catalysts leading to two main products such as styrene oxide and benzaldehyde in different ratios. However, the CTF, with extended π- conjugated acceptor/donor/acceptor system (CTF-BT-Ph_2) led to relatively higher styrene oxide selectivity in comparison to the other CTFs, with high photogeneration of singlet oxygen and high *in-situ* generation of hydrogen peroxide. Further, a mechanistic insight of the reaction is discussed.

5.2.2. Synthesis and characterization of CTF based photocatalysts

In this work, a series of CTF-based materials were obtained through a facile and direct solvent-free trimerization reaction of nitrile-functionalized monomers catalyzed by triflic acid vapors (TfOH) at 100 °C. This strategy is indeed eco-friendlier alternative to prepare CTFs in comparison to the traditional high-temperature ionothermal method, which requires relatively harsh conditions (> 400 °C) in molten $ZnCl_2$.[177] To expand the active surface area and gain extra compatibility in water, mesoporous silica particles (SBA-15) with pore size of ~ 4.1 nm were used as support and template. The detailed procedure is described in the Experimental Section **6.2.3**. **Scheme 2** summarizes the building blocks employed for the synthesis of CTFs, in which different electron donor (D)-acceptor (A) moieties were combined. For instance, 1,3,5-triazine and 2,1,3-benzothiadiazole (BT) moieties are known to be very strong electron

acceptors, while thiophene units (Th) and benzene units (Ph) are electron donors with different electron affinities.

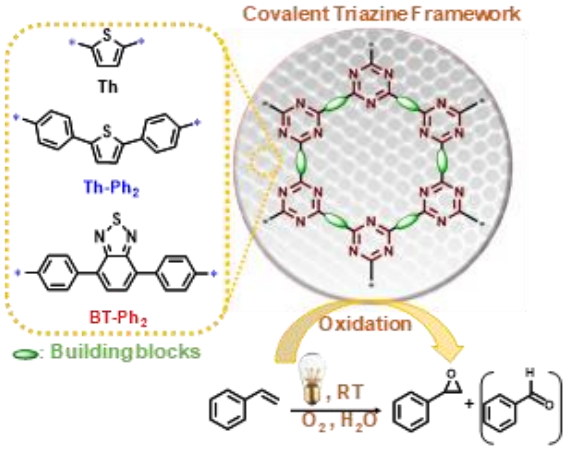

Scheme 2. Structural design of a series of covalent triazine frameworks (CTFs) via integration of different building blocks.

We confirmed the successful synthesis of the nitrile functionalized monomers/building blocks through proton ^{1}H and carbon ^{13}C-Nuclear magnetic resonance (NMR) spectroscopy (**Figure 35-Figure *37*)**. They were obtained as solid powders, which are insoluble in all common organic solvents. The extended π-conjugated structures with donor-acceptor arrangements would improve the intermolecular electron delocalization in photocatalytic reactions and expand the visible-light responsivity.[315]

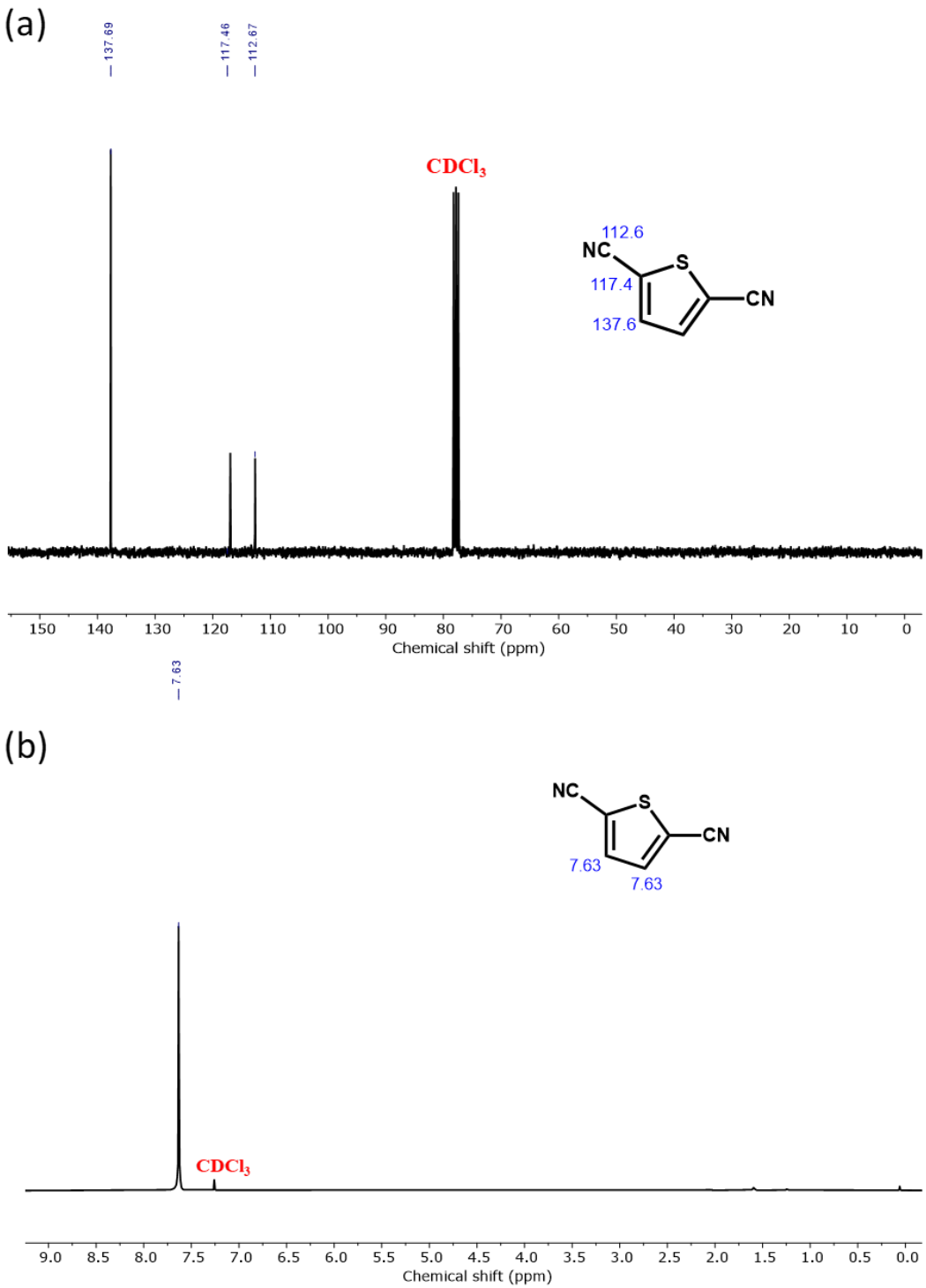

Figure 35. a) ^{13}C and (b) ^{1}H-NMR spectra of CN-Th-CN recorded in $CDCl_3$.

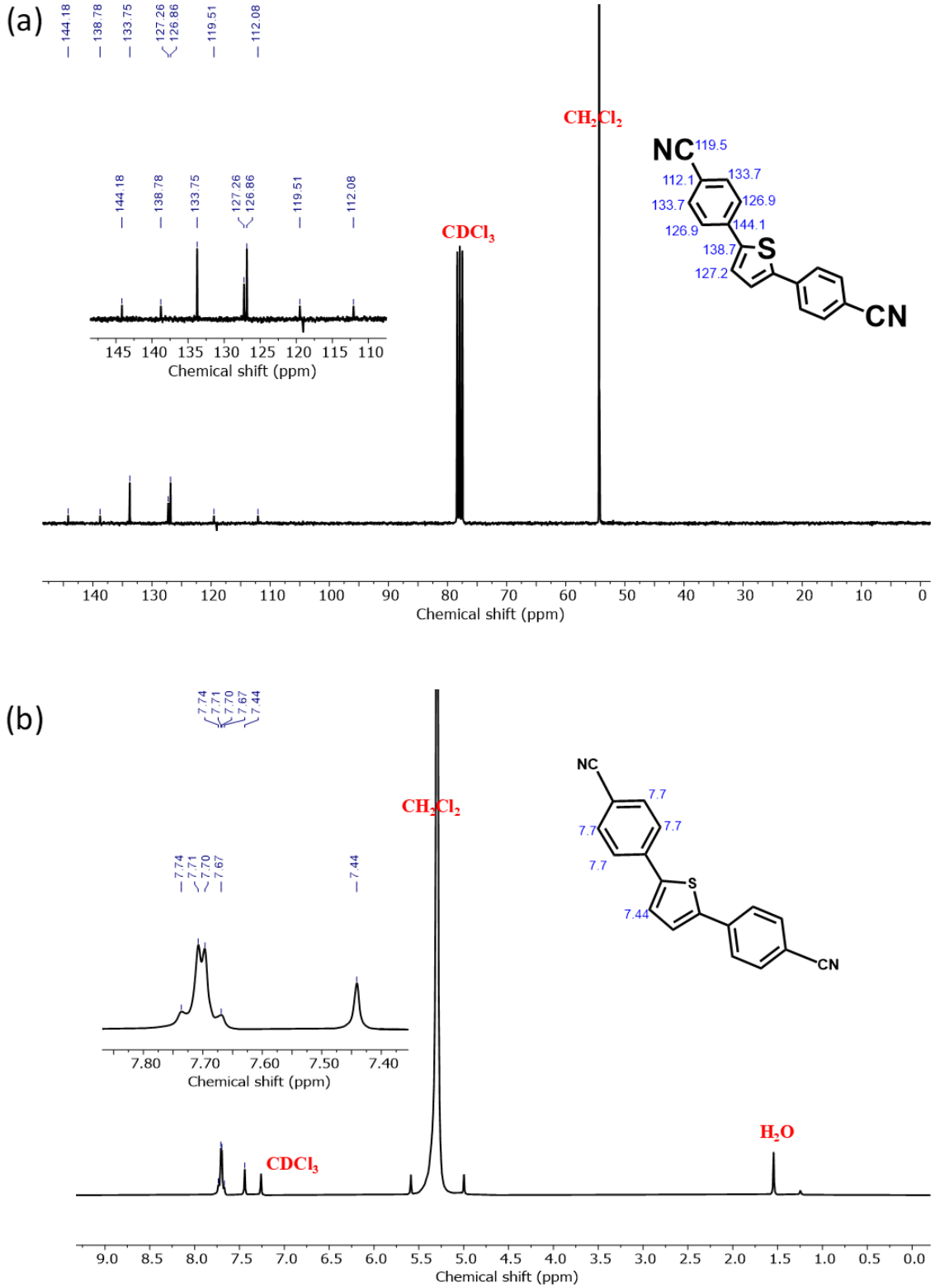

Figure 36. (a) ^{13}C and (b)^{1}H-NMR spectra of CN-Ph-Th-Ph-CN recorded in $CDCl_3$.

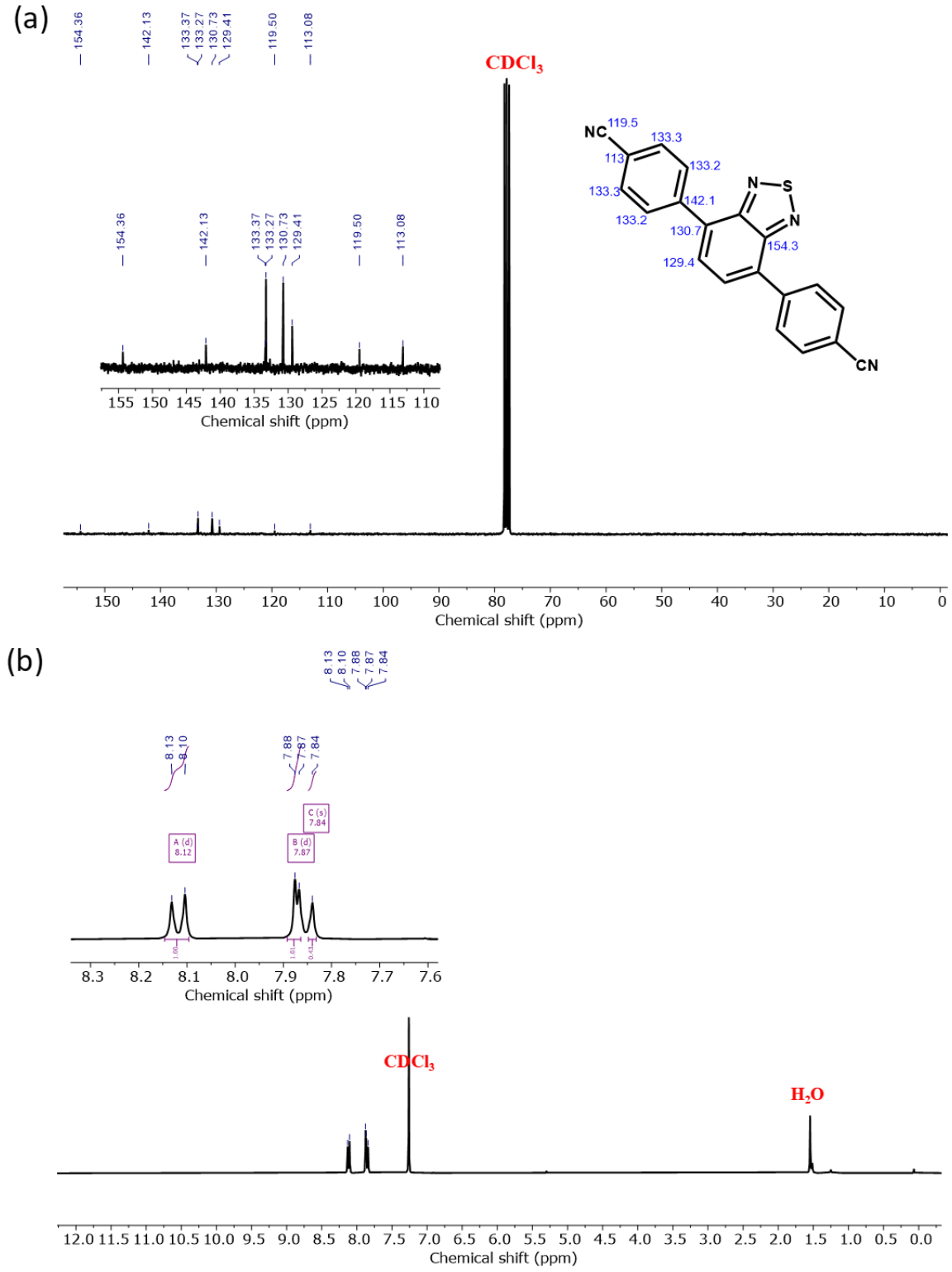

Figure 37. ^{13}C and (b) ^{1}H-NMR spectra of CN-Ph-BT-Ph-CN recorded in $CDCl_3$.

Scanning electron microscopy (SEM) and high-resolution transmission electron microscopy (HR-TEM) were used to investigate the morphologies of the as-designed CTFs. As displayed in **Figure 38**, the SEM images of the synthesized materials revealed the presence of cylindrical pore channels in a hexagonal arrangement of ca. 600 nm of diameter.

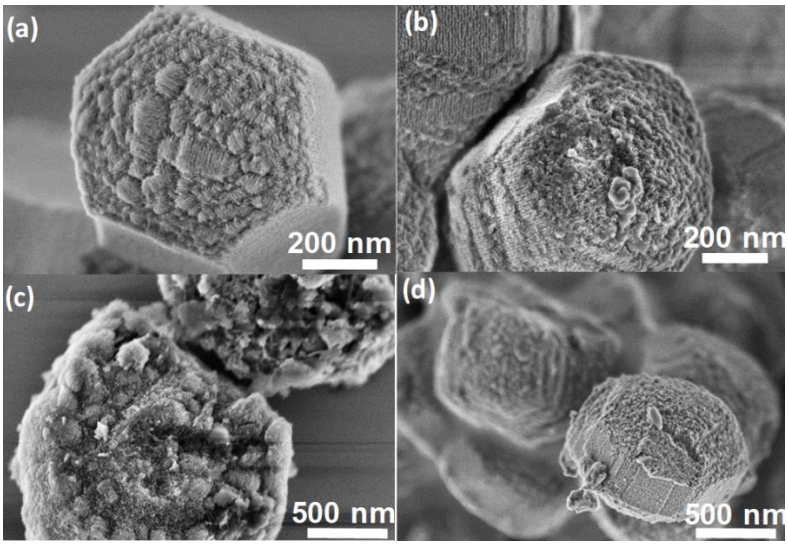

Figure 38. SEM images of (a) pure SBA-15, (b) CTF-Th, (c) CTF-Th-Ph_2 and (d) CTF-BT-Ph_2.

HR-TEM confirmed the presence of mesopores with uniform size distribution in all the samples **(Figure 39).**

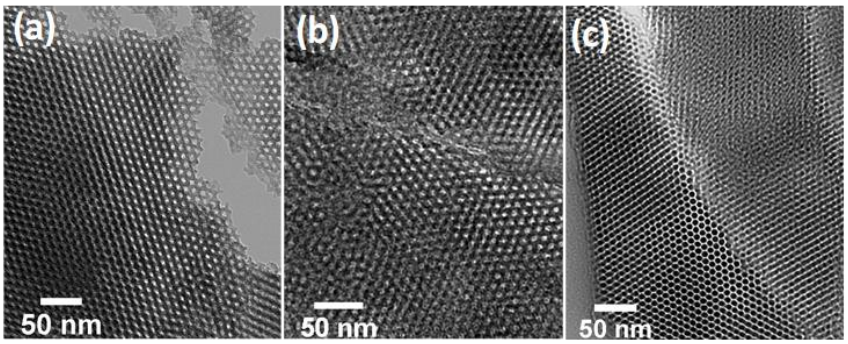

Figure 39. HR-TEM images of (a) CTF-Th, (b) CTF-Th-Ph_2 and (c)-CTF-BT- Ph_2.

The Brunauer–Emmett–Teller (BET) surface areas of the CTF-Th, CTF-Th-Ph_2 and CTF-BT-PH_2 revealed typical type-IV adsorption isotherms with noticeable H1-type hysteresis loops in the relative pressure (P/P0) region of 0.6–0.8.

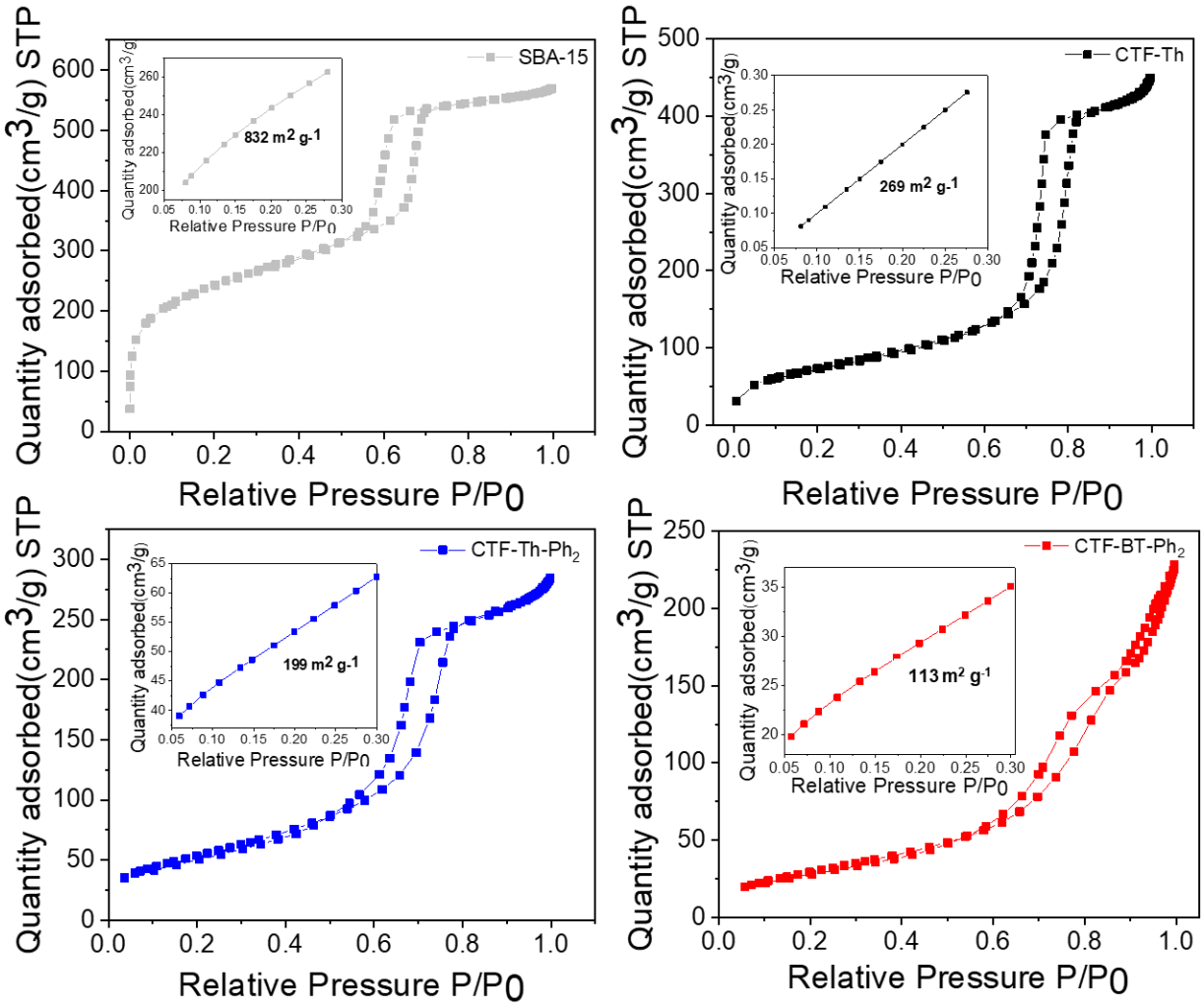

Figure 40. N_2 absorption and desorption at 77K of pure SBA-15 and the as-designed CTFs. Insert shows region used to calculate the BET surface area.

A linear increase in the absorbed volume at low pressures (< 0.3) was observed. These are in concord with the HR-TEM results, suggesting further the mesoporous structure **(Figure 40).** In addition to the morphological effect, SBA-15 endowed the materials with relatively high surface areas ranging from 113 m^2g^{-1} to 269 m^2g^{-1} **(Figure 40-Inset)**. **Figure 41** displays the pore size distribution using BJH method. CTF-Th, CTF-Th-Ph_2 and CTF-BT-Ph_2 possess pore sizes of 9.4, 7.3, and 10.1 nm, respectively, which are even larger than that of SBA-15 (5.1 nm).

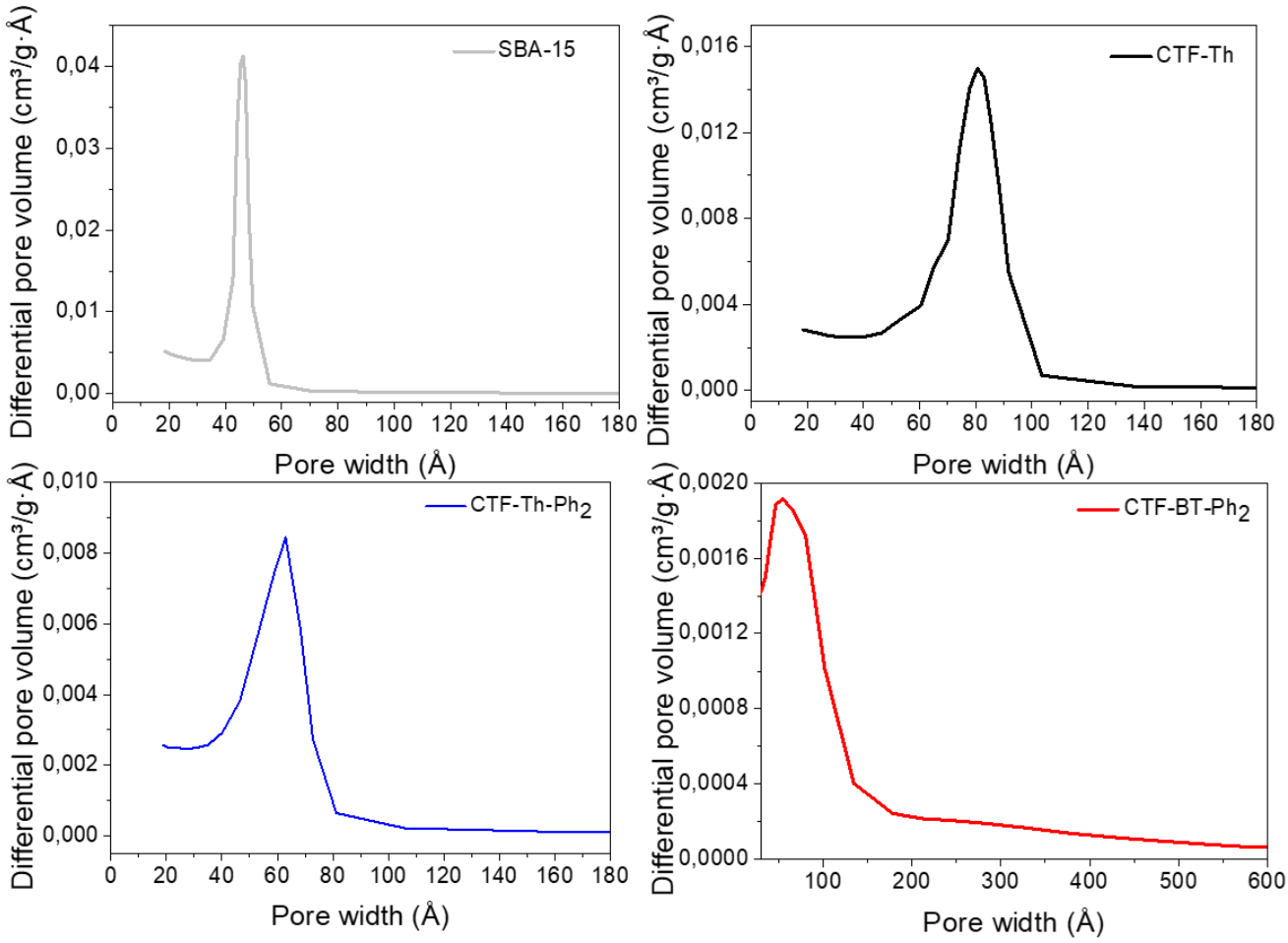

Figure 41. Pore size distribution by Barrett-Joyner-Halenda (BJH) method.

To evaluate the degree of hydrophilicity of the materials, water contact angles (θ) were recorded. It was found out that all CTFs exhibited water contact angles inferior to 90°, indicating the added hydrophilicity feature induced by the presence of SBA-15 support **(Figure 42)**. This would enhance their dispersibility in water and thus enable the catalytic reaction in aqueous environment.

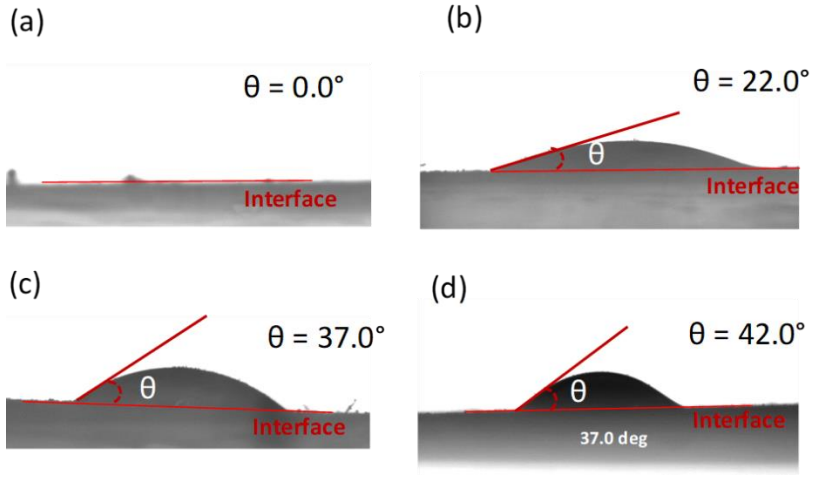

Figure 42. Water contact angle measurement of coated (a) SBA-15, (b) CTF-Th, (c) CTF-Th-Ph$_2$ and (d) CTF-BT-Ph$_2$.

Table 3 lists all the physical properties of the designed CTFs.

Table 3. Physical properties of the designed CTFs.

CTF	S_{BET} ($m^2\ g^{-1}$)	Pore volume ($cm^3\ g^{-1}$)	Pore size (nm)	Band gap (eV)	θ (°)
CTF-Th	269	0.52	6.7	2.95	22
CTF-Th-Ph_2	199	0.3	5.3	2.55	37
CTF-BT-Ph_2	113	0.27	8	2.48	42
SBA-15	832	0.4	4.2	4.1	0

The Fourier-transform infrared (FTIR) spectra of all CTFs are displayed in **Figure 43a**. The typical bands at 1359 cm^{-1} and 1428 cm^{-1}, can be assigned to the aromatic C=N stretching and breathing modes in the triazine unit, respectively. The absence of the band at ~ 2220 cm^{-1} (typical for terminal cyano groups in the monomers) further confirms the complete trimerization of the nitrile-functionalized monomers.[316] Characteristic absorption bands at 1017-1122 cm^{-1} corresponds to the Si–O–Si symmetric and asymmetric stretching in SBA-15.[317]

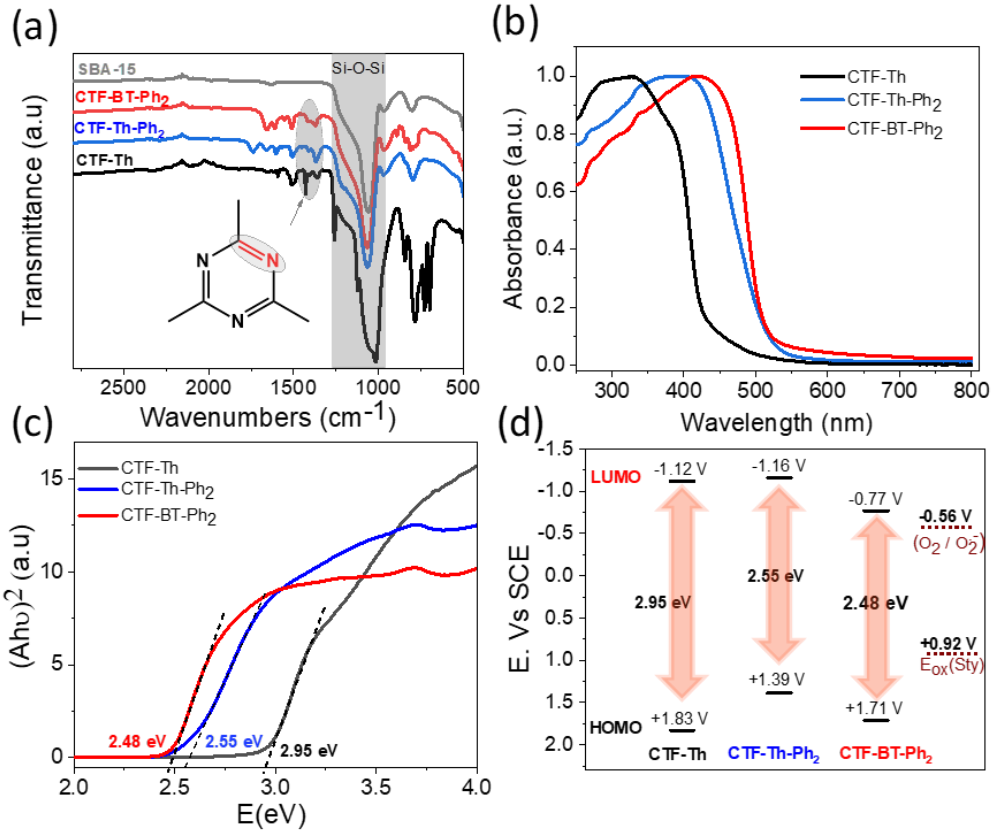

Figure 43. (a) FT-IR, (b) UV-vis diffuse reflectance spectra, (c) Tauc plot and (d) highest occupied molecular orbital (HOMO) and lowest unoccupied molecular orbital (LUMO) band positions of the designed CTFs.

Solid-state ^{13}C/MAS NMR spectra of the CTFs revealed a common characteristic peak at 167-170 ppm, which can be assigned to the sp^2 carbon in the triazine ring. The rest of the peaks appearing in the range of 120-154 ppm can be ascribed to the sp^2 aromatic carbons of the CTF core **(Figure 44)**.[251, 316] Thermogravimetric analysis (TGA) revealed that all CTFs are very stable up to 300 °C under oxygen atmosphere followed by gradual weight loss up to 1000 °C **(Figure 45)**. **Figure 43b** displays the UV/vis diffuse reflectance (DR) spectra of the CTFs: CTF-Th-Ph_2 and CTF-BT-Ph_2 showed broader absorption bands in the visible range up to 530 nm, in comparison to CTF-Th, which only absorbed up to 420 nm. This could be due to the extension of conjugation induced by the introduction of phenyl unit in the structures that maximize the delocalization of π electron over the CTFs backbone, broadening thus the light harvesting in the visible region.[154, 318] The optical band gap values of the CTFs were calculated using the Tauc's plot and determined to be 2.95 eV for CTF-Th, 2.55 eV for CTF-Th-Ph_2 and 2.48 eV for CTF-BT-Ph_2 **(Figure 43c** and **Figure 46)**. The trend of the experimental band gaps is also consistent with those deduced from the theoretical simulations using time-dependent density functional theory (TD-DFT-**Figure 47**).

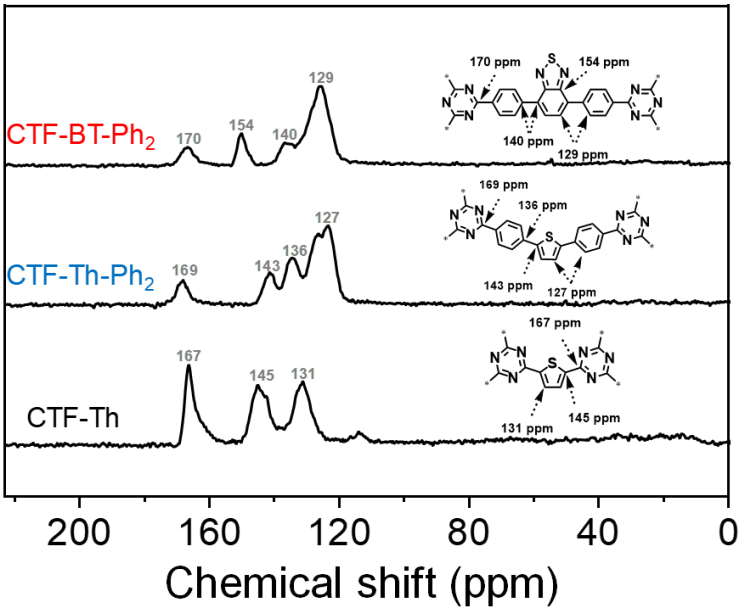

Figure 44. ^{13}C CP/MAS NMR spectra of the designed CTFs.

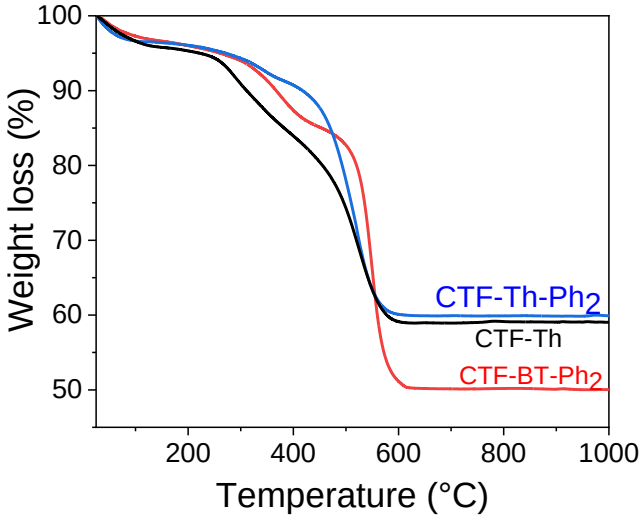

Figure 45. TGA spectra of the materials under O_2 atmosphere with a heating rate of 10 ºC/min.

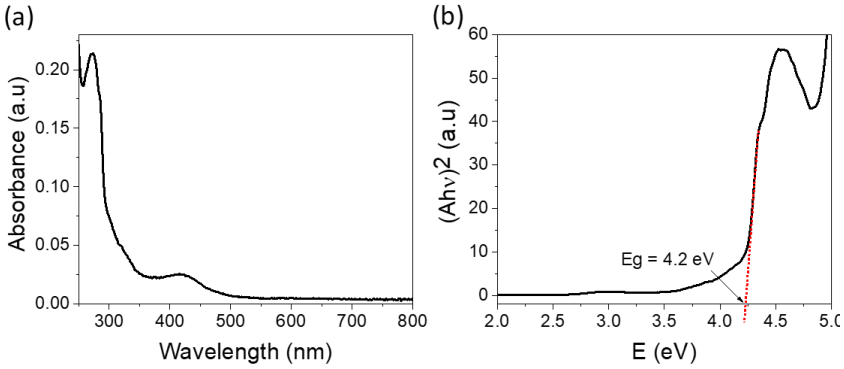

Figure 46. (a) UV-vis diffuse reflectance spectra and (b) Tauc plot of pure SBA-15.

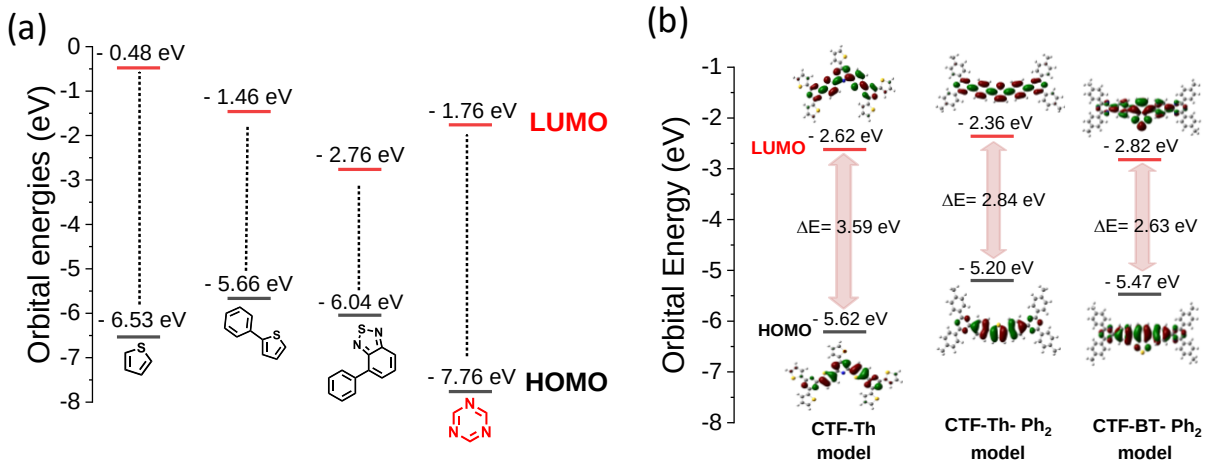

Figure 47. (a) Orbital energy levels of building blocks based on the theoretical calculations and (b) charge density distribution of HOMO and LUMO orbitals for CTFs models. All energies are referenced with respect to the vacuum level.

The cyclic voltammetry (CV) measurements were performed to examine the energy band structure of the designed CTFs.

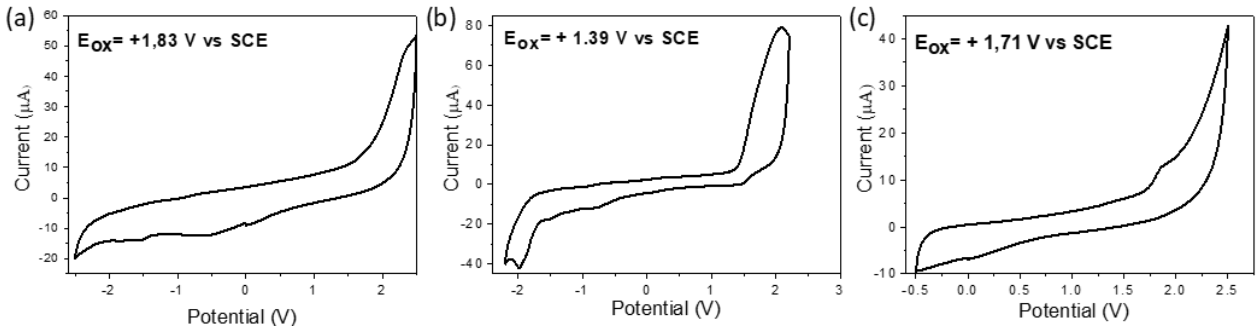

Figure 48. Cyclic voltammograms of (a) CTF-Th, (b) CTF-Th-Ph_2 and (c) CTF-BT-Ph_2.

As shown in **Figure 43d** and **Figure 48-Figure *49***, all CTFs favor the reduction of molecular oxygen (E_{red}= -0.56 V. vs. SCE) and the oxidation of the styrene substrate (E_{ox}= + 0.92 V vs. SCE), with thermodynamically sufficient redox potentials. However, it is worthy to mention that CTF-BT-Ph_2, which has the narrowest band gap, would generate more charges under visible light irradiation and thus would have possible superior photocatalytic activity.

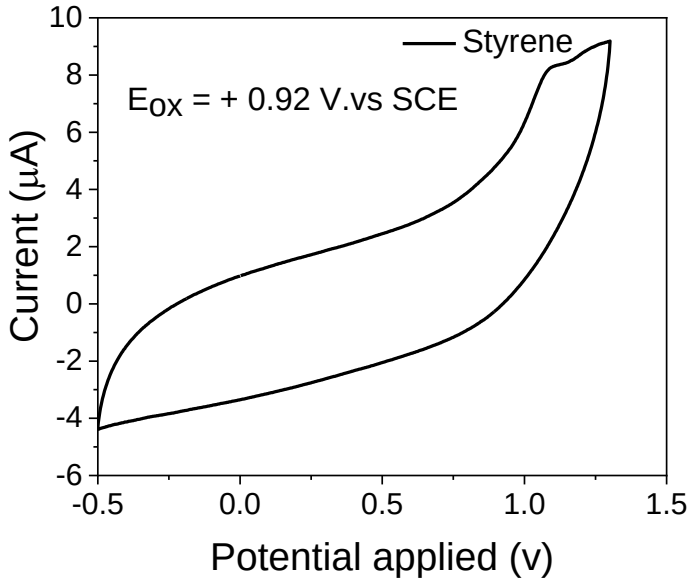

Figure 49. Oxidation potential of styrene measured by cyclic voltammetry. (Preparation: 0.05 mmol of styrene in 5 ml of Bu_4NPF_6 electrolyte solution)

5.2.3. Visible-light promoted photocatalytic epoxidation of styrene in aqueous medium

To investigate the photocatalytic performance of the designed CTFs, we tested the visible light promoted styrene epoxidation in water and in presence of bicarbonate sodium $NaHCO_3$ as promoter and molecular oxygen as oxidant. The reaction kinetics and the product distribution are summarized in **Figure 50** and **Table 4.** The photocatalytic reactions could be conducted with almost quantitative conversion with all catalysts leading to two main products such as styrene oxide and benzaldehyde in various ratios **(Figure 50a** and **entries 1-3 in Table 4)**. Phenylacetaldehyde and 1-phenylethan-1,2-diol were also observed as by-products and most likely originated from the rearrangement of the styrene oxide. In particular, CTF-BT-Ph_2 showed the highest selectivity toward styrene oxide (> 50%) after only 30 min of irradiation in comparison to those obtained in presence of the other CTFs (< 40%) **(Figure 50b).** Further extending the irradiation time (up to 7 h) increased significantly the conversion of styrene (> 90%). However, the product distribution remained almost unchanged over time. No increase of the styrene oxide selectivity in favor of that of benzaldehyde or vice versa were noticed **(Figure 51).** Therefore, we suggest the involvement of two parallel reaction pathways leading either to styrene oxide via epoxidation reaction or to benzaldehyde via oxidative C-C double bond cleavage. Note that SBA-15 used as support did not contribute in the reaction as it showed almost no photocatalytic activity under visible light irradiation **(entry 4 in Table 4).**

Table 4. Photocatalytic oxidation of styrene using CTF-based photocatalysts and under various reaction conditions.

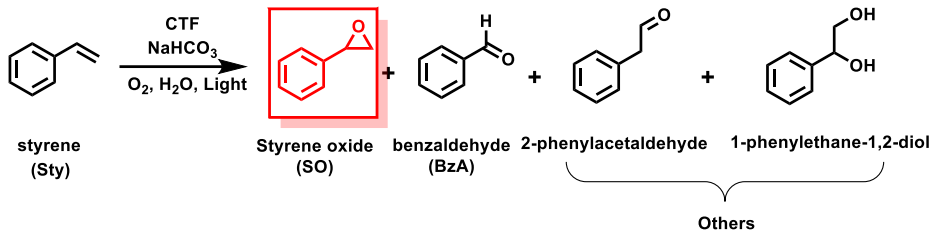

Entry[a]	Catalyst	Light	O_2	$NaHCO_3$ (mmol)	Scavengers	Conversion[b] (%)	Selectivity [c] SO (%)	BzA (%)	Others (%)
1	CTF-BT-Ph_2	+	+	1	-	98 (23)	41 (53)	50 (46)	9 (1)
2	CTF-Th-Ph_2	+	+	1	-	78 (31)	18 (37)	59 (57)	23 (6)
3	CTF-Th	+	+	1	-	91 (19)	34 (34)	58 (57)	8 (9)
4[d]	SBA-15	+	+	1	-	4	n.d	> 99	n.d
5[e]	BBT	+	+	1	-	57	16	63	21
6[f]	CTF-BT-Ph_2	-	+	1	-	< 1	n.d	n.d	n.d
7[j]	-	+	+	1	-	< 1	n.d	n.d	n.d
8[h]	CTF-BT-Ph_2	+	+	-	-	82	n.d	74	26
9[i]	CTF-BT-Ph_2	+	+	1	KI	> 99	36	51	13
10[j]	CTF-BT-Ph_2	+	+	1	BQ	3	n.d	> 99	n.d
11[k]	CTF-BT-Ph_2	+	+	1	NaN_3	> 99	n.d	98	2
12[l]	CTF-BT-Ph_2	+	+	1	IsPr	> 99	27	56	17
13[m]	CTF-BT-Ph_2	+	+	1	catalase	> 99	21	47	32

[a)] Standard reaction conditions: 0.1 mmol of styrene, 10 mg of photocatalyst in 5 ml of water under the irradiation of a blue LED lamp (460 nm, 65 mW cm^{-2}), 1 atm. O_2, room temperature. [b)] Conversion determined by GC-MS, t = 7 h. [c)] Selectivity toward the products, t = 7 h. Values between parentheses are related to the results at 30 min of photoirradiation. [d)] pure SBA-15, under light, 1atm O_2, 5 ml H_2O. [e)] benzothiadiazole based conjugated microporous polymer (BBT), under light, 1atm O_2, 5 ml H_2O. [f)] CTF-BT-Ph_2, no light, 1atm O_2, 5 ml H_2O. [j)] without catalyst, under light, 1atm O_2, 5 ml H_2O. [h)] CTF-BT-Ph_2, without $NaHCO_3$, under light, 1atm O_2, 5 ml H_2O. [i)] Potassium iodide (KI) as a hole scavenger, [j)] Benzoquinone (BQ) as superoxide scavenger. [k)] Sodium azide (NaN_3) as singlet oxygen scavenger. [l)] Isopropanol (IsPr) as Hydroxyl radical scavenger. [m)] Catalase as $H2O_2$ scavenger. n.d: not detected.

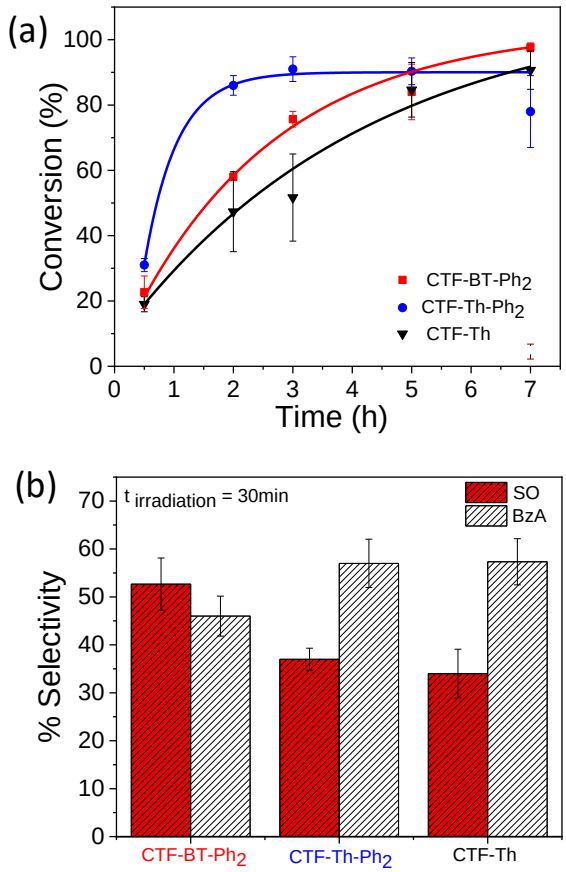

Figure 50. (a) Photocatalytic styrene conversion over the as synthesized CTFs under visible light irradiation (λ = 460 nm) and at different reaction times and (b) styrene oxide and benzaldehyde selectivity after 30 min of irradiation.

In comparison, a benzothiadiazole based CPP (BBT), which in our previous work[47] proved its efficiency in oxidizing styrene, has shown low styrene oxide selectivity of 16% in the current study (entry 5 in **Table 4**). This further highlight the superior photocatalytic performance of the CTF-BT-Ph_2.

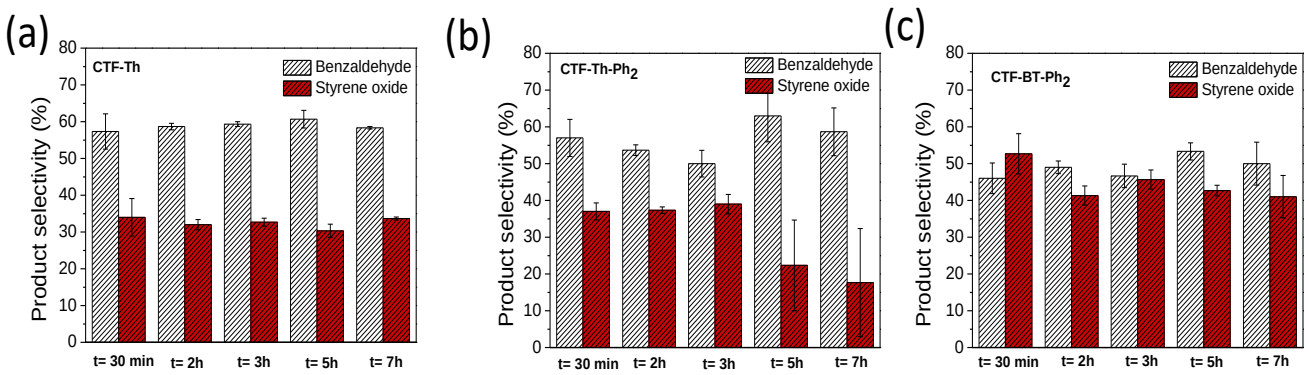

Figure 51. Product distribution over time under blue light irradiation and in presence of (a) CTF-Th, (b) CTF-Th-Ph_2 and (c) CTF-BT-Ph_2.

To further study the reaction mechanism of the photocatalytic epoxidation reaction, several control experiments were conducted using CTF-BT-Ph_2 as model photocatalyst. The results are summarized in **Figure 52Figure *53*,** and in **Table 4.**

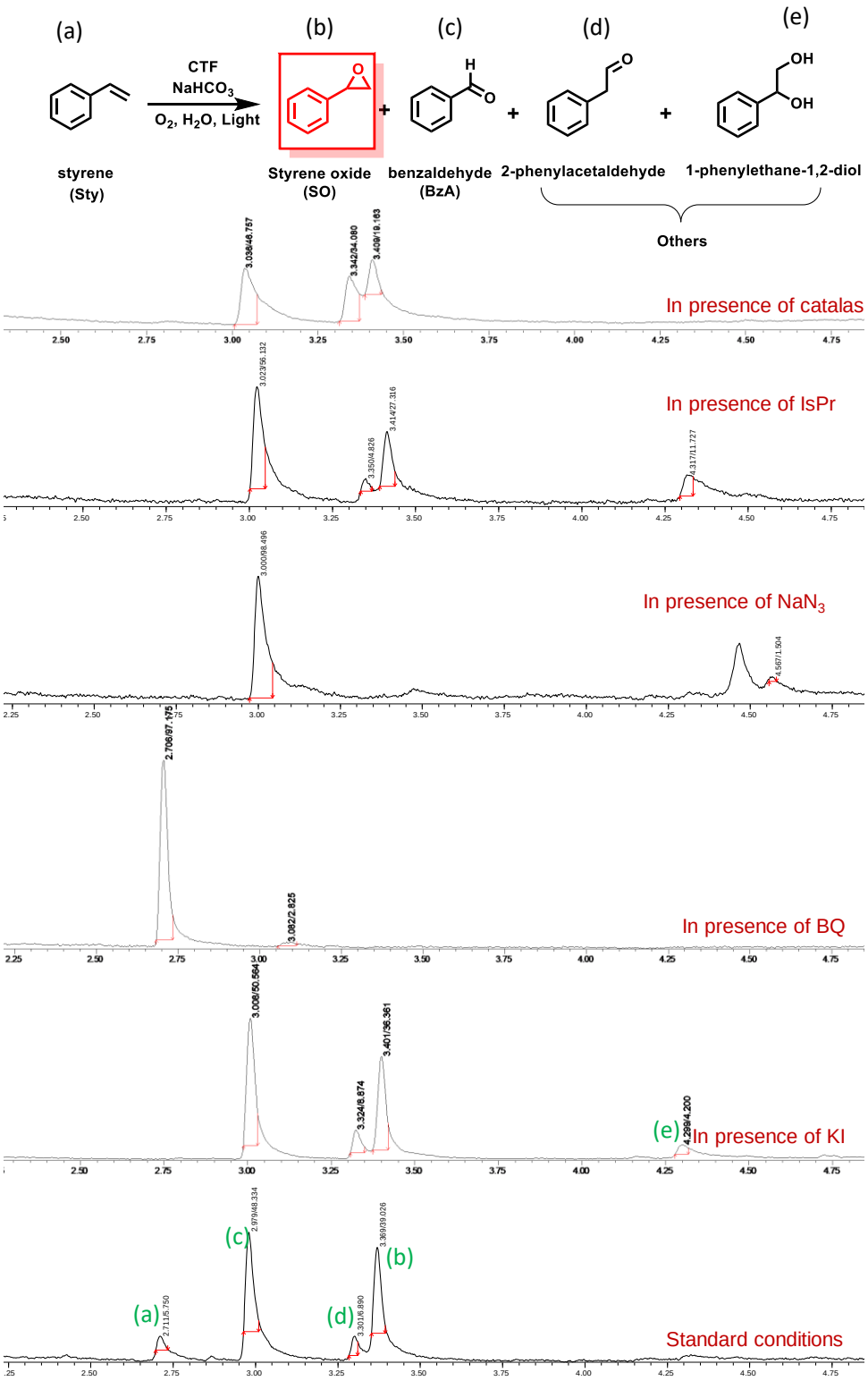

Figure 52. Annotated GCMS spectra of compounds produced after photocatalytic styrene oxidation using CTF-BT-Ph_2 as photocatalyst under different reaction conditions. Irradiation time = 7h.

No reaction has occurred without using light irradiation **(**entry 6 in **Table 4)** or photocatalyst **(**entry 7 in **Table 4).** Under standard conditions, but without using $NaHCO_3$ as promoter, a high conversion of 82% can be still achieved. However, only benzaldehyde was obtained with high selectivity (74%) and no styrene oxide could be detected **(**entry 8 in **Table 4).** This confirms the crucial role of light, photocatalyst and $NaHCO_3$ in epoxidizing styrene.

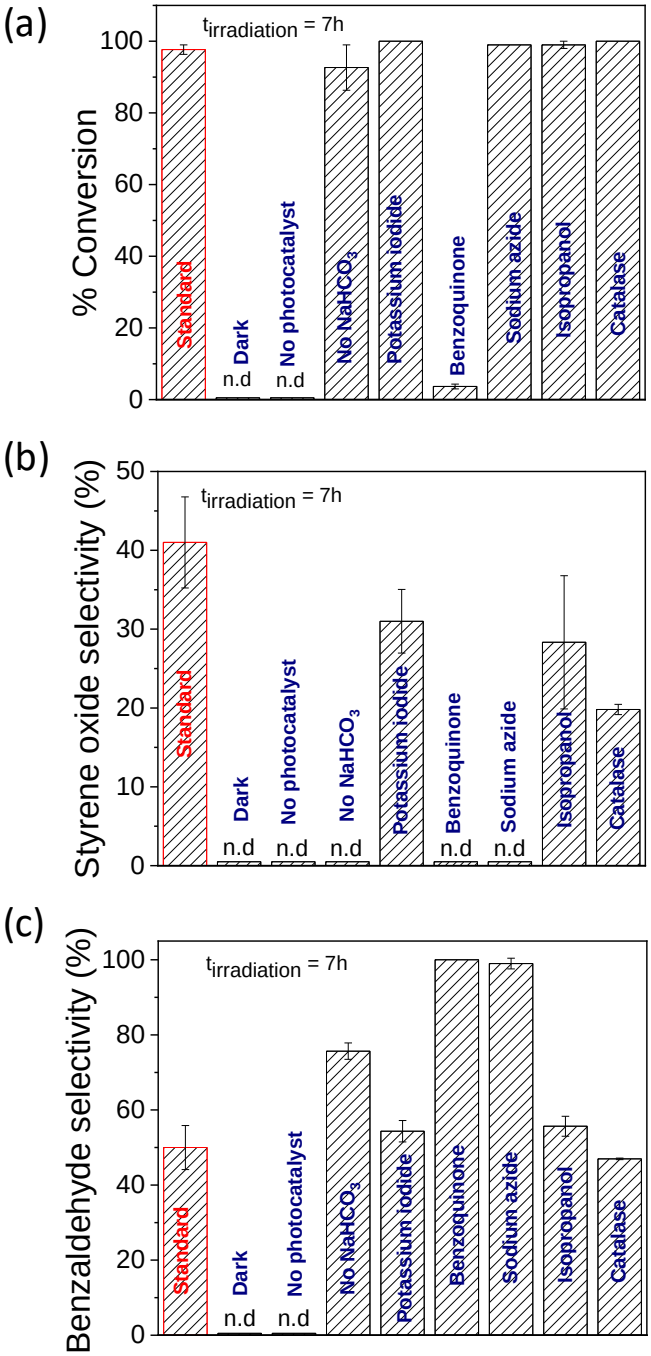

Figure 53. Control experiments for the photocatalytic styrene oxidation using CTF-BT-Ph_2 and their impact on the (a) conversion, (b) the styrene oxide selectivity and (c) the benzaldehyde selectivity. Standard reaction conditions: 0.1 mmol of styrene, 5 mg of CTF-BT-Ph_2 in 5 ml of water under the irradiation of a blue LED lamp (460 nm, 65 mW cm^{-2}), 1 atm O_2 room temperature, 7 h.

To reveal the specific role of the photo-generated electron hole pairs during the photocatalytic process, specific chemical scavengers were added into the reaction mixture. The addition of potassium Iodide (KI) as hole scavenger led to the decrease of styrene oxide selectivity to 36% **(**entry 9 in **Table 4)**. By adding benzoquinone (BQ) as superoxide scavenger, almost no conversion reaction was determined **(**entry 10 in **Table 4)**. By adding sodium azide (NaN_3) as singlet oxygen scavenger, benzaldehyde was determined as main product (98%) and no styrene oxide was formed **(**entry 11 in **Table 4).** Use of isopropanol (IsPr) as a hydroxyl scavenger reduced the selectivity to styrene oxide to 21% **(**entry 12 in **Table 4).** This demonstrated the important role of photogenerated species and particularly the reactive oxygen species (ROS) in the reaction mechanism. To further examine the possible generation of the ROS by CTF-BT-Ph_2 during the photocatalytic process, electron spin resonance (EPR) experiments were performed using 5,5-dimethyl-1-pyrroline N-oxide (DMPO) as superoxide trapping agent and tetramethylpiperidine (TEMP) as singlet oxygen trapping agent, in water. CTF-Th and CTF-Th-Ph_2 were also tested under similar conditions for comparison purpose.

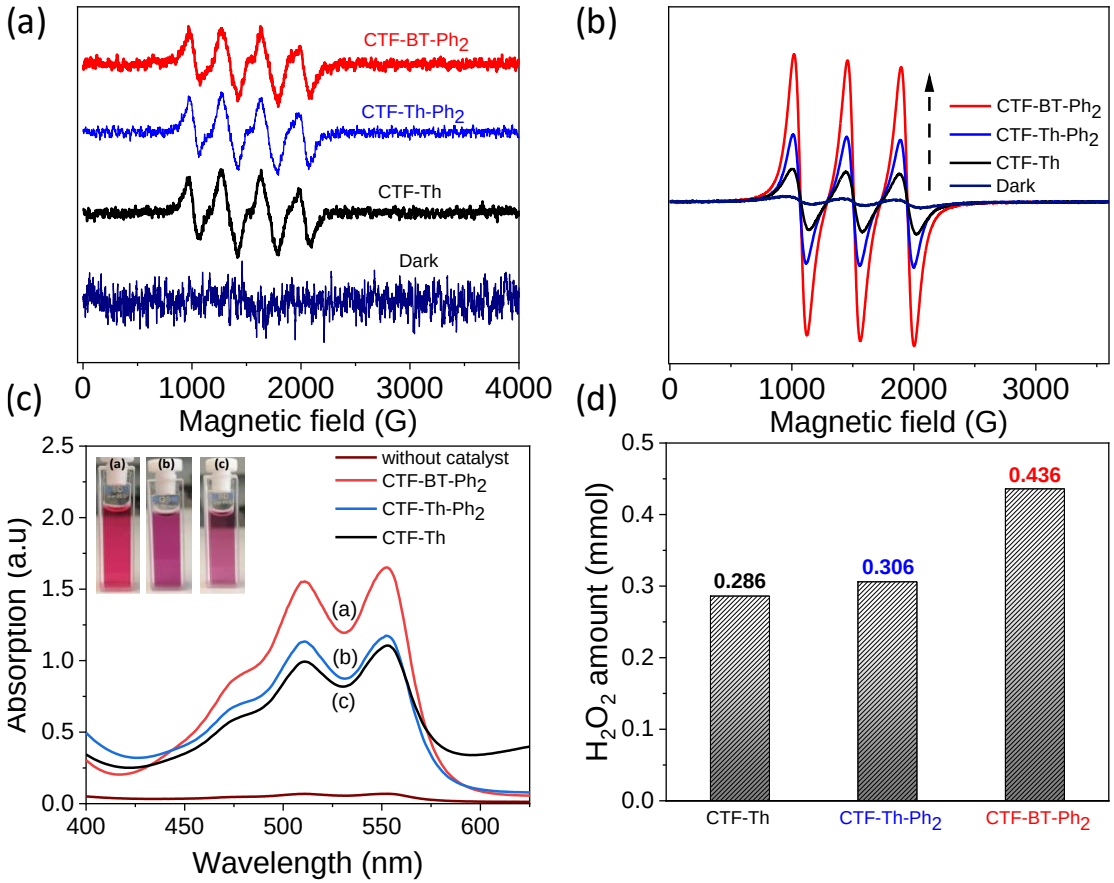

Figure 54. EPR spectra of (a) DMPO-O_2 and (b) TEMP-$^1O_2$ using the as-designed CTF-based photocatalysts in the dark and under light irradiation (λ = 460 nm, 65 mW cm^{-2}). (c,d) spectrophotometric determination and quantification of the in-situ generated hydrogen peroxide H_2O_2 over the synthesized CTFs based on the peroxidase-catalyzed oxidation reaction of DPD.

Typical signals of DMPO-•O_2^- and TEMP-$^1O_2$ adducts were detected in presence of all catalysts and under visible light irradiation **(Figure 54 a,b)**. No difference in the DMPO-•O_2^- signals were noticed, whereas CTF-BT-Ph_2 was able to generate the most intense TEMPO-$^1O_2$ signal among all the polymer series. This suggests its superior capacity in photogenerating $^1O_2$, and would possibly explain its superior epoxidizing performance. It is noteworthy to shed light again on the critical role of $NaHCO_3$ in this reaction. Indeed, the epoxidation of alkenes in presence of bicarbonate activated peroxide system (BAP= $NaHCO_3/H_2O_2$) is known and has been introduced and discussed by Richardson *et al*., since 2000.[319] The merit of such system was focused on its capacity to generate peroxymonocarbonate species (HCO_4^-) which are more reactive nucleophile than H_2O_2 and responsible for epoxidizing alkenes via formation of butterfly transitional states ($H_2O_2 + HCO_3^- \rightarrow H_2O + HCO_4^-$).[320] However, only molecular oxygen was used as oxidant in the studied reaction and no hydrogen peroxide was added. Therefore, we strongly suspect an in-situ generation of hydrogen peroxide in presence of the photocatalyst under visible light irradiation. To verify this hypothesis, the catalytic oxidation of N, N-diethyl-1,4-phenylenediammonium sulfate (DPD) by horseradish peroxidase (POD) was chosen as a selective and efficient enzymatic method to detect H_2O_2 in aqueous solution.[321, 322] It consisted of adding DPD and POD to the reaction media. In case of presence of H_2O_2, DPD would oxidize to its corresponding cationic radical ($DPD^{\cdot+}$), forming a stable red-purple colored compound with absorption maxima at 510 nm and 551 nm, easily detectable by spectroscopy. As illustrated in **Figure 54c,d**, we can confirm the presence of H_2O_2 in the aqueous reaction media, with CTF-BT-Ph_2 generating the most amount of H_2O_2. Note that in water not subjected to light irradiation, there were no substantial formation of hydrogen peroxide. To further highlight the contribution of H_2O_2 in the epoxidation mechanism, catalase, an H_2O_2 scavenger, was added to the reaction medium. Clearly, a significant decrease in the selectivity of styrene oxide to 21% was observed **(**entry 13 in **Table 4)**, confirming thus the role of H_2O_2 in the reaction. Although the exact styrene photo-epoxidation mechanism is still a subject of debate, we believe that CTF-BT-Ph_2 exhibited high selectivity to styrene oxide due to its highest photogeneration of $^1O_2$, which promoted the oxidation of water, generating thus the highest amount of H_2O_2 under visible-light irradiation.[323, 324] Superoxide anion radicals would also participate in the process of formation of H_2O_2.[323] The latter would then be activated in presence of $NaHCO_3$, leading to (HCO_4^-), as oxidizing agent in the catalytic epoxidation process **(Figure 55)**.

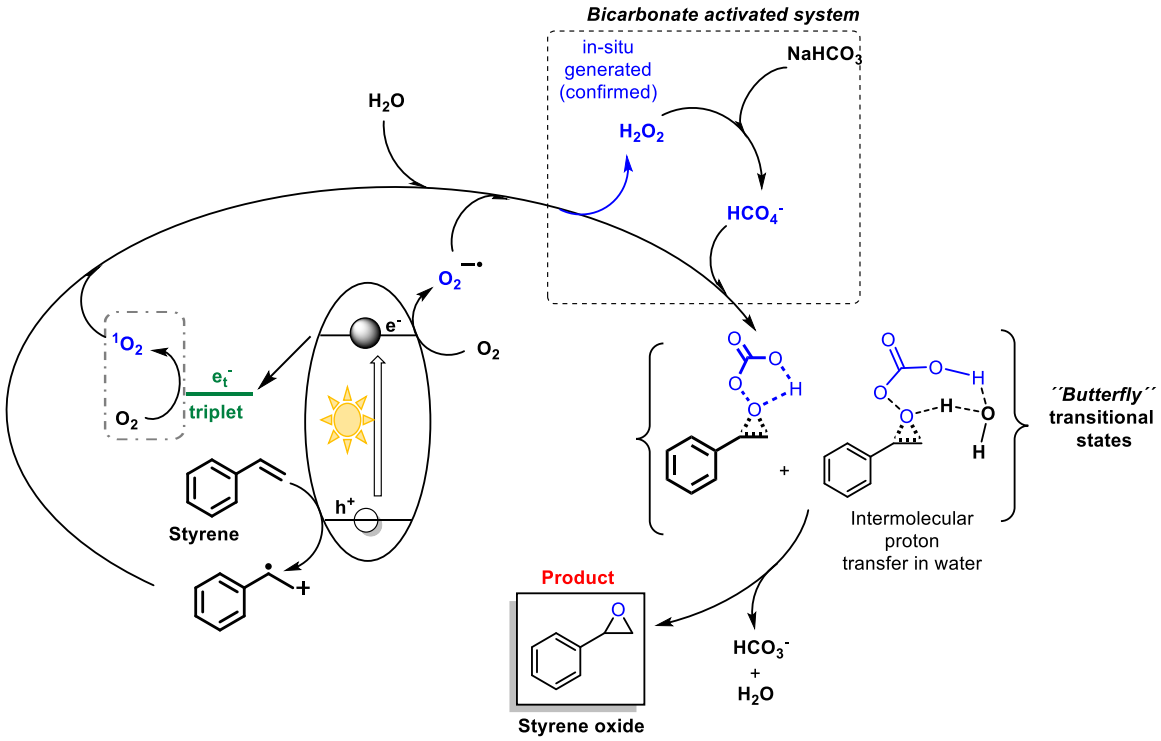

Figure 55. Mechanistic insight of the photocatalytic epoxidation of styrene in presence of CTF-BT-Ph_2 and under visible light irradiation.

To investigate the stability and reusability of CTF-BT-Ph_2, five repeating experiments were carried out under the same conditions. As shown in **Figure 56** and **Figure 57a**, the catalyst can be used up to 3 cycles at least without loss in its performance. A slight slow-down of the reaction was observed over the 4^{th} and 5^{th} cycles. However, the styrene oxide selectivity remained almost unaffected by the recycling **(Figure 57b)**. Furthermore, no apparent change of the UV-vis DR spectra of CTF-BT-Ph_2 after the photocatalytic reaction was observed, indicating its high stability and recyclability under visible light irradiation **(Figure 57d).**

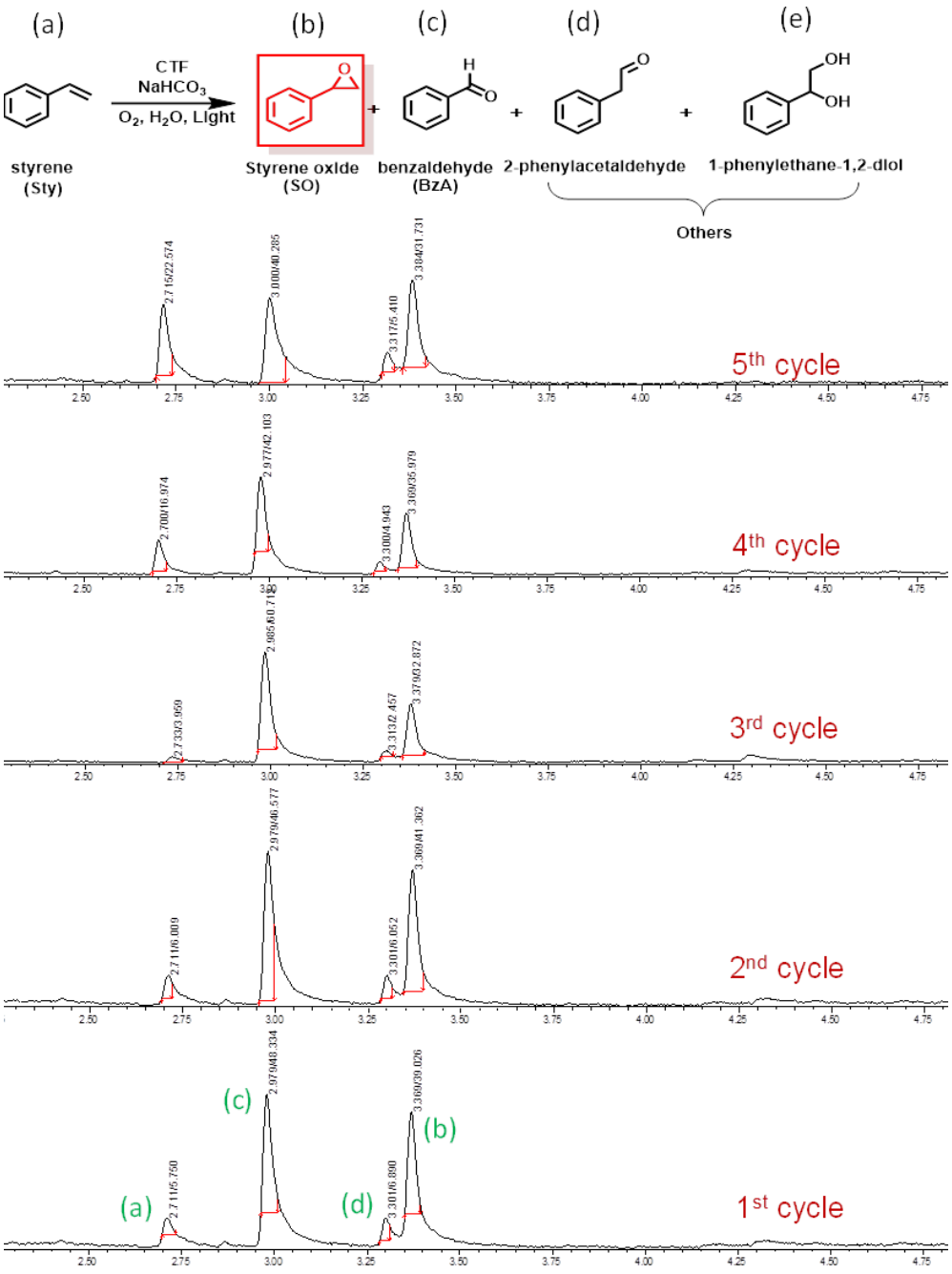

Figure 56. Annotated GCMS spectra of compounds produced after five cycles of photocatalytic styrene oxidation using CTF-BT-Ph_2 as photocatalyst. Irradiation time = 7h.

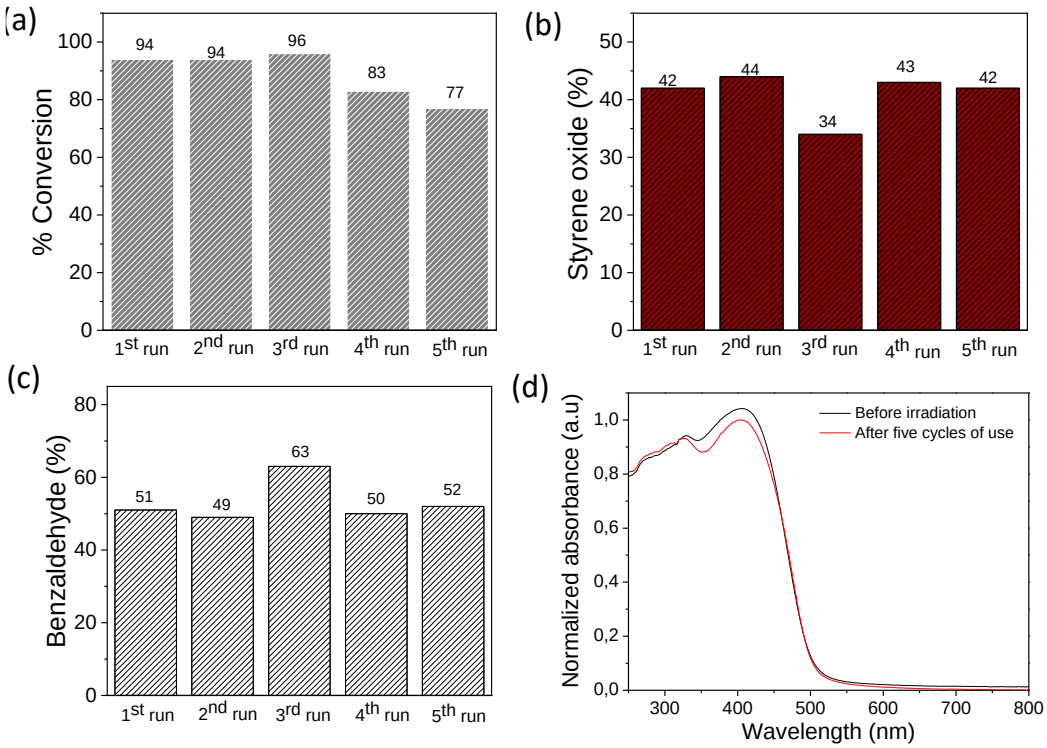

Figure 57. (a) Photocatalytic oxidation of styrene over CTF-BT-Ph_2 under five successive cycles (b) styrene oxide selectivity after five cycles of use, (c) benzaldehyde selectivity after five cycles and (d) UV-visible absorption spectra of CTF-BT-Ph_2 before (black) and after (red) 5 repeating cycles of the photocatalytic oxidation of styrene. Irradiation time = 7 h.

5.2.4. Conclusion and outlook

In summary, we designed covalent triazine based frameworks (CTFs), with different electron donor-acceptor combinations, as heterogeneous, visible-light active photocatalysts for the photocatalytic epoxidation reaction of styrene in water and in presence of $NaHCO_3$ and O_2. The electron acceptor (triazine)- donor (phenyl)–acceptor (benzothiazole)-based CTF (CTF-BT-Ph_2) was found to be the most efficient photocatalyst in epoxidizing styrene in high selectivity (> 50%). Such special structure with an extended π-conjugated framework allows an enhanced charge transfer efficiency, suppresses the rapid recombination of the hole−electron pairs, which in turn oxidizes water and reduces molecular oxygen to generate reactive oxygen species (ROS) under visible-light irradiation. Particularly, CTF-BT-Ph_2 showed high and efficient singlet oxygen generation among the polymer series, which led, in presence of water, to an enhanced *in-situ* generation of hydrogen peroxide. A mechanism was proposed, suggesting that, in presence of bicarbonate $NaHCO_3$, the in-situ hydrogen peroxide can be activated leading to the formation of peroxymonocarbonate (HCO_4^-) as powerful epoxidizing agent. Furthermore, CTF-BT-Ph_2 can be recycled and reused without significant loss in conversion and selectivity. Overall, we believe that this study provides a versatile photocatalyst, which can be applied in various oxidative transformation, with *in-situ* generation of hydrogen peroxide under visible light irradiation.

5.3. Designing a covalent triazine framework for photocatalytic partial oxidation of 5-hydroxymethylfurfural (HMF) to 2,5-diformylfuran (DFF) in water

This subchapter is based on the published article "Photocatalytic partial oxidation of 5-hydroxymethylfurfural (HMF) to 2,5-diformylfuran (DFF) over a covalent triazine framework in water".[2] Cyrine Ayed designed and performed the experiments, analyzed the data and drafted the manuscript. Dr. Wei Huang contributed in the sample preparation and conducted a preliminary experiment. Dr. Gönül Kizilsavas performed the EPR measurements. Cyrine Ayed, Prof. Dr. Kai Zhang and Prof. Dr. Katharina Landfester contributed to the final version of the manuscript. Prof. Dr. Kai Zhang and Prof. Dr. Katharina Landfester supervised the project.

Herein, a strategy design of an ordered mesoporous covalent triazine framework (CTF) as a highly stable and porous organic photoactive polymer for the photocatalytic partial oxidation of HMF to DFF in water is presented. By incorporating thiophene groups into the polymer backbone, the material exhibited a broad visible light absorbance and high oxidation potential. The accessible mesoporous structure and strong oxidation potential contributed to its excellent catalytic activity for the photocatalytic partial oxidation of 5-hydroxymethylfurfural (HMF) to 2,5-diformylfuran (DFF) in water.

5.3.1. Motivation

Biomass is a highly abundant and renewable organic carbon resource in nature. It can be converted as chemical feedstock into high value compounds, reducing thus the heavy dependence on unsustainable petroleum-based resources.[325, 326] As example, 5-hydroxymethylfurfural (HMF), which is usually obtained by dehydration product of C6-based carbohydrates (such as glucose and fructose), can be partially oxidized to 2,5-diformylfuran (DFF).[327-329] As a valuable precursor, DFF can be further used for a vast number of important materials as various poly-Schiff bases, furan-based biopolymers, intermediates of pharmaceuticals, antifungal agents, organic conductors, cross-linking agents of poly (vinyl alcohol), and for different applications as in photography, analytical chemistry, metal electroplating, and electrooptical devices.[330-335] Currently, DFF is commonly produced under thermal catalytic conditions,[336-341] under those conditions, selectivity of DFF usually ranges from 60 to 99%. For example, Li *et al.* reported the use of trifunctional polyoxometalate-

[2]Ayed, C., Huang, W., Kizilsavas, G., Landfester,K., Zhang, K. A. I., *ChemPhotoChem, 2020. 4(8): p. 571-576.* Published by Wiley-VCH Verlag GmbH & Co. KGaA under the terms of Creative Commons CC BY license. Reproduced with permission.

decorated chitosan nanofibers catalysts (HPMoV/CS-f) as active catalyst and achieved 94.1% yield of DFF in DMSO and 56.2% yield in water (≥ 120°).[341] Efficient aerobic oxidation of HMF to DFF over a nitrogen-doped manganese oxide catalyst (N-MnO_2) has been also performed at room temperature and led to > 99.9% selectivity of DFF in toluene.[342] More recently, electrocatalytic oxidation of HMF has been proven to be an effective method to produce highly selective DFF mediated by TEMPO as catalyst and under basic conditions.[343]

Photocatalysis is nowadays is considered as a promising, economic and clean alternative strategy to thermal catalysis that holds a great potential for organic synthesis. Several attempts have been made to oxidize HMF photocatalytically and selectively to 2,5-diformylfuran (DFF). Mainly metal or metal oxide-based photocatalysts have previously been used including Nb_2O_5,[344] bimetallic Au-Ru nanoparticles supported on reduced graphene oxides,[345] ultrathin Ni/CdS nanosheets.[346] Only a few reports have utilized metal-modified g-C_3N_4[347] or pure g-C_3N_4 as metal-free photocatalysts.[344] There is therefore need for the development of further metal-free, pure organic, photocatalytic systems with high stability and reusability. Covalent triazine frameworks (CTFs), as a sub-class of CPPs, can indeed be a promising candidate for this reaction owning to their outstanding properties.[18, 47, 154, 348, 349] Particularly, the photocatalytic partial oxidation of HMF to DFF over CTF-containing photocatalysts has not been reported so far.

Much attention has also been devoted to find sustainable reaction media. In particular, interest has increasingly turned to water as the solvent for chemical reactions owning to its low-cost, availability and non-toxicity.[50, 228, 350, 351]

In this work, we report the use of a thiophene containing covalent triazine framework for visible-light promoted partial oxidation of HMF to DFF in aqueous medium. This reaction could be performed with moderate conversion toward the target product DFF. A detailed mechanistic study on the reaction including two pathways is discussed. Moreover, the reusability and stability of the catalyst are investigated.

5.3.2. Synthesis and characterization of a CTF-based photocatalyst

A new batch of thiophene-containing covalent triazine framework (CTF-Th) was prepared via a solvent-free polymerization procedure under triflic acid vapors (TfOH), similar to our previous reports (**Figure 58a**).[352] To achieve high dispersibility in water during the photocatalytic process, CTF-Th was directly synthesized on mesoporous silica (SBA-15) to form CTF-Th@SBA-15. It is worth to note here that a nontoxic and environmentally benign synthetic route of the monomer 2,5-dicyanothiophene (DCT) was further developed via

cyanation of 2,5-dibromothiophene.[353] Cheap and stable CuI/imidazole system together with potassium hexacyanoferrate ($K_4[Fe(CN)_6$) were employed as the least toxic cyanide source conceivable.[353]

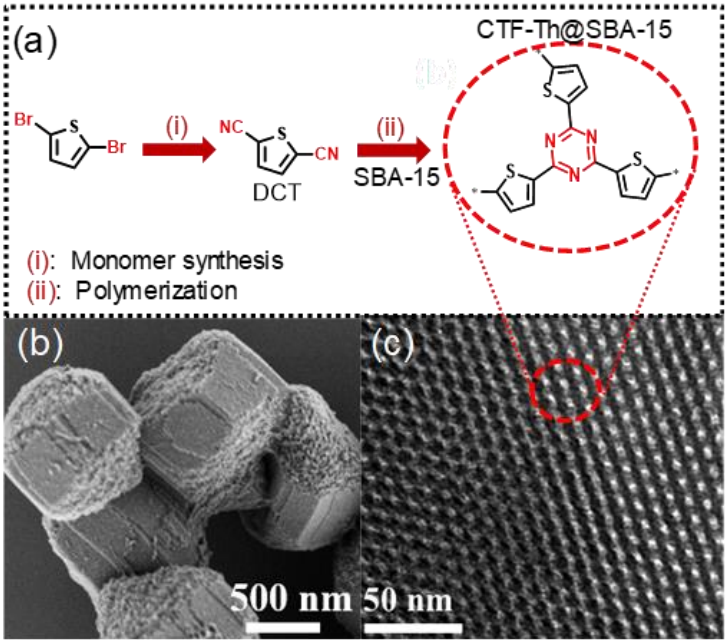

Figure 58. (a) Chemical structure and synthesis routes, (a) SEM and (b) TEM images of CTF-Th@SBA-15.

The structure of DCT was confirmed by proton and carbon nuclear magnetic resonance (^{1}H-NMR and ^{13}C- NMR) characterization (**Figure 59a,b**).

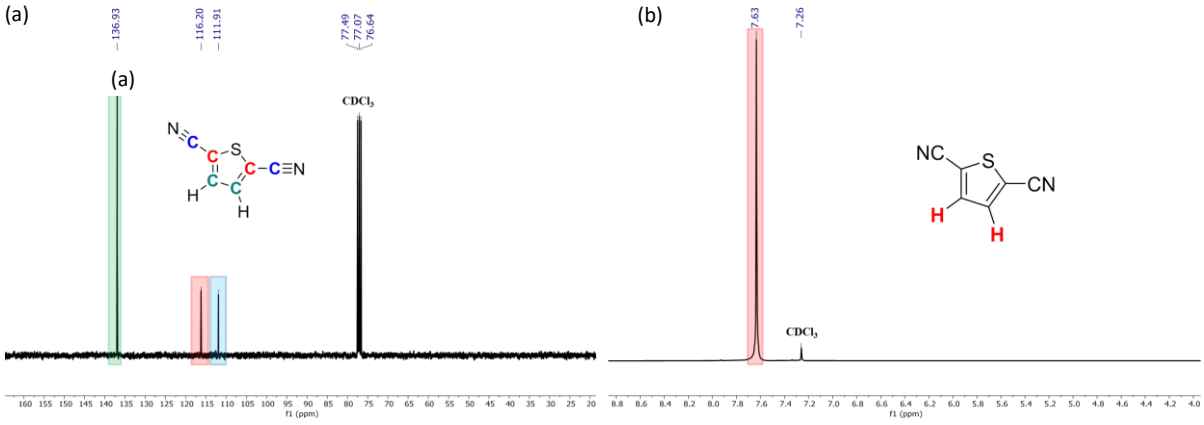

Figure 59. (a) ^{13}C NMR and (b) ^{1}H NMR spectra of 2,5-dicyanothiophene (DCT)in $CDCl_3$.

Scanning electron microscopy (SEM) and high-resolution transmission electron microscopy (HR-TEM) images showed that the synthesized CTF-Th@SBA-15 possesses highly ordered hexagonal mesoporous structure of ca. 600 nm of diameter with cylindrical pore

channels (**Figure 58b and Figure 58c, respectively**). Elemental mapping (C, S and Si) indicated that CTF-Th was uniformly formed throughout SBA-15 (**Figure 60**).

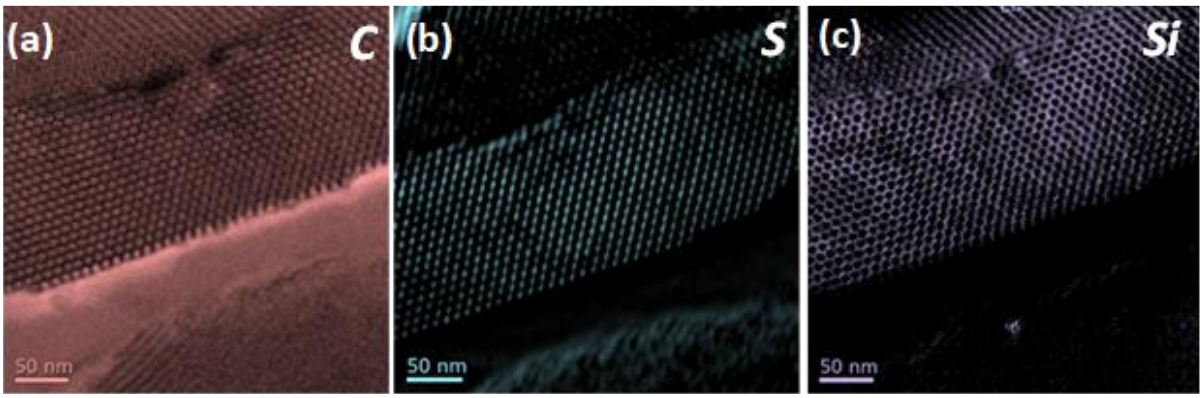

Figure 60. Element mapping images in (a) carbon, (b) sulfur, and (c) silicium.

The SBA-15 template endowed the CTF-Th with high Brunauer-Emmett-Teller (BET) surface area of 428 m^2/g (**Figure 61**).

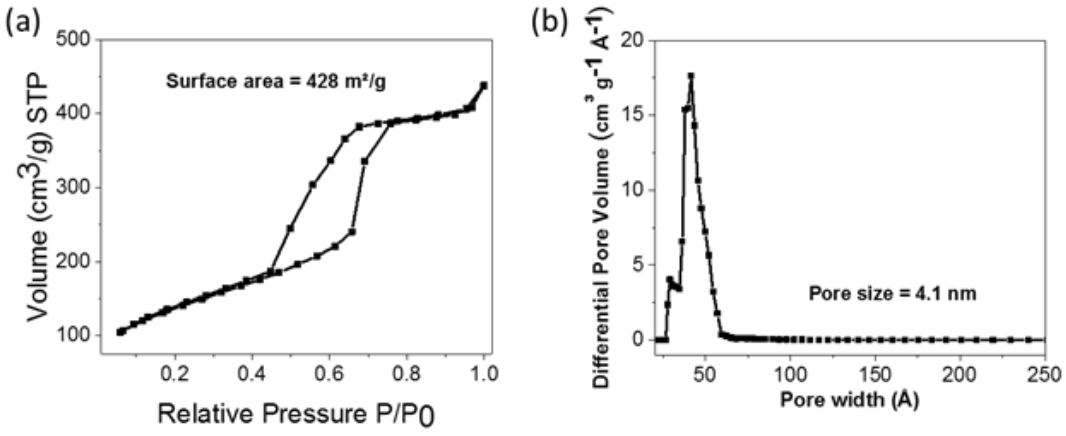

Figure 61. (a) Nitrogen sorption and desorption isotherm and (b) pore size distribution of CTF-Th@SBA-15. Isotherm of type IV typical for mesoporous materials according to IUPAC classification.

Additionally, the material showed a water contact angle of 27°, which confirms the added hydrophilicity (**Figure 62**), enabling catalytic reactions in aqueous environment.

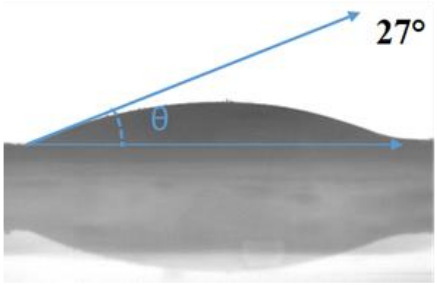

Figure 62. Angle contact measurement of a water droplet (volume of ca. 5 μl) on the surface of CTF-Th@SBA-15.

Solid-state ^{13}C cross-polarization magic-angle-spinning (CP-MAS) NMR spectroscopy verified the presence of sp^2 carbons at 168 ppm in the triazine and in the thiophene ring at 146 and 131 ppm (**Figure 63a**). Fourier transform infrared (FT-IR) spectroscopy (**Figure 63b**) showed two characteristic bands at 1428 and 1359 cm^{-1}, which can be assigned to the aromatic C–N stretching and breathing modes in the triazine unit. Characteristic absorption bands at 1018 and 1121 cm^{-1} are attributed to the asymmetric mode of Si–O–Si groups.[354]

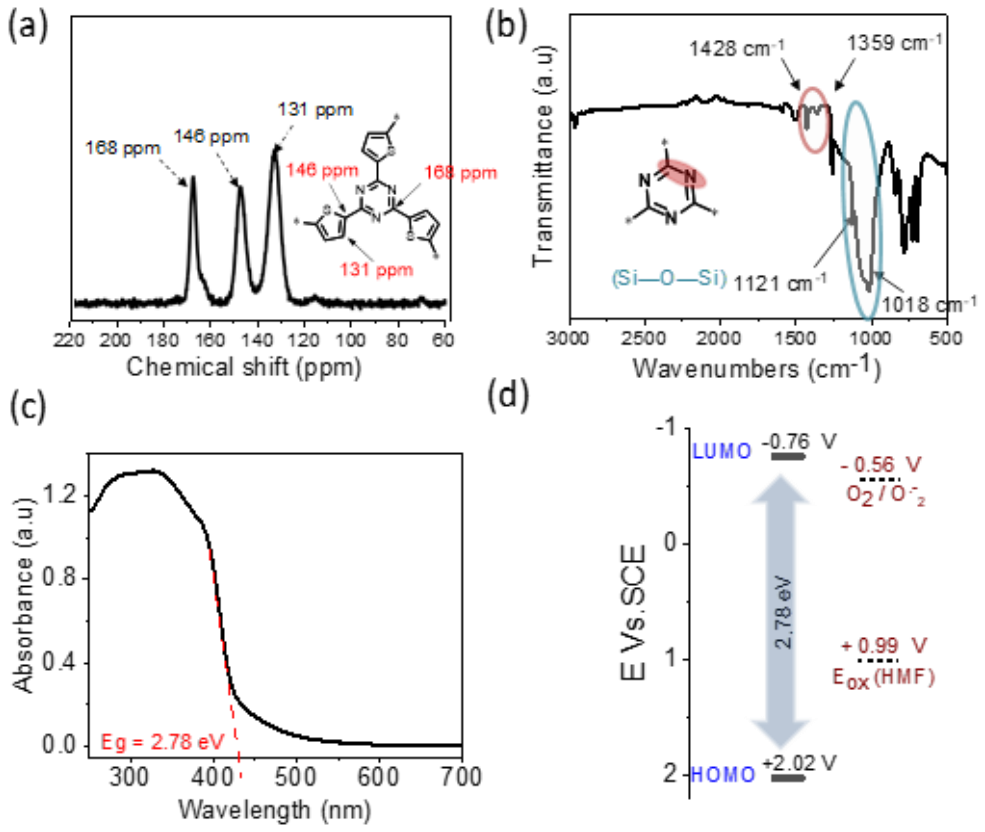

Figure 63. (a) Solid state ^{13}C CP/MAS NMR , (b) FTIR, (c) UV/vis DR spectra, and (d) highest occupied molecular orbital (HOMO) and lowest unoccupied molecular orbital (LUMO) band positions of CTF-Th@SBA-15.

Figure 63c illustrates the UV/vis diffuse reflectance (DR) spectrum of the CTF-Th@SBA-15. A light absorption covering the visible range was observed, with absorption edge extending to about 440 nm. Optical band gap energy was determined to be 2.78 eV by extrapolation of the linear section of the absorption spectrum onto the X-axis. The cyclic voltammetry (CV) measurements were conducted to reveal the energy band structure of the designed material. The electronic band positions of the CTF-Th@SBA-15 are displayed in **Figure 63d**. The corresponding lowest unoccupied molecular orbital (LUMO) was estimated to be – 0.76 V vs. SCE, with the highest occupied molecular orbital (HOMO) at +2.02 V vs SCE (**Figure 64a**).

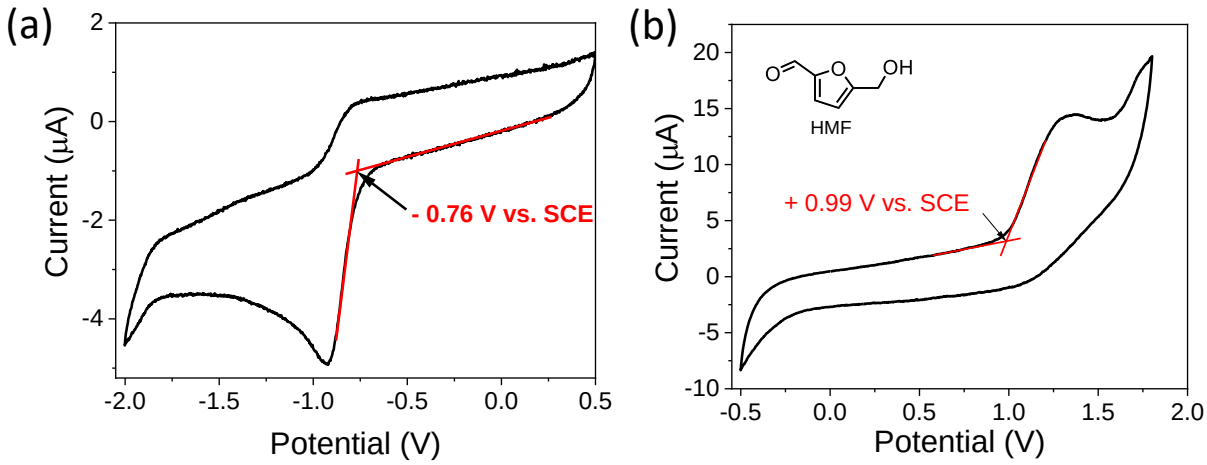

Figure 64. (a) Reduction potential of CTF-Th@SBA-15 measured by cyclic voltammetry and (b) oxidation potential of 5-hydroxymethylfurfural (HMF) measured by cyclic voltammetry. (Preparation: 0.05 mmol of HMF in 5 mL of Bu_4NPF_6 electrolyte solution)

5.3.3. Visible light promoted photocatalytic partial oxidation of 5-hydroxymethylfurfural (HMF) to 2,5-diformylfuran (DFF) in water

The photocatalytic performance of CTF-Th@SBA-15 was tested for HMF partial oxidation (0.1 mmol) in water, with O_2 as oxidant, using a blue LED lamp (460 nm, 65 mW cm^{-2}) as light source. It appeared that CTF-Th@SBA-15 is capable of oxidizing HMF molecules, as its oxidation potential is determined to be + 0.99 V. vs SCE (**Figure 64b**). Additionally, the reduction potential of CTF-Th is high enough to undergo molecular oxygen reduction via electron transfer and energy transfer to generate the reactive oxygen species (ROS) such as superoxide ($O_2^{\bullet -}$) and singlet oxygen ($^1O_2$) (**Figure 63d**). HMF partial oxidation to DFF was undertaken and monitored using ^{1}H-NMR (**Figure 66**). The conversion was determined according to the characteristic signals of HMF and DFF (**see** Experimental Section 6.3.7). As HMF could be further oxidized to a variety of products[345, 355] such as 5-(hydroxymethyl)furan-2-carboxylic acid (HMFCA), 5-formylfuran-2-carboxylic acid (FFCA), furan-2,5-dicarboxylic acid (FDCA) (**Scheme 3** in Experimental Section **6.3.7**), the ^{1}H NMR spectra of so-called standards were also collected for comparison purpose (**Figure 100** in the Experimental Section **6.3.7**). CTF-Th@SBA-15 showed relatively good catalytic activity for the partial oxidation of HMF with an average of 57% conversion of HMF after 30 h, and with more than 99% selectivity to DFF (**Figure 65Figure *66***).

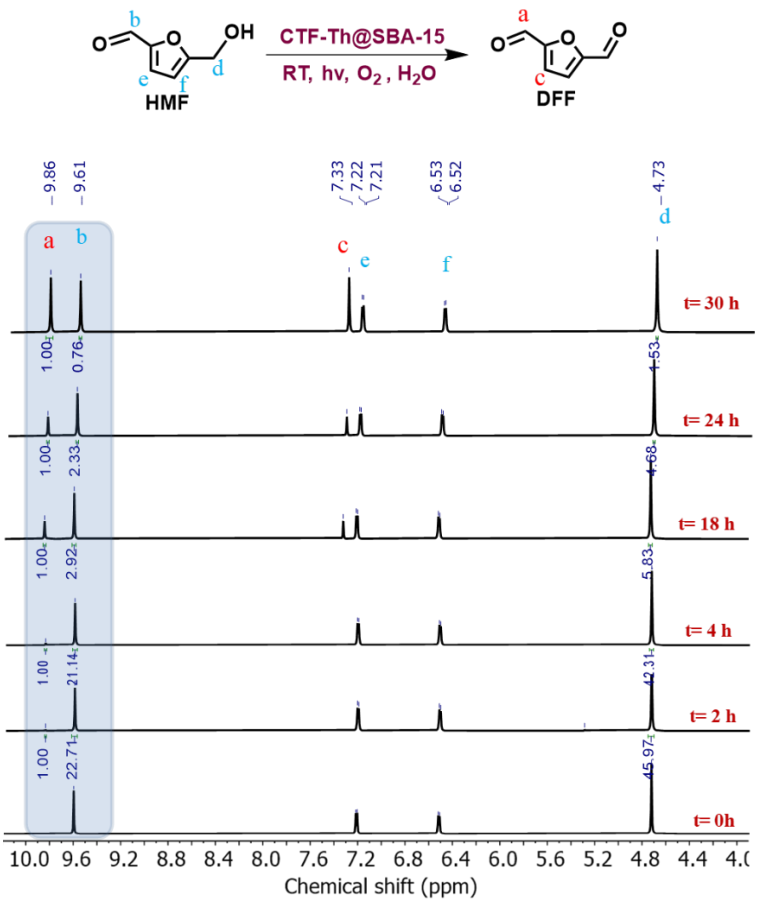

Figure 65. Kinetic study of the photocatalytic oxidation of HMF to DFF under standard conditions; trial 1. ^{1}H NMR spectra of the reaction medium at different time intervals in $CDCl_3$ (δ ($CHCl_3$)) = 7.26 ppm, not shown in the spectrum). Conditions: 10 mg of CTF-Th@SBA-15; 10 ml of H_2O; 0.1 mmol HMF; illumination for 30 h.

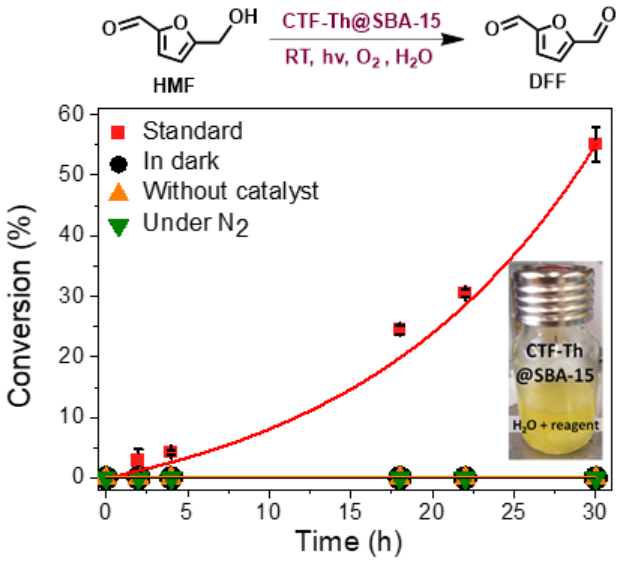

Figure 66. Screening and control experiments of the photocatalytic partial oxidation of HMF to DFF using CTF-Th@SBA-15. Standard reaction conditions: 0.1 mmol of HMF, 10 mg of CTF-Th@SBA-15 in 10 mL of water under the irradiation of a blue LED lamp (460 nm, 65 mW cm^{-2}), 1 atm. O_2 room temperature, 30 h. Conversion determined by ^{1}H-NMR spectroscopy.

This result is much higher than that obtained in many previous reports.[345, 347, 356, 357] Extension of reaction time of 48 h only led to a minimal increase of conversion. Control experiments were undertaken in the dark, in an oxygen-free atmosphere and in absence of photocatalytic material as shown also in **Figure 66-Figure *67*.** No conversion of HMF occurred under these latter conditions. This indicates that the photocatalyst, light source and O_2 play key roles in the oxidation of HMF to DFF. To gain a deeper insight into the reaction mechanism and reveal the specific role of the photogenerated electron–hole pair and active oxygen species during the photocatalytic process, we conducted a set of control experiments, using CTF-Th@SBA-15 as the photocatalyst and in presence of specific scavengers (**Figure 68** and **Figure 69a**). Lower conversion (35%) was obtained in presence of benzoquinone (BQ) as a superoxide scavenger. The addition of sodium azide (NaN_3) as singlet oxygen scavenger and potassium iodide (KI) as hole scavenger led to large decrease of the conversions to 9.2% and 4.2% respectively. No significate change of the conversion was observed in presence of isopropanol as a hydroxyl scavenger. So far, these results indicate that the activated oxygen species (superoxide and singlet oxygen), and the photogenerated hole participate during the photocatalytic oxidation of HMF to DFF.

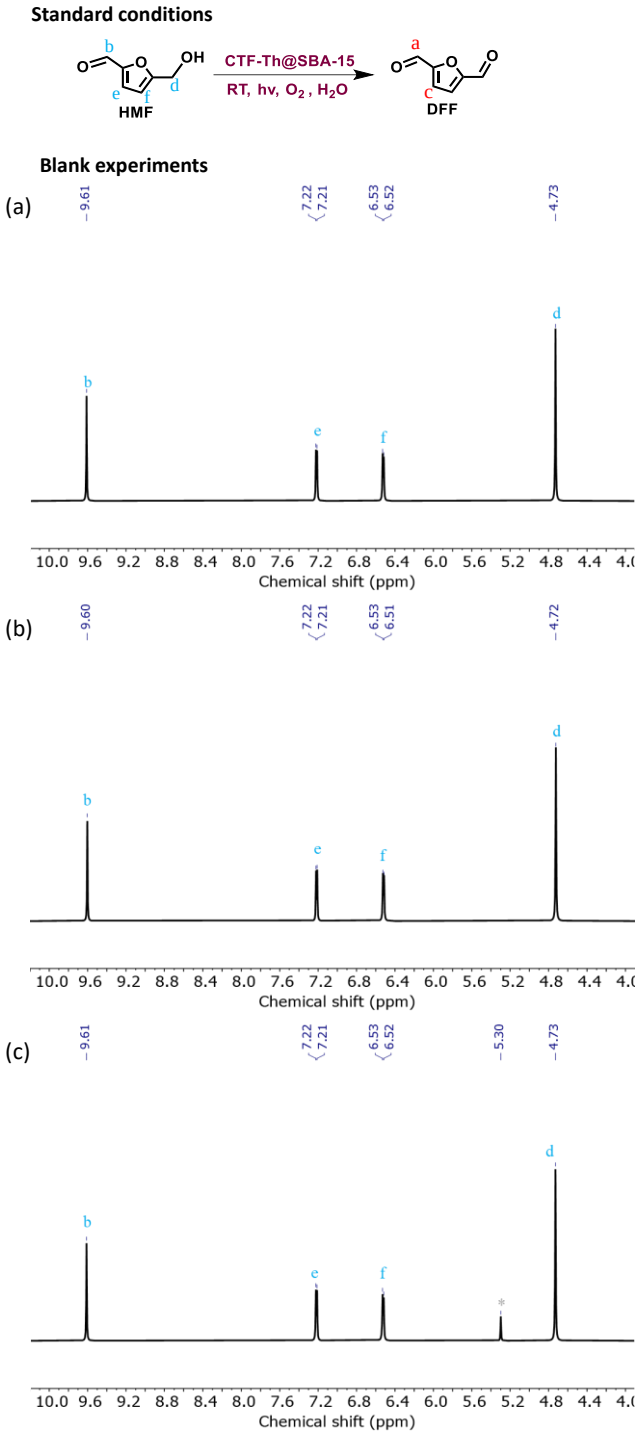

Figure 67. ^{1}H NMR spectrum of the reaction medium after extraction in $CDCl_3$ (δ ($CHCl_3$)) = 7.26 ppm, not shown in the spectrum) kept (a) under dark, (b) under nitrogen atmosphere and (c) in absence of photocatalyst for 30 h. Conditions: 10 mg of CTF-Th@SBA-15; 10 ml of H_2O; 0.1 mmol HMF.

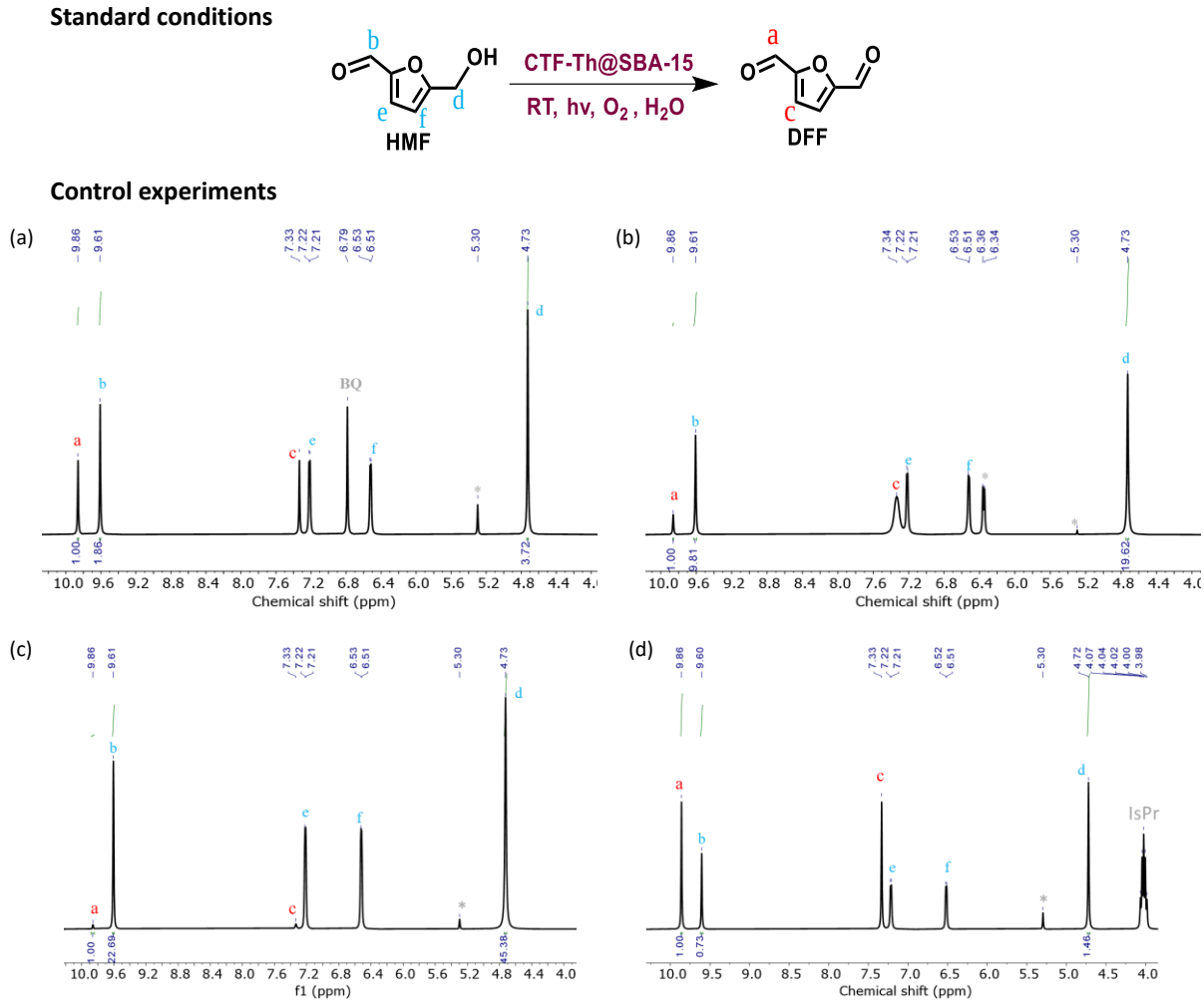

Figure 68. ^{1}H NMR spectrum of the reaction medium after extraction in $CDCl_3$ (δ = 7.26 ppm, not shown in the spectrum) and in presence of (a) **benzoquinone (BQ)** as superoxide scavenger, (b) **sodium azide** (NaN_3) as singlet oxygen scavenger, (c) potassium iodide KI as hole scavenger and (d) **isopropanol (IsPr)** as hydroxyl radical scavenger.
Conditions: 10 mg of CTF-Th@SBA-15; 10 ml of H_2O; 0.1 mmol HMF; 0.1 mmol of specific scavenger; illumination for 30 h; (*: unidentified side product)

To further confirm the possible generation of the ROS during the photocatalytic reaction, we conducted electron spin resonance (EPR) experiments using tetramethylpiperidine (TEMP) and 5,5-dimethyl-1-pyrrolineN-oxide (DMPO) as singlet oxygen and superoxide trapping agents, respectively. Indeed, the oxidation of TEMP (2,2,6,6-tetramethylpiperidine) by singlet oxygen yields the TEMPO (2,2,6,6-tetramethyl-1-piperidinyloxyl) free radical with distinctive line pattern easily detected by EPR. **Figure 69b** confirms the generation of singlet oxygen by CTF-Th@SBA-15 and under light irradiation. It is noteworthy to mention that a small TEMPO signal was also observed under dark condition. This TEMPO signal is not associated with singlet oxygen production and may come from the electron transfer oxidation of TEMP to TEMPO in the presence of molecular oxygen [358, 359] (see explanation in Experimental Section **6.3.5**).

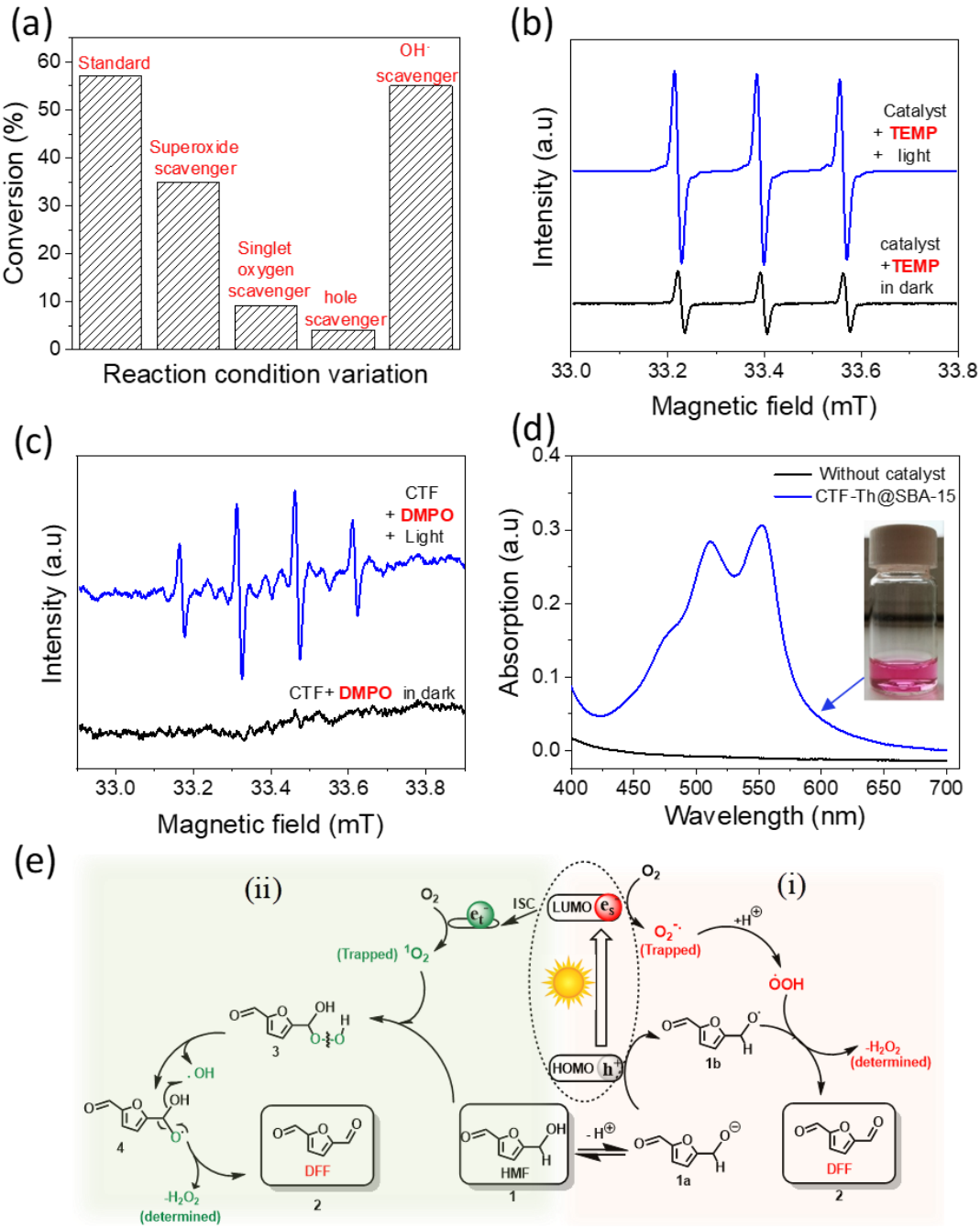

Figure 69. (a) Evaluation of the addition of scavengers on partial oxidation of HMF to DFF. Conditions: 10 mg of CTF-Th@SBA-15, 0.1 mmol of HMF, 0.1 mmol of additive (scavengers) in 10 mL of water, under the irradiation of a blue LED lamp (460 nm, 65 mW cm^{-2}), 1 atm O_2 room temperature, 30 h. Benzoquinone (BQ) used as a superoxide scavenger, sodium azide (NaN_3) as a singlet oxygen scavenger, potassium iodide (KI) as a hole scavenger, and isopropanol as a hydroxyl radical scavenger. (b) TEMPO/EPR signals obtained for H_2O solution of TEMP (0.1 M, 3 ml) in the presence of 3 mg of CTF-Th@SBA-15 under dark (black line) and after 2 h of blue light irradiation (blue line), (c) DMPO/EPR signals obtained for H_2O solution of DMPO (0.1 M, 3 ml) in the presence of 3 mg of CTF-Th@SBA-15 under dark (black line) and after 2h of blue light irradiation (blue line). (d) UV-Vis absorption spectra of the reaction system without and with the presence of CTF-Th@SBA-15 after adding DPD and POD for H_2O_2 determination and (e) Proposed reaction mechanism for the photocatalytic partial oxidation of HMF to DFF using CTF-Th@SBA-15 via two possible separate routes using either the singlet oxygen or the superoxide. ISC: Inter system crossing.

Regarding superoxide detection and in presence of DMPO, the latter would reacts and give rise to a DMPO-OOH spin adduct with typical 12-line EPR pattern.[360] Due to its short lifetime and thus its instability, the spin adduct DMPO-OOH tends to decompose in DMPO-OH, making it difficult to detect.[361, 362] **Figure 69c** shows the typical EPR pattern of DMPO-OH, which confirms in part the generation of superoxide.

Based on the observations described above, we suggest two possible reaction pathways involving independently generated active oxygen species, i.e. superoxide and singlet oxygen. As displayed in **Figure 69e**, (i) under visible light irradiation, charge separation occurs within the CTF-Th@SBA-15 photocatalyst. The photogenerated electron undergoes molecular oxygen reduction and forms its activated form ($O_2^{\bullet-}$). The latter extracts one proton of HMF (1) and leads to the formation of the corresponding anionic alkoxide (1a) and the highly reactive $^{\bullet}$OOH species.[344] Note that the deprotonation of HMF is more promoted due to the basic character of CTF-Th@SBA-15 (nitrogen-rich triazine units).[363] Meanwhile, the formed alkoxide anion (1a) can react with the photogenerated hole by electron transfer and form the corresponding alkoxide radical (1b). Recombining this radical with $^{\bullet}$OOH species conducts to the final product DFF (2) with formal liberation of H_2O_2.[344, 363-365]

A singlet oxygen-driven oxidation of HMF to the target DFF can also be hypothesized based on this reported study:[366] (ii) singlet oxygen, which can be photogenerated through intersystem crossing (ISC), is inserted into the C–H bond of the alcohol function of HMF (1) and forms 5-(hydroperoxy(hydroxy)methyl)furan-2-carbaldehyde (3). This intermediate can undertake independent photolysis[367] resulting in the formation of (4) that decomposes further to the final product DFF (2), with H_2O_2 as a by-product. The formation of H_2O_2 could be approved by using the catalytic oxidation of N,N-diethyl-1,4-phenylenediammonium sulfate (DPD) by horseradish peroxidase (POD).[321] This enzymatic method is highly selective, sensitive and fast. It consists of the oxidation by H_2O_2 of POD to a higher valent state, that in turn oxidizes two molecules of DPD to the corresponding cationic radical ($DPD^{\bullet+}$). The latter forms a stable red-purple colored chromogenic compound with two absorption maxima at 510 nm and 551 nm (**Figure 69d**) We have confirmed the existence of H_2O_2 and its amount is determined to be 60.4 µmol in the original reaction mixture (**Figure 70**).

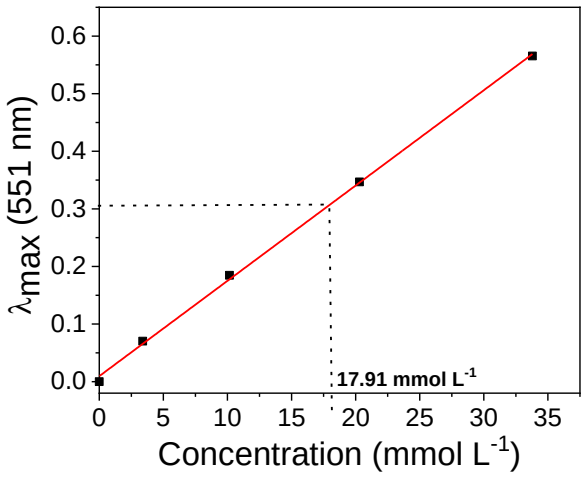

Figure 70. Standard curve of H_2O_2 concentration based on its absorption maximum at 551 nm. [H_2O_2] = 17.91 mM in the treated solution (V_f = 3.37 ml).

To investigate the stability and reusability of CTF-Th@SBA-15, we carried out four repeating experiments of the photocatalytic oxidation of HMF under the same conditions. As shown in **Figure 71** and **Figure 72a**, the catalyst can be used up to 4 cycles at least without losing significantly its performance. No apparent change of the UV-vis DR of the photocatalyst could be observed after four runs indicating its high stability and recyclability under visible light irradiation (**Figure 72b**).

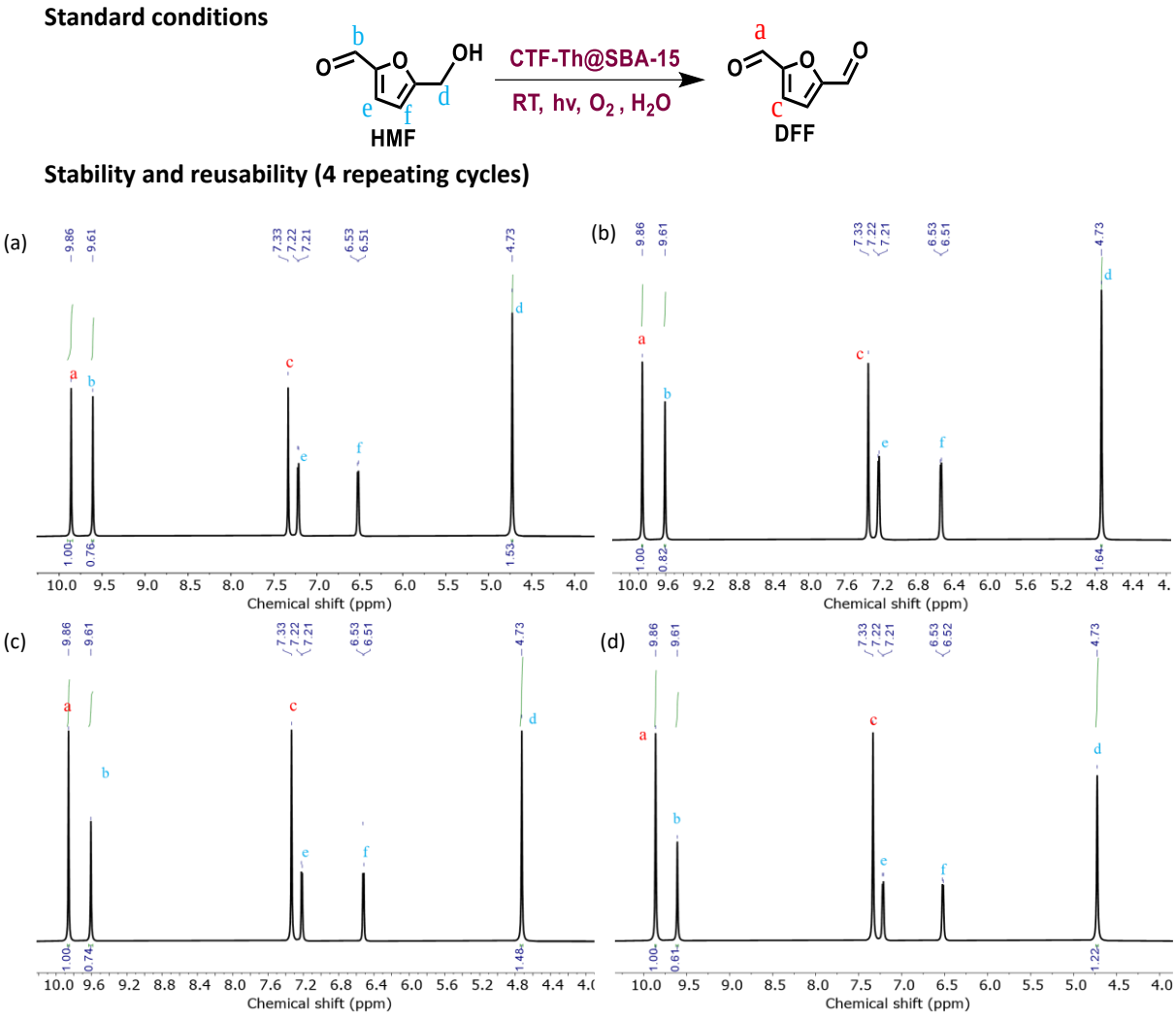

Figure 71. ^{1}H NMR spectra of the reaction medium after extraction in $CDCl_3$ after the (a) 1st , (b) 2nd, (c) 3rd, and (d) 4th cycles (δ = 7.26 ppm, not shown in the spectrum).
Conditions: 10 mg of CTF-Th@SBA-15; 10 ml of H_2O; 0.1 mmol HMF; illumination for 30 h.

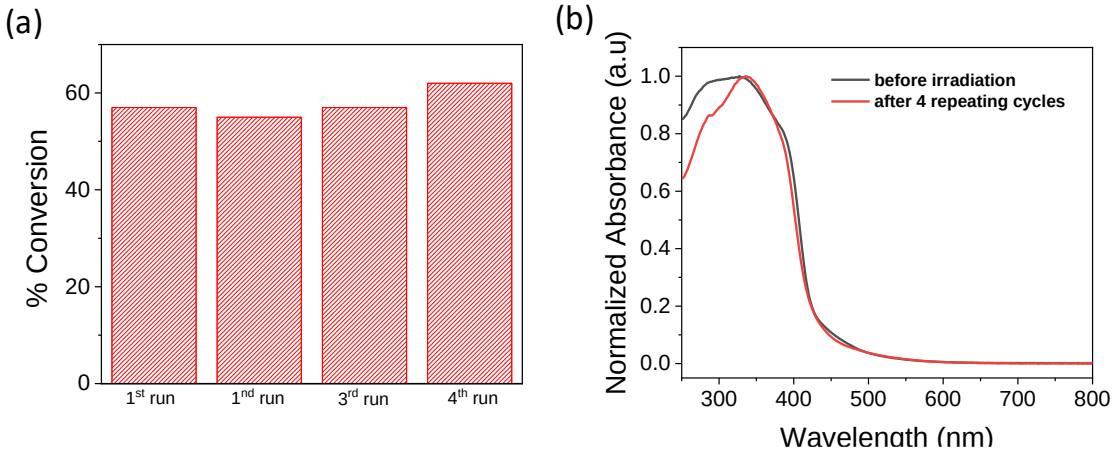

Figure 72. (a) Photocatalytic partial oxidation of HMF over CTF-Th@SBA-15 under four successive cycles and (b) DR spectra of CTF-Th@SBA-15 before (black) and after (red) 4 repeating cycles of the photocatalytic oxidation of HMF.

5.3.3. Conclusion and outlook

In summary, we have employed a thiophene-containing covalent triazine framework on mesoporous silica (SBA-15) as heterogeneous photocatalyst for partial oxidation of 5-hydroxymethylfurfural (HMF) to 2,5-diformylfuran (DFF) in water, under pure oxygen as green oxidant and visible light irradiation. The low solubility of DFF in water at room temperature could provide an easy separation method. Our catalyst could efficiently convert HMF to DFF with 100% selectivity, higher than previously reported. Moreover, it showed good stability upon recyclability and maintained relatively high photocatalytic activity. Two mechanisms were suggested involving either singlet oxygen or superoxide. This study demonstrates the potential of efficient metal-free photoactive CTFs material for various applications under non-toxic and environmentally friendly environment.

5.4. Designing covalent triazine framework for the degradation of organic dyes in aqueous and solid media

This subchapter is based on the published article "Covalent triazine framework@SBA-15 with efficient photocatalytic activity in aqueous and solid media".[3] Cyrine Ayed designed and performed the experiments, analysed the data and drafted the manuscript. Dr. Wei Huang contributed in the sample preparation and conducted a preliminary experiment. Cyrine Ayed, and Prof. Dr. Kai Zhang contributed to the final version of the manuscript. Prof. Dr. Kai Zhang supervised the project.

As shown in the previous chapters, we have extended the range of the application media of CTFs and have designed hybrid material of a thiophene containing CTF and mesoporous silica (SBA-15) with high dispersibility into water. The material has demonstrated efficient conversion of 5-hydroxymethylfurfural to high-value chemicals (DFF) in aqueous medium. Herein, we aim to use similar photocatalytic material (newly synthesized) for photocatalytic degradation of organic dyes. Such application can be later of great interest for the textile industry, offering a very effective and green way for the treatment of real textile wastewater and reducing its environmental impact. The as-synthesized hybrid material demonstrated excellent adsorption of organic molecules in water, due to the high surface area and the added hydrophilic properties by silica. This leads not only to high photocatalytic performance of the hybrid material for the degradation of organic dyes in water, but also for efficient photocatalysis in solvent-free and solid state. Furthermore, the reusability, stability and easy recovery of the hybrid material offers promising metal-free heterogeneous photocatalyst for broader applications in different reaction media.

5.4.1. Motivation

Covalent triazine frameworks (CTFs) represent an interesting class of porous organic polymers (POP), which exhibit considerable unique properties. Nevertheless, the impact of the adsorption properties of organic molecules on CTFs during the application process is not well understood yet. Since the adsorptive power is of key-importance, particularly in the field of heterogeneous catalysis, where the catalytic reactions occurs at the surface rather than in the solution. Therefore, the surface properties of CTFs become critical for their catalytic efficiencies. In this regard, few studies were interested in investigating closely the adsorptive

[3]Ayed, C., Huang, W., Zhang, K. A. I., *Front Chem Sci Eng, 2020. **14**(3): p. 397-404.* Published by Springer Nature under the terms of the Creative Commons CC BY license. Reproduced with permission.

behavior of CTFs to organic compounds or pollutants. It has been found that these properties [46, 234, 368] depends partly on the surface chemistry of adsorbents.[369, 370] This statement was further confirmed by Kuhn *et al.*,.[371] The authors have found out that good adsorption properties should be ideally achieved with a structure that have extremely high surface area, well defined porosity and good accessibility throughout the pore channel of the functional materials. Thus, the development of porous systems with well-defined morphology is highly beneficial for promoting the adsorption and diffusion of the target molecules and therefore enhancing the performance of the materials, here in particular of this study, the catalysis.

Herein, we report the design of a hybrid photocatalytic system consisting of a thiophene-containing CTF (CTF-Th) in a mesoporous silica (SBA-15) for visible-light promoted efficient degradation of organic contaminants in aqueous media. The presence of mesoporous silica in the hybrid material (CTF-Th@SBA-15) with an ordered mesoporous structure in SBA-15 made the designed system a highly suitable host matrix with two main benefits: (1) the high surface area and ordered pore structure can enhance the diffusion and adsorption of guest molecules, which can boost the photocatalytic efficiency of the CTF. (2) the added hydrophilicity of silica to the photocatalytic CTF can largely extend its application range from organic to aqueous media. The hybrid material consisting of CTF-Th and SBA-15 demonstrated excellent adsorption of organic molecules in water and excellent photodegradation performance of the dyes. Furthermore, after the quick adsorption of the organic dyes in water, the hybrid material also demonstrated its high photocatalytic activity in dry and solid state. Thus, such system opens up new opportunities for efficient adsorption of organic contaminants from water in a wider range of environmentally relevant applications.

5.4.2. Synthesis and characterization of a CTF-based photocatalyst

A new batch of CTF-Th@SBA-15 was synthesized onto mesoporous silica SBA-15 via cyclization polymerization of DCT under TfOH vapor, obtaining CTF-Th@SBA-15 as a type of mesoporous nanoreactor. The synthetic pathway with detailed characterization methods of the materials are described in Experimental Section **6.4.** The hybrid photocatalyst was obtained as an insoluble yellow powder with the structure shown below **(Figure 73a)**. HR-TEM revealed two-dimensional (2D) hexagonal channels of the CTF-Th@SBA-15, as displayed in **Figure 73b**. SEM confirmed the hexagonal cylinder morphology with a diameter of ca. 500 nm **(Figure 73c)**.

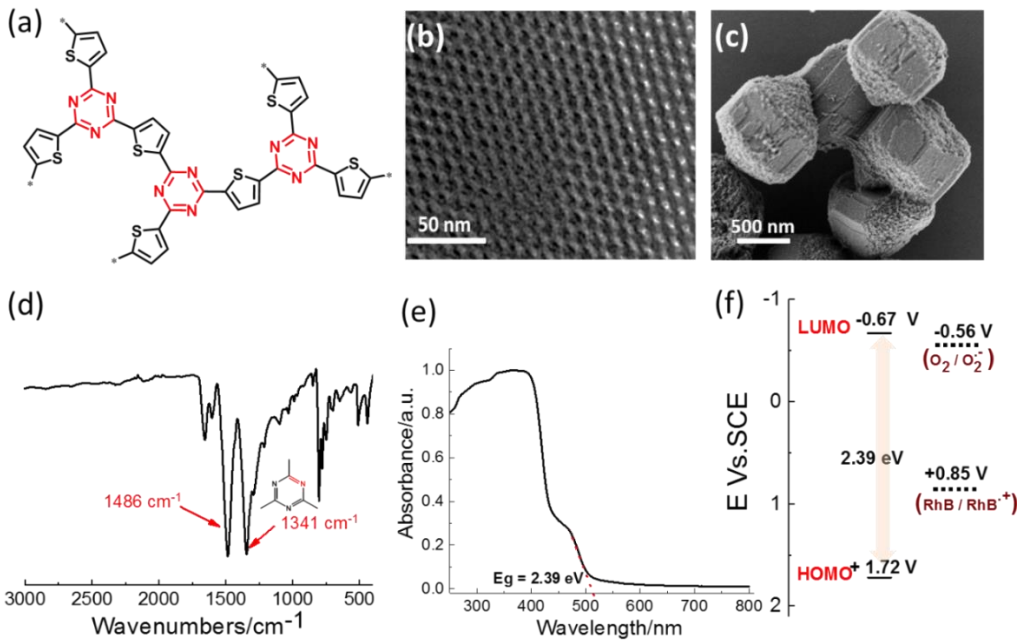

Figure 73. (a) Structure; (b) HR-TEM; (c) SEM; (d) FTIR; (e) UV vis DR spectra and (f) energy band positions of CTF-Th@SBA15.

The nitrogen gas sorption isotherms and pore size distributions are displayed in **Figure 74**. A typical hysteresis at a relative pressure of 0.4 <P/P_0< 0.8 for mesopores is shown for both pristine of SBA-15 as well as the CTF-Th@SBA-15.

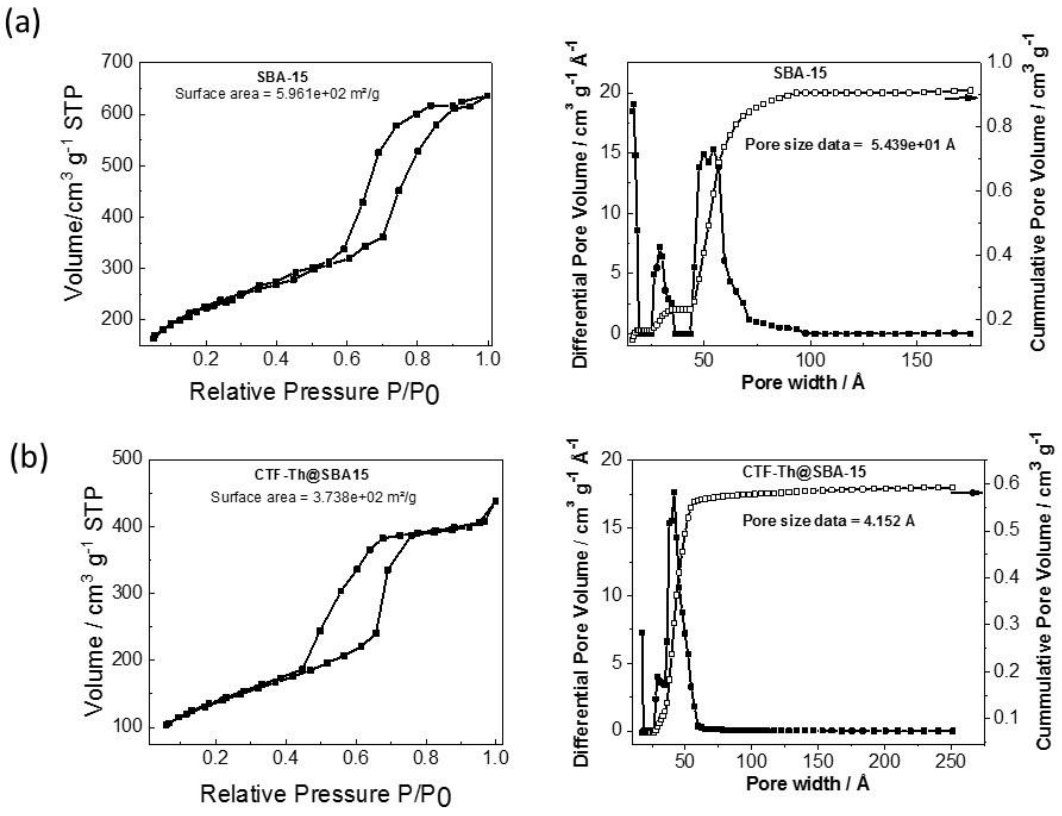

Figure 74. Nitrogen sorption and desorption isotherms and Pore size distributions of (a) pure SBA-15 and (b) CTF-Th@SBA-15.

The corresponding data are summarized in **Table 5.**

Table 5. Physical Properties of the CTF and reference materials.

Sample	S_{BET} / m^2 g^{-1}	Pore volume / cm^3 g^{-1}	Average pore size / nm
SBA-15	596	0.91	5.4
CTF-Th	57	0.28	19.3
CTF-Th@SBA-15	374	0.59	4.1

The Brunauer−Emmett−Teller (BET) surface area of CTF-Th@SBA-15 was measured to be 374 m^2/g, with a pore volume of 0.59 cm^3/g, which is lower than the BET surface area of pristine SBA-15, which is 596 m^2/g with a pore volume of 0.9 cm^3/g. Note that CTF-Th@SBA-15 exhibited a narrower pore size distribution at ca. 4.1 nm comparing to that of the pristine SBA-15 of ca. 5.4 nm. This confirms the formation of layer of CTF-Th of an average thickness of ca.1.3 nm in the mesopores of SBA-15. In contrast, pure CTF-Th exhibited very low BET surface area due to the absence of the mesoporous channels, as shown in our previous study.[46].

FTIR spectra **(Figure 73d)** showed two intensive peaks at 1486 and 1341 cm^{-1}, which can be assigned to the aromatic C−N stretching and breathing modes in the triazine unit. **Figure 73e** illustrates the UV/vis diffuse reflectance (DR) spectra of the CTF-Th@SBA-15. The latter showed a broad absorption up to ca. 570 nm. An optical band gap of 2.39 eV could be calculated. These values showed that the as-prepared CTF-Th@SBA-15 is a semiconductor that can be excited by visible light. To gain further insight into the electronic properties, CV measurements were conducted to reveal the energy band structure of the designed material. The electronic band position of the CTF-Th@SBA-15 is displayed in **Figure 73f.** The corresponding Highest Occupied Molecular Orbital (HOMO) level at +1.72 V vs SCE could be estimated by subtracting the Lowest Unoccupied Molecular Orbital (LUMO) level from the optical bandgap **(Figure 75)**, indicating a possible high oxidative power of CTF-Th@SBA-15.

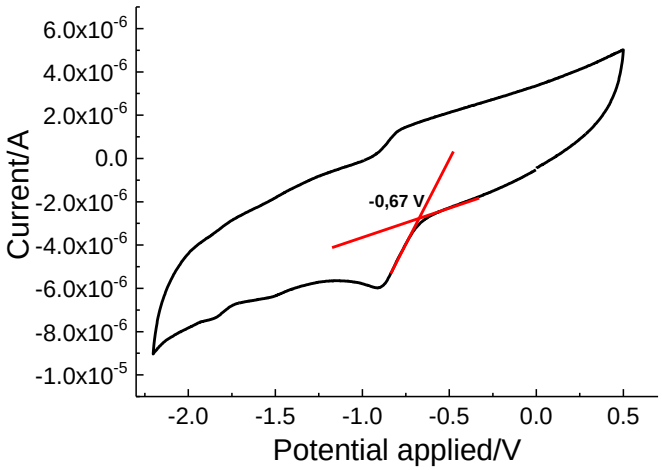

Figure 75. Reduction potential of CTF-Th@SBA-15 measured by cyclic voltammetry.

To address the wetting property of the hybrid CTF-Th@SBA-15 with respect to water, the contact angle of a water droplet on the corresponding surface has been measured. The wettability of the pure CTF-Th and pure SBA-15 have been also evaluated as references. The images are shown in **Figure 76**. It was found that water had a contact angle of 24° on the surface of the hybrid CTF-Th@SBA-15, while this contact angle was of 141° on the pure CTF-Th, of hydrophobic nature. Such a low value (< 90°) based on the reported literature [372] confirms the gained hydrophilicity of the CTF-Th@SBA-15 due to the presence of SBA-15 and explains the excellent dispersibility into water.

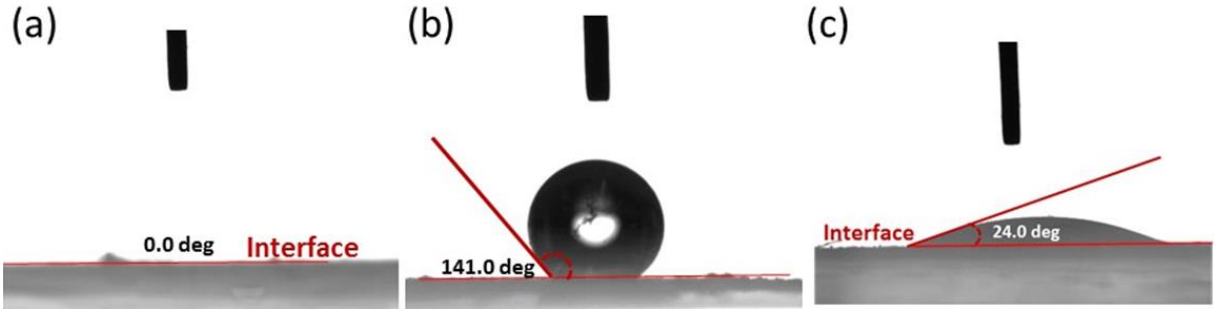

Figure 76. Angle contact measurements of a water droplet on the surface of (a) pure SBA-15, (b) pure CTF-Th and (c) CTF-Th@SBA-15.

5.4.3. Visible-light promoted photocatalytic degradation of organic dyes

The as-prepared CTF-Th@SBA-15 was used for the photodegradation of RhB in aqueous medium and under visible light illumination (λ = 460 nm, 0.16 W/cm^2). **Figure 77a** shows the degradation results of RhB using the CTF-Th@SBA-15 as photocatalyst. The concentration of RhB decreased sharply within 8 min of reaction and gradually reached zero after 16 min of reaction. This observation is with accordance to the photographs of RhB solutions before and after 16 min of light irradiation **(Figure 78)**. The dye solution, although in

a high concentration (50 mg L^{-1}), became completely colorless within 16 min, which means that the RhB molecules were totally degraded. Thus, CTF-Th@SBA-15 was found to be an excellent catalyst for photodegradation of RhB under visible light illumination. For quantitatively determining the photodegradation rate of RhB, the $\ln(C/C_0)$ vs. time plot **(Figure 77a inset)** was also obtained according to the UV-Vis absorption intensity at 570 nm. The degradation process conforms to a first order kinetic equation since the $\ln(C/C_0)$ vs. time plot was linear with a high photodegradation rate of RhB (0.3651 min^{-1}). In contrast, pure CTF-Th, which was used as reference, shows low photodegradation rate of 0.0850 min^{-1} **(Figure 79)**.

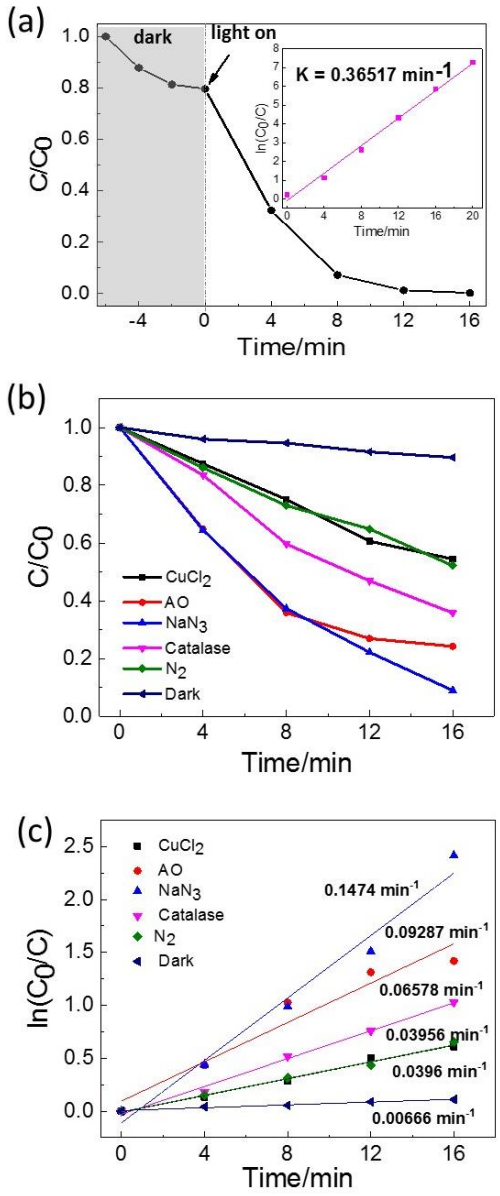

Figure 77. (a) Visible light-driven degradation of Rhodamine B in water by CTF-Th@SBA15. Conditions: CTF-Th @SBA15 (3 mg), Rh B aqueous solution (50 mg/L, 10 ml), Blue lamp (λ=460 nm); (b) Control experiments with different scavengers and (c) Photodegradation rates of the control experiments. C is the concentration of RhB after light irradiation for a certain period and C_0 is the concentration of RhB after reaching adsorption/desorption equilibrium in the dark.

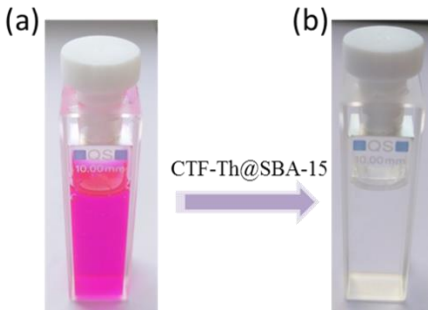

Figure 78. Photography of (a) initial RhB solution (50 mg/L) and (b) after adsorption by CTF-Th@SBA-15 for 20 min.

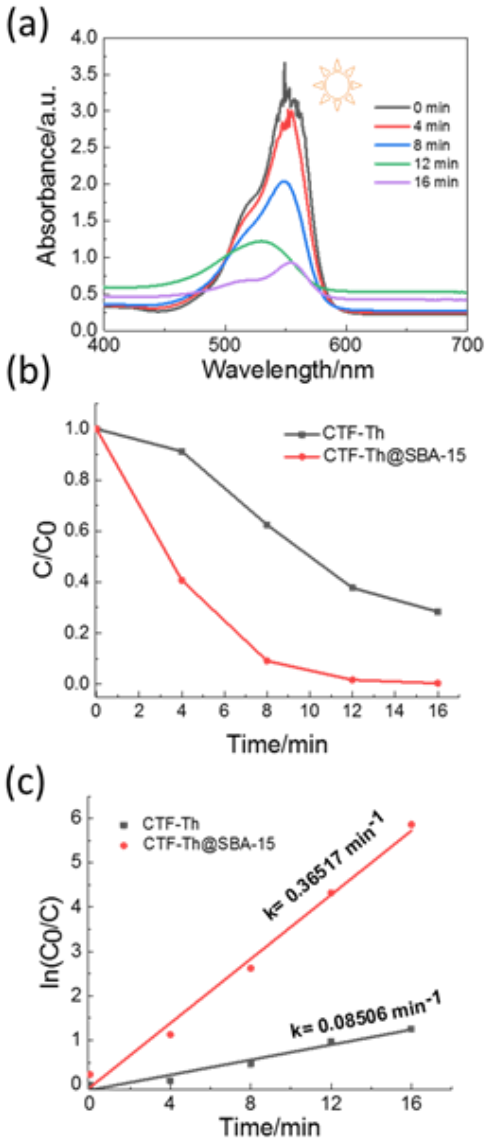

Figure 79. UV/vis DR spectral changes with reaction time of RhB solution (50 mg L^{-1}, 10 ml) in presence of 3 mg of pure CTF-Th, kept under 16 min of blue light irradiation (λ=460 nm), (b) visible light-driven degradation of RhB solution by pure CTF-Th and by CTF-Th@SBA-15 for comparison purpose, and (c) Photodegradation rates of RhB solution in presence of pure CTF-Th and hybrid CTF-Th@SBA-15. C is the concentration of RhB after light irradiation for a certain period and C_0 is the concentration of RhB after reaching adsorption/desorption equilibrium in the dark.

The enhanced photocatalytic efficiency could be explained by three key points: (i) high BET surface area (374 m^2 g^{-1}) of the hybrid system, which offers a large reactive interface during the catalytic process, (ii) very efficient diffusion of the dye molecules within the mesopores and (iii) excellent adsorption ability in water toward dyes molecules caused by SBA-15.[373]

To investigate the reaction mechanism and reveal the responsible species involved in the reaction process, we conducted a number of control experiments using CTF-Th@SBA-15 as photocatalyst. As shown in **Figure 77 b,c**, in the absence of light, almost no degradation of RhB occurred (rate = 0.0066 min^{-1}), whereas under oxygen-free atmosphere, the reaction can still occur but with a very low degradation rate (0.039 min^{-1}). It is important to mention, that in the photodegradation process of organic dyes in water, it is well known that the reactive species such as superoxide ($O_2^{\bullet-}$), singlet oxygen ($^1O_2$), and the photogenerated hole (h+) play important roles in the photocatalytic process.[21, 50, 374] To underline the contribution of these active species in the RhB degradation using CTF-Th@SBA-15, further control experiments were carried out using the following radical scavengers: catalase as H_2O_2 scavenger, sodium azide (NaN_3) as the $^1O_2$ scavenger, copper chloride ($CuCl_2$) as the $O_2^{\bullet-}$ scavenger, and ammonium oxalate (AO) as the h^+ scavenger. Visibly, the addition of copper chloride in the reaction led to an expressive decrease in the photodegradation process of RhB to 0.0395 min^{-1} compared to 0.3651 min^{-1} under normal conditions. This result confirmed the ability of CTF-Th@SBA-15 in forming radical oxygen species by reducing oxygen under visible light irradiation, which was already proven in our previous work.[46] These species are responsible for the degradation of RhB, with the main contribution of superoxide ($O_2^{\bullet-}$). Additionally, the photocatalytic reaction rates decreased significantly by the addition of catalase as H_2O_2 scavenger (0.0658 min^{-1}), Aluminum oxalate as the hole scavenger (0.0929 min^{-1}), sodium azide as singlet oxygen scavenger (0.1474 min^{-1}). Therefore, all elements such as the photogenerated hole, active oxygen species, in-situ generated H_2O_2 play a role in the direct photooxidation of RhB.[375] Based on the observations drawn from the experiments described above, we could suggest the following reaction mechanism as shown in **Figure 80**: under light irradiation, the charge separation, that occurs within the hybrid CTF photocatalyst, generates electron-hole pairs. The photogenerated hole oxidizes RhB molecules, possessing an oxidation potential of + 0.85 V vs SCE.[376] In the same time, the electron from the LUMO of the CTF-Th@SBA-15 assisted the reductive activation of molecular oxygen into superoxide ($O_2^{\bullet-}$), which further react with the oxidized RhB molecules causing the degradation of RhB.[377]

Note that singlet oxygen ($^1O_2$), originating either from energy transfer or from secondary reactions, also took part in the mechanism.[378, 379]

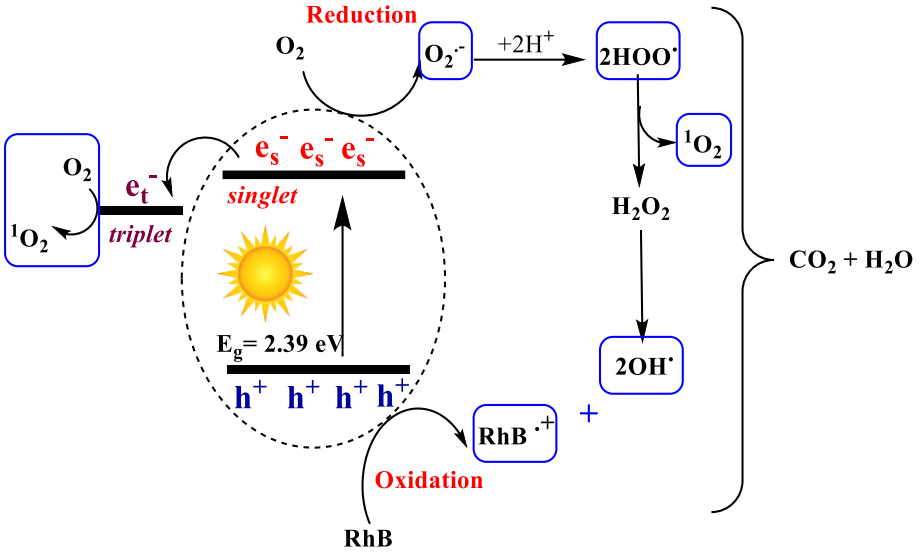

Figure 80. Suggested reaction mechanism of the photodegradation of Rhodamine B using CTF-Th@SBA-15 as photocatalyst.

As we have mentioned previously, the efficient photocatalytic activity of CTF-Th@SBA-15 could be partly attributed to the adsorptive power of SBA-15 present in the photocatalytic system. In order to prove it, we carried out the photodegradation of RhB in solid-state rather that in aqueous medium **(**see Experimental Section **6.4.4).** As shown in the photographs in **Figure 81a**, the RhB molecules adsorbed clearly on the surface of the CTF-Th@SBA-15, in which the color turned to dark pink. The dye-adsorbed photocatalyst was then subjected to blue light irradiation and the results are presented in **Figure 82a**. The UV-Vis peak at around 570 nm was very strong for the RhB solution without photodegradation. However, the peak was sharply attenuated after 16 min of reaction and disappeared after 28 min of illumination. Its concentration gradually reached zero with a rate of 0.1197 min^{-1} **(Figure 81 b,c)**. Chen et *al.*,[373] explained this result by a possible establishment of a strong hydrogen bond interaction between a large number of active hydroxyls on the surface of mesoporous silica and the nitrogen atoms or carbonyl in RhB dye molecules. Note that the degradation rate of RhB over CTF-Th@SBA-15 in solid state was three times lower than in water (0.3651 min^{-1}). This might be due to the better diffusion the dye molecules into the mesopores in aqueous solution.

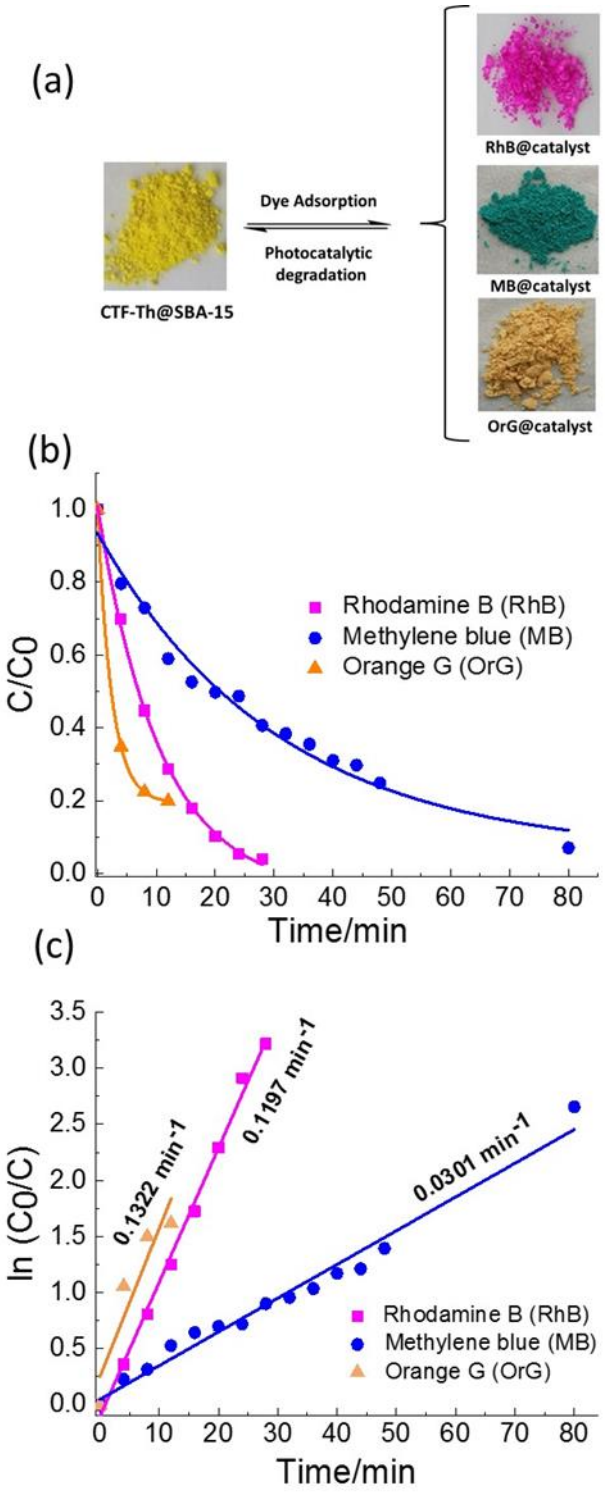

Figure 81. (a) Photographs of CTF-Th@SBA-15 before and after dye adsorption/degradation; (b) Visible light-driven degradation of three different dyes in solid state by CTF-Th@SBA-15 and (c) Photodegradation rates of the three dyes.

To further confirm the high adsorption properties of the hybrid photocatalytic system, two more dyes such as MB and OrG were tested and subjected to light irradiation. Samely, the catalyst's color, initially yellow, turned to green in case of MB and orange in case of OrG as shown in Fig. 4a, testifying the good adsorption of the dye molecules on the surface and thus

confirming the result described above. The concentration of MB decreased gradually and reached almost zero within 80 min, with a very low degradation rate of 0.0301 min-1. In contrast, the OrG photodegradation was faster. (0.1322 min-1) **(Figure 82 b,c).**

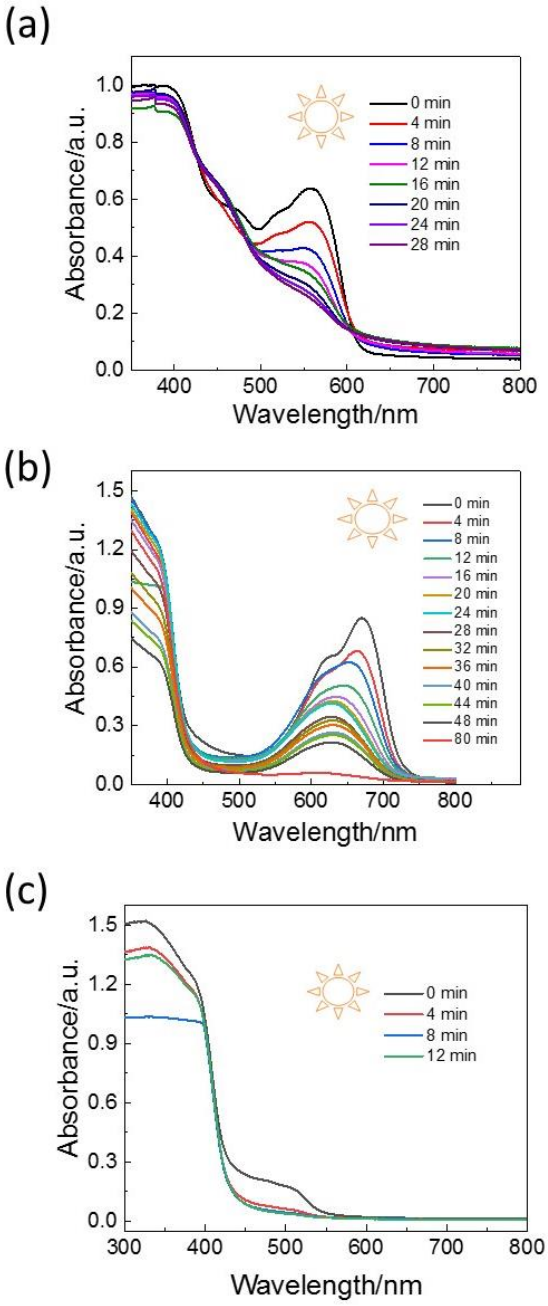

Figure 82. UV/vis DR spectral changes with reaction time of (a) RhB@catalyst, (b) MB@catalyst and (c) OrG@catalyst.

5.4.4. Conclusion and outlook

In conclusion, a thiophene-containing covalent traizine framework (CTF-Th) on a mesoporous silica SBA-15 was prepared via cyclization polymerization of dicyanide monomer and under TfOH vapor in a solid state synthesis. The as-prepared CTF-Th@SBA-15 was found to be an efficient, visible-light-active photocatalyst for complete dyes removal both in solvent and dry state. The presence of mesoporous silica SBA-15 played a key role in the rapid degradation of rhodamine B, either in aqueous medium or in solid state. A high capacity removal of methylene blue and orange G over the hybrid photocatalytic system in solid state was also demonstrated. This could likely be due to the high surface area that SBA-15 imparts to the photocatalytic system as well as its high adsorption capacity toward organic dye molecules. We believe that this study could strength the use of CTFs as a highly efficient visible light photocatalyst for a broader application field and particularly the contaminants removal and water treatment.

5.5. Designing conjugated microporous polymers with immobilized TiO_2 nanoparticles for enhanced visible light photocatalysis

This subchapter is based on the published article "Conjugated Microporous Polymers with Immobilized TiO_2 Nanoparticles for Enhanced Visible Light Photocatalysis".[4] Cyrine Ayed designed and performed the experiments, analyzed the data and drafted the manuscript. Dr. Wei Huang and Dr. Run Li contributed in the sample preparation and characterization. Dr. Di Wang performed the EPR measurements. Dr. Lucas Caire da Silva performed the ^{13}C solid-state NMR measurements. Oksana Suraeva performed the TEM measurements. Cyrine Ayed and Prof. Dr. Kai Zhang contributed to the final version of the manuscript. Prof. Dr. Kai Zhang and Prof. Dr. Wahiba Najjar supervised the project.

Over the last decade, enormous efforts has been devoted to the use of CMPs as a robust platform for visible-light photocatalysis. Particularly, attention has been drawn to the factors, which can influence strongly the catalytic efficiency of CMPs. To name a few, molecular structure, linkage geometry, morphology and band gap of CMPs have been identified as key-parameters, which can affect the charge separation and transfer efficiency, playing a crucial role in the photocatalytic process. Notably, the incorporation of functional nanomaterials with different band structures into the polymer network (heterojunction) has been found to be a promising strategy for the enhancement of the photocatalytic performance. Indeed, the formed heterojunction can enhance the light absorption in the overall solar spectrum, as well as improve the photo-charge generation, separation and transport and reduce thus the recombination rate. [81, 227]

Herein, we report on a series of hybrid photocatalysts consisting of conjugated microporous polymer-based organic semiconductors with immobilized TiO_2 nanoparticles. The organic/inorganic semiconductor-based hybrid photocatalytic system can enhance the photo-induced charge separation and thereby increasing the photocatalytic efficiency. As model reactions, the photocatalytic oxidative coupling reaction of amines and the selective oxidation of organic sulfides can be catalyzed with almost quantitative conversion and selectivity. The catalytic efficiency of the hybrid photocatalyst is higher than that of the pristine single photocatalytic systems as the conjugated microporous polymer and TiO_2. Furthermore, the mechanistic study of the photoredox reactions is also described.

[4]Ayed, C., Huang, W., Li, R., da Silva, L. C., Wang, D., Suraeva, O., Najjar, W., Zhang, K. A. I., *Particle & Particle Systems Characterization, 2018. **35**(1): p. 1700234.* Reprinted with permission with copyright (2017) from WILEY-VCH Verlag GmbH & Co. KGaA, Weinheim.

5.5.1. Motivation

Conjugated microporous polymers (CMPs), combining adjustable conjugated skeleton and permanent microporous properties, have recently emerged as efficient and stable platform for heterogeneous visible light-promoted chemical transformations. Recent research activities showed their application in photocatalytic molecular oxygen activation,[22, 380] selective oxidation of organic sulfides,[287] C-C or C-N bond formation,[82, 203, 289, 291, 381] reductive dehalogenation reaction,[290] oxidative hydroxylation of arylboronic acids,[292] visible light-initiated free radical and cationic polymerization,[293, 294] cycloaddition,[295] and light-induced hydrogen evolution**.**[222, 224]

However, the CMPs are single photocatalytic systems, whose efficiency can still be inhibited by direct recombination of the photogenerated electron/hole pair. Taking organic photovoltaic (OPV) devices as role model, in which the efficiency can be enhanced by separating the electron donor and acceptor materials in solid state. The electron/hole recombination can be delayed in the bulk-heterojunction (BHJ) manner.[382-386]

In this direction, numerous studies have focused on the establishment of heterojunction system in order to enhance the charge separation and increase the catalytic performance. For example, Chen *et al*. have reported the use of conjugated microporous poly(benzothiadiazole)@C_3N_4 composite for the photocatalytic degradation of sulfathiazole and reduction of Cr(VI) under visible light irradiation. The hybrid system exhibited enhanced photocatalytic performance, in comparison to those of single pristine (either CMPs or g-C_3N_4), due to improved light-absorption ability and efficient separation of photogenerated carriers.[387] Xiong and Xu *et al.*, have described the use of a polymer-based van der Waals heterostructure as efficient Z-scheme photocatalytic system for overall water splitting. The hybrid system, consisting of ultrathin 2D aza-CMPs and C_2N nanosheets with proper band structure alignment, have successfully performed the overall water splitting leading to a 2 : 1 stoichiometric molar ratio of H_2 and O_2 respectively, while none of the single polymer nanosheets was capable of splitting pure water under visible light irradiation. The authors attributed the promising catalytic efficiency of the aza-CMPs@C_2N to the rapid charge-carrier separation between the overlapping interfaces as well as the suppressed electron-hole recombination.[388] Recently, our research group has employed a conjugated microporous poly(benzoxadiazole) (B-BO_3) with 3 wt.% immobilized Pd nanoparticles for photocatalytic Suzuki coupling of various aryl halide and phenylboronic acid under visible light irradiation. The formed heterojunction resulted in photoamplified Schottky effect at the Pd-B-BO_3

interface, and led to excellent reaction conversions, whereas pure B-BO_3 was almost inactive for this reaction.[82]

Herein, we report on the design and application of a hybrid photocatalytic systems consisting of conjugated microporous polymer-based organic semiconductors with immobilized TiO_2 nanoparticles. The organic/inorganic semiconductor-based hybrid photocatalyst can enhance the photo-induced charge separation and therefore increase the photocatalytic efficiency. The photocatalytic oxidative coupling reaction of amines and the selective oxidation of organic sulfides were chosen as model reactions. It was shown that both photocatalytic reactions could be conducted with almost quantitative conversion and selectivity. The catalytic efficiency of the hybrid photocatalyst was higher than that of the pristine single photocatalytic systems either only consisting of the conjugated microporous polymer or TiO_2. Furthermore, the mechanistic insight of the photoredox reactions was investigated.

5.5.2. Synthesis and characterization of CMP@TiO_2 photocatalysts

The TiO_2 nanoparticles with average size of ca. 10 nm **(Figure 83 a,b)** were synthesized according to the method reported in the literature.[389] They were obtained in pure anatase phase as shown by the X-ray diffraction pattern **(Figure 83c)**.

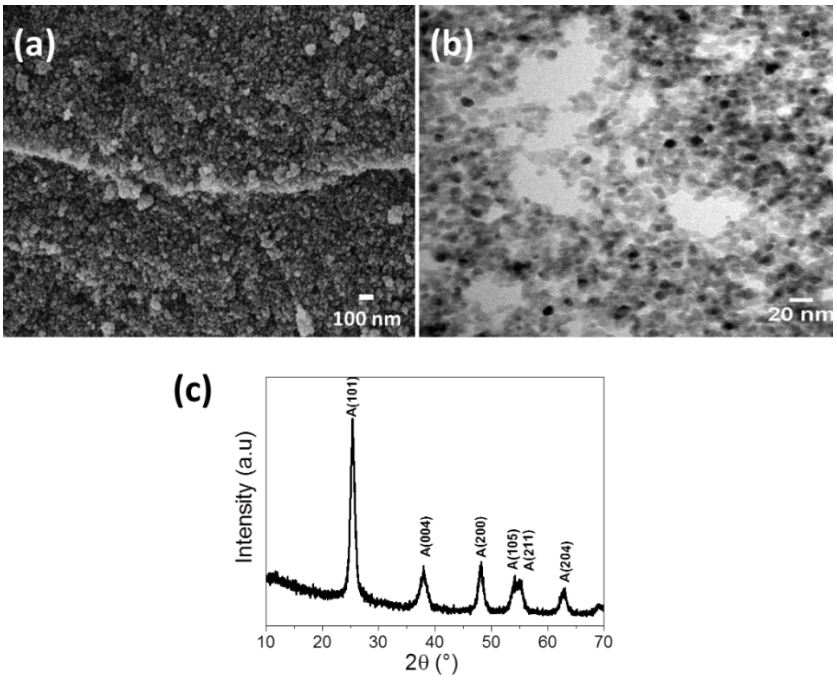

Figure 83. (a) SEM, (b) TEM images sand (c) X-ray diffraction pattern of the prepared TiO_2 nanoparticles.

The series of the hybrid photocatalysts consisting of the conjugated microporous polymers with immobilized TiO_2 nanoparticles were obtained via the direct polymerization of 1,3,5-triethynylbenzene as cross-linker and 4,7-dibromo-2,1,3-benzothiadiazole as co-

monomer using the palladium-catalyzed Sonogashira cross-coupling reactions in a dispersion of TiO_2 nanoparticles. Defined ratio between the conjugated microporous polymer, which is addressed as BBT, and TiO_2 nanoparticles were chosen. The hybrid photocatalyts are addressed as BBT@TiO_2-X, where X refers to the specific ratio between BBT and TiO_2. For example, the photocatalyst BBT@TiO_2-0.2 refers to the hybrid material containing 20 wt.% of BBT with respect to the total weight. The synthetic and characterization details are described in Experimental Section **6.5**.

The SEM and TEM images of BBT and BBT@TiO_2-0.8 are shown in **Figure 84**. The pure BBT exhibited a nano-fiber like morphology. After the immobilization of TiO_2 nanoparticles, similar fiber-like morphology was observed for the hybrid material BBT@TiO_2-0.8. Similar morphologies were observed for the other hybrid materials as shown in **Figure 85**.

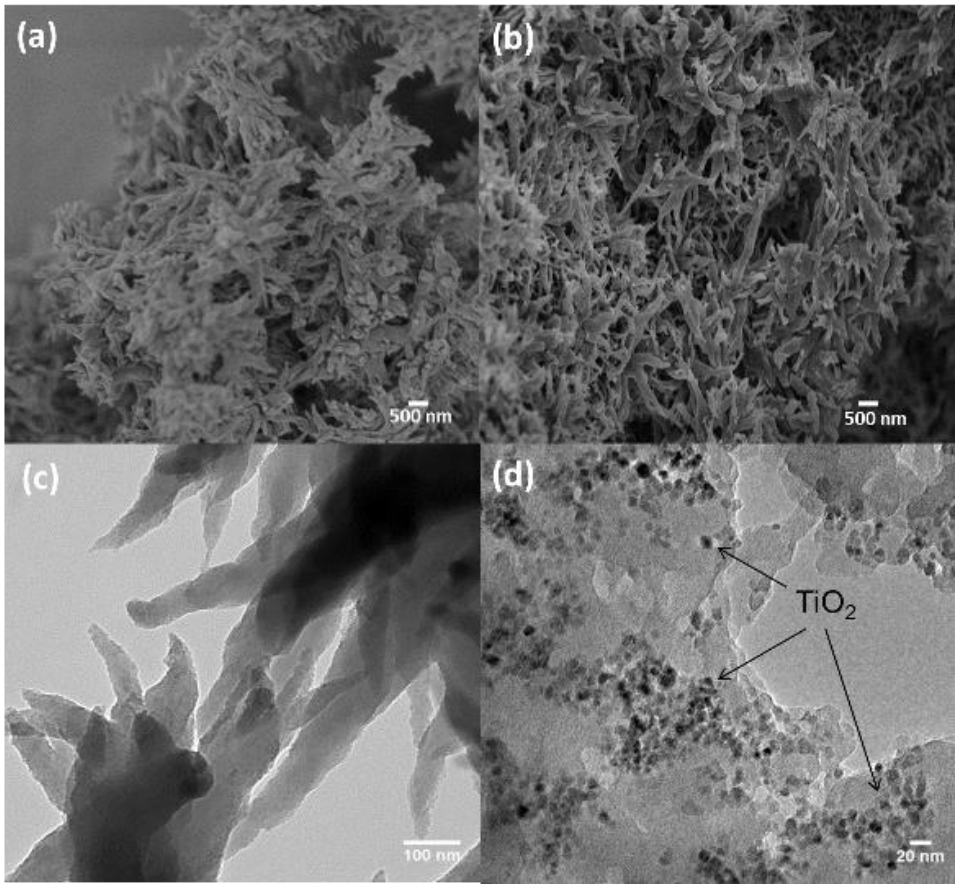

Figure 84. SEM images of (a) BBT and (b) BBT@TiO_2-0.8; TEM images of (c) BBT and (d) BBT@TiO_2-0.8.

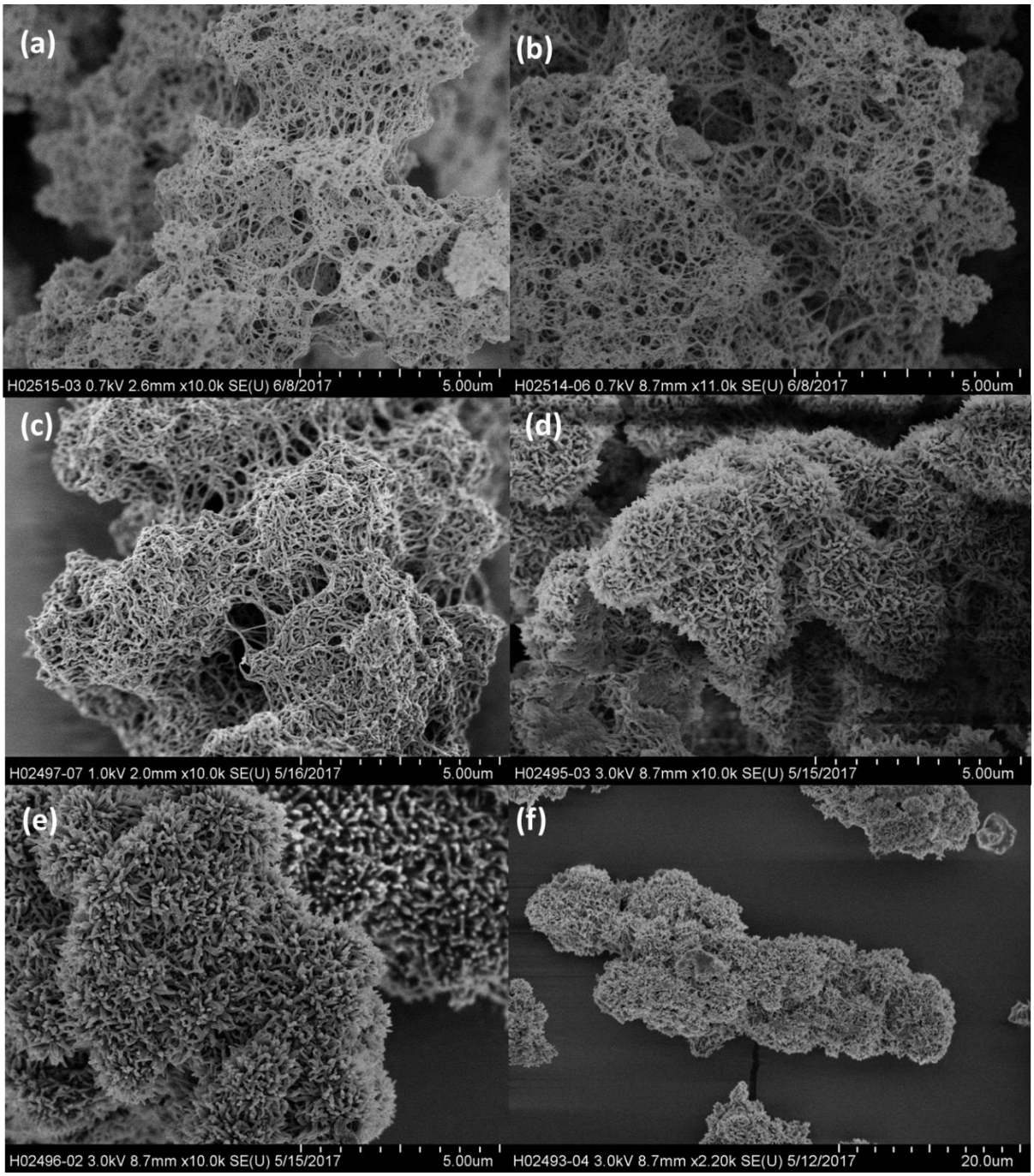

Figure 85. SEM images of (a) BBT@TiO_2-0.2, (b) BBT@TiO_2-0.4, (c) BBT@TiO_2-0.5, (d) BBT@TiO_2-0.6, (e) BBT@TiO_2-0.7 and (f) BBT@TiO_2-0.9.

The Brunauer-Emmett-Teller (BET) surface areas of BBT and TiO_2 NPs were measured to be 129 $m^2 g^{-1}$ and 201 $m^2 g^{-1}$. By increasing the amount of BBT in the hybrid materials, the BET surface areas decreased gradually. The nitrogen gas sorption isotherms and pore size distributions are displayed in **Figure 86** and **Figure 87**.

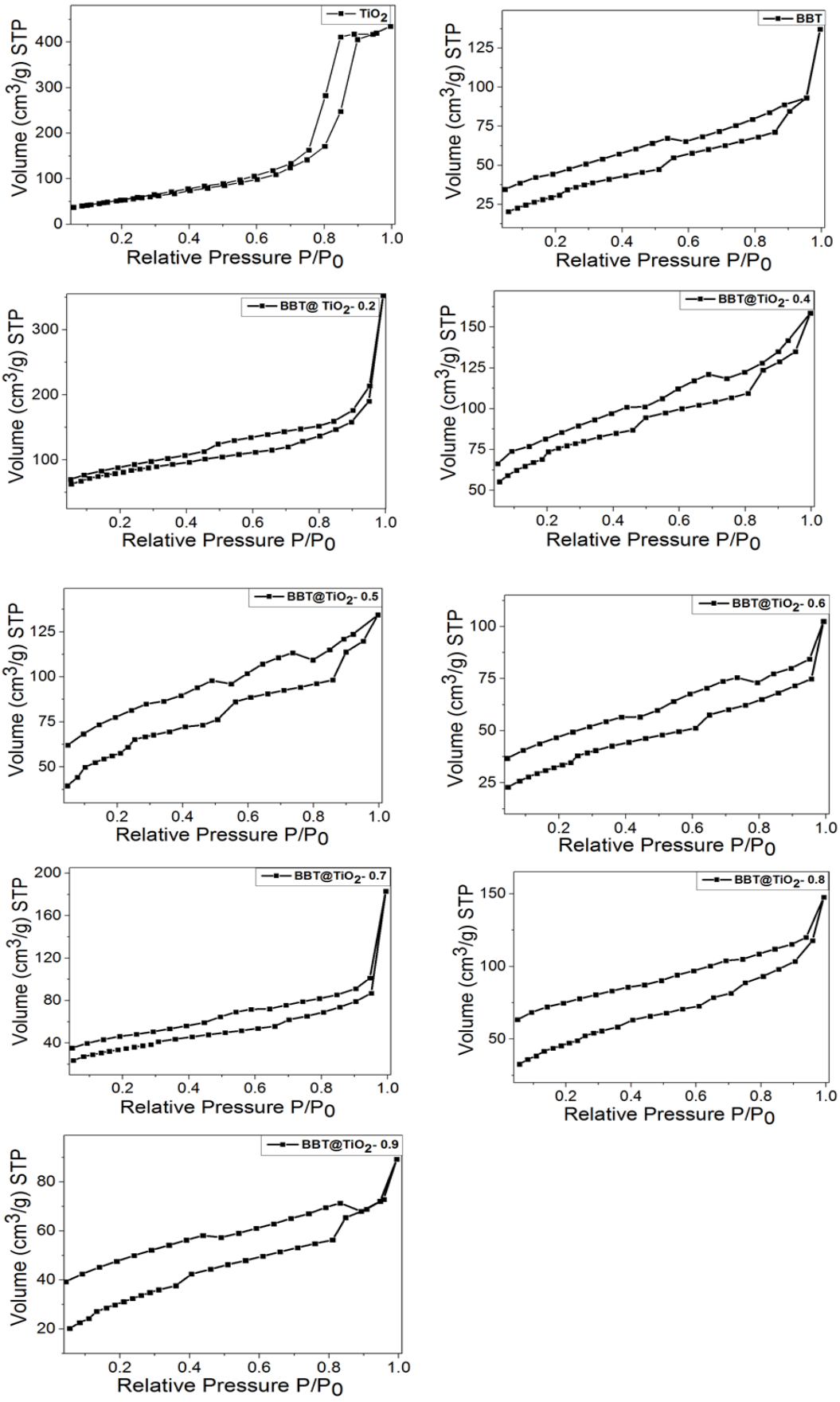

Figure 86. Nitrogen sorption and desorption isotherms of the materials.

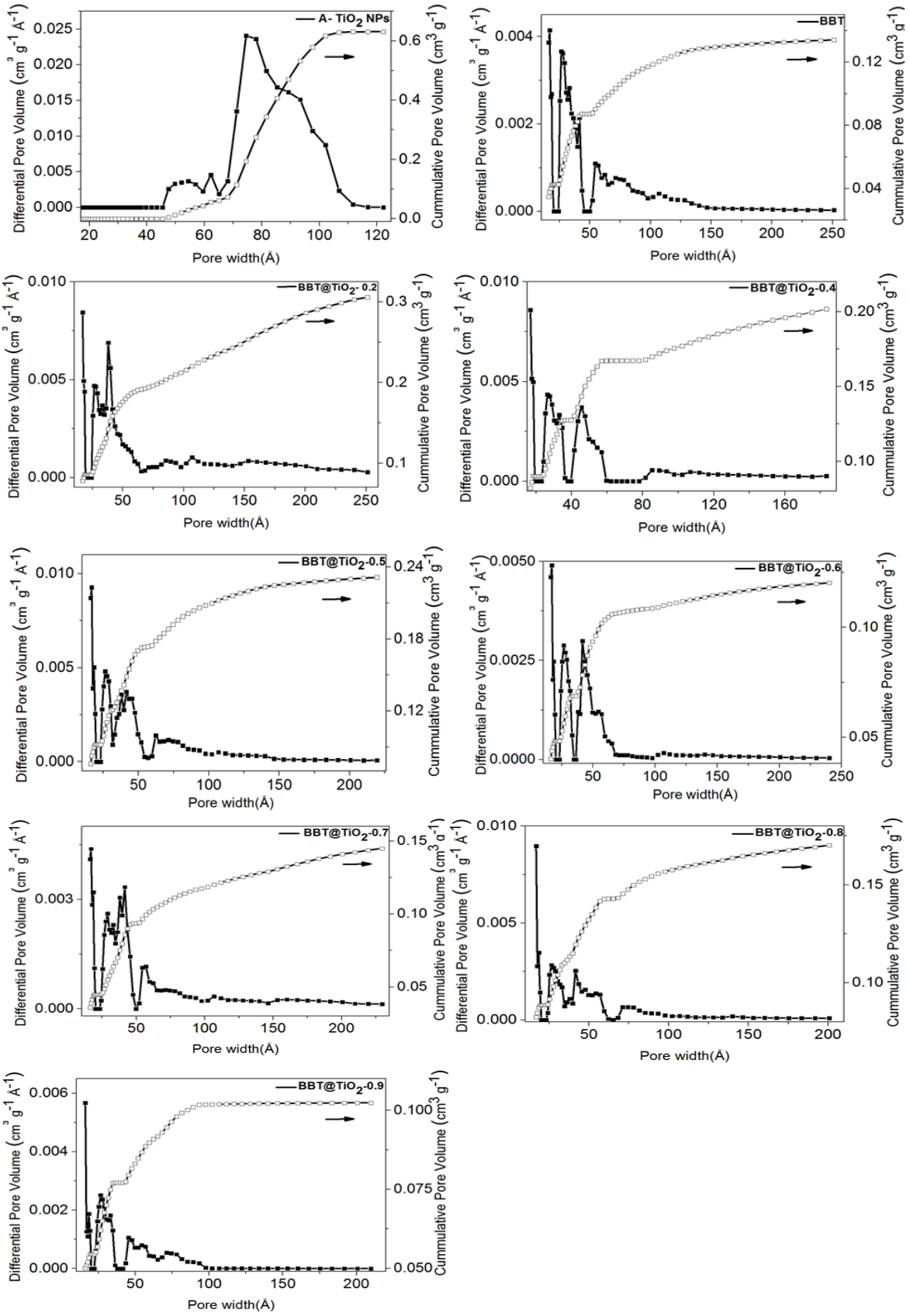

Figure 87. Pore size distributions of the materials.

The physical properties of BBT, TiO_2 NPs and the hybrid materials are listed in **Table 6**.

Table 6. Physical Properties of TiO_2 NPs, pure BBT and the different BBT@TiO_2 samples.

Samples	TiO_2 content (wt.%)	BBT content (wt.%)	S_{BET} ($m^2\ g^{-1}$)	Pore volume ($cm^3\ g^{-1}$)	Pore size (nm)	Band gap (eV)
TiO_2 NPs	100	-	201	0.631	7.4	3.2
BBT	0	100	129	0.134	1.7	2.12
BBT@TiO_2- 0.2	80	20	277	0.306	1.7	2.26
BBT@TiO_2- 0.4	60	40	252	0.202	1.7	2.17
BBT@TiO_2- 0.5	50	50	216	0.176	1.6	2.16
BBT@TiO_2- 0.6	40	60	129	0.120	1.7	1.98
BBT@TiO_2- 0.7	30	70	125	0.145	1.7	2.04
BBT@TiO_2- 0.8	20	80	129	0.110	1.7	2.11
BBT@TiO_2- 0.9	10	90	116	0.102	1.6	2.05

The Fourier Transform Infrared spectra (FTIR) of the entire series of the materials are displayed in **Figure 88a**. The hybrid materials showed a typical signal between 600-400 cm^{-1} which could be assigned to the Ti-O-Ti stretching mode in anatase morphology.[389-391] For BBT, the characteristic signals at around 1570 cm-1, 1480 cm-1 and 2300 cm-1 which could be assigned respectively to the =N-S- , the -C=N- of the BT unit of the polymeric network and the -C≡C- stretching modes.[38] A clear tendency can be observed that the typical signal of TiO_2 decreased while increasing the BBT amount.

The solid state ^{13}C CP/MAS NMR spectra of BBT and the hybrid material BBT@TiO_2-0.8 are displayed in **Figure 88b**. The signals between 110 ppm and 160 ppm correspond to the aromatics carbons of the BT unit and the peaks between 70-100 ppm can be assigned to triple bonds.[392] The hybrid material showed clearly similar signals, which indicates that the immobilization of TiO_2 nanoparticles did not affect the chemical structure of the polymer.

Figure 88c illustrates the UV/vis diffuse reflectance (DR) spectra of the TiO_2 NPs, BBT and the hybrid materials. As expected, TiO_2 NPs mainly absorbed in the UV range, whereas BBT and the hybrid materials possessed broader absorption range up to 800 nm with the absorption maxima between 400 and 500 nm. The results indicate the visible light activity of the hybrid materials, which can be used in possible visible light-driven photocatalytic processes.[231]

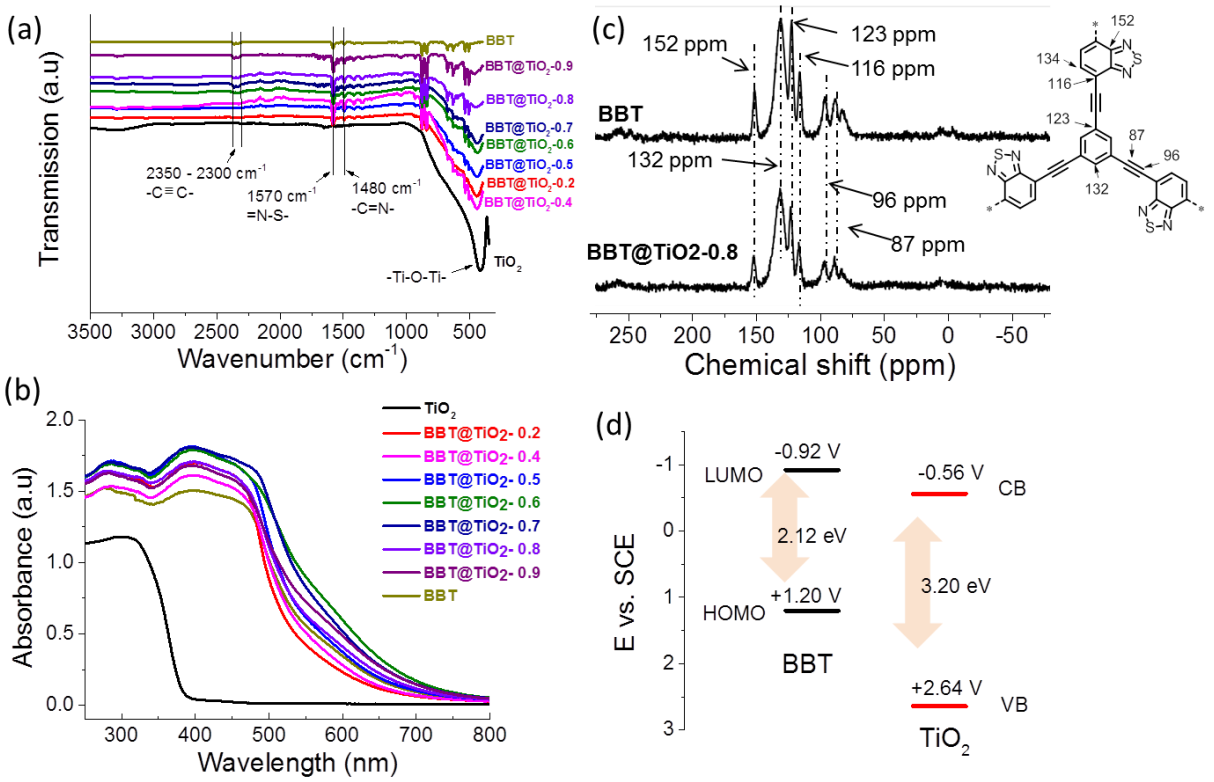

Figure 88. (a) FTIR and (b) UV/vis DR spectra of the pure TiO_2, BBT and the series of the hybrid materials; (c) comparison of the solid state ^{13}C CP/MAS NMR spectra of BBT and BBT@TiO_2-0.8; (d) energy band structures of pure TiO_2 and BBT.

For semiconductor-based photocatalysts, the energetic band positions represent their light-induced redox potentials. Therefore, cyclic voltammetry (CV) measurements were conducted to reveal the energy band structure of the designed materials **(Figure 89)**.

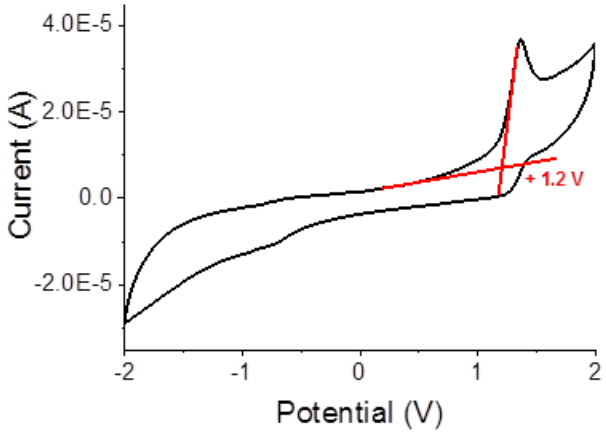

Figure 89. Cyclic voltammogram of BBT.

As shown in **Figure 88d**, the highest occupied molecular orbital (HOMO) and the lowest unoccupied molecular orbital (LUMO) of BBT were determined to be +1.2 V vs SCE and -0.92 V vs SCE, respectively. Similarly, the valence band (VB) and the conduction band (CB) of the prepared TiO_2 were +2.64 V vs SCE and -0.56 V vs SCE. The energy diagram of

the hybrid material containing both organic and inorganic semiconductors might indicate a possible light-induced electron transfer between both species. Thermogravimetric analysis **(Figure 90)** showed that BBT and the hybrid materials were stable up to 300 °C and at higher temperature (800 °C), the content of the residue should correspond to the TiO_2 amount.

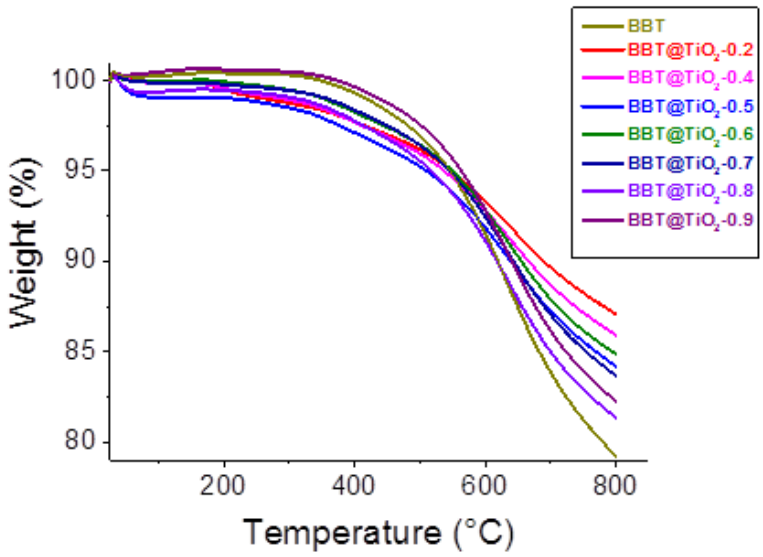

Figure 90. TGA spectra of the materials under N_2 atmosphere with a heating rate of 10 ºC/min.

5.5.3. Visible-light promoted photocatalytic oxidation reactions

5.5.3.1. Visible-light oxidative coupling of benzylamines over BBT@TiO₂ photocatalysts

To investigate the photocatalytic performance of the designed hybrid materials, we first tested the oxidative coupling of benzylamines under visible light irradiation at room temperature. As listed in **Table 7**, the reaction catalyzed by BBT@TiO_2-0.8 (entry 7 in **Table 7**) achieved the highest conversion (98%) compared to those catalyzed by pure BBT and the other hybrid materials (entries 2, 3, 4, 5, 6 and 8 in **Table 7**) while TiO_2 NPs was nearly catalytically inactive for this reaction (entry 1 in **Table 7**).

Table 7. Oxidative coupling of benzylamines using the TiO_2 NPs, the pure BBT and the hybrid materials as photocatalysts.

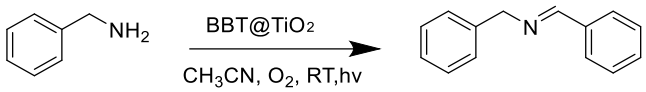

Entry[a]	Catalyst	O_2	Light	Additive	Conversion (%)[b]
1	TiO_2	+	+	-	<1
2	BBT@TiO_2-0.2	+	+	-	57
3	BBT@TiO_2-0.4	+	+	-	66
4	BBT@TiO_2-0.5	+	+	-	69
5	BBT@TiO_2-0.6	+	+	-	72
6	BBT@TiO_2-0.7	+	+	-	93
7	BBT@TiO_2-0.8	+	+	-	98
8	BBT@TiO_2-0.9	+	+	-	90
9[c]	BBT	+	+	-	82
10[d]	-	+	+	-	<1
11[e]	BBT@TiO_2-0.8	+	-	-	<1
12[f]	BBT@TiO_2-0.8	-	+	-	26
13[g]	BBT@TiO_2-0.8	+	+	Hole scavenger	35
14[h]	BBT@TiO_2-0.8	+	+	Singlet oxygen scavenger	54
15[i]	BBT@TiO_2-0.8	+	+	Hydroxyl radical scavenger	73
16[j]	BBT@TiO_2-0.8	+	+	Superoxide scavenger	85

[a)]Standard reaction conditions: 1 mmol of substrate, 5 mg of catalyst in 3 mL CH_3CN under the irradiation of a blue LED lamp (460 nm, 0.16 W cm^{-2}), 1 atm. O_2, room temperature, 6h.[b)]Conversion determined by 1H NMR, [c)]with pure BBT, [d)]without catalyst, under light,1atm O_2,[e)] BBT@ TiO_2-0.8, no light,1atm O_2. [f)] with BBT@ TiO_2-0.8, under light, no O_2. [g)]KI as a hole scavenger. [h)]NaN_3 as singlet oxygen scavenger, [i)] Isopropanol as Hydroxyl radical scavenger, [j)]Benzoquinone (BQ) as superoxide scavenger.

A kinetic study of this reaction **(Figure 91a)** was also carried out with the model reaction. It was clearly shown that BBT@TiO_2-0.8 showed the highest photooxidative ability during the entire catalytic process. Interesting, the hybrid photocatalyst with low BBT ratios, in particular, BBT@TiO_2-0.2, BBT@TiO_2-0.4, BBT@TiO_2-0.5 and BBT@TiO_2-0.6 exhibited lower photocatalytic efficiencies than pure BBT, while the hybrid materials with high amount of BBT, in particular BBT@TiO_2-0.7, BBT@TiO_2-0.8, and BBT@TiO_2-0.9 were more

efficient than BBT. It could be caused by the light induced electron transfer between TiO_2 and BBT within the hybrid photocatalyst, which is obviously affected by the exact composition of both active semiconductors species. To further confirm this result, further derivatives of benzylamine bearing either an electron-withdrawing group (-F) or an electron-donating group ($-OCH_3$) were tested. As shown in **Figure 91b**, BBT@TiO_2-0.8 remained the best photocatalyst for the oxidation reaction.

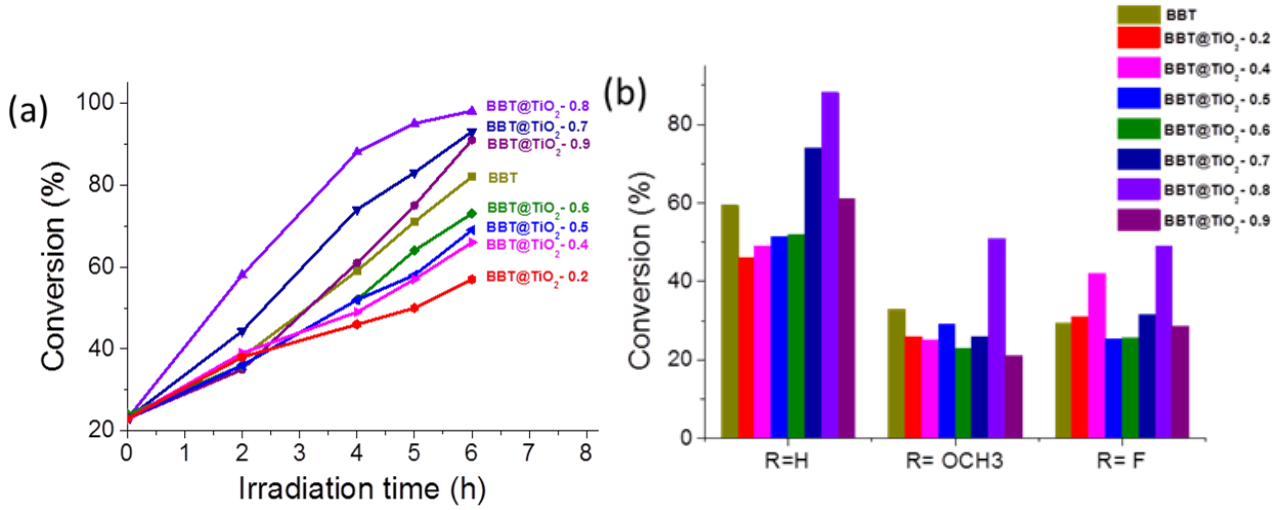

Figure 91. (a) Kinetics for the conversion of the oxidative coupling reaction of benzylamine in the presence of different catalysts, conversion determined via ^1H NMR spectra; (b) Comparison of the different photocatalysts for the oxidative coupling of benzylamine and its derivatives. Reaction Conditions: 1 mmol of substrate, 5 mg of photocatalyst in 3 mL CH_3CN under the irradiation of blue LED lamp (460 nm, 0.16 W cm^{-2}), 1 atm. O_2, room temperature, 6 h.

To further investigate the mechanistic insight of the photocatalytic oxidative coupling of benzylamines using the designed hybrid photocatalyst and the role of the photogenerated electron and hole species, we extended the study by conducting control experiments, especially with different hole and electron scavengers. The results are also listed in **Table 7**. In the absence of light, photocatalyst, no reaction conversion was determined (entries 10 and 11 in **Table 7**). Without using molecular oxygen, only low conversion of 26% was determined (entry 12 in **Table 7**). The results indicate that all three components are indispensable. The reactions were conducted in low conversion by adding scavengers. For example, the conversion was 35% in the presence of potassium iodide KI as a hole scavenger (entry 13 in **Table 7**), 54% in the presence of sodium azide NaN_3 as a singlet oxygen scavenger (entry 14 in **Table 7**), 73% in the presence of isopropanol as hydroxyl scavenger (entry 15 in **Table 7**) and 85% in the presence of benzoquinone as superoxide scavenger (entry 16 in **Table 7**). These results indicate that the activated oxygen species (superoxide and singlet oxygen), hydroxyl radicals and hole all

participate during the oxidative coupling of benzylamine with the most crucial role being attributed to the photogenerated hole.

To precisely analyze the possible active oxygen species (superoxide and singlet oxygen) and their exact contribution during the photocatalytic reaction, we further conducted electron spin resonance (EPR) experiments using 5,5-dimethyl-1-pyrroline N-oxide (DMPO) and 2,2,6,6-tetramethylpiperidine (TEMP) as superoxide and singlet oxygen trapping agents, respectively. As shown in **Figure 92**, both active oxygen species could be determined, confirming their active roles for the reaction.

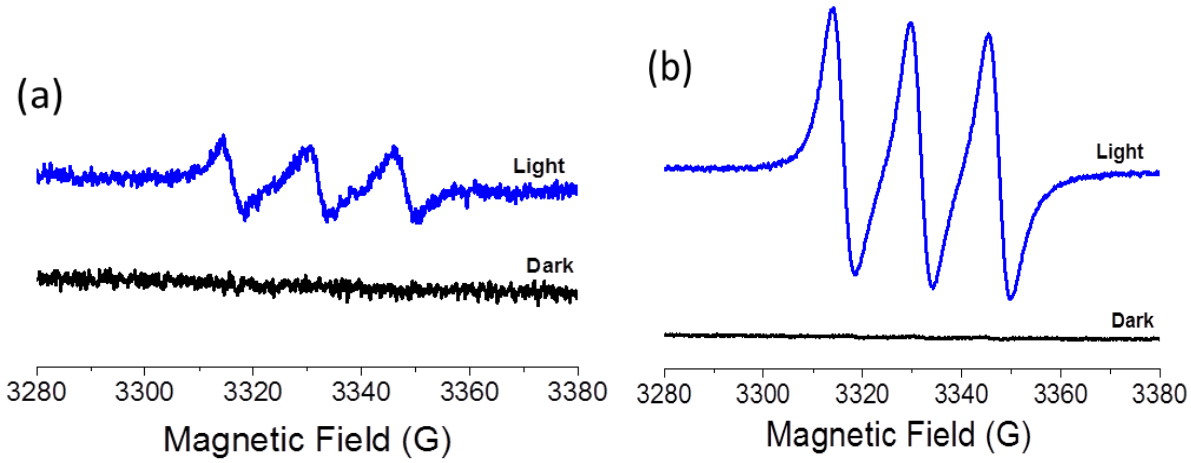

Figure 92. EPR spectra of DMPO-$O_2^{\bullet-}$ (a) and TEMP-$^1O_2$ adducts (b) using BBT@TiO_2-0.8 as photocatalyst in dark and under light irradiation.

Based on the observations drawn from the experiments described above, we suggest a modified reaction mechanism **(Figure 93)** similar to the literature.[38, 393, 394] Under visible light irradiation, the charge separation occurs within BBT. The photogenerated hole of BBT oxidized benzylamine into its cationic radical. In the same time, the electron from the LUMO of BBT is transferred on the CB of TiO_2 assisting the reduction of molecular oxygen into superoxide ($O_2^{\bullet-}$),[395] which reacts with the cationic radical of benzylamine to form the intermediate hydroperoxy (phenyl)methanamine. To note, singlet oxygen ($^1O_2$) also took part of the oxidation step. However, the singlet oxygen species should be generated directly from the photogenerated electron of BBT via the inter system crossing from the singlet to the triplet state. Here, the triplet electron is not transferred to the CB of TiO_2. After elimination of H_2O_2, an imine species is formed, which further reacts with an additional benzylamine molecule, forming the N-benzyl-1-phenylmethanediamine intermediate. In this process, the obtained •OH could also extract a proton from the oxidized benzylamine cationic radical and thus form the

imine species. Similar to previous studies,[38, 393, 394] the importance of both photogenerated electron hole species is highlighted in this reaction.

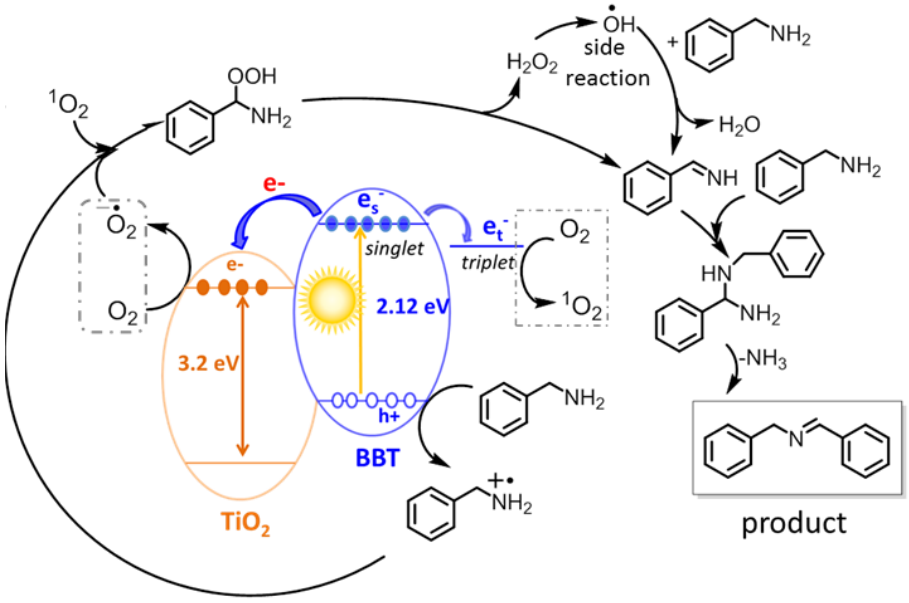

Figure 93. Suggested reaction mechanisms of both photocatalytic reactions using BBT@TiO_2-0.8 as photocatalyst for (a) oxidative coupling reaction of benzylamine.

In order to demonstrate the general applicability of BBT@TiO_2-0.8 as photocatalyst, the screening experiments with various benzylamines derivatives have been carried out under the same conditions and the results are listed in **Table 8**. After a reaction time of 6 h, the reactions with benzylamines containing electron-withdrawing (such –F or –Cl) groups led to lower conversion than the model reaction. The reaction with para-chlorobenzylamine showed higher conversion than the reaction with para-fluorobenzylamine (entries 2 and 3 in **Table 8**). For the reactions with benzylamines bearing electron-donating groups (entries 4, 5 and 6 in **Table 8**), the reaction conversion decreased by increasing electropositive effect of the substituents. This could be caused by the stabilization effect of the electron-donating groups on the cationic benzylamine radical which inhibits the formation of the target product.

Table 8. Photocatalytic oxidative coupling of benzylamine derivatives using BBT@TiO_2-0.8 as photocatalyst.

Entry	Substrate	Product	Conversion (%)
1	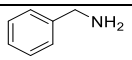	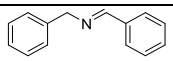	98
2	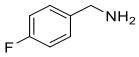	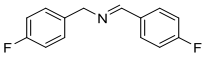	58
3	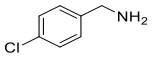	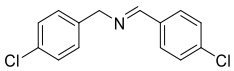	73
4	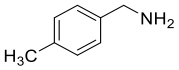	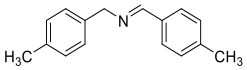	87
5	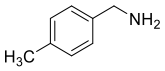	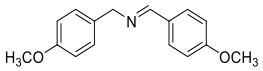	42
6	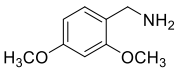	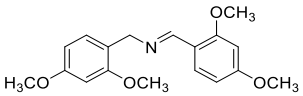	12

All experiments were conducted with 1 mmol of substrate,5 mg of BBT@TiO_2-0.8 in 3 mL CH_3CN under the irradiation of Blue LED (460 nm, 0.16 W cm^{-2}) for 6h (1 atm. O_2, room temperature).[b)]Conversion determined by ^1H NMR.

The repeating experiments with the model reaction showed that BBT@TiO_2-0.8 could catalyze the reaction for 5 additional cycles without significantly suffering its catalytic efficiency **(Figure 94a)**. No apparent changes were observed in the UV/vis DR spectra of BBT@TiO_2-0.8 after the repeating experiments, which confirmed its stability as highly reusable photocatalyst (**Figure 94b).**

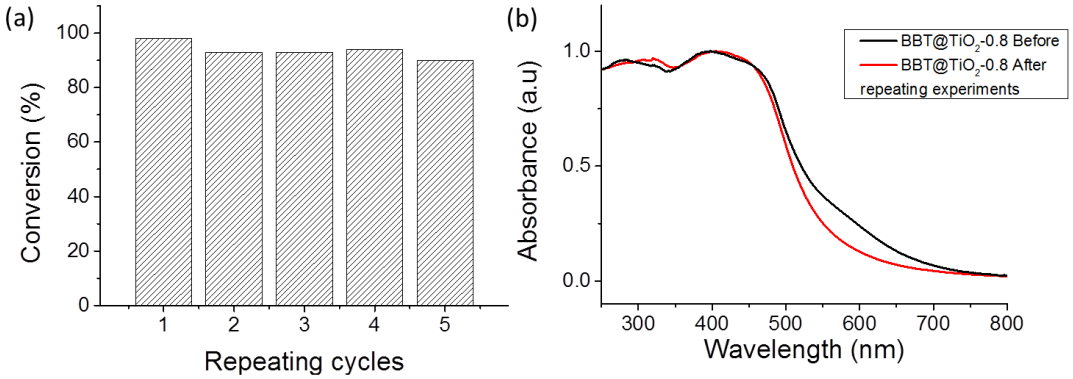

Figure 94. (a) Repeating experiments of the photocatalytic oxidative coupling of benzylamine using BBT@TiO_2-0.8 as photocatalyst. (b) UV/vis DR spectra of BBT@TiO_2-0.8 before and after the repeating experiments.

5.5.3.2. Visible-light oxidation of sulfides over BBT@TiO_2-0.8

To further evaluate the photocatalytic activity of BBT@TiO_2-0.8, the selective oxidation of sulfides into sulfoxides was chosen as a second model reaction, given the fact that sulfoxides are widely used in various fields such as organic synthesis, medicinal chemistry and natural compounds production.[396] The reaction was performed at room temperature under

visible light irradiation and an oxygen atmosphere. Blank experiments were also conducted by using BBT@TiO_2-0.8 as photocatalyst either without light irradiation or without molecular oxygen. No target products were determined signifying that both oxygen and light are mandatory in this reaction. Various organic sulfides derivatives bearing electron- donating or electron-withdrawing groups were also examined under the same conditions. The results are summarized in **Table 9.**

Table 9. Selective oxidation of sulfides using BBT@TiO_2-0.8 as photocatalyst.

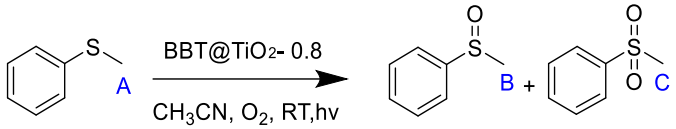

Entry	Sulfide derivatives	Conversion (%)	Selectivity (%)	
			B	C
1	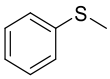	>99	96	4
2	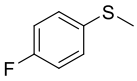	>99	95	5
3	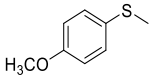	>99	93	7
4	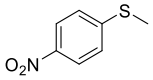	26	>99	-
5	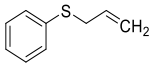	32	78	22
6	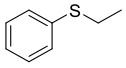	8	>99	-

All experiments were conducted with 1 mmol of substrate,5 mg of catalyst in 3 mL CH_3CN under the irradiation of a blue LED lamp (460 nm, 0.16 W cm^{-2}), 1 atm. O_2, room temperature, 20h. [b] Conversion determined by ^1H NMR, [c]BBT@ TiO_2-0.8,no light,1atm O_2. [d] with BBT@ TiO_2- 0.8, under light, no O_2

As it can be seen, BBT@TiO_2-0.8 promoted efficiently the oxidation of sulfides derivatives into the corresponding sulfoxides achieving high selectivity. The model reaction and the reactions with the sulphide derivatives bearing a fluoro and methoxy groups were conducted in almost quantitative manner (entries 1, 2 and 3 in **Table 9**). The derivative with a strong electron-withdrawing group as nitro unit led to a low conversion (entry 4 in **Table 9**). Furthermore, allyl phenyl sulphides with a considerable selectivity (entry 5 in **Table 9**) and ethyl phenyl sulphide (entry 6 in **Table 9**) with high selectivity were carried out to investigate the chemoselectivity of the photooxidation reaction.

Here, we also propose a modified reaction mechanism similar to the literature[397] as shown in **Figure 95**. Comparable to the photocatalytic oxidative coupling reaction of benzylamine as studied before, the first step should be the oxidation of the sulfide by the photogenerated hole of BBT, forming its cationic radical. The cationic radical reacts then with the simultaneously generated active oxygen species, in particular superoxide and singlet oxygen species, leading to the formation of persulfoxide as intermediate. The persulfoxide species reacts with another sulfide molecule to form two sulfoxide molecules as final product.

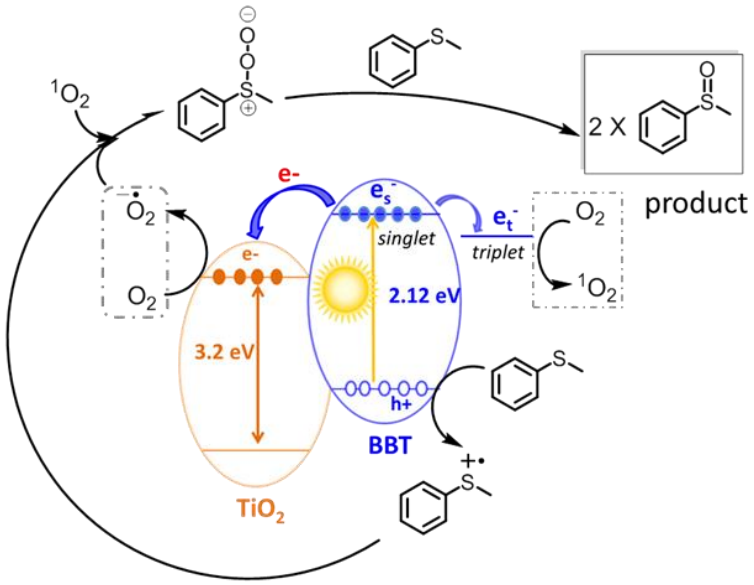

Figure 95. Suggested reaction mechanisms of both photocatalytic reactions using BBT@TiO_2-0.8 as photocatalyst for selective oxidation of organic sulfides.

5.5.4. Conclusion and outlook

In summary, we have designed a hybrid photocatalytic systems consisting of conjugated microporous polymer-based organic semiconductors with immobilized TiO_2 nanoparticles. The hybrid photocatalysts have been successfully used for visible light driven organic photoredox reactions. The organic/inorganic semiconductor-based hybrid photocatalyst can enhance the photo-induced charge separation and therefore increase the photocatalytic efficiency. As model reactions, the photocatalytic oxidative coupling reaction of amines and the selective oxidation of organic sulfides were investigated with high conversion and selectivity. The catalytic efficiency of the hybrid photocatalyst was higher than that of the pristine single photocatalytic systems either only consisting of the conjugated microporous polymer or TiO_2. We believe that the hybrid photocatalyst design consisting of organic and inorganic semiconductors can serve as a powerful and robust photocatalyst to mediate other synthetic transformations in different fields.

6. Experimental Section

6.1. Designing conjugated microporous polymers for visible light-promoted photocatalytic carbon-carbon double bond cleavage in aqueous medium

6.1.1. Materials

Copper (I) iodide (99%), tetrakis (triphenylphosphine) palladium (0) (99%), p-benzoquinone (98%), sodium azide (99%), potassium iodide (> 99.9%), triethylamine (99%) and 2,5-dibromothiophene (96%), were purchased from Sigma Aldrich. 1,3,5-Triethynylbenzene (>98%) and 4,4-dibromobiphenyl (98%) were purchased from Alfa Aesar (Massachusetts, USA). 4,7-Dibromo-2,1,3-benzothiadiazole (97%) (Br-BT) was purchased from COMBI-BLOCKS. Isopropanol (99.5%), N,N-dimethylformamide anhydrous (99.8%) were purchased from Acros organics. Acetonitrile was purchased from Fischer Chemical. Styrene and styrene derivatives were purified by elution through neutral aluminium oxide (50-200 um) and anhydrous $CaCl_2$ (w/w, 95/5) in order to remove peroxides and other impurities. Chemicals and solvents purchased from commercial sources were used as received unless otherwise noted.

6.1.2. Characterization methods

X-ray diffraction (XRD) patterns were carried out using a Philips PW1050 diffractometer with CuKa radiation at k = 1.5418 Å. UV/vis absorption spectra were measured using a Perkin-Elmer Lambda 25 UV-Vis spectrometer. FTIR spectra were obtained using a FTIR spectrophotometer TENSOR II Bruker equipped with platinum ATR. Solid state ^{13}C CP/MAS NMR measurements were performed at 300 MHz Lamor Frequency equipped with a standard 4mm magic angle spinning MAS double resonance probe head. TGA measurements were carried out on a Mettler Toledo TGA-851 system. The temperature was increased from 25 °C to 800 °C (10 °C min^{-1}) under nitrogen atmosphere. Electron paramagnetic resonance (EPR) was operated using a Magnettech MS 200 spectrometer. The nitrogen sorption data were measured to determine the surface area and the pore size distribution; the data were recorded at 77.3 K on an Autosorb 1 using the QuadraWin Software (Quantchrome instruments). CV and photocurrent measurements were conducted using an Autolab Potentiostat PGSTAT204 (Metrohm). A glassy carbon working electrode, a Pt counter electrode and a SCE reference electrode were used. The SEM images were collected by a LEO Gemini 1530 (Carl Zeiss AG, Germany) with an in lens SE detector.

6.1.3. Synthesis of BTh, BThBT and BBT

The synthesis of BBT, BThBT and BTh was performed via palladium catalyzed Sonogashira-Hagihara cross coupling reactions. The cross-linker 1,3,5-Triethynylbenzene (150 mg, 1 mmol, 1 equiv.), tetrakis(triphenylphosphine)palladium(0) (35 mg, 0.03 mmol, 0.03 equiv.) and copper(I) iodide (5.7 mg, 0.03 mmol, 0.03 equiv.) were dissolved in 20 mL of DMF/ Triethylamine mixture with a volume ratio of 1:1. Then, the co-monomers 4,7-dibromo-2,1,3-benzothiadiazole (294 mg, 1 mmol,1 equiv.) was added for BBT, and the co-monomer 2,5-dibromothiophene (119 µL, 1 mmol,1 equiv.) was added for BTh. As for the BThBT, both co-monomers (4,7-dibromo-2,1,3-benzothiadiazole and 2,5-dibromothiophene) were added in equal ratio. The reaction mixtures were degassed with N_2 for 10 min. After degassing process, the reactive mixtures were heated at 80 °C for 48 h. After cooling, the precipitated powders were washed with methanol, acetone and water several times. The crude products were then extracted in a Soxhlet extractor for 24 h using a mixture of dichloromethane and methanol. Finally, the products were dried overnight at 60 °C under vacuum. Yield (BTh) = 52% ,yield (BThBT)= 64% and yield (BBT) = 55%.

Metal residue analysis. BBT: ICP(Pd) = 3.75 ppm, ICP(Cu)= 0.05 ppm; BThBT: ICP(Pd)= 10 ppm, ICP(Cu)= 0.22 ppm; BTh: ICP(Pd)= 3.77 ppm ICP(Cu)= n.d. (not determined)

6.1.4. General procedure for the C=C bond cleavage using CMPs as photocatalysts

0.1 mmol of styrene or its derivatives or alkenes, 10 mg of the photocatalyst were added into 1.5 mL of a solvent in a glass vial equipped with an oxygen balloon. A blue LED lamp (460 nm, 0.065 Wcm^{-2}, OSA Opto Light GmbH) was used as the light source. The reaction mixture was stirred at room temperature and under irradiation for 18 h. The conversion and selectivity were determined via GC-MS. The GCMS spectra are displayed in ESI. For the repeating experiments, the CMP was filtrated and washed several times with methanol, CH_2Cl_2 and acetone, then dried under vacuum before being used for the repeating experiments.

6.1.5. Detection of reaction intermediates: formaldehyde

Formaldehyde is a small molecule containing one carbon and one heterogeneous oxygen atom. This molecule could not be detected by gas chromatographic (GC) with flame ionization detection (FID). Additionally, formaldehyde is not easily ionizable and cannot be easily analyzed by mass spectrometry (MS). Therefore, the high-performance liquid chromatography (HPLC) method can be the best option to detect formaldehyde. However, Formaldehyde is reactive and might be challenging to separate and detect without prior derivatization with 2,4-dinitrophenylhydrazine, which might be complex when we have a complex reaction media. Moreover, we might be dealing with a very low ppm levels of formaldehyde, which would make the detection difficult. HPLC analysis were carried out using our reaction media after a certain time of irradiation, different kind of columns, different solvent gradient and different wavelengths for the UV detection. No significant results were obtained. As alternative, ^{1}H NMR was used to monitor the model reaction. 0.1 mmol of styrene and 10 mg of BBT were dispersed in 1.5 ml of deuterated solvents in a molar ratio of D_2O: CD_3CN (24:1), and kept under blue light irradiation for 12 h. The sampling was done before irradiation (t = 0 h) and after 12 h of irradiation. The pure formaldehyde ^{1}H NMR spectra was also recorded for comparison purpose. As shown in the **Figure 96**, after 12 h of irradiation, there is appearance of a singlet around 10 ppm, which corresponds to the aldehyde group in the benzaldehyde molecule (**H**C=O), with almost a complete disappearance of the signals characteristics of styrene (range from 5 to 6 ppm). Furthermore, a small signal appears around 9.6 ppm, that may correspond to the formaldehyde (HC=O).

6.1.5. Spectra

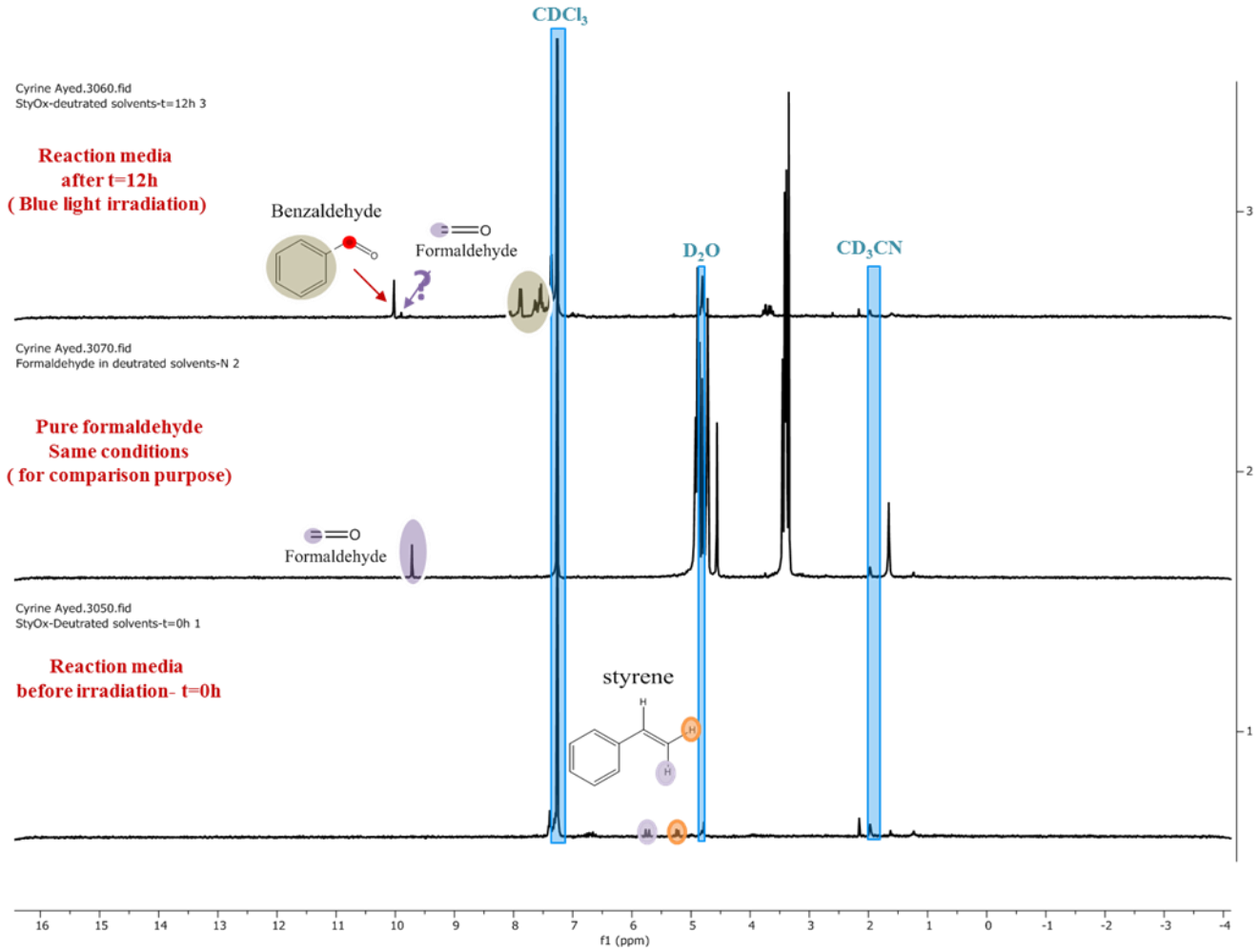

Figure 96. ^{1}H NMR spectra of the starting compound and product for the photocatalytic selective oxidation of styrene: formaldehyde detection.
Reaction conditions: 0.1 mmol of styrene, 10 mg of BBT in 1,5 mL of D_2O: CD_3CN (24:1) under the irradiation of a blue LED lamp (460 nm, 0.16 W cm^{-2}), 1 atm. O_2, room temperature. The samples were taken at point 0 and 12h.

❖ Photooxidation of styrene, in water-based biphasic system, under Blue light irradiation and using different CMPs

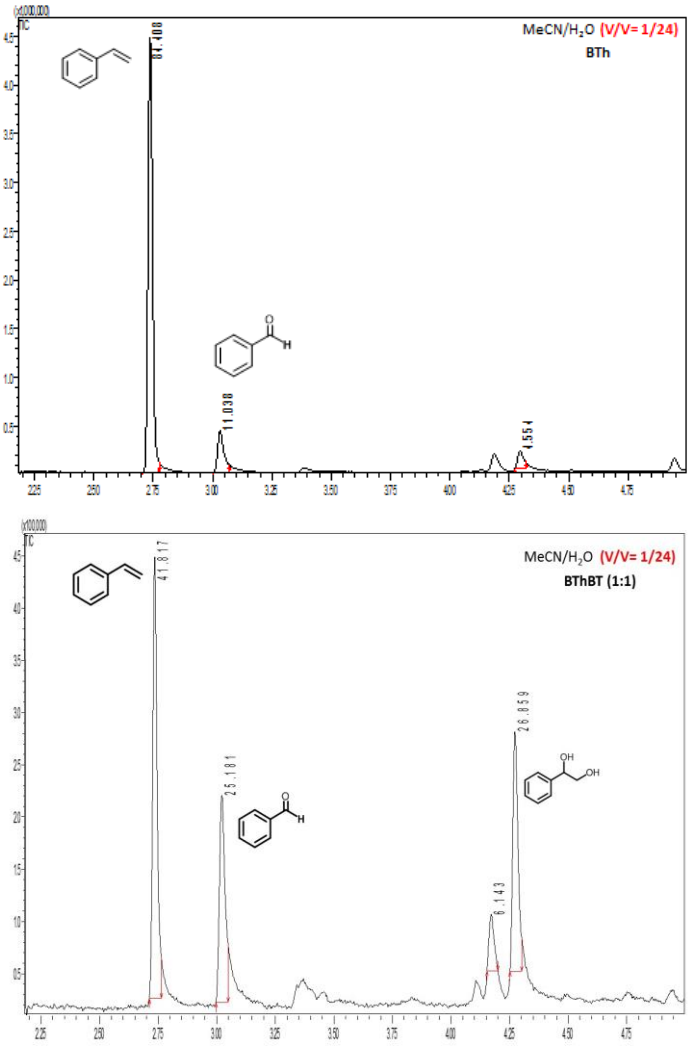

Figure 97. Photooxidation of styrene, in water-based biphasic system, under Blue light irradiation and using different CMPs.

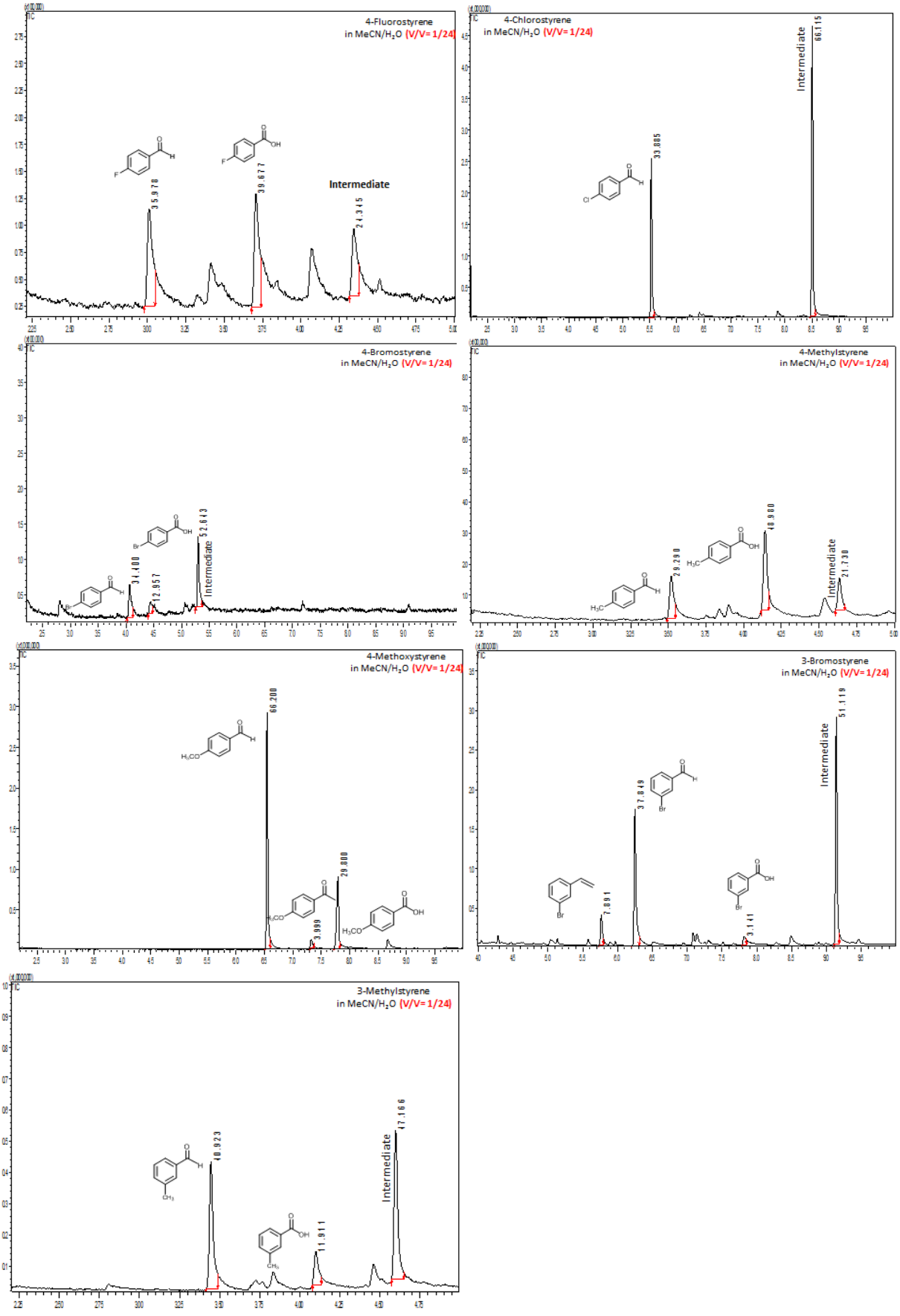

Figure 98. Scope of the aerobic oxidative photocleavage reactions of styrene derivatives.

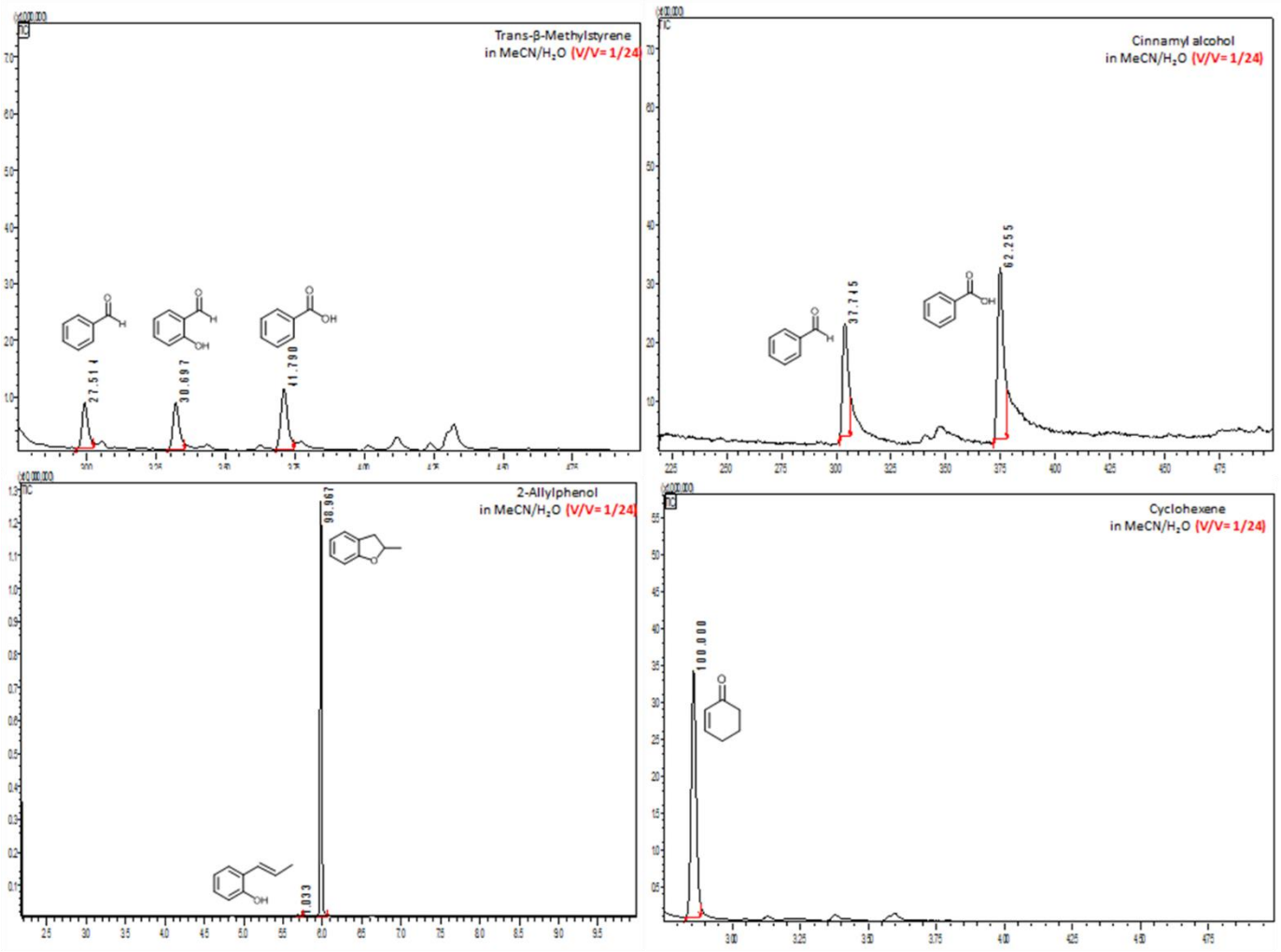

Figure 99. Scope of the aerobic oxidative photocleavage reactions of secondary alkenes.

6.2. Designing covalent triazine framework for photocatalytic epoxidation of styrene with in-situ generated hydrogen peroxide in aqueous medium

6.2.1. Materials

All the chemicals and solvents were purchased from commercially available sources (Sigma Aldrich GmbH, Santa Cruz Biotechnology, Fisher Scientific GmbH, Carl Roth GmbH and TCI Deutschland) and were used as received without further purification except otherwise noted. Styrene was purified by elution through neutral aluminum oxide (50-200 um) and anhydrous $CaCl_2$(w/w, 95/5) for polymerization inhibitor (hydroquinone) and water traces removal before use. The reactions' conversions were monitored by Gas Chromatography Mass Spectrometry (GC-MS).

6.2.2. Characterization methods

Ultraviolet–visible (UV-Vis) absorption and Fourier Transform Infrared spectra (FT-IR) were measured at room temperature on a Perkin Elmer Lambda 100 and on a Varian 1000 FT-IR spectrometers, respectively. Solid-state Cross-Polarization Magic Angle Spinning Carbon-13 and Proton Nuclear Magnetic Resonance (13C, 1H CP MAS NMR) measurements were collected using Bruker Avance II solid state NMR spectrometer operating at 300 MHz Larmor frequency equipped with a standard 4mm magic angle spinning (MAS) double resonance probe head. High resolution Transmission microscope (HR-TEM) and Scanning electron microscope (SEM) images were acquired on a FEI Tecnai F20 with an EDX detector and on a LEO Gemini 1530 (Carl Zeiss AG), with a lens SE detector, respectively. To prepare the samples for the HR-TEM, we proceed to embedding the powders in epoxy resin and sectionning into thin slices by using ultramicrotomy before placing them on Cu grid. The Brunauer-Emmett-Teller (BET) method was utilized to determinate the specific surface area and the pore size distribution on a Tristar II Plus device using the tristar plus II Software (MICROMETRICS). The Brunauer-Emmett-Teller (BET) surface area was calculated based on data points obtained from $0<P/P0<0.3$. The materials were degassed at 120 °C overnight before analysis. The Barrett, Joyner and Halenda (BJH) method was used for calculation of the pore size distribution and the pore volume from the adsorption branches of the isotherms. Inductively coupled plasma atomic emission spectroscopy (ICP-AES) for metal traces quantification was performed on a Jobin-Yvon Activa M spectrometer. Thermal gravimetric analysis (TGA) measurements were carried out on a Mettler Toledo TGA-851 system. The temperature was increased from 25 to 1000 °C (10 °C min^{-1}) under oxygen atmosphere. Electron paramagnetic resonance (EPR) spectroscopy at X-band (~9.4 GHz) was recorded with

a Magnettech MiniScope MS200 benchtop at room temperature (Berlin, Germany). Cyclic voltammetry (CV) measurement was performed using an Autolab PGSTAT204 potentiostat/galvanostat (Metrohm). The electrolyte cell consists of a glassy carbon electrode as the working electrode, a Pt wire as the counter electrode and a Hg/HgCl (in saturated KCl solution) electrode as the reference electrode. An electrolyte solution was prepared in acetonitrile using tetrabutylammonium hexafluorophosphate (Bu4NPF6) as electrolyte (0.1 M). Theoretical calculations were made to estimate the electronic structure and confirm the donor–acceptor pairing within the CTF-cores using the Gaussian 09 program package. The B3LYP functional and the 6-311G (d, p) basis set were used in the calculation. The water contact angle measurements were performed on a Data Physics OCA 35 (Optical Contact Angle) device, with water droplet volume of ca. 5 μl, placed with a motor-driven syringe onto the sample surface.

6.2.3. Synthesis of the CTF-based materials

6.2.3.1. Synthesis of the monomer 2,5-dicyanothiophene (CN-Th-CN)

Potassium ferrocyanide trihydrate ($K_4[Fe(CN)_6]\cdot 3H_2O$, fine powder) was used as the cyanation source. Prior to use, few milligrams of ($K_4[Fe(CN)_6]\cdot 3H_2O$) was dried under vacuum at 80 °C overnight. Then, dried $K_4[Fe(CN)_6]$ (6 mmol, 2.21 g), copper iodide (3 mmol, 0.57 g), and 2,5-dibromothiophene (15 mmol, 3.63 g) and 1-methylimmidazole (5 ml) were placed in a pressure tube under nitrogen. The pressure tube was sealed and heated for 24 h at 140° C. After cooling to r.t., the reaction mixture was washed with H_2O and extracted with CH_2Cl_2 (100 ml x 3). The organic layer was dried over anhydrous sodium sulfate Na_2SO_4, concentrated on a rotary evaporator and a brown oil was obtained. The latter was further purified through silica column chromatography using a mixture of EtOAc/petrolether (1:10) as eluent. The crude product was obtained as colorless needles (yield 22%).

^{1}H NMR (300 MHz, $CDCl_3$) δ (7.63, 2H); ^{13}C NMR (300 MHz, $CDCl_3$) δ136. 93, 116.2, 111.91.

6.2.3.2. Synthesis of the monomer 2,5-bis(4-bromophenyl)thiophene (CN-Ph-Th-Ph-CN)

2,5-dibromothiophene (1g, 4.13 mmol) and 4-Cyanophenylboronic acid pinacol ester (2.3 g, 10 mmol) were dispersed in DME (40 ml) and bubbled with N_2 for 10 min. Then, Pd $(P(Ph)_3)_4$ (477 mg, 5 mol%) and aqueous Na_2CO_3 (2M, 10 ml) were added into the above solution under N_2. The mixture was heated for 24 h at 80 °C under reflux. After cooled down to r.t, the reaction mixture was extracted with DCM (150 ml ×3). The combined organic layer was washed with water, dried over anhydrous $MgSO_4$ and further purified by column

chromatography using dichloromethane as eluent. The material was obtained as yellow crystal (yield 84%).

^{1}H NMR (300 MHz, $CDCl_3$): δ 7.67-7.74 (m, 8H), 7.44 (s, 2H); ^{13}C NMR (300 MHz, $CDCl_3$): δ 144.1, 138.7, 133.7, 127.2, 126.8, 119.5, 112.1

6.2.3.3. Synthesis of the monomer 4,7-bis(4-bromophenyl)benzo[c][1,2,5]thiadiazole (CN-Ph-BT-Ph-CN)

4,7-bis(4,4,5,5-tetramethyl-1,3,2-dioxaborolan-2-yl)benzo[c][1,2,5]thiadiazole (1.0 g, 2.6 mmol) and 4-bromobenzonitrile (1,4 g, 7.7 mmol) were dispersed in 50 ml dioxane. Then, Pd $(P(Ph)_3)_4$ (300 mg, 260 mmol) and aqueous $NaCO_3$ (2 M, 20 ml) were added into the above solution. The mixture was heated under nitrogen for 24 h at 120 °C. The reaction was quenched by addition of Milli Q water (30 ml) and filtered. The collected solid was washed thoroughly with Milli Q water, methanol and dichloromethane, respectively and further purified through silica column using dichloromethane as elute. The crude product was obtained as light yellow powder (yield 72%).

^{1}H NMR (300 MHz, CDCl3): δ 8.12 (d, 4H, ArH), δ 7.87 (d, 4H, ArH),δ 7.84 (s, 2H, ArH).

^{13}C NMR (300 MHz, CDCl3): δ 154.3, 142.1, 133.3, 133.2, 130.7, 129.4, 119.5, 113.

6.2.3.4. Synthesis of mesoporous silica SBA-15

1.3 g pluronic P123 was dispersed in a mixture of 10 ml of Mill-Q water and 40 ml of 2M HCl aqueous solution and left under vigourous stirring for 5 h in an oil bath at 35 °C. Then 2.83 mL of tetraethyl orthosilicate (TEOS) was added dropwise into the solution under continuous stirring for 5 min. The mixture was aged for 24h at 35 °C, after which it was submitted to hydrothermal treatment at 100 °C for another 24 h. The resulting precipitate was collected by centrifugation, washed thoroughly with water and dried overnight. The product was calcinated in air for 4h at 550 °C. The crude product was obtained as white solid powder (m = 738 mg)

6.2.3.5. Synthesis of CTF-based material

The CTF-based material onto mesoporous silica (SBA-15) were obtained via a solvent-free polymerization procedure similar to our previous work. First, 50 mg of the monomer and 100 mg of silica SBA-15 were added to 2 ml of tetrahydrofuran. The mixture was ultra-sonicated under vacuum for at least 2h to give the monomer casted precursor (monomer@SBA-15) and further annealed at 80 °C for 2 h. The resulting powder was then transferred in a small vial and placed into a conical flask, which contained another 0.3 ml of trifilic acid (TfOH),

disposed in different vial. The system was sealed under vacuum and heated up to 100 °C for 24 h to initiate the polymerization. After cooling down to r.t, the mixture was first washed sequentially with an alkaline distilled aqueous ammonia to remove residual TfOH, then with water and acetone before being dried under vacuum overnight. Metal residue analysis by ICP: [Cu] = 0.02 mg / g catalyst

6.2.4. General procedure for photocatalytic oxidation of styrene in aqueous medium

Typically, 0.1 mmol (1 eq) of styrene, 1 mmol (10 eq) of sodium bicarbonate $NaHCO_3$ (after optimization) and 10 mg of photocatalyst were dispersed in 5 ml of distilled water in a glass vial equipped with an oxygen balloon. Subsequently, the suspension was irradiated under blue LED lamp (460 nm, 65 mW cm-2, OSA Opto Light GmbH) for 7 h with different time sampling (t=30 min, 2h, 3h, 5h, 7h). The aliquots were extracted with dichloromethane, dried with magnesium sulfate before being analyzed by Gas Chromatography Mass Spectroscopy (GCMS). For the control experiments, chemical scavengers were added to the reaction suspension in order to highlight the contribution of each element in the reaction mechanism. To do so, chromatograms were collected to evaluate the impact of the scavengers' addition on the reaction conversions and selectivity. For the repeating experiments, the photocatayst was filtrated out and washed three times with water and acetone, then dried under vacuum (80 °C) before being reused for the next repeating cycle.

6.2.5. Tools for mechanistic study

6.2.5.1. Experimental determination of reactive oxygen species (ROS) generated upon irradiation

Electron Paramagnetic Resonance (EPR) technique was employed to investigate the possible generation of reactive oxygen species in water (reaction medium), in the presence of a photoactive material, under light irradiation and an oxygen atmosphere. The spin trap reagents used were 5,5-dimethylpyrroline N-oxide (DMPO) and 2,2,6,6-tetramethylpiperidine (TEMP) to detect superoxide radical ($\mathbf{O_2^{\cdot -}}$) and singlet oxygen ($^1O_2$), respectively.

Experimentally, 3 mg of the photoactive material (1 mg ml-1) were dispersed in a glass vial containing 3 ml of H2O, 0.1 mmol of DMPO (or TEMP) and bubbled with O_2. The suspension was irradiated by a blue LED lamp for 1h (460 nm, 65 mW cm^{-2}). The aliquot was then analyzed. Note that the as-designed CTFs were examined under the same conditions for comparison purposes. The experimental parameters were a modulation amplitude of 0.1 mT, a sweep width of 8 mT and scan numbers of 10.

6.2.5.2. Spectrophotometric determination of hydrogen peroxide in reaction media with peroxidase-catalyzed oxidation of of N,N-diethyl-p-phenylenediamine (DPD)

DPD and POD reagents were freshly prepared and stored in the dark at ~4 °C as follow: 0.1 g of N,N-diethyl-l,4-phenylenediammonium sulfate salt (DPD) were dissolved in 10 mL of 0.05 M H_2SO_4, and 10 mg of peroxidase from horseradish (POD) were dissolved in 10 ml of distilled water. For the experimental protocol, 10 mg of the photocatalyst and styrene reagent (0.1 mmol) were dispersed in 5 ml of water. The mixture was then irradiated under blue LED lamp (460 nm, 65 mW cm−2) and an oxygen atmosphere for 3 h. Next, the photocatalyst was recovered via centrifugation and the water supernatant was subjected to liquid-liquid extraction in order to remove the possible organic products formed under irradiation. The aqueous phase constitutes (S0). 2 ml of S0 were diluted up to 10 ml (S1). We defined a sample test (S2) as a mixture of 3 ml of S1 and 0.33 ml of phosphate-buffered saline PBS (pH=7), in which 20 µl of each DPD and POD reagents were added simultaneously. The resulting solution (S2) was transferred into 1 cm quartz cell to measure the absorbance in this wavelenghth range [400–700 nm].

6.3. Designing a covalent triazine framework for photocatalytic partial oxidation of 5-hydroxymethylfurfural (HMF) to 2,5-diformylfuran (DFF) in water

6.3.1. Materials

5-Dibromothiophene, tetraethylorthosilicate (TEOS), trifluromethanesulfonic acid (TfOH), sodium azide (99%), Pluronic P123 (Average M_n ~5,800 g mol^{-1}), 5,5-dimethyl-1-pyrroline N-oxide DMPO (≥97%,), N,N-Diethyl-p-phenylenediamine sulfate salt DPD (98%), peroxidase from horseradish POD (lyophilized, powder, beige, ~150 U mg^{-1}), 5-hydroxymethyl-2-furancarboxylic acid, (>= 95%) were purchased from Sigma-Aldich Chemie GmbH. Copper Iodide was purchased from Santa Cruz Biotechnology, Inc. 1-methylimmidazole (99%) and 2,5- diformylfuran (>98%), 5-formyl-2-furancarboxylic acid (> 98%) were purchased from TCI Deutschland. Potassium ferrocyanide trihydrate (+ 99%) was purchased from Fischer Scientific GmbH. 5-hydroxymethylfurfural (97%) was purchased from Carl Roth GmbH. Furan-2,5-dicarboxylic acid (> 98%) and 2,2,6,6-tetramethylpiperidine (98%) were purchased from Fisher Scientific GmbH. All chemicals and solvents were used without further purification.

6.3.2. Characterization methods

Ultraviolet–visible (UV-Vis) absorption was measured at room temperature on a Perkin Elmer Lambda 100 spectrophotometer. Fourier transform infrared spectra (FT-IR) were obtained on a Varian 1000 FT-IR spectrometer. Solid-state cross-polarization magic angle spinning carbon-13 and proton nuclear magnetic resonance (^{13}C, ^{1}H CP MAS NMR) measurements were recorded using Bruker Avance II solid state NMR spectrometer operating at 300 MHz Larmor frequency equipped with a standard 4mm magic angle spinning (MAS) double resonance probe head. Liquid ^{1}H NMR and ^{13}C NMR measurements were conducted on Bruker AVANCE 300 system. High resolution transmission electron microscope (HR-TEM) images were performed on a FEI Tecnai F20 with an EDX detector, whereas Scanning electron microscope (SEM) images were acquired on a LEO Gemini 1530 (Carl Zeiss AG), using an in lens SE detector. The Brunauer-Emmett-Teller (BET) method was utilized to determinate the specific surface area and the pore size distribution on an Autosorb 1 using QuadraWin Software (Quantchrome instruments). The BET surface area was calculated based on data points obtained from $0 < P/P_0 < 0.25$ and the non-local density functional theory (NLDFT) equilibrium model was used for calculation of the pore size distribution and the pore volume from the adsorption branches of the isotherms using Quenched Solid Density Functional Theory (QSDFT, N_2, assuming carbon adsorbent with slit pores). Inductively coupled plasma atomic

emission spectroscopy (ICP-AES) was performed on a Jobin-Yvon Activa M spectrometer. Electron paramagnetic resonance (EPR) spectroscopy at X-band (~9.4 GHz) was performed using a Magnettech (Berlin, Germany) MiniScope MS200 benchtop at room temperature. Cyclic voltammetry (CV) measurement was performed using an Autolab PGSTAT204 potentiostat/galvanostat (Metrohm). Glassy carbon electrode drop-casted with the polymer as the working electrode, Pt wire as the counter electrode, Hg/HgCl (in saturated KCl solution) electrode as the reference electrode, Bu_4NPF_6 (0.1 M in acetonitrile) was used as electrolyte. The water contact angle measurement was recorded by Data Physics OCA 35 (Optical Contact Angle) device, with water droplet volume of ca. 5 μL, placed with a motor-driven syringe onto the sample surface.

6.3.3. Synthesis of CTF-Th@SBA-15

6.3.3.1. Synthesis of the monomer 2,5-dicyanothiophene (DCT)

2,5-Dicyanothiophene (DCT) was synthesized according to the reported literature. First, Potassium ferrocyanide trihydrate ($K_4[Fe(CN)_6]\cdot 3H_2O$, fine powder) was dried under vacuum at 80 °C overnight. Then, 6 mmol (2.21 g) dry $K_4[Fe(CN)_6]$, 3 mmol (0.57 g) copper iodide, and 15 mmol 2,5-dibromothiophene (3.63 g), 5 ml 1-methylimmidazole were placed in a pressure tube under argon. The pressure tube is sealed and heated for 24 h at 140° C. After cooling to r.t., the reaction mixture was washed with H_2O and CH_2Cl_2 (3 times) and the organic phase is dried over sodium sulfate Na_2SO_4, concentrated under reduced pressure on a rotary evaporator. The crude product was obtained as a brown oil and was further subjected to column chromatography (EtOAc/petrolether (1:10)). Finally, the material was obtained as colorless needles (yield 22%). ^{1}H NMR (300 MHz, $CDCl_3$) δ (7.63, 2H); ^{13}C NMR (300 MHz, $CDCl_3$) δ136. 93, 116.2, 111.91.

6.3.3.2. Synthesis of mesoporous silica SBA-15

Silica SBA-15 was synthesized according to the reported literature. Simply, 4.0 g pluronic P123, 30 mL of Mill-Q water and 120 mL of 2M HCl aqueous solution were mixed together and kept under stirring at 35 °C for 12 h. Then 9.1 mL of TEOS was added dropwise into the solution under continuous stirring. The mixture was left for 24 h at 35 °C, and then hydrothermally heated to 100 °C for another 24 h. the resulting precipitate was separated by centrifugation, washed with water and dried overnight. The product was obtained as white solid powder after being calcined in air for 4 h at 550 °C.

6.3.3.3. Synthesis of CTF-Th@SBA-15

The CTF-Th@SBA-15 was obtained according to the solid-phase polymerization method similar to our previous work. Briefly, 200 mg of silica SBA-15 and 100 mg of the monomer (DCT) were dispersed in 2 mL of tetrahydrofuran. The mixture was ultra-sonicated under vacuum for at least 2h to give the monomer casted precursor DCT@SBA-15 followed by annealing at 80 °C for 2 h. The precursor was then transferred into a conical flask in the presence of 0.3 mL TfOH containing vial. The conical flask was sealed under nitrogen atmosphere and heated up to 100 °C for 24 h. After cooling down to room temperature, the product was dispersed into an alkaline distilled aqueous ammonia (pH = 8 to 9) to remove TfOH traces. The sample was further washed with water and acetone and dried under vacuum overnight. CTF-Th@SBA-15 was obtained as yellow powder. Metal residue analysis by ICP: [Cu] = 0.02 mg / $g_{catalyst}$.

6.3.4. General procedure for photocatalytic oxidation of 5- hydromethylfurfural in aqueous medium

Typically, a mixture of 5-hydromethylfurfural (0.1 mmol), CTF-Th@SBA-15 (10 mg) and distilled water (10 ml) were added in a glass vial equipped with an oxygen balloon. Subsequently, the suspension was irradiated under blue LED lamp (460 nm, 65 $mWcm^{-2}$, OSA Opto Light GmbH) for 30 h with different time sampling (*t* = 2 h, 4 h, 18 h, 24 h, 30 h). The conversion was estimated by Proton nuclear magnetic resonance spectroscopy (^{1}H NMR) with 64 scans acquired. Calculations were obtained from the integration of the C**H**O signal of the product DFF (9.86 ppm, **1H**, s) relative to the 1H-equivalent signal of C**H$_2$**OH (4.73 ppm, **2H**, s) or the C**H**O signal (9.60 ppm, **1H**, s) from the substrate HMF based on the molar ratio formula.

For **the work-up procedure**, the solution and the solid photocatalyst were separated by centrifugation and the supernatant was extracted with deuterated chloroform $CDCl_3$. This procedure was necessary because DFF is only slightly soluble in water and can precipitate in the reaction medium or deposit on the surface of the photocatalyst. To overcome this challenge, few drops of $CDCl_3$ were added to the residual solid photocatalyst. Through agitation, the eventual deposited/accumulated DFF particles on the surface of the photocatalyst would migrate into the liquid phase, which can be further separated from the solid catalyst through filtration (extraction solid-liquid).

For **the control experiments**, specific additives (chemical scavengers) were added to the reaction suspension in order to highlight the contribution of each element in the reaction

mechanism. ^{1}H-NMR samples were then collected and measured to evaluate the impact of the scavengers' addition on the reaction conversions.

For **the repeating experiments**, the photocatalyst was filtrated out using fritted glass filter (porosity 3) under vacuum and washed several times with water (3* 10 ml) and acetone (3* 10 ml), then dried under vacuum (80 °C). Fresh photocatalyst was added to compensate the weight loss (~10-20%) during the recovery process, before being reused for the next repeating cycle.

6.3.5. Experimental determination of reactive oxygen species (ROS) produced upon irradiation

The reactive oxygen species susceptible to be generated by the photocatalyst CTF-Th@SBA-15 in the aqueous reaction medium, upon light irradiation and an oxygen atmosphere, was investigated using the electron paramagnetic resonance (EPR) technique employing spin trap agents. The trap reagents, including 5,5-dimethylpyrroline N-oxide (DMPO) and 2,2,6,6-tetramethylpiperidine (TEMP), were used for the detection of superoxide radical ($O_2^{\cdot-}$) and singlet oxygen ($^1O_2$), respectively, as shown in the following reactions:

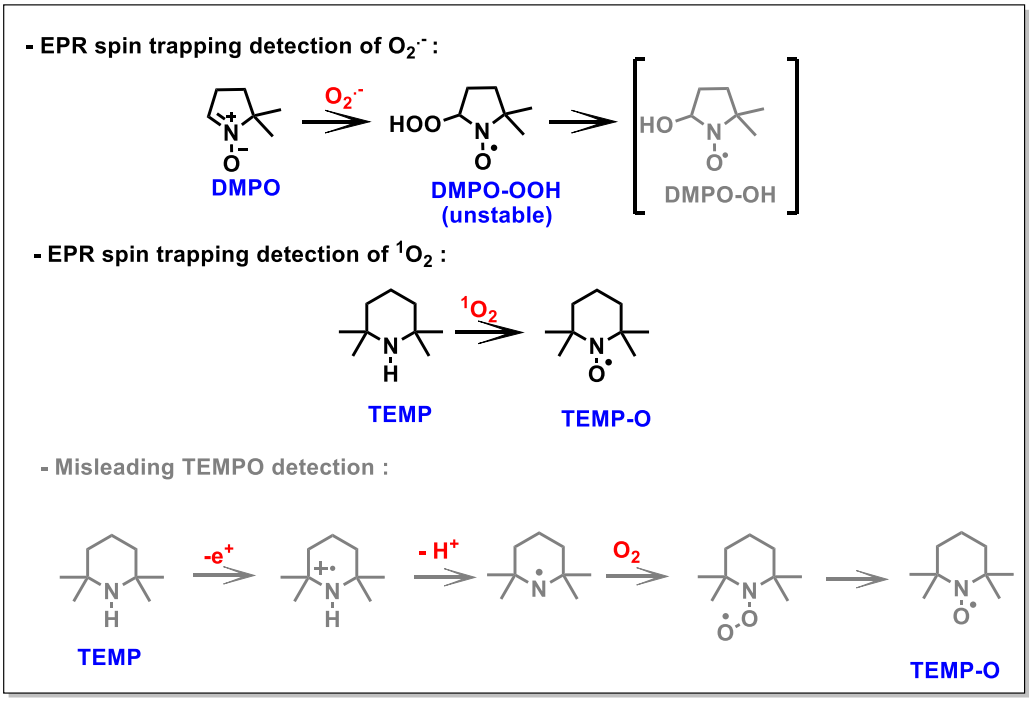

For the experimental protocol, 3 mg of CTF-Th@SBA-15 (1mg ml^{-1}), 0.1 mmol of TEMP (or DMPO for superoxide trapping) were added to a glass vial containing 3 ml of H_2O and equipped with an oxygen balloon. Then, the suspension was subjected to blue LED lamp (460 nm, 0.065 Wcm^{-2}) for 2 h. Next, the photocatalyst were filtered out and the EPR of the fresh filtrate sample was measured immediately. Note that the sample volume was always large

enough to fill the complete resonator volume in the probehead and was kept constant. Typical experimental parameters were a modulation amplitude of 0.1 mT and a sweep width of 8 and 10 mT. Gain and microwave attenuation were kept constant for TEMP and DMPO respectively. Blank experiments were carried out to discard the generation of ROS under dark and in a catalyst-free environment.

6.3.6. Experimental determination of hydrogen peroxide H_2O_2 by the peroxidase (POD) catalyzed oxidation of N,N-diethyl-p-phenylenediamine (DPD)

DPD reagent: 0.1 g of N,N-diethyl-l,4-phenylenediammonium sulfate salt (DPD) were dissolved in 10 mL of 0.05 M H_2SO_4 and stored in the dark at ~4 °C.

POD reagent: l0 mg of peroxidase from horseradish (POD) were dissolved in 10 ml of distilled water and stored in the dark at ~4 °C.

Procedure:

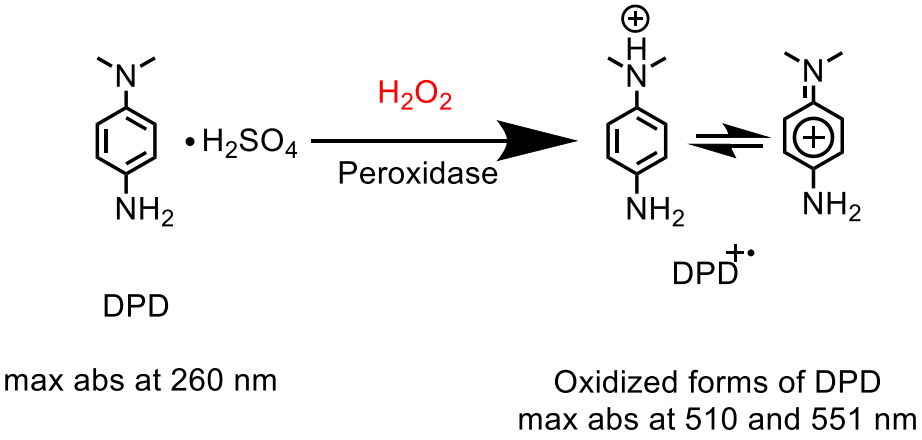

10 mg of CTF-Th@SBA-15 and HMF reagent (0.1 mmol) were dispersed in 10 mL of water. The mixture was kept with oxygen bubbling under blue light irradiation (460 nm, 0.065 W cm^{-2}) at room temperature overnight. Once stopped, CTF-Th@SBA-15 was recovered via centrifuge and the supernatant (reaction medium: water) was extracted with dichloromethane DCM to remove the organic compounds **(S_0)**. 2 ml of the aqueous solution **(S_0)** was taken out and diluted up to 10 mL by adding 8 mL of distilled water **(S_1)**. 3 mL of **S_1** was added together with 0.33 ml of phosphate-buffered saline PBS (pH=7) into a vessel, and used as the test sample **(S_2)**. Then 20 µL of freshly prepared DPD reagent solution and 20 µL of freshly prepared POD reagent solution were added in rapid succession to **S_2**. The solution **S_2** was then transferred into the photometric cell to measure the absorption spectrum from 400 nm-700 nm. The same procedure is repeated without the presence of CTF-Th@SBA-15.

6.3.7. Photocatalytic performance and ^{1}H-NMR spectra

HMF is a versatile and highly reactive molecule that can be converted into various furan –based compounds. Its structure contains a furan ring, an aldehyde functional group and a hydroxymethyl group and can be upgraded by selective redox reactions, to 5-(hydroxymethyl)furan-2-carboxylic acid (HMFCA), 2,5-diformylfuran (DFF), 5-formylfuran-2-carboxylic acid (FFCA), furan-2,5-dicarboxylic acid (FDCA) as shown in the Scheme 3.

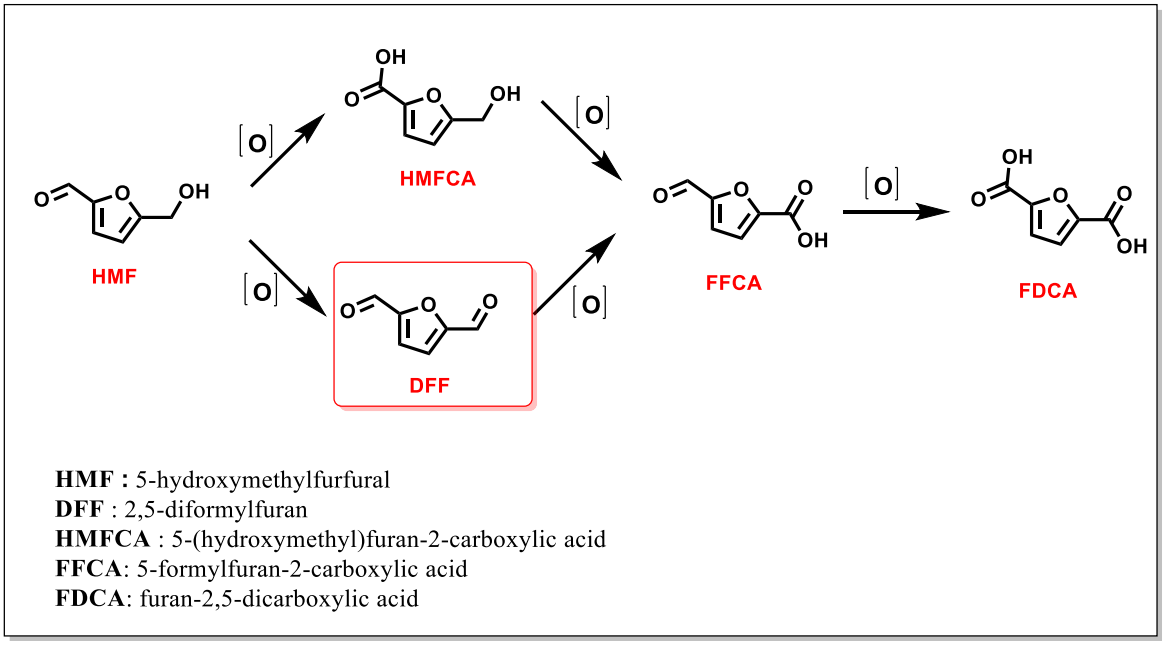

Scheme 3. Catalytic transformation of 5-hydroxymethylfurfural into highly valuable furan-derivatives.

Although herein we focus on the photocatalytic partial oxidation of HMF to DFF, we should not neglect the possible formation of other oxidized products of HMF. Thus, we performed ^{1}H-NMR spectroscopy of the so-called standards and compared them to the results of the current study (**Figure 100**)

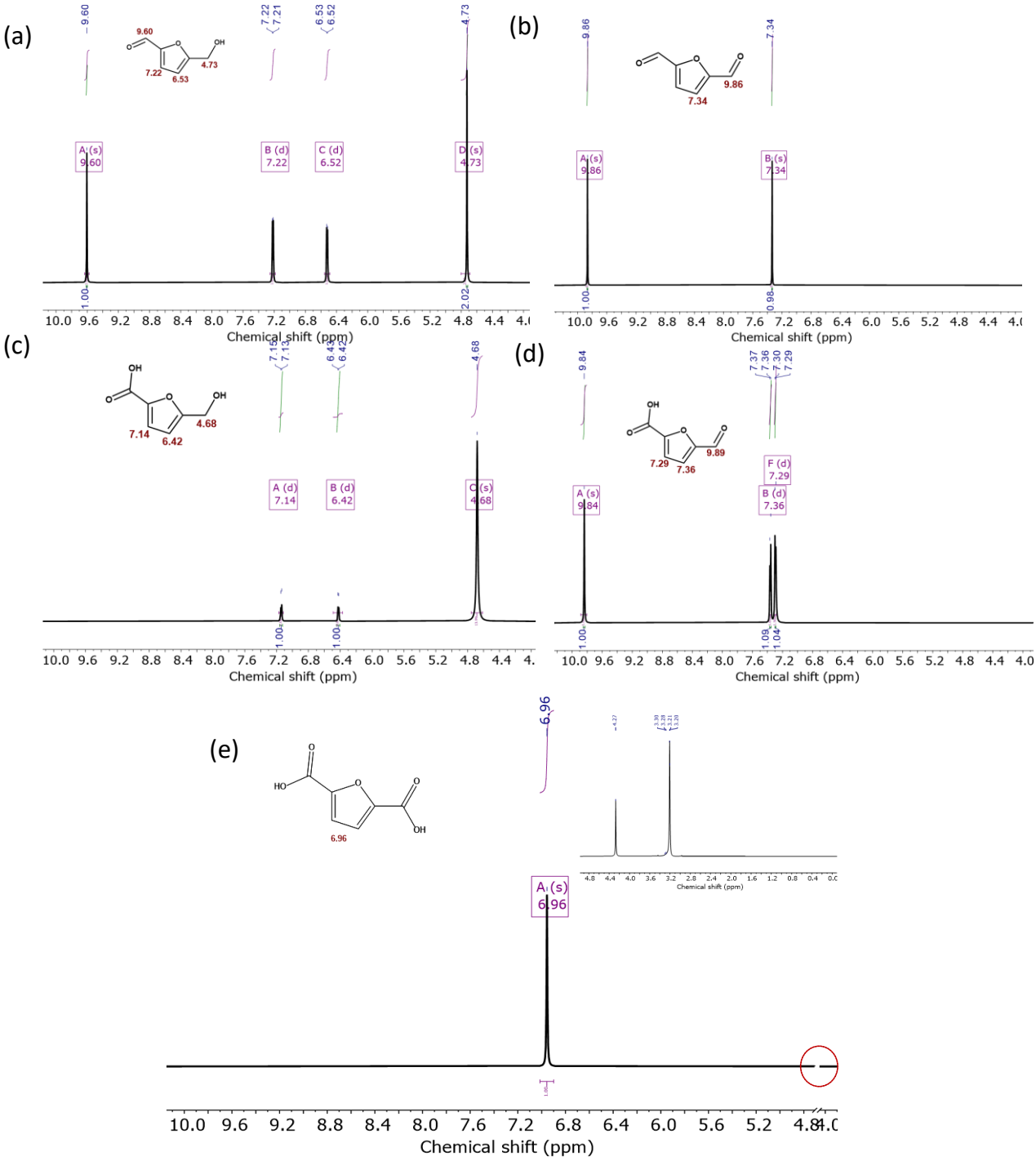

Figure 100. ^{1}H- NMR spectra of pure commercially available (a) HMF, (b) DFF, (c) HMFCA, (d) FFCA and (e) FDCA[5] in $CDCl_3$. (δ ($CHCl_3$) = 7.26 ppm, not shown in the spectrum).

[5]For comparison purpose, the measurement was recorded in $CDCl_3$ despite the slight solubility of FDCA in $CDCl_3$. To overcome this issue, FDCA was dissolved in a little volume of methanol prior to the measurement. Inset: ^{1}H-NMR spectrum of methanol in $CDCl_3$.

6.4. Designing covalent triazine framework for the degradation of organic dyes in aqueous and solid media

6.4.1. Materials

5-dibromothiophene, copper cyanide, tetraethylorthosilicate (TEOS), trifluromethanesulfonic acid (TfOH), ferric chloride hexahydrate ($FeCl_3$, $6H_2O$), hydrochloric acid (HCl, 37%), copper (II) chloride (97%), ammonium oxalate (99%), sodium azide (99%), rhodamine B (99%), orange G and methylene blue (≥ 82%) and all other solvents were purchased from Sigma-Aldich.

All chemicals and solvents were used without further purification.

6.4.2. Characterization methods

Ultraviolet–visible (UV-Vis) absorption was performed at room temperature on a Perkin Elmer Lambda 100 spectrophotometer. Fourier Transform Infrared spectra (FT-IR) were obtained on a Varian 1000 FT-IR spectrometer. Solid-state Cross-Polarization Magic Angle Spinning Carbon-13 Nuclear Magnetic Resonance (^{13}C CP MAS NMR) measurements were carried out using Bruker Avance II solid state NMR spectrometer operating at 300 MHz Larmor frequency equipped with a standard 4mm magic angle spinning (MAS) double resonance probe head. The nitrogen sorption data were measured to determine the surface area and the pore size distribution; the data were recorded at 77.3 K on an Autosorb 1 using QuadraWin Software (Quantchrome instruments). The samples were degassed at 120 ^oC overnight under high vacuum before analysis. High resolution Transmission electron microscope (HR-TEM) images were performed on a FEI Tecnai F20 with an EDX detector, whereas Scanning electron microscope (SEM) images were acquired on a LEO Gemini 1530 (Carl Zeiss AG), using an in lens SE detector. Cyclic voltammetry (CV) measurement was performed using an Autolab PGSTAT204 potentiostat/galvanostat (Metrohm). Glassy carbon electrode drop-casted with the polymer as the working electrode, Pt wire as the counter electrode, Hg/HgCl (in saturated KCl solution) electrode as the reference electrode, Bu_4NPF_6 (0.1 M in acetonitrile) was used as electrolyte. The water contact angle measurements were recorded by Data Physics OCA 35 (Optical Contact Angle) device, with water droplet volume of ca. 5 μL, placed with a motor-driven syringe onto the sample surface.

6.4.3. Synthesis of a CTF based photocatalyst

6.4.3.1. Synthesis of 2,5-dicyanothiophene (DCT)

2,5-dicyanothiophene was synthesized according to the reported literature.[46] Typically, 2,5-dibromothiophene (2.0 g, 8.3 mmol, 1 eq), CuCN (2.2 g, 24.6 mmol, 3 eq) and N,N-dimethylmethanamide (10 mL) were mixed in a 50 ml flash and heated at reflux at 140 ºC under an inert atmosphere of nitrogen for 12 h. After cooling down to 60 ºC, $FeCl_3 \cdot 6H_2O$ (13 g) in 2M HCl (30 mL) was added and then mixed vigorously for 4 h. The reaction mixture was then cooled down to room temperature and extracted with dichloromethane (100 mL × 3). The combined organic phase was washed with diluted HCl and Milli Q water, dried with anhydrous Na_2SO_4 and concentrated under vacuum. The crude product was obtained as colorless needles (yield 54%) after being purified through a silica column using hexane: dichloromethane (1:1) as eluent. ^{13}C NMR (300 MHz, $CDCl_3$) δ 136. 93, 116.1, 111.91. **(Figure 101).**

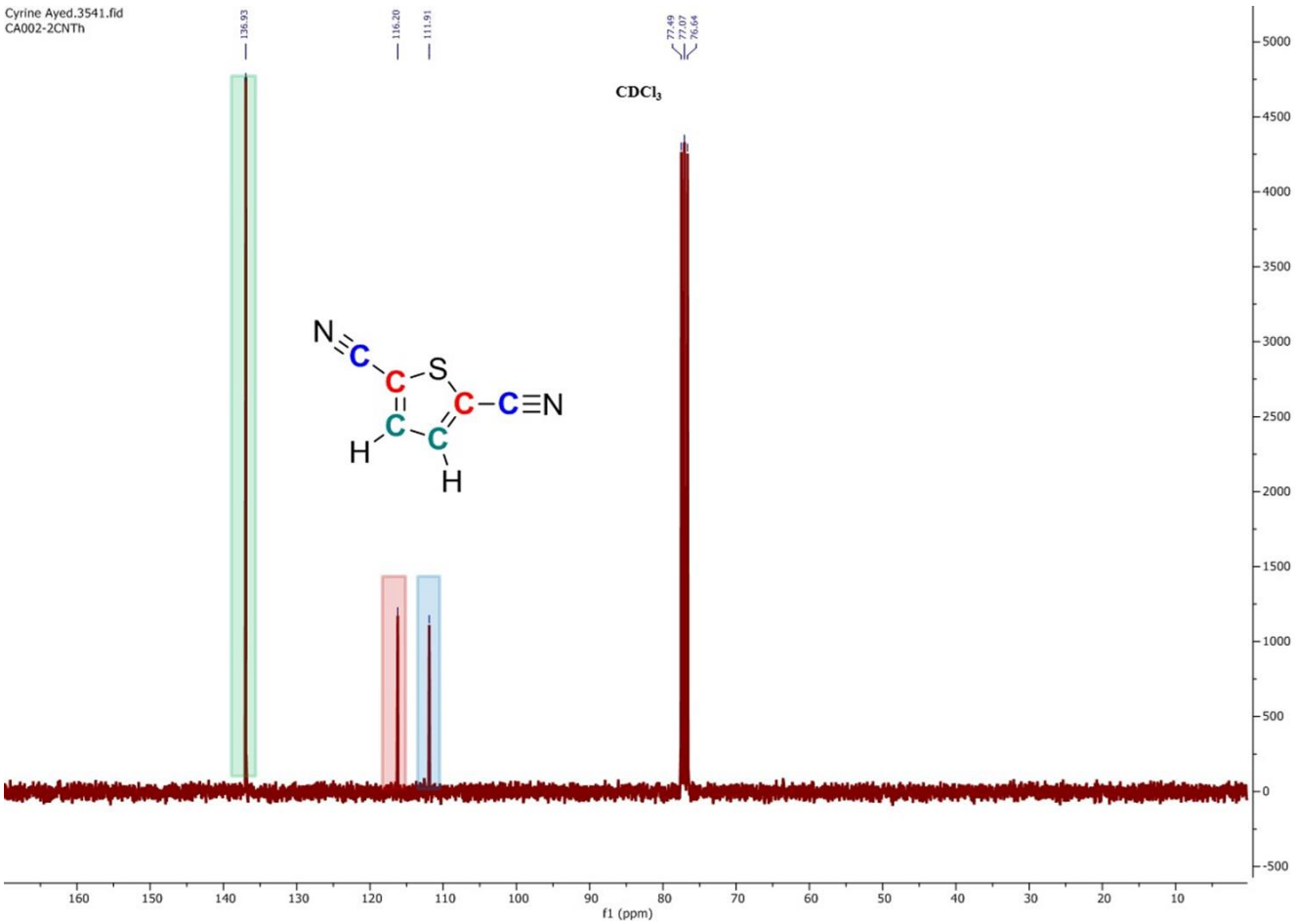

Figure 101. ^{13}C NMR spectra of 2,5-dicyanothiophene (DCT) in $CDCl_3$.

6.4.3.1. Synthesis of mesoporous silica SBA-15

Silica SBA-15 was synthesized according to the reported literature [46]. Simply, a mixture of 4.0 g pluronic P123, 30 mL of Mill-Q water and 120 mL of 2M HCl aqueous solution was stirred at 35 °C overnight. Then 9.1 mL of TEOS was slowly added into the solution under vigorous stirring. The mixture was first kept at 35 °C for 24 h under static conditions, and then heated to 100 °C for another 24 h. After collection by centrifugation; the resulting precipitate was washed with water, dried and calcined at 550 °C in air for 4 h. The product was obtained as white solid powder.

6.4.3.4 Fabrication of CTF-Th@SBA-15

The CTF-Th@SBA-15 was obtained via TfOH vapor-assisted solid phase reaction routine according to our previous work [398]. Typically, 200 mg vacuum-dried silica SBA-15 and 100 mg of DCT were first dispersed in 2 ml of tetrahydrofuran, then stirred for 2 h under vacuum. The resulting mixture was concentrated under vacuum to give the monomer casted precursor DCT/SBA-15 and further annealed at 80 °C for 2 h. The precursor was then transferred into a conical flask, in which there was another vial with 0.3 mL TfOH. The conical flask was kept under an inert atmosphere of nitrogen, sealed and heated up to 100 °C in an oven for 24 h. After cooling down to room temperature, the product was submerged in alkaline distilled aqueous ammonia (pH = 8 to 9) to remove the residual TfOH. Further purification was conducted by washing the sample with water and small volume of acetone, and then dried at 80 °C under vacuum overnight. The solid catalyst was obtained as a yellow powder.

6.4.4. General procedure for photocatalytic degradation of organic dyes in aqueous and solid media

The photocatalytic performance of CTF-Th@SBA-15 was first tested for the degradation of Rhodamine B (RhB) in **aqueous solution**. A mixture of CTF-Th@SBA-15 photocatalyst dispersed in water (0.3 mg mL^{-1}) and RhB solution (50 mg/L, 10 mL) was stirred under dark condition for 60 min in order to reach the adsorption/desorption equilibrium between the catalyst and the solution. Then, the mixture was irradiated with blue LED lamp (λ = 460 nm, 0.16 W/cm^2) during different time intervals in air. Changes in RhB concentration were monitored using UV-vis spectroscopy. A control experiment with the reaction mixture under N_2, therefore, without oxygen in the reaction, was also performed. The reaction was also tested using pure CTF-Th (without SBA-15) as photocatalyst and under the same conditions. The radical scavenger experiments were performed using ammonium oxalate, copper chloride,

sodium azide and catalase, in excess (0.05 mmol L^{-1}). Each of the radical scavengers was added to a mixture of CTF-Th@SBA-15 (3 mg, 10 mL) and RhB solution (50 mg L^{-1}).

For the **solid-state photodegradation experiment**, the procedure is described as below: 25 mg of CTF-Th@SBA-15 were added to an aqueous solution of RhB (50 mg L^{-1}, 10 mL) and vigorously stirred for at least 1h, until the dye particles were completely adsorbed on the surface of the catalyst. Then, the dispersion was filtrated under vacuum and the resulting solid was simply collected. Afterwards, the dried dye-adsorbed catalyst was casted on a flat surface of tape to form a thin layer of powder. The blue LED lamp was also used continuously in this experiment by placing it 1 cm ahead from the powder layer. The dye degradation was monitored by the measurement of the UV-visible spectra after certain time intervals. The reaction is considered as finished when the catalyst reacquired its initial color (yellow), due to the complete degradation of the dye particles. Note that two more organic dyes such as methylene blue (MB) and orange G (OrG) were tested following the same procedure described above.

6.5. Designing conjugated microporous polymers with immobilized TiO_2 nanoparticles for enhanced visible light photocatalysis

6.5.1. Materials

Titanium isopropoxide (97%), Copper (I) Iodide (99%), tetrakis (triphenylphosphine) Palladium (0) (99%), *p*-benzoquinone (98%), sodium azide (99%), potassium iodide (> 99.9%), triethylamine (99%), 4-fluorobenzylamine (97%), 4-chlorobenzylamine (98%), 4-methoxybenzylamine (98%), 2,4-dimethoxybenzylamine (98%), 4-methoxythioanisole(97%), 4-nitrothioanisole (96%), were purchased from Sigma Aldrich. Ethylacetoacetate (98%), benzylamine were purchased from FLUKA. Nitric Acid (72%) was purchased from ReAgent Chemicals. 1,3,5-Triethynylbenzene (>98%), thioanisole (99%), 4-fluorothioanisole (97%), ethylphenylsulfide (97%), allylphenyl sulfide (97%) were purchased from Alfa Aesar. 4,7-Dibromo-2,1,3-benzothiadiazole (97%), (Br-BT) was purchased from COMBI BLOCKS. 4-Methylbenzylamine (98%), isopropanol (99.5%), N,N-dimethylformamide anhydrous (99.8%) were purchased from Acros organics. Acetonitrile was purchased from Fischer Chemical. All chemicals and solvents were used as received, without further purification unless otherwise specified.

6.5.2. Characterization methods

X-ray diffraction (XRD) patterns were carried out using a Philips PW1050 diffractometer with CuKa radiation at k = 1.5418 Å. The phases were identified according to the JCPDS cards references. UV/vis absorption spectra were measured using a Perkin-Elmer Lambda 25 UV-Vis spectrometer. FTIR spectra were obtained using a FTIR spectrophotometer TENSOR II Bruker equipped with platinum ATR. Solid state ^{13}C CP/MAS NMR measurements were performed at 300 MHz Lamor Frequency equipped with a standard 4mm magic angle spinning MAS double resonance probe head. Liquid-state NMR spectra were taken on a Bruker AVANCE 300 Spectrometer. TGA measurements were carried out on a Mettler Toledo TGA-851 system. The temperature was increased from 25 °C to 800 °C (10 °C min^{-1}) under nitrogen atmosphere. Electron paramagnetic resonance (EPR) was operated using a Magnettech MS 200 spectrometer. The nitrogen sorption data were measured to determine the surface area and the pore size distribution, the data were recorded at 77.3 K on an Autosorb 1 using the QuadraWin Software (Quantchrome instruments). CV measurements were done using an Autolab Potentiostat PGSTAT204 (Metrohm). A glassy carbon working electrode (WE), a Pt counter electrode (CE) and a SCE reference electrode (RE) were used. The SEM images were collected

by a LEO Gemini 1530 (Carl Zeiss AG, Germany) with an in lens SE detector, whereas TEM images were captured with a JEM 1400 (JEOL, USA).

6.5.3. Synthesis of TiO_2 nanoparticles

The synthesis of the titanium dioxide was carried out following a Sol-Gel method using titanium isopropoxide as precursor, isopropanol as solvent and ethylacetylacetate as complexing agent. The reaction mixture was stirred for 30 min. Then, a homogeneous gel was obtained after the addition of HNO_3 (0.1 M) which corresponded to the H_2O/Ti molar ratio = 10 according to the previous work.[389] The obtained gel was dried in an autoclave under supercritical conditions of isopropanol (T = 235 °C, P = 48 bar) to obtain an aerogel. Finally, the solid was calcined under oxygen at 500 °C for 3h.

6.5.4. Synthesis of the conjugated microporous polymer BBT and the hybrid materials with immobilized TiO_2 nanoparticles

The conjugated microporous polymer (CMP) BBT was synthesized according to the reported procedure.[38] The hybrid materials were obtained by impregnation of the TiO_2 nanoparticles on the CMP in a one pot synthesis. Typically, a defined amount of TiO_2 was dispersed in 10 mL DMF and stirred in an ultrasonic bath for 15 min. Then, the organic precursors, the cross-linker 1,3,5-triethynylbenzene (150 mg, 1 mmol, 1 equiv.), the co-monomer 4,7-dibromo-2,1,3-benzothiadiazole (294 mg, 1 mmol,1 equiv.), copper (I) Iodide (5.7 mg, 0.03 mmol, 0.03 equiv.), tetrakis(triphenylphosphine) palladium(0) (35 mg, 0.03 mmol, 0.03 equiv.) and 10 mL of trimethylamine were added to the TiO_2 dispersion and the reaction mixture was degassed for 10 min. The BBT/TiO_2 ratio in the hybrid materials was defined as described below. Then, the reaction mixture was stirred at 80 °C for 24h under nitrogen atmosphere. After cooling, the precipitated powder was washed with methanol, acetone and water several times. The crude product was then extracted in a Soxhlet extractor for 24h using a mixture of dichloromethane and methanol. Finally, the product was dried overnight at 60 °C under vacuum. In this work, seven BBT@TiO_2 hybrid materials were synthesized. For example, the sample BBT@TiO_2-0.2 refers to the hybrid material containing 20 wt.% of the co-monomers with respect to the total weight of the co-monomers and the TiO_2 nanoparticles. The rest of the hybrid materials are referenced as follows: BBT@TiO_2-0.4, BBT@TiO_2-0.5, BBT@TiO_2- 0.6, BBT@TiO_2-0.7, BBT@TiO_2- 0.8, BBT@TiO_2- 0.9.

6.5.5. General procedure for the photocatalytic oxidative coupling of benzylamines

1 mmol of benzylamine or its derivatives, 5 mg of the photocatalyst are added into 3 mL of acetonitrile in a glass vial equipped with an oxygen balloon. A blue LED lamp (460 nm, 0.16 Wcm^{-2}) was used as the light source. The reaction mixture was stirred at room temperature and under irradiation for 6h. The conversion was determined via ^{1}H NMR spectroscopy. For the monitoring experiments, samples were taken in defined time intervals. For the repeating experiments, the photocatalyst was filtrated and washed several times with methanol, CH_2Cl_2 and acetone, then dried under vacuum before being reused for the next cycles.

6.5.6. General procedure for the selective oxidation of organic sulfides

1 mmol of thioanisole or its derivatives, 5 mg of the photocatalyst were added into 3 mL of acetonitrile in a glass vial equipped with an oxygen balloon. A blue LED lamp (460 nm, 0.16 Wcm^{-2}) was used as the light source. The reaction mixture was stirred at room temperature and under irradiation for 6h. The conversion was determined via ^{1}H NMR spectroscopy.

7. Overall summary and outlook

In this thesis, conjugated porous polymers, with particular focus on conjugated microporous polymers (CMPs) and covalent triazine frameworks (CTFs), were developed as efficient heterogeneous visible-light active photocatalysts for challenging photoredox reactions under green reaction conditions. In particular, visible light-driven organic transformations, including the conversion of basic, abundant and cheap chemicals into value-added compounds, were examined in depth. Various chemical and photophysical characterization methods were performed for a deeper understanding of the physical, structural, textural, opto-electronic, and catalytic properties of the designed photocatalysts. The kinetics of the photocatalytic reactions, with eventual identification of reactive intermediates, were investigated to reveal the role of reactive species in most photo-induced redox reactions and propose plausible mechanisms.

First, a structural design strategy of conjugated microporous polymers (CMPs) as a class of metal-free, heterogeneous, stable and reusable photocatalyst for the visible light-promoted oxidative cleavage of the C=C bonds of alkenes, notably styrene, was presented. Different electron donor and acceptor combinations in the CMP backbone structure were studied. Then, the structure influence of the as synthesized CMPs on their optical and electrochemical properties were systematically investigated in order to reveal the structure and performance relation in the photocatalytic C=C double bond cleavage reaction of styrene. The CMP (BBT) with the specific electron donor acceptor combination containing benzothiazole (BT) as strong electron withdrawing and phenyl (Ph) as weak electron donating unit was found to be the most efficient photocatalyst, leading to almost quantitative conversion (ca. 91%) and high selectivity toward benzaldehyde (ca. 86%) in water-acetonitrile mixture (24:1 (v/v)). The higher photocatalytic efficiency of BBT could be explained by the most efficient photogenerated charge separation within the polymer network. However, it is noteworthy to mention that the reaction gave a poor conversion of 13% in pure water, which is probably due to the hydrophobic nature of BBT, being weakly dispersible in water.

To promote photocatalytic reactions in pure aqueous environment, a new design strategy of CPPs was proposed: a series of mesoporous covalent triazine frameworks (CTFs), with varied electron donor/acceptor combinations, were prepared using hydrophilic mesoporous silica (SBA-15) as support. This latter endowed the CTFs with high surface areas and mesoporous structure. Moreover, the resulting materials showed water contact angles lower than 90 °, which confirmed their gained hydrophilic features, ensuring an enhanced

dispersibility into water. These CTFs were then examined as heterogeneous photocatalysts for the photo-oxidation reaction of styrene under visible-light irradiation, using pure water as reaction media, sodium bicarbonate ($NaHCO_3$) as promoter and molecular oxygen as oxidant. Two main products were obtained in various ratios: benzaldehyde and styrene oxide. This latter is indeed of particular interest due to its versatile utilization in the preparation of petrochemicals, pharmaceuticals and fine chemicals. The structure of CTFs on the photocatalytic efficiency as well as the selectivity toward the target products were also explored in depth: it was found out that the CTF with the most extended π- conjugated acceptor/donor/acceptor system, bearing benzothiazole (BT) as electron acceptor, phenyl (Ph) as electron donor and triazine (Tr) as electron acceptor, exhibited the highest styrene oxide selectivity (> 50%), among the polymer series. This might be due to the extension of conjugation within the polymer backbone, which in turn, expands the visible-light responsivity, improves the intermolecular electron delocalization, enhance charge transfer efficiency and suppresses the rapid recombination of the hole−electron pairs. In contrast, a benzothiadiazole based-CMP (BBT), which in the first project, proved its efficiency in oxidizing styrene to benzaldehyde, has shown much lower styrene oxide selectivity (ca. 16%) in the current study. This further highlighted the superior photocatalytic performance of the CTF based material. The mechanistic study, based on advanced analytical tools, was conducted, revealing the entities responsible for the oxidation reaction and particularly the epoxidation process.

To exploit further challenging light-driven organic transformations, a thiophene-containing CTF (CTF-Th) was found to be an excellent candidate given its strong oxidation potential. Moreover, the alternation between the thiophene and triazine moieties, as electron donor / acceptor units, respectively, within the polymer backbone, was expected to promote the π-electron delocalization over the molecular skeleton, and enlarge the visible light absorbance and charge separation. Similarly to the previous project, hydrophilic SBA-15 was used as support to impart CTF-Th with certain hydrophilicity, favoring the catalytic reaction in pure water. The photocatalytic performance of CTF-Th@SBA-15 was then demonstrated through the photocatalytic partial oxidation of biomass derived- 5-hydroxymethylfurfural (HMF) to 2,5-diformylfuran (DFF) in pure water with moderate conversion (ca. 57%) and high selectivity (ca. 99%). A detailed mechanistic study on the reaction including two pathways was discussed. Moreover, the reusability and stability of the catalyst were investigated.

Beside its great potential in organic synthesis, the application field of CTF-Th@SBA-15 was further extended to environmental applications such as the visible-light degradation of

organic contaminants in aqueous media. Indeed, CTF-Th@SBA-15 exhibited efficient photocatalytic performance for complete and rapid Rhodamine B (RhB) degradation in aqueous medium. Interestingly, RhB molecules were adsorbed on the CTF-Th@SBA-15 due to the excellent adsorptive power of SBA-15 and the degradation tests were successfully performed in solvent-free medium. A high capacity removal of more organic dyes, e.g., methylene blue (MB) and orange G (OrG), over the CTF material was also demonstrated in solid-state.

Last but not least, a particular focus was paid to the factors, which allow CPP based photocatalysts to perform more efficiently. Indeed, the more effective the photoinduced charge separation and transfer are, the more efficient the photocatalytic activity is. In the previous projects, the molecular structure of CPPs, played a crucial role in improving their photocatalytic performances, by varying different electron donor/acceptor combinations. Herein, a design strategy of heterojunctions consisting of CPP with immobilized TiO_2 nanoparticles was presented. The hybrid systems were successfully used for visible light driven organic photoredox reactions. They could enhance the light absorption in the overall solar spectrum, improve the photo-induced charge separation and therefore increase the photocatalytic efficiency. As model reactions, the photocatalytic oxidative coupling reaction of amines and the selective oxidation of organic sulfides were investigated with high conversion and selectivity. The catalytic efficiency of the formed heterojunction was higher than that of the single photocatalytic systems either only consisting of the conjugated microporous polymer or TiO_2. Furthermore, the mechanistic insight of the photoredox reactions was investigated.

In summary, this thesis highlights various design strategies of conjugated porous polymers as efficient heterogeneous, visible light active photocatalysts for a wide range of applications under environmentally benign reaction conditions.

8. References

1. Garcia, H., *Revolutionary Times.* Chemistry – A European Journal, 2020. **26**(1): p. 14-18.
2. Lewis, N.S. and D.G. Nocera, *Powering the planet: Chemical challenges in solar energy utilization.* Proceedings of the National Academy of Sciences, 2006. **103**(43): p. 15729-15735.
3. Šima, J., *Photochemistry — development and achievements.* 2017. **10**(2): p. 84.
4. Ciamician, G., *THE PHOTOCHEMISTRY OF THE FUTURE.* Science, 1912. **36**(926): p. 385-394.
5. Pape, M., *Industrial applications of photochemistry.* Pure and Applied Chemistry, 1975. **41**: p. 535 - 558.
6. Šima, J., *Photochemistry — development and achievements.* Acta Chimica Slovaca, 2017. **10**(2): p. 84.
7. Prier, C.K., D.A. Rankic, and D.W.C. MacMillan, *Visible Light Photoredox Catalysis with Transition Metal Complexes: Applications in Organic Synthesis.* Chemical Reviews, 2013. **113**(7): p. 5322-5363.
8. Hockin, B.M., et al., *Photoredox catalysts based on earth-abundant metal complexes.* Catalysis Science & Technology, 2019. **9**(4): p. 889-915.
9. Kalyanasundaram, K., *Photophysics, photochemistry and solar energy conversion with tris(bipyridyl)ruthenium(II) and its analogues.* Coordination Chemistry Reviews, 1982. **46**: p. 159-244.
10. Teegardin, K., et al., *Advances in Photocatalysis: A Microreview of Visible Light Mediated Ruthenium and Iridium Catalyzed Organic Transformations.* Organic Process Research & Development, 2016. **20**(7): p. 1156-1163.
11. Ayed, C., et al., *Photocatalytic Partial Oxidation of 5-Hydroxymethylfurfural (HMF) to 2,5-Diformylfuran (DFF) Over a Covalent Triazine Framework in Water.* ChemPhotoChem, 2020. **4**(8): p. 571-576.
12. Romero, N.A. and D.A. Nicewicz, *Organic Photoredox Catalysis.* Chemical Reviews, 2016. **116**(17): p. 10075-10166.
13. Nicewicz, D.A. and T.M. Nguyen, *Recent Applications of Organic Dyes as Photoredox Catalysts in Organic Synthesis.* ACS Catalysis, 2014. **4**(1): p. 355-360.
14. Hari, D.P. and B. König, *Synthetic applications of eosin Y in photoredox catalysis.* Chemical Communications, 2014. **50**(51): p. 6688-6699.
15. Joshi-Pangu, A., et al., *Acridinium-Based Photocatalysts: A Sustainable Option in Photoredox Catalysis.* The Journal of Organic Chemistry, 2016. **81**(16): p. 7244-7249.
16. Ayed, C., W. Huang, and K.A.I. Zhang, *Covalent triazine framework with efficient photocatalytic activity in aqueous and solid media.* Frontiers of Chemical Science and Engineering, 2020. **14**(3): p. 397-404.
17. Wang, X., et al., *A metal-free polymeric photocatalyst for hydrogen production from water under visible light.* Nature materials, 2008. **8**: p. 76-80.
18. Xu, Y., et al., *Conjugated microporous polymers: design, synthesis and application.* Chemical Society Reviews, 2013. **42**(20): p. 8012-8031.
19. Lu, J. and J. Zhang, *Photocatalytic applications of conjugated microporous polymers*, in *Photochemistry: Volume 45*. 2018, The Royal Society of Chemistry. p. 191-220.
20. Zhi, Y., et al., *Robust porous organic polymers as efficient heterogeneous organo-photocatalysts for aerobic oxidation reactions.* Journal of Materials Chemistry A, 2017. **5**(18): p. 8697-8704.
21. Zhang, K., et al., *π-Conjugated polyHIPEs as highly efficient and reusable heterogeneous photosensitizers.* Chemical Communications, 2013. **49**(95): p. 11158-11160.
22. Ghasimi, S., et al., *Heterophase Photocatalysts from Water-Soluble Conjugated Polyelectrolytes: An Example of Self-Initiation under Visible Light.* Angewandte Chemie International Edition, 2015. **54**(48): p. 14549-14553.
23. Xu, Y., et al., *Conjugated microporous polymers: design, synthesis and application.* Chemical Society Reviews, 2013.

24. Wong, Y.-L., et al., *Conjugated Porous Polymers for Photocatalytic Applications.* J. Mater. Chem. A, 2016. **4**.
25. Yu, J., et al., *Donor-acceptor type triazine-based conjugated porous polymer for visible-light-driven photocatalytic hydrogen evolution.* Applied Catalysis B: Environmental, 2019. **257**: p. 117935.
26. Wang, L., et al., *Conjugated Microporous Polymer Nanosheets for Overall Water Splitting Using Visible Light.* Advanced Materials, 2017. **29**(38): p. 1702428.
27. Kong, D., et al., *Tunable Covalent Triazine-Based Frameworks (CTF-0) for Visible-Light-Driven Hydrogen and Oxygen Generation from Water Splitting.* ACS Catalysis, 2019. **9**(9): p. 7697-7707.
28. Jiang, X., P. Wang, and J. Zhao, *2D covalent triazine framework: a new class of organic photocatalyst for water splitting.* Journal of Materials Chemistry A, 2015. **3**(15): p. 7750-7758.
29. Meier, C.B., et al., *Structurally Diverse Covalent Triazine-Based Framework Materials for Photocatalytic Hydrogen Evolution from Water.* Chemistry of Materials, 2019. **31**(21): p. 8830-8838.
30. Ma, B., et al., *Enhanced Visible Light Promoted Antibacterial Efficiency of Conjugated Microporous Polymer Nanoparticles via Molecular Doping.* J. Mater. Chem. B, 2016. **4**.
31. Liao, Y., et al., *Highly Efficient and Reversible Iodine Capture in Hexaphenylbenzene-Based Conjugated Microporous Polymers.* Macromolecules, 2016. **49**(17): p. 6322-6333.
32. Wang, J., et al., *Highly efficient removal of organic pollutants by ultrahigh-surface-area-ethynylbenzene-based conjugated microporous polymers via adsorption–photocatalysis synergy.* Catalysis Science & Technology, 2018. **8**(19): p. 5024-5033.
33. Yang, H., et al., *Highly efficient removal of organic pollutants by ultrahigh-surface-area-ethynylbenzene-based conjugated microporous polymers: Via adsorption-photocatalysis synergy.* Catalysis Science & Technology, 2018. **8**.
34. Li, Q., et al., *Conjugated microporous polymers bearing metallophthalocyanine moieties with enhanced visible-light photocatalytic activity.* Dyes and Pigments, 2018. **149**: p. 261-267.
35. Niu, F., et al., *A covalent triazine framework as an efficient catalyst for photodegradation of methylene blue under visible light illumination.* New Journal of Chemistry, 2014. **38**(12): p. 5695-5699.
36. Dai, C. and B. Liu, *Conjugated polymers for visible-light-driven photocatalysis.* Energy & Environmental Science, 2020. **13**(1): p. 24-52.
37. Zhang, T., et al., *Porous organic polymers: a promising platform for efficient photocatalysis.* Materials Chemistry Frontiers, 2020. **4**(2): p. 332-353.
38. Wang, Z.J., et al., *Conjugated Microporous Poly(Benzochalcogenadiazole)s for Photocatalytic Oxidative Coupling of Amines under Visible Light.* ChemSusChem, 2015. **8**(20): p. 3459-3464.
39. Ayed, C., et al., *Conjugated Microporous Polymers with Immobilized TiO2 Nanoparticles for Enhanced Visible Light Photocatalysis.* Particle & Particle Systems Characterization, 2018. **35**(1): p. 1700234.
40. Zhang, J.-J., et al., *Activating Oxygen Molecules over Carbonyl-Modified Graphitic Carbon Nitride: Merging Supramolecular Oxidation with Photocatalysis in a Metal-Free Catalyst for Oxidative Coupling of Amines into Imines.* ChemCatChem, 2016. **8**(22): p. 3441-3445.
41. Kang, N., et al., *Tandem Synthesis of Photoactive Benzodifuran Moieties in the Formation of Microporous Organic Networks.* Angewandte Chemie International Edition, 2013. **52**(24): p. 6228-6232.
42. Wang, Z.J., et al., *Porous conjugated polymer via metal-free synthesis for visible light-promoted oxidative hydroxylation of arylboronic acids.* Polymer, 2017. **126**: p. 291-295.
43. Wang, Z.J., et al., *Highly porous conjugated polymers for selective oxidation of organic sulfides under visible light.* Chemical Communications, 2014. **50**(60): p. 8177-8180.
44. López-Calixto, C.G., et al., *Conjugated porous polymer based on BOPHY dyes as photocatalyst under visible light.* Applied Catalysis B: Environmental, 2019. **258**: p. 117933.

45. Jiménez-Almarza, A., et al., *Imine-Based Covalent Organic Frameworks as Photocatalysts for Metal Free Oxidation Processes under Visible Light Conditions.* ChemCatChem, 2019. **11**(19): p. 4916-4922.
46. Huang, W., et al., *Visible-Light-Promoted Selective Oxidation of Alcohols Using a Covalent Triazine Framework.* ACS Catalysis, 2017. **7**(8): p. 5438-5442.
47. Ayed, C., et al., *Designing conjugated microporous polymers for visible light-promoted photocatalytic carbon–carbon double bond cleavage in aqueous medium.* Journal of Materials Chemistry A, 2018. **6**(44): p. 22145-22151.
48. Sheldon, R.A., *Green solvents for sustainable organic synthesis: state of the art.* Green Chemistry, 2005. **7**(5): p. 267-278.
49. Simon, M.-O. and C.-J. Li, *Green chemistry oriented organic synthesis in water.* Chemical Society Reviews, 2012. **41**(4): p. 1415-1427.
50. Urakami, H., K. Zhang, and F. Vilela, *Modification of conjugated microporous poly-benzothiadiazole for photosensitized singlet oxygen generation in water.* Chemical Communications, 2013. **49**(23): p. 2353-2355.
51. Ghasimi, S., K. Landfester, and K.A.I. Zhang, *Water Compatible Conjugated Microporous Polyazulene Networks as Visible-Light Photocatalysts in Aqueous Medium.* ChemCatChem, 2016. **8**(4): p. 694-698.
52. Coronado, J.M., *A Historical Introduction to Photocatalysis*, in *Design of Advanced Photocatalytic Materials for Energy and Environmental Applications*, J.M. Coronado, et al., Editors. 2013, Springer London: London. p. 1-4.
53. Baur, E. and A. Perret, *Über die Einwirkung von Licht auf gelöste Silbersalze in Gegenwart von Zinkoxyd.* Helvetica Chimica Acta, 1924. **7**(1): p. 910-915.
54. Renz, C., *Über die Einwirkung von Oxyden auf Silbernitrat und Goldchlorid im Licht.* Helvetica Chimica Acta, 1932. **15**(1): p. 1077-1084.
55. Goodeve, C.F. and J.A. Kitchener, *The mechanism of photosensitisation by solids.* Transactions of the Faraday Society, 1938. **34**(0): p. 902-908.
56. Fujishima, A. and K. Honda, *Electrochemical Photolysis of Water at a Semiconductor Electrode.* Nature, 1972. **238**(5358): p. 37-38.
57. Frank, S.N. and A.J. Bard, *Heterogeneous photocatalytic oxidation of cyanide and sulfite in aqueous solutions at semiconductor powders.* The Journal of Physical Chemistry, 1977. **81**(15): p. 1484-1488.
58. Inoue, T., et al., *Photoelectrocatalytic reduction of carbon dioxide in aqueous suspensions of semiconductor powders.* Nature, 1979. **277**(5698): p. 637-638.
59. Braslavsky, S.E., *Glossary of terms used in photochemistry, 3rd edition (IUPAC Recommendations 2006).* 2007. **79**(3): p. 293.
60. Ohtani, B., *Principle of Photocatalysis and Design of Active Photocatalysts*. 2013. p. 121-144.
61. Ohtani, B., *Revisiting the fundamental physical chemistry in heterogeneous photocatalysis: its thermodynamics and kinetics.* Physical Chemistry Chemical Physics, 2014. **16**(5): p. 1788-1797.
62. Zhu, S. and D. Wang, *Photocatalysis: Basic Principles, Diverse Forms of Implementations and Emerging Scientific Opportunities.* Advanced Energy Materials, 2017. **7**.
63. Marci, G. and L. Palmisano, *Heterogeneous photocatalysis : relationships with heterogeneous catalysis and perspectives.* 2019.
64. Chen, S., T. Takata, and K. Domen, *Particulate photocatalysts for overall water splitting.* Nature Reviews Materials, 2017. **2**(10): p. 17050.
65. Acar, C., I. Dincer, and C. Zamfirescu, *A review on selected heterogeneous photocatalysts for hydrogen production.* International Journal of Energy Research, 2014. **38**(15): p. 1903-1920.
66. Bunsho, O., *Preparing Articles on Photocatalysis—Beyond the Illusions, Misconceptions, and Speculation.* Chemistry Letters, 2008. **37**(3): p. 216-229.
67. Twilton, J., et al., *The merger of transition metal and photocatalysis.* Nature Reviews Chemistry, 2017. **1**(7): p. 0052.

68. Ravelli, D. and M. Fagnoni, *Dyes as Visible Light Photoredox Organocatalysts.* ChemCatChem, 2012. **4**(2): p. 169-171.
69. Srivastava, V. and P.P. Singh, *Eosin Y catalysed photoredox synthesis: a review.* RSC Advances, 2017. **7**(50): p. 31377-31392.
70. Tambe, S.D., R.S. Rohokale, and U.A. Kshirsagar, *Visible-Light-Mediated Eosin Y Photoredox-Catalyzed Vicinal Thioamination of Alkynes: Radical Cascade Annulation Strategy for 2-Substituted-3-sulfenylindoles.* European Journal of Organic Chemistry, 2018. **2018**(18): p. 2117-2121.
71. Sideri, I.K., E. Voutyritsa, and C.G. Kokotos, *Photoorganocatalysis, small organic molecules and light in the service of organic synthesis: the awakening of a sleeping giant.* Organic & Biomolecular Chemistry, 2018. **16**(25): p. 4596-4614.
72. Miyabe, H., *Organic Reactions Promoted by Metal-Free Organic Dyes Under Visible Light Irradiation*. 2018.
73. Hao, H. and X. Lang, *Metal Sulfide Photocatalysis: Visible-Light-Induced Organic Transformations.* ChemCatChem, 2019. **11**(5): p. 1378-1393.
74. Khan, M.M., S.F. Adil, and A. Al-Mayouf, *Metal oxides as photocatalysts.* Journal of Saudi Chemical Society, 2015. **19**(5): p. 462-464.
75. Pelizzetti, E. and C. Minero, *Metal Oxides as Photocatalysts for Environmental Detoxification.* Comments on Inorganic Chemistry, 1994. **15**(5-6): p. 297-337.
76. Marschall, R. and L. Wang, *Non-metal doping of transition metal oxides for visible-light photocatalysis.* Catalysis Today, 2014. **225**: p. 111-135.
77. Akhundi, A., et al., *Graphitic carbon nitride-based photocatalysts: Toward efficient organic transformation for value-added chemicals production.* Molecular Catalysis, 2020. **488**: p. 110902.
78. Markushyna, Y., C.A. Smith, and A. Savateev, *Organic Photocatalysis: Carbon Nitride Semiconductors vs. Molecular Catalysts.* European Journal of Organic Chemistry, 2020. **2020**(10): p. 1294-1309.
79. Maina, J.W., et al., *Inorganic Nanoparticles/Metal Organic Framework Hybrid Membrane Reactors for Efficient Photocatalytic Conversion of CO2.* ACS Applied Materials & Interfaces, 2017. **9**(40): p. 35010-35017.
80. Zhang, H., et al., *Metal–Organic Frameworks and Their Derived Materials as Electrocatalysts and Photocatalysts for CO2 Reduction: Progress, Challenges, and Perspectives.* Chemistry – A European Journal, 2018. **24**(69): p. 18137-18157.
81. Liras, M., M. Barawi, and V.A. de la Peña O'Shea, *Hybrid materials based on conjugated polymers and inorganic semiconductors as photocatalysts: from environmental to energy applications.* Chemical Society Reviews, 2019. **48**(22): p. 5454-5487.
82. Wang, Z.J., et al., *Photocatalytic Suzuki Coupling Reaction Using Conjugated Microporous Polymer with Immobilized Palladium Nanoparticles under Visible Light.* Chemistry of Materials, 2015. **27**(6): p. 1921-1924.
83. Zhu, S. and D. Wang, *Photocatalysis: Basic Principles, Diverse Forms of Implementations and Emerging Scientific Opportunities.* Advanced Energy Materials, 2017. **7**(23): p. 1700841.
84. Yoon, T.P., M.A. Ischay, and J. Du, *Visible light photocatalysis as a greener approach to photochemical synthesis.* Nature Chemistry, 2010. **2**(7): p. 527-532.
85. Gisbertz, S. and B. Pieber, *Heterogeneous Photocatalysis in Organic Synthesis.* ChemPhotoChem, 2020. **4**(7): p. 456-475.
86. Schultz, D.M. and T.P. Yoon, *Solar Synthesis: Prospects in Visible Light Photocatalysis.* Science, 2014. **343**(6174): p. 1239176.
87. Narayanam, J.M.R. and C.R.J. Stephenson, *Visible light photoredox catalysis: applications in organic synthesis.* Chemical Society Reviews, 2011. **40**(1): p. 102-113.
88. Lang, X., X. Chen, and J. Zhao, *Heterogeneous visible light photocatalysis for selective organic transformations.* Chemical Society Reviews, 2014. **43**(1): p. 473-486.

89. Jespersen, D., et al., *Solubility of Iridium and Ruthenium Organometallic Photoredox Catalysts.* Organic process research & development, 2019. **23**(5): p. 1087-1095.
90. Traub, L. and O. Reiser, *Homogeneous visible light mediated transition metal catalysis other than Ruthenium and Iridium.* Physical Sciences Reviews, 2019. **4**.
91. Minozzi, C., et al., *Heteroleptic Copper(I)-Based Complexes for Photocatalysis: Combinatorial Assembly, Discovery, and Optimization.* Angewandte Chemie International Edition, 2018. **57**(19): p. 5477-5481.
92. Lennox, A.J.J., et al., *Copper-Based Photosensitisers in Water Reduction: A More Efficient In Situ Formed System and Improved Mechanistic Understanding.* Chemistry – A European Journal, 2016. **22**(4): p. 1233-1238.
93. Takeda, H., et al., *Development of Visible-Light Driven Cu(I) Complex Photosensitizers for Photocatalytic CO2 Reduction.* Frontiers in Chemistry, 2019. **7**(418).
94. Liu, W.-J., et al., *A Copper(II) Molecular Catalyst for Efficient and Selective Photochemical Reduction of CO2 to CO in a Water-Containing System.* Chemistry – A European Journal, 2018. **24**(18): p. 4503-4508.
95. Zou, Y.-Q., et al., *Highly Efficient Aerobic Oxidative Hydroxylation of Arylboronic Acids: Photoredox Catalysis Using Visible Light.* Angewandte Chemie International Edition, 2012. **51**(3): p. 784-788.
96. Pitre, S.P., et al., *Mechanistic Insights and Kinetic Analysis for the Oxidative Hydroxylation of Arylboronic Acids by Visible Light Photoredox Catalysis: A Metal-Free Alternative.* Journal of the American Chemical Society, 2013. **135**(36): p. 13286-13289.
97. Gao, C., et al., *Coordination chemistry in the design of heterogeneous photocatalysts.* Chemical Society Reviews, 2017. **46**(10): p. 2799-2823.
98. Friedmann, D., et al., *Heterogeneous photocatalytic organic synthesis: state-of-the-art and future perspectives.* Green Chemistry, 2016. **18**(20): p. 5391-5411.
99. Schneider, J., et al., *Understanding TiO2 Photocatalysis: Mechanisms and Materials.* Chemical Reviews, 2014. **114**(19): p. 9919-9986.
100. Riente, P. and T. Noël, *Application of metal oxide semiconductors in light-driven organic transformations.* Catalysis Science & Technology, 2019. **9**(19): p. 5186-5232.
101. Hoffmann, N., *Photocatalysis with TiO2 Applied to Organic Synthesis.* Australian Journal of Chemistry, 2015. **68**(11): p. 1621-1639.
102. Cheng, H. and W. Xu, *Recent advances in modified TiO2 for photo-induced organic synthesis.* Organic & Biomolecular Chemistry, 2019. **17**(47): p. 9977-9989.
103. Zoller, J., D.C. Fabry, and M. Rueping, *Unexpected Dual Role of Titanium Dioxide in the Visible Light Heterogeneous Catalyzed C–H Arylation of Heteroarenes.* ACS Catalysis, 2015. **5**(6): p. 3900-3904.
104. Zhang, L. and J.M. Cole, *Anchoring Groups for Dye-Sensitized Solar Cells.* ACS Applied Materials & Interfaces, 2015. **7**(6): p. 3427-3455.
105. Ooyama, Y. and Y. Harima, *Photophysical and Electrochemical Properties, and Molecular Structures of Organic Dyes for Dye-Sensitized Solar Cells.* ChemPhysChem, 2012. **13**(18): p. 4032-4080.
106. Ren, L., et al., *Visible-Light Photocatalysis Employing Dye-Sensitized Semiconductor: Selective Aerobic Oxidation of Benzyl Ethers.* ACS Catalysis, 2017. **7**(12): p. 8134-8138.
107. Elmehasseb, I., S. Kandil, and K. Elgendy, *Advanced visible-light applications utilizing modified Zn-doped TiO2 nanoparticles via non-metal in situ dual doping for wastewater detoxification.* Optik, 2020. **213**: p. 164654.
108. Basavarajappa, P.S., et al., *Recent progress in metal-doped TiO2, non-metal doped/codoped TiO2 and TiO2 nanostructured hybrids for enhanced photocatalysis.* International Journal of Hydrogen Energy, 2020. **45**(13): p. 7764-7778.
109. Tang, J., et al., *Visible Light Mediated Cyclization of Tertiary Anilines with Maleimides Using Nickel(II) Oxide Surface-Modified Titanium Dioxide Catalyst.* The Journal of Organic Chemistry, 2015. **80**(5): p. 2724-2732.

110. Rueping, M., et al., *Light-Mediated Heterogeneous Cross Dehydrogenative Coupling Reactions: Metal Oxides as Efficient, Recyclable, Photoredox Catalysts in C□C Bond-Forming Reactions.* Chemistry – A European Journal, 2012. **18**(12): p. 3478-3481.
111. Jeena, V. and R.S. Robinson, *Convenient photooxidation of alcohols using dye sensitised zinc oxide in combination with silver nitrate and TEMPO.* Chemical Communications, 2012. **48**(2): p. 299-301.
112. Wang, J., et al., *Synthesis, properties and applications of ZnO nanomaterials with oxygen vacancies: A review.* Ceramics International, 2018. **44**(7): p. 7357-7377.
113. Shishido, T., et al., *Mechanism of Photooxidation of Alcohol over Nb2O5.* The Journal of Physical Chemistry C, 2009. **113**(43): p. 18713-18718.
114. Furukawa, S., et al., *Selective Amine Oxidation Using Nb2O5 Photocatalyst and O2.* ACS Catalysis, 2011. **1**(10): p. 1150-1153.
115. Su, Y., et al., *Surface hydrogen bonds assisted meso-porous WO3 photocatalysts for high selective oxidation of benzylalcohol to benzylaldehyde.* Applied Catalysis B: Environmental, 2017. **217**: p. 108-114.
116. Tomita, O., et al., *Partial Oxidation of Alcohols on Visible-Light-Responsive WO3 Photocatalysts Loaded with Palladium Oxide Cocatalyst.* ACS Catalysis, 2016. **6**(2): p. 1134-1144.
117. Osamu, T., A. Ryu, and O. Bunsho, *Direct Synthesis of Phenol from Benzene over Platinum-loaded Tungsten(VI) Oxide Photocatalysts with Water and Molecular Oxygen.* Chemistry Letters, 2011. **40**(12): p. 1405-1407.
118. Riente, P. and M.A. Pericàs, *Visible Light-Driven Atom Transfer Radical Addition to Olefins using Bi2O3 as Photocatalyst.* ChemSusChem, 2015. **8**(11): p. 1841-1844.
119. Buglioni, L., et al., *Visible-Light-Promoted Arylation Reactions Photocatalyzed by Bismuth(III) Oxide.* European Journal of Organic Chemistry, 2017. **2017**(46): p. 6986-6990.
120. Riente, P., et al., *Light-Driven Organocatalysis Using Inexpensive, Nontoxic Bi2O3 as the Photocatalyst.* Angewandte Chemie International Edition, 2014. **53**(36): p. 9613-9616.
121. Zhang, L., et al., *Sonochemical synthesis of nanocrystallite Bi2O3 as a visible-light-driven photocatalyst.* Applied Catalysis A: General, 2006. **308**: p. 105-110.
122. Yuan, B., et al., *Photocatalytic aerobic oxidation of amines to imines on BiVO4 under visible light irradiation.* Chemical Communications, 2014. **50**(98): p. 15593-15596.
123. Liu, Y.-Y., et al., *Practical heterogeneous photoredox/nickel dual catalysis for C–N and C–O coupling reactions.* Chemical Communications, 2019. **55**(33): p. 4853-4856.
124. Zhao, W., et al., *Porous single-crystalline CdS nanosheets as efficient visible light catalysts for aerobic oxidative coupling of amines to imines.* RSC Advances, 2013. **3**(45): p. 22944-22948.
125. Liu, C., et al., *Controllable deuteration of halogenated compounds by photocatalytic D2O splitting.* Nature Communications, 2018. **9**(1): p. 80.
126. Enright, M.J., et al., *Photolytic C–O Bond Cleavage with Quantum Dots.* Chemistry of Materials, 2019. **31**(7): p. 2677-2682.
127. Yoffe, A.D., *Semiconductor quantum dots and related systems: Electronic, optical, luminescence and related properties of low dimensional systems.* Advances in Physics, 2001. **50**(1): p. 1-208.
128. Saparov, B. and D.B. Mitzi, *Organic–Inorganic Perovskites: Structural Versatility for Functional Materials Design.* Chemical Reviews, 2016. **116**(7): p. 4558-4596.
129. Wu, W.-B., et al., *Photo-induced thiol coupling and C–H activation using nanocrystalline lead-halide perovskite catalysts.* Catalysis Science & Technology, 2018. **8**(16): p. 4257-4263.
130. Ong, W.-J., et al., *Graphitic Carbon Nitride (g-C3N4)-Based Photocatalysts for Artificial Photosynthesis and Environmental Remediation: Are We a Step Closer To Achieving Sustainability?* Chemical Reviews, 2016. **116**(12): p. 7159-7329.
131. Savateev, A., et al., *Photoredox Catalytic Organic Transformations using Heterogeneous Carbon Nitrides.* Angewandte Chemie International Edition, 2018. **57**(49): p. 15936-15947.

132. Vinu, A., *Two-Dimensional Hexagonally-Ordered Mesoporous Carbon Nitrides with Tunable Pore Diameter, Surface Area and Nitrogen Content.* Advanced Functional Materials, 2008. **18**(5): p. 816-827.
133. Cao, S., et al., *Polymeric Photocatalysts Based on Graphitic Carbon Nitride.* Advanced Materials, 2015. **27**(13): p. 2150-2176.
134. Kurpil, B., et al., *Hexaazatriphenylene doped carbon nitrides—Biomimetic photocatalyst with superior oxidation power.* Applied Catalysis B: Environmental, 2017. **217**: p. 622-628.
135. Wang, B., et al., *Enhanced photocatalytic hydrogen evolution by partially replaced corner-site C atom with P in g-C3N4.* Applied Catalysis B: Environmental, 2019. **244**: p. 486-493.
136. Yang, Z., Y. Zhang, and Z. Schnepp, *Soft and hard templating of graphitic carbon nitride.* Journal of Materials Chemistry A, 2015. **3**(27): p. 14081-14092.
137. Zhao, Z., Y. Sun, and F. Dong, *Graphitic carbon nitride based nanocomposites: a review.* Nanoscale, 2015. **7**(1): p. 15-37.
138. Vyas, V.S., V.W.-h. Lau, and B.V. Lotsch, *Soft Photocatalysis: Organic Polymers for Solar Fuel Production.* Chemistry of Materials, 2016. **28**(15): p. 5191-5204.
139. Ye, S., et al., *A review on g-C3N4 for photocatalytic water splitting and CO2 reduction.* Applied Surface Science, 2015. **358**: p. 15-27.
140. Li, D., et al., *Photo reduction of CO2 to CH4 on g-C3N4: The effect of concentrating light and pretreatment.* AIP Conference Proceedings, 2018. **1971**(1): p. 020006.
141. Ullah, N., et al., *Photoinduced Water–Heptazine Electron-Driven Proton Transfer: Perspective for Water Splitting with g-C3N4.* The Journal of Physical Chemistry Letters, 2019. **10**(15): p. 4310-4316.
142. Lam, S.-M., J.-C. Sin, and A.R. Mohamed, *A review on photocatalytic application of g-C3N4/semiconductor (CNS) nanocomposites towards the erasure of dyeing wastewater.* Materials Science in Semiconductor Processing, 2016. **47**: p. 62-84.
143. Mamba, G. and A.K. Mishra, *Graphitic carbon nitride (g-C3N4) nanocomposites: A new and exciting generation of visible light driven photocatalysts for environmental pollution remediation.* Applied Catalysis B: Environmental, 2016. **198**: p. 347-377.
144. Ding, F., et al., *Graphitic carbon nitride-based nanocomposites as visible-light driven photocatalysts for environmental purification.* Environmental Science: Nano, 2017. **4**(7): p. 1455-1469.
145. Su, F., et al., *mpg-C3N4-Catalyzed Selective Oxidation of Alcohols Using O2 and Visible Light.* Journal of the American Chemical Society, 2010. **132**(46): p. 16299-16301.
146. Verma, S., et al., *Selective Oxidation of Alcohols Using Photoactive VO@g-C3N4.* ACS Sustainable Chemistry & Engineering, 2016. **4**(3): p. 1094-1098.
147. Bellardita, M., et al., *Selective photocatalytic oxidation of aromatic alcohols in water by using P-doped g-C3N4.* Applied Catalysis B: Environmental, 2018. **220**: p. 222-233.
148. Samanta, S., et al., *An Efficient, Visible Light Driven, Selective Oxidation of Aromatic Alcohols and Amines with O2 Using BiVO4/g-C3N4 Nanocomposite: A Systematic and Comprehensive Study toward the Development of a Photocatalytic Process.* ACS Sustainable Chemistry & Engineering, 2017. **5**(3): p. 2562-2577.
149. Zhang, S., et al., *Nickel-decorated g-C3N4 hollow spheres as an efficient photocatalyst for hydrogen evolution and oxidation of amines to imines.* New Journal of Chemistry, 2020. **44**(27): p. 11710-11719.
150. Zhang, P., et al., *Metal-free oxidation of sulfides by carbon nitride with visible light illumination at room temperature.* Green Chemistry, 2012. **14**(7): p. 1904-1908.
151. Verma, S., et al., *Hydroxylation of Benzene via C–H Activation Using Bimetallic CuAg@g-C3N4.* ACS Sustainable Chemistry & Engineering, 2017. **5**(5): p. 3637-3640.
152. Zhao, Y. and M. Antonietti, *Visible-Light-Irradiated Graphitic Carbon Nitride Photocatalyzed Diels–Alder Reactions with Dioxygen as Sustainable Mediator for Photoinduced Electrons.* Angewandte Chemie International Edition, 2017. **56**(32): p. 9336-9340.

153. Chen, X., et al., *Ordered Mesoporous SBA-15 Type Graphitic Carbon Nitride: A Semiconductor Host Structure for Photocatalytic Hydrogen Evolution with Visible Light.* Chemistry of Materials, 2009. **21**(18): p. 4093-4095.
154. Byun, J. and K.A.I. Zhang, *Designing conjugated porous polymers for visible light-driven photocatalytic chemical transformations.* Materials Horizons, 2020. **7**(1): p. 15-31.
155. Taylor, D., et al., *Conjugated porous polymers: incredibly versatile materials with far-reaching applications.* Chemical Society Reviews, 2020. **49**(12): p. 3981-4042.
156. Jiang, J.-X., et al., *Conjugated Microporous Poly(aryleneethynylene) Networks.* Angewandte Chemie International Edition, 2007. **46**(45): p. 8574-8578.
157. Chen, J.-T. and C.-S. Hsu, *Conjugated polymer nanostructures for organic solar cell applications.* Polymer Chemistry, 2011. **2**(12): p. 2707-2722.
158. Vilela, F., K. Zhang, and M. Antonietti, *Conjugated porous polymers for energy applications.* Energy & Environmental Science, 2012. **5**(7): p. 7819-7832.
159. Gupta, S.K., et al., *Bulky Isopropyl Group Loaded Tetraaryl Pyrene Based Azo-Linked Covalent Organic Polymer for Nitroaromatics Sensing and CO2 Adsorption.* ACS Omega, 2017. **2**(7): p. 3572-3582.
160. Novotney, J.L. and W.R. Dichtel, *Conjugated Porous Polymers For TNT Vapor Detection.* ACS Macro Letters, 2013. **2**(5): p. 423-426.
161. Liu, X., Y. Xu, and D. Jiang, *Conjugated Microporous Polymers as Molecular Sensing Devices: Microporous Architecture Enables Rapid Response and Enhances Sensitivity in Fluorescence-On and Fluorescence-Off Sensing.* Journal of the American Chemical Society, 2012. **134**(21): p. 8738-8741.
162. Wong, Y.L., et al., *Conjugated porous polymers for photocatalytic applications.* Journal of Materials Chemistry A, 2016. **4**(48): p. 18677-18686.
163. Ma, B.C., et al., *Conjugated microporous polymer nanoparticles with enhanced dispersibility and water compatibility for photocatalytic applications.* Journal of Materials Chemistry A, 2015. **3**(31): p. 16064-16071.
164. Wang, Z.J., K. Landfester, and K.A.I. Zhang, *Hierarchically porous π-conjugated polyHIPE as a heterogeneous photoinitiator for free radical polymerization under visible light.* Polymer Chemistry, 2014. **5**(11): p. 3559-3562.
165. Zhang, K., et al., *Surface Area Control and Photocatalytic Activity of Conjugated Microporous Poly(benzothiadiazole) Networks.* Angewandte Chemie International Edition, 2013. **52**(5): p. 1432-1436.
166. Schmidt, J., M. Werner, and A. Thomas, *Conjugated Microporous Polymer Networks via Yamamoto Polymerization.* Macromolecules, 2009. **42**(13): p. 4426-4429.
167. Sun, L., et al., *Luminescent microporous organic polymers containing the 1,3,5-tri(4-ethenylphenyl)benzene unit constructed by Heck coupling reaction.* Polymer Chemistry, 2013. **4**(6): p. 1932-1938.
168. Lu, G., et al., *Synthesis of a conjugated porous Co(ii) porphyrinylene–ethynylene framework through alkyne metathesis and its catalytic activity study.* Journal of Materials Chemistry A, 2015. **3**(9): p. 4954-4959.
169. Senkovskyy, V., I. Senkovska, and A. Kiriy, *Surface-Initiated Synthesis of Conjugated Microporous Polymers: Chain-Growth Kumada Catalyst-Transfer Polycondensation at Work.* ACS Macro Letters, 2012. **1**(4): p. 494-498.
170. Hayashi, S., et al., *Synthesis of π-conjugated porous polymers via direct arylation of fluoroarenes with three-arm triazine.* Polymer, 2016. **90**: p. 187-192.
171. Hayashi, S., et al., *Synthesis of π-conjugated network polymers based on fluoroarene and fluorescent units via direct arylation polycondensation and their porosity and fluorescent properties.* Journal of Polymer Science Part A: Polymer Chemistry, 2017. **55**(23): p. 3862-3867.
172. Jiang, X., et al., *Hypercrosslinked conjugated microporous polymers for carbon capture and energy storage.* New Journal of Chemistry, 2017. **41**(10): p. 3915-3919.

173. Ding, X. and B.-H. Han, *Copper phthalocyanine-based CMPs with various internal structures and functionalities.* Chemical Communications, 2015. **51**(64): p. 12783-12786.
174. Ding, X. and B.-H. Han, *Metallophthalocyanine-Based Conjugated Microporous Polymers as Highly Efficient Photosensitizers for Singlet Oxygen Generation.* Angewandte Chemie International Edition, 2015. **54**(22): p. 6536-6539.
175. Guo, Z., et al., *Amorphous Porous Organic Polymers Based on Schiff-Base Chemistry for Highly Efficient Iodine Capture.* Chemistry – An Asian Journal, 2018. **13**(16): p. 2046-2053.
176. Kang, C.W., et al., *Conjugated macro–microporous polymer films bearing tetraphenylethylenes for the enhanced sensing of nitrotoluenes.* Journal of Materials Chemistry A, 2018. **6**(36): p. 17312-17317.
177. Liu, M., et al., *Covalent triazine frameworks: synthesis and applications.* Journal of Materials Chemistry A, 2019. **7**(10): p. 5153-5172.
178. Lee, J.-S.M. and A.I. Cooper, *Advances in Conjugated Microporous Polymers.* Chemical Reviews, 2020. **120**(4): p. 2171-2214.
179. Luo, S., et al., *Recent advances in conjugated microporous polymers for photocatalysis: designs, applications, and prospects.* Journal of Materials Chemistry A, 2020. **8**(14): p. 6434-6470.
180. Kiskan, B. and J. Weber, *Versatile Postmodification of Conjugated Microporous Polymers Using Thiol-yne Chemistry.* ACS Macro Letters, 2012. **1**(1): p. 37-40.
181. Ratvijitvech, T., et al., *Post-synthetic modification of conjugated microporous polymers.* Polymer, 2014. **55**(1): p. 321-325.
182. Sonogashira, K., Y. Tohda, and N. Hagihara, *A convenient synthesis of acetylenes: catalytic substitutions of acetylenic hydrogen with bromoalkenes, iodoarenes and bromopyridines.* Tetrahedron Letters, 1975. **16**(50): p. 4467-4470.
183. Trunk, M., et al., *Copper-Free Sonogashira Coupling for High-Surface-Area Conjugated Microporous Poly(aryleneethynylene) Networks.* Chemistry – A European Journal, 2016. **22**(21): p. 7179-7183.
184. Liu, J., et al., *Facile synthesis of a conjugated microporous polymeric monolith via copper-free Sonogashira–Hagihara cross-coupling in water under aerobic conditions.* Polymer Chemistry, 2015. **6**(41): p. 7251-7255.
185. Doucet, H. and J.-C. Hierso, *Palladium-Based Catalytic Systems for the Synthesis of Conjugated Enynes by Sonogashira Reactions and Related Alkynylations.* Angewandte Chemie International Edition, 2007. **46**(6): p. 834-871.
186. Thorand, S. and N. Krause, *Improved Procedures for the Palladium-Catalyzed Coupling of Terminal Alkynes with Aryl Bromides (Sonogashira Coupling).* The Journal of Organic Chemistry, 1998. **63**(23): p. 8551-8553.
187. Dawson, R., et al., *High Surface Area Conjugated Microporous Polymers: The Importance of Reaction Solvent Choice.* Macromolecules, 2010. **43**(20): p. 8524-8530.
188. Jiang, J.-X., et al., *Conjugated microporous poly(phenylene butadiynylene)s.* Chemical Communications, 2008(4): p. 486-488.
189. Chinchilla, R. and C. Nájera, *Recent advances in Sonogashira reactions.* Chemical Society Reviews, 2011. **40**(10): p. 5084-5121.
190. Budarin, V.L., et al., *Industrial Applications of C-C Coupling Reactions.* CURRENT ORGANIC SYNTHESIS, 2010. **7**(6): p. 614-627.
191. *Palladium-Catalyzed Cross-Coupling Reactions – Industrial Applications*, in *Palladium-Catalyzed Coupling Reactions*. p. 445-489.
192. Bakherad, M., *Recent progress and current applications of Sonogashira coupling reaction in water.* Applied Organometallic Chemistry, 2013. **27**(3): p. 125-140.
193. Zhao, Y., et al., *A perfluorinated covalent triazine-based framework for highly selective and water–tolerant CO2 capture.* Energy & Environmental Science, 2013. **6**(12): p. 3684-3692.
194. Lindemann, P., et al., *Preparation of Freestanding Conjugated Microporous Polymer Nanomembranes for Gas Separation.* Chemistry of Materials, 2014. **26**(24): p. 7189-7193.

195. Talapaneni, S.N., et al., *Pillar[5]arene Based Conjugated Microporous Polymers for Propane/Methane Separation through Host–Guest Complexation.* Chemistry of Materials, 2016. **28**(12): p. 4460-4466.
196. Xie, Y., et al., *Capture and conversion of CO2 at ambient conditions by a conjugated microporous polymer.* Nature Communications, 2013. **4**(1): p. 1960.
197. Liu, Y., et al., *Hydroxyl-Based Hyper-Cross-Linked Microporous Polymers and Their Excellent Performance for CO2 Capture.* Industrial & Engineering Chemistry Research, 2018. **57**(50): p. 17259-17265.
198. Dawson, R., et al., *Functionalized Conjugated Microporous Polymers.* Macromolecules, 2009. **42**(22): p. 8809-8816.
199. Venkata Rao, K., et al., *Dynamic, conjugated microporous polymers: visible light harvesting via guest-responsive reversible swelling.* Physical Chemistry Chemical Physics, 2016. **18**(1): p. 156-163.
200. Chen, L., Y. Yang, and D. Jiang, *CMPs as Scaffolds for Constructing Porous Catalytic Frameworks: A Built-in Heterogeneous Catalyst with High Activity and Selectivity Based on Nanoporous Metalloporphyrin Polymers.* Journal of the American Chemical Society, 2010. **132**(26): p. 9138-9143.
201. Wu, Z.-S., et al., *High-Performance Electrocatalysts for Oxygen Reduction Derived from Cobalt Porphyrin-Based Conjugated Mesoporous Polymers.* Advanced Materials, 2014. **26**(9): p. 1450-1455.
202. He, Y., et al., *Highly Efficient Electrocatalysts for Oxygen Reduction Reaction Based on 1D Ternary Doped Porous Carbons Derived from Carbon Nanotube Directed Conjugated Microporous Polymers.* Advanced Functional Materials, 2016. **26**(45): p. 8255-8265.
203. Jiang, J.-X., et al., *Conjugated Microporous Polymers with Rose Bengal Dye for Highly Efficient Heterogeneous Organo-Photocatalysis.* Macromolecules, 2013. **46**(22): p. 8779-8783.
204. Li, R., et al., *Poly(benzothiadiazoles) and Their Derivatives as Heterogeneous Photocatalysts for Visible-Light-Driven Chemical Transformations.* ACS Catalysis, 2018. **8**(6): p. 4735-4750.
205. Liras, M., M. Iglesias, and F. Sánchez, *Conjugated Microporous Polymers Incorporating BODIPY Moieties as Light-Emitting Materials and Recyclable Visible-Light Photocatalysts.* Macromolecules, 2016. **49**(5): p. 1666-1673.
206. Wang, Z.J., et al., *Bandgap Engineering of Conjugated Nanoporous Poly-benzobisthiadiazoles via Copolymerization for Enhanced Photocatalytic 1,2,3,4-Tetrahydroquinoline Synthesis under Visible Light.* Advanced Synthesis & Catalysis, 2016. **358**(16): p. 2576-2582.
207. Jiang, J.-X., et al., *Band gap engineering in fluorescent conjugated microporous polymers.* Chemical Science, 2011. **2**(9): p. 1777-1781.
208. Xu, Y., A. Nagai, and D. Jiang, *Core–shell conjugated microporous polymers: a new strategy for exploring color-tunable and -controllable light emissions.* Chemical Communications, 2013. **49**(16): p. 1591-1593.
209. Xu, Y., et al., *Light-Emitting Conjugated Polymers with Microporous Network Architecture: Interweaving Scaffold Promotes Electronic Conjugation, Facilitates Exciton Migration, and Improves Luminescence.* Journal of the American Chemical Society, 2011. **133**(44): p. 17622-17625.
210. Liu, X., et al., *Triarylboron-based fluorescent conjugated microporous polymers.* RSC Advances, 2013. **3**(44): p. 21267-21270.
211. Zhang, P., et al., *From Hyperbranched Polymer to Nanoscale CMP (NCMP): Improved Microscopic Porosity, Enhanced Light Harvesting, and Enabled Solution Processing into White-Emitting Dye@NCMP Films.* ACS Macro Letters, 2014. **3**(11): p. 1139-1144.
212. Li, Z., et al., *Triarylboron-Linked Conjugated Microporous Polymers: Sensing and Removal of Fluoride Ions.* Chemistry – A European Journal, 2015. **21**(48): p. 17355-17362.
213. Geng, T.-M., et al., *Conjugated microporous polymer-based carbazole derivatives as fluorescence chemosensors for picronitric acid.* Journal of Materials Science, 2016. **51**(8): p. 4104-4114.

214. Xu, F., et al., *Redox-active conjugated microporous polymers: a new organic platform for highly efficient energy storage.* Chemical Communications, 2014. **50**(37): p. 4788-4790.
215. Liao, Y., et al., *Efficient Supercapacitor Energy Storage Using Conjugated Microporous Polymer Networks Synthesized from Buchwald–Hartwig Coupling.* Advanced Materials, 2018. **30**(12): p. 1705710.
216. Lee, J.-S.M., et al., *Porosity-engineered carbons for supercapacitive energy storage using conjugated microporous polymer precursors.* Journal of Materials Chemistry A, 2016. **4**(20): p. 7665-7673.
217. Li, X.-C., et al., *Redox-active triazatruxene-based conjugated microporous polymers for high-performance supercapacitors.* Chemical Science, 2017. **8**(4): p. 2959-2965.
218. Mothika, V.S., et al., *Regulating Charge-Transfer in Conjugated Microporous Polymers for Photocatalytic Hydrogen Evolution.* Chemistry – A European Journal, 2019. **25**(15): p. 3867-3874.
219. Ma, B.C., et al., *Enhanced visible light promoted antibacterial efficiency of conjugated microporous polymer nanoparticles via molecular doping.* Journal of Materials Chemistry B, 2016. **4**(30): p. 5112-5118.
220. Ma, B.C., et al., *Polymer-Based Module for NAD+ Regeneration with Visible Light.* ChemBioChem, 2019. **20**(20): p. 2593-2596.
221. Qian, Z. and K.A.I. Zhang, *Recent Advances of Conjugated Microporous Polymers in Visible Light-Promoted Chemical Transformations.* Solar RRL. **n/a**(n/a).
222. Yang, C., et al., *Molecular Engineering of Conjugated Polybenzothiadiazoles for Enhanced Hydrogen Production by Photosynthesis.* Angewandte Chemie International Edition, 2016. **55**(32): p. 9202-9206.
223. Li, L., et al., *Rational Design of Porous Conjugated Polymers and Roles of Residual Palladium for Photocatalytic Hydrogen Production.* Journal of the American Chemical Society, 2016. **138**(24): p. 7681-7686.
224. Sprick, R.S., et al., *Tunable Organic Photocatalysts for Visible-Light-Driven Hydrogen Evolution.* Journal of the American Chemical Society, 2015. **137**(9): p. 3265-3270.
225. Yu, X., et al., *Eosin Y-Functionalized Conjugated Organic Polymers for Visible-Light-Driven CO2 Reduction with H2O to CO with High Efficiency.* Angewandte Chemie International Edition, 2019. **58**(2): p. 632-636.
226. Yang, C., et al., *Functional Conjugated Polymers for CO2 Reduction Using Visible Light.* Chemistry – A European Journal, 2018. **24**(66): p. 17454-17458.
227. Li, J., et al., *Adsorption and visible-light photodegradation of organic dyes with TiO2/conjugated microporous polymer composites.* RSC Advances, 2018. **8**(60): p. 34560-34565.
228. Ghasimi, S., et al., *A Conjugated Microporous Polymer for Palladium-Free, Visible Light-Promoted Photocatalytic Stille-Type Coupling Reactions.* Advanced Science, 2017. **4**(8): p. 1700101.
229. Li, R., et al., *Photocatalytic Regioselective and Stereoselective [2 + 2] Cycloaddition of Styrene Derivatives Using a Heterogeneous Organic Photocatalyst.* ACS Catalysis, 2017. **7**(5): p. 3097-3101.
230. Wei, F., et al., *A 1,2,3-triazolyl based conjugated microporous polymer for sensitive detection of p-nitroaniline and Au nanoparticle immobilization.* Polymer Chemistry, 2018. **9**(27): p. 3832-3839.
231. Hou, H.-J., et al., *Conjugated microporous poly(benzothiadiazole)/TiO2 heterojunction for visible-light-driven H2 production and pollutant removal.* Applied Catalysis B: Environmental, 2017. **203**: p. 563-571.
232. Krishnaraj, C., et al., *Covalent triazine frameworks – a sustainable perspective.* Green Chemistry, 2020. **22**(4): p. 1038-1071.
233. Zhang, Y. and S. Jin, *Recent Advancements in the Synthesis of Covalent Triazine Frameworks for Energy and Environmental Applications.* Polymers, 2018. **11**.

234. Xie, J., et al., *Efficient visible light-driven water oxidation and proton reduction by an ordered covalent triazine-based framework.* Energy & Environmental Science, 2018. **11**(6): p. 1617-1624.
235. Katekomol, P., et al., *Covalent Triazine Frameworks Prepared from 1,3,5-Tricyanobenzene.* Chemistry of Materials, 2013. **25**(9): p. 1542-1548.
236. Bojdys, M.J., et al., *Rational Extension of the Family of Layered, Covalent, Triazine-Based Frameworks with Regular Porosity.* Advanced Materials, 2010. **22**(19): p. 2202-2205.
237. Hug, S., et al., *A functional triazine framework based on N-heterocyclic building blocks.* Journal of Materials Chemistry, 2012. **22**(28): p. 13956-13964.
238. Bavykina, A.V., et al., *Facile Method for the Preparation of Covalent Triazine Framework coated Monoliths as Catalyst Support: Applications in C1 Catalysis.* ACS Applied Materials & Interfaces, 2017. **9**(31): p. 26060-26065.
239. Hug, S., et al., *Nitrogen-Rich Covalent Triazine Frameworks as High-Performance Platforms for Selective Carbon Capture and Storage.* Chemistry of Materials, 2015. **27**(23): p. 8001-8010.
240. Mukherjee, S., et al., *Newly designed 1,2,3-triazole functionalized covalent triazine frameworks with exceptionally high uptake capacity for both CO2 and H2.* Journal of Materials Chemistry A, 2019. **7**(3): p. 1055-1068.
241. Wang, K., et al., *A thiophene-containing covalent triazine-based framework with ultramicropore for CO2 capture.* Journal of Energy Chemistry, 2017. **26**(5): p. 902-908.
242. Geng, T., et al., *A covalent triazine-based framework from tetraphenylthiophene and 2,4,6-trichloro-1,3,5-triazine motifs for sensing o-nitrophenol and effective I2 uptake.* Polymer Chemistry, 2018. **9**(6): p. 777-784.
243. Kuhn, P., M. Antonietti, and A. Thomas, *Porous, Covalent Triazine-Based Frameworks Prepared by Ionothermal Synthesis.* Angewandte Chemie International Edition, 2008. **47**(18): p. 3450-3453.
244. Osadchii, D.Y., et al., *Revisiting Nitrogen Species in Covalent Triazine Frameworks.* Langmuir, 2017. **33**(50): p. 14278-14285.
245. Ren, S., et al., *Porous, Fluorescent, Covalent Triazine-Based Frameworks Via Room-Temperature and Microwave-Assisted Synthesis.* Advanced Materials, 2012. **24**(17): p. 2357-2361.
246. Liu, J., et al., *Solution Synthesis of Semiconducting Two-Dimensional Polymer via Trimerization of Carbonitrile.* Journal of the American Chemical Society, 2017. **139**(34): p. 11666-11669.
247. Yu, S.-Y., et al., *Direct Synthesis of a Covalent Triazine-Based Framework from Aromatic Amides.* Angewandte Chemie International Edition, 2018. **57**(28): p. 8438-8442.
248. Liu, M., et al., *Crystalline Covalent Triazine Frameworks by In Situ Oxidation of Alcohols to Aldehyde Monomers.* Angewandte Chemie International Edition, 2018. **57**(37): p. 11968-11972.
249. Wang, K., et al., *Covalent Triazine Frameworks via a Low-Temperature Polycondensation Approach.* Angewandte Chemie International Edition, 2017. **56**(45): p. 14149-14153.
250. Puthiaraj, P., et al., *Microporous covalent triazine polymers: efficient Friedel–Crafts synthesis and adsorption/storage of CO2 and CH4.* Journal of Materials Chemistry A, 2015. **3**(13): p. 6792-6797.
251. Huang, W., et al., *Hollow nanoporous covalent triazine frameworks via acid vapor-assisted solid phase synthesis for enhanced visible light photoactivity.* Journal of Materials Chemistry A, 2016. **4**(20): p. 7555-7559.
252. Bi, J., et al., *Covalent Triazine-Based Frameworks as Visible Light Photocatalysts for the Splitting of Water.* Macromolecular Rapid Communications, 2015. **36**(20): p. 1799-1805.
253. Huang, W., et al., *Asymmetric Covalent Triazine Framework for Enhanced Visible-Light Photoredox Catalysis via Energy Transfer Cascade.* Angewandte Chemie International Edition, 2018. **57**(27): p. 8316-8320.

254. Varma, R.S., *Journey on greener pathways: from the use of alternate energy inputs and benign reaction media to sustainable applications of nano-catalysts in synthesis and environmental remediation.* Green Chemistry, 2014. **16**(4): p. 2027-2041.
255. Hailes, H.C., *Reaction Solvent Selection: The Potential of Water as a Solvent for Organic Transformations.* Organic Process Research & Development, 2007. **11**(1): p. 114-120.
256. Varma, R.S., *Greener and Sustainable Chemistry.* Applied Sciences, 2014. **4**(4).
257. Marcott, C., *Modern Techniques in Applied Molecular Spectroscopy: Techniques in Analytical Chemistry Edited by Francis M. Mirabella (Equistar Chemicals, LP). John Wiley & Sons: New York. 1998. xvi + 410 pp. $59.95. ISBN 0-471-12359-5.* Journal of the American Chemical Society, 1999. **121**(15): p. 3809-3810.
258. Maikowski, M.A., *G. Kortüm: Reflexionsspektroskopie. Grundlagen, Methodik, Anwendungen. Springer-Verlag, Berlin, Heidelberg, New York 1969. VIII, 378 Seiten, 160 Abbildungen. Preis: DM 86,—.* Berichte der Bunsengesellschaft für physikalische Chemie, 1969. **73**(8-9): p. 935-936.
259. Escobar-Barrios, V., et al., *FTIR - An Essential Characterization Technique for Polymeric Materials*. 2012.
260. Goldstein, J., et al., *Scanning electron microscopy and x-ray microanalysis*. 2018, New York, NY: Springer.
261. Franken, L.E., et al., *A Technical Introduction to Transmission Electron Microscopy for Soft-Matter: Imaging, Possibilities, Choices, and Technical Developments.* Small, 2020. **16**(14): p. 1906198.
262. Brunauer, S., P.H. Emmett, and E. Teller, *Adsorption of Gases in Multimolecular Layers.* Journal of the American Chemical Society, 1938. **60**(2): p. 309-319.
263. Yurdakal, S., et al., *Chapter 4 - (Photo)catalyst Characterization Techniques: Adsorption Isotherms and BET, SEM, FTIR, UV–Vis, Photoluminescence, and Electrochemical Characterizations*, in *Heterogeneous Photocatalysis*, G. Marcì and L. Palmisano, Editors. 2019, Elsevier. p. 87-152.
264. Bardestani, R., G.S. Patience, and S. Kaliaguine, *Experimental methods in chemical engineering: specific surface area and pore size distribution measurements—BET, BJH, and DFT.* The Canadian Journal of Chemical Engineering, 2019. **97**(11): p. 2781-2791.
265. Sing, K., *Reporting Physisorption Data for Gas/Solid Systems with Special Reference to the Determination of Surface Area and Porosity.* Pure and Applied Chemistry - PURE APPL CHEM, 1982. **54**: p. 2201-2218.
266. Borchert, H., *Cyclic Voltammetry*, in *Solar Cells Based on Colloidal Nanocrystals*, H. Borchert, Editor. 2014, Springer International Publishing: Cham. p. 111-117.
267. Elgrishi, N., et al., *A Practical Beginner's Guide to Cyclic Voltammetry.* Journal of Chemical Education, 2018. **95**(2): p. 197-206.
268. Goodman, B.A. and P.L. Hall, *Electron paramagnetic resonance spectroscopy*, in *Clay Mineralogy: Spectroscopic and Chemical Determinative Methods*, M.J. Wilson, Editor. 1994, Springer Netherlands: Dordrecht. p. 173-225.
269. Junk, M.J.N., *Electron Paramagnetic Resonance Theory*, in *Assessing the Functional Structure of Molecular Transporters by EPR Spectroscopy*, M. J.N.Junk, Editor. 2012, Springer Berlin Heidelberg: Berlin, Heidelberg. p. 7-52.
270. Reber, E.A., *Gas Chromatography-Mass Spectrometry (GC-MS): Applications in Archaeology*, in *Encyclopedia of Global Archaeology*. 2018, Springer International Publishing: Cham. p. 1-17.
271. Kogan, V., M.M. Quintal, and R. Neumann, *Regioselective Alkene Carbon−Carbon Bond Cleavage to Aldehydes and Chemoselective Alcohol Oxidation of Allylic Alcohols with Hydrogen Peroxide Catalyzed by [cis-Ru(II)(dmp)2(H2O)2]2+ (dmp = 2,9-dimethylphenanthroline).* Organic Letters, 2005. **7**(22): p. 5039-5042.
272. Liu, B., et al., *Au–Carbon Electronic Interaction Mediated Selective Oxidation of Styrene.* ACS Catalysis, 2017. **7**(5): p. 3483-3488.

273. Oliveira, A.P.S., et al., *Catalytic performance of MnFeSi composite in selective oxidation of styrene, ethylbenzene and benzyl alcohol.* Molecular Catalysis, 2017. **436**: p. 29-42.
274. Rubinstein, A., et al., *Aerobic Carbon–Carbon Bond Cleavage of Alkenes to Aldehydes Catalyzed by First-Row Transition-Metal-Substituted Polyoxometalates in the Presence of Nitrogen Dioxide.* Journal of the American Chemical Society, 2014. **136**(31): p. 10941-10948.
275. Wang, B., et al., *Selective oxidation of styrene to 1,2-epoxyethylbenzene by hydrogen peroxide over heterogeneous phosphomolybdic acid supported on ionic liquid modified MCM-41.* Chemical Engineering Journal, 2015. **260**: p. 172-177.
276. Liu, B., et al., *Wacker-Type Oxidation Using an Iron Catalyst and Ambient Air: Application to Late-Stage Oxidation of Complex Molecules.* Angewandte Chemie International Edition, 2017. **56**(41): p. 12712-12717.
277. Khemnar, A.B. and B.M. Bhanage, *Iron catalyzed efficient synthesis of 2-arylbenzothiazoles from benzothiazole and olefins using environmentally benign molecular oxygen as oxidant.* RSC Advances, 2014. **4**(18): p. 8939-8942.
278. Oliveira, A.P.S., et al., *Styrene Oxidation to Valuable Compounds over Nanosized FeCo-Based Catalysts: Effect of the Third Metal Addition.* Catalysts, 2017. **7**(11): p. 323.
279. Feng, B., et al., *Selective aerobic oxidation of styrene to benzaldehyde catalyzed by water-soluble palladium(II) complex in water.* Green Chemistry, 2009. **11**(9): p. 1446-1452.
280. Zhang, Z., et al., *Wacker Oxidation of Terminal Alkenes Over ZrO2-Supported Pd Nanoparticles Under Acid- and Cocatalyst-Free Conditions.* ChemSusChem, 2017. **10**(17): p. 3482-3489.
281. Guo, Y., et al., *Highly selective epoxidation of styrene over mesoporous Au–Ti–SBA-15 via photocatalysis process: Synthesis, characterization, and catalytic application.* Applied Surface Science, 2011. **258**(3): p. 1082-1090.
282. Shen, D., et al., *Photocatalytic Asymmetric Epoxidation of Terminal Olefins Using Water as an Oxygen Source in the Presence of a Mononuclear Non-Heme Chiral Manganese Complex.* Journal of the American Chemical Society, 2016. **138**(49): p. 15857-15860.
283. Singh, A.K., R. Chawla, and L.D.S. Yadav, *Eosin Y catalyzed visible light mediated aerobic photo-oxidative cleavage of the C–C double bond of styrenes.* Tetrahedron Letters, 2015. **56**(5): p. 653-656.
284. Zhang, K., et al., *Surface area control and photocatalytic activity of conjugated microporous poly(benzothiadiazole) networks.* Angewandte Chemie International Edition, 2013. **52**(5): p. 1432-6.
285. Ghasimi, S., et al., *A Conjugated Microporous Polymer for Palladium-Free, Visible Light-Promoted Photocatalytic Stille-Type Coupling Reactions.* Advanced Science, 2017. **4**(8): p. 1700101-n/a.
286. Jeehye, B., et al., *CO2-Triggered Switchable Hydrophilicity of a Heterogeneous Conjugated Polymer Photocatalyst for Enhanced Catalytic Activity in Water.* Angewandte Chemie International Edition, 2018. **57**(11): p. 2967-2971.
287. Wang, Z.J., et al., *Highly porous conjugated polymers for selective oxidation of organic sulfides under visible light.* Chemical Communications, 2014. **50**: p. 8177-8180.
288. Wang, Z.J., et al., *Molecular Structural Design of Conjugated Microporous Poly(Benzooxadiazole) Networks for Enhanced Photocatalytic Activity with Visible Light.* Adv Mater, 2015. **27**(40): p. 6265-70.
289. Kang, N., et al., *Tandem synthesis of photoactive benzodifuran moieties in the formation of microporous organic networks.* Angewandte Chemie-International Edition, 2013. **52**(24): p. 6228-32.
290. Wang, Z.J., et al., *A conjugated porous poly-benzobisthiadiazole network for a visible light-driven photoredox reaction.* Journal of Materials Chemistry A, 2014. **2**(44): p. 18720-18724.
291. Huang, W., et al., *A fixed-bed photoreactor using conjugated nanoporous polymer-coated glass fibers for visible light-promoted continuous photoredox reactions.* Journal of Materials Chemistry A, 2017. **5**(8): p. 3792-3797.

292. Luo, J., X. Zhang, and J. Zhang, *Carbazolic Porous Organic Framework as an Efficient, Metal-Free Visible-Light Photocatalyst for Organic Synthesis.* ACS Catalysis, 2015. **5**(4): p. 2250-2254.
293. Wang, Z.J., K. Landfester, and K.A.I. Zhang, *Hierarchically Porous pi-Conjugated PolyHIPE as Heterogeneous Photoinitiator for Free Radical Polymerization under Visible Light.* Polym. Chem., 2014. **5**: p. 3559-3562.
294. Dadashi-Silab, S., et al., *Microporous Thioxanthone Polymers as Heterogeneous Photoinitiators for Visible Light Induced Free Radical and Cationic Polymerizations.* Macromolecules, 2014. **47**(14): p. 4607-4614.
295. Li, R., et al., *Photocatalytic Regioselective and Stereoselective [2 + 2] Cycloaddition of Styrene Derivatives Using a Heterogeneous Organic Photocatalyst.* ACS Catalysis, 2017. **7**: p. 3097-3101.
296. Battula, V.R., et al., *Natural Sunlight Driven Oxidative Homocoupling of Amines by a Truxene-Based Conjugated Microporous Polymer.* ACS Catalysis, 2018: p. 6751-6759.
297. Zhang, W., et al., *Visible Light-Driven C-3 Functionalization of Indoles over Conjugat-ed Microporous Polymers.* ACS Catalysis, 2018.
298. Sprick, R.S., et al., *Maximising the hydrogen evolution activity in organic photocatalysts by co-polymerisation.* Journal of Materials Chemistry A, 2018. **6**(25): p. 11994-12003.
299. Ayed, C., et al., *Conjugated Microporous Polymers with Immobilized TiO2 Nanoparticles for Enhanced Visible Light Photocatalysis.* Particle & Particle Systems Characterization, 2018. **35**(1): p. 1700234-n/a.
300. Latonen, R.-M., C. Kvarnström, and A. Ivaska, *In situ UV–vis and FTIR attenuated total reflectance studies on the electrochemically synthesized copolymer from biphenyl and 3-octylthiophene.* Journal of Electroanalytical Chemistry, 2001. **512**(1): p. 36-48.
301. Ghosh, S., et al., *Visible-light active conducting polymer nanostructures with superior photocatalytic activity.* Scientific Reports, 2015. **5**: p. 18002.
302. Li, R., et al., *Photocatalytic Selective Bromination of Electron-Rich Aromatic Compounds Using Microporous Organic Polymers with Visible Light.* ACS Catalysis, 2016. **6**(2): p. 1113-1121.
303. Ren, Y., et al., *Selective photooxidation of styrene in organic-water biphasic media.* New Journal of Chemistry, 2004. **28**(12): p. 1464-1469.
304. Yadav, G.D. and A.A. Pujari, *Epoxidation of Styrene to Styrene Oxide: Synergism of Heteropoly Acid and Phase-Transfer Catalyst under Ishii−Venturello Mechanism.* Organic Process Research & Development, 2000. **4**(2): p. 88-93.
305. Handley, M.F., *Production of styrene oxide*. 1957, DOW CHEMICAL CO: United States.
306. Khan, N.-u.H.G., IN), Razi Abdi, Sayed Hasan (Gujarat, IN), Kureshy, Rukhsana Ilyas (Gujarat, IN), Singh, Surendra (Gujarat, IN), Ahmed, Irshad (Gujarat, IN), Jasra, Raksh Vir (Gujarat, IN), Ghosh, Pushpito Kumar (Gujarat, IN), *Catalytic process for the preparation of epoxides from alkenes*. 2005: United States.
307. Nishibe, K.T., JP), Rengakuji, Seiichi (Toyama, JP), Inoue, Masami (Toyama, JP), Ohura, Osami (Fuji, JP), Nitoh, Hirohisa (Fuji, JP), *Process for preparing styrene oxide*. 1992, Tokai Denka Kogyo Kabushiki Kaisha (Tokyo, JP): United States.
308. Chandra, B., K.K. Singh, and S.S. Gupta, *Selective photocatalytic hydroxylation and epoxidation reactions by an iron complex using water as the oxygen source.* Chemical Science, 2017. **8**(11): p. 7545-7551.
309. Huang, Y., et al., *Stable Copper Nanoparticle Photocatalysts for Selective Epoxidation of Alkenes with Visible Light.* ACS Catalysis, 2017. **7**(8): p. 4975-4985.
310. Li, X. and C. Kutal, *Photocatalytic selective epoxidation of styrene by molecular oxygen over highly dispersed titanium dioxide species on silica.* Journal of Materials Science Letters, 2002. **21**(19): p. 1525-1527.
311. Wang, G., et al., *Styrene epoxidation over V-SBA-15 with alkaline-earth metal ion promotion under photo-assisted conditions.* Applied Catalysis A: General, 2012. **413-414**: p. 52-61.

312. Muñoz-Batista, M.J., et al., *Green photo-oxidation of styrene over W–Ti composite catalysts.* Journal of Catalysis, 2014. **309**: p. 428-438.
313. Ding, Z., et al., *Synthesis of Transition Metal-Modified Carbon Nitride Polymers for Selective Hydrocarbon Oxidation.* ChemSusChem, 2011. **4**(2): p. 274-281.
314. Bian, G., et al., *Light driven epoxidation of olefins using a graphene oxide/g-C3N4 supported Mo (salen) complex.* New Journal of Chemistry, 2018. **42**(1): p. 85-90.
315. Guo, L., et al., *Engineering heteroatoms with atomic precision in donor–acceptor covalent triazine frameworks to boost photocatalytic hydrogen production.* Journal of Materials Chemistry A, 2018. **6**(40): p. 19775-19781.
316. Chen, T., et al., *Direct synthesis of covalent triazine-based frameworks (CTFs) through aromatic nucleophilic substitution reactions.* RSC Advances, 2019. **9**(31): p. 18008-18012.
317. Rubio, F., J. Rubio, and J.L. Oteo, *A FT-IR Study of the Hydrolysis of Tetraethylorthosilicate (TEOS).* Spectroscopy Letters, 1998. **31**: p. 199.
318. Jayakumar, J. and H.-H. Chou, *Recent Advances in Visible-Light-Driven Hydrogen Evolution from Water using Polymer Photocatalysts.* ChemCatChem, 2020. **12**(3): p. 689-704.
319. Yao, H. and D.E. Richardson, *Epoxidation of Alkenes with Bicarbonate-Activated Hydrogen Peroxide.* Journal of the American Chemical Society, 2000. **122**(13): p. 3220-3221.
320. Ansari, M.B., E.-Y. Jeong, and S.-E. Park, *Styrene Epoxidation in Aqueous over Triazine-Based Microporous Polymeric Network as a Metal-Free Catalyst.* Green and Sustainable Chemistry, 2012. **02**.
321. Bader, H., V. Sturzenegger, and J. Hoigné, *Photometric method for the determination of low concentrations of hydrogen peroxide by the peroxidase catalyzed oxidation of N,N-diethyl-p-phenylenediamine (DPD).* Water Research, 1988. **22**(9): p. 1109-1115.
322. Zou, J., et al., *Spectrophotometric determination of trace hydrogen peroxide via the oxidative coloration of DPD using a Fenton system.* Chemosphere, 2019. **224**: p. 646-652.
323. Gudkov, S.V., et al., *Generation of reactive oxygen species in water under exposure to visible or infrared irradiation at absorption bands of molecular oxygen.* Biophysics, 2012. **57**(1): p. 1-8.
324. Kofuji, Y., et al., *Graphitic Carbon Nitride Doped with Biphenyl Diimide: Efficient Photocatalyst for Hydrogen Peroxide Production from Water and Molecular Oxygen by Sunlight.* ACS Catalysis, 2016. **6**(10): p. 7021-7029.
325. Hu, L., et al., *Recent advances in catalytic transformation of biomass-derived 5-hydroxymethylfurfural into the innovative fuels and chemicals.* Renewable and Sustainable Energy Reviews, 2017. **74**: p. 230-257.
326. Kucherov, F.A., et al., *Chemical Transformations of Biomass-Derived C6-Furanic Platform Chemicals for Sustainable Energy Research, Materials Science, and Synthetic Building Blocks.* ACS Sustainable Chemistry & Engineering, 2018. **6**(7): p. 8064-8092.
327. Sudarsanam, P., et al., *Functionalised heterogeneous catalysts for sustainable biomass valorisation.* Chemical Society Reviews, 2018. **47**(22): p. 8349-8402.
328. Kong, X., et al., *Catalytic conversion of 5-hydroxymethylfurfural to some value-added derivatives.* Green Chemistry, 2018. **20**(16): p. 3657-3682.
329. Xia, H., et al., *Efficient conversion of 5-hydroxymethylfurfural to high-value chemicals by chemo- and bio-catalysis.* RSC Advances, 2018. **8**(54): p. 30875-30886.
330. Yang, Z., et al., *3D Flower-like Micro/Nano Ce–Mo Composite Oxides as Effective Bifunctional Catalysts for One-Pot Conversion of Fructose to 2,5-Diformylfuran.* ACS Sustainable Chemistry & Engineering, 2017. **5**(5): p. 4179-4187.
331. Zhang, Z., et al., *Iron Oxide Encapsulated by Ruthenium Hydroxyapatite as Heterogeneous Catalyst for the Synthesis of 2,5-Diformylfuran.* ChemSusChem, 2014. **7**(12): p. 3496-3504.
332. Rosatella, A.A., et al., *5-Hydroxymethylfurfural (HMF) as a building block platform: Biological properties, synthesis and synthetic applications.* Green Chemistry, 2011. **13**(4): p. 754-793.
333. Li, H., et al., *Zeolite and zeotype-catalysed transformations of biofuranic compounds.* Green Chemistry, 2016. **18**(21): p. 5701-5735.

334. Gallezot, P., *Conversion of biomass to selected chemical products.* Chemical Society Reviews, 2012. **41**(4): p. 1538-1558.
335. Ma, J. and Z. Sun, *Mutual Information Is Copula Entropy.* Tsinghua Science & Technology, 2011. **16**(1): p. 51-54.
336. Sarmah, B., B. Satpati, and R. Srivastava, *Selective Oxidation of Biomass-Derived Alcohols and Aromatic and Aliphatic Alcohols to Aldehydes with O2/Air Using a RuO2-Supported Mn3O4 Catalyst.* ACS Omega, 2018. **3**(7): p. 7944-7954.
337. Gui, Z., et al., *Highly Selective Aerobic Oxidation of 5-Hydroxymethyl Furfural into 2,5-Diformylfuran over Mn–Co Binary Oxides.* ChemistrySelect, 2017. **2**(23): p. 6632-6639.
338. Artz, J., S. Mallmann, and R. Palkovits, *Selective Aerobic Oxidation of HMF to 2,5-Diformylfuran on Covalent Triazine Frameworks-Supported Ru Catalysts.* ChemSusChem, 2015. **8**(4): p. 672-679.
339. Nie, J. and H. Liu, *Efficient aerobic oxidation of 5-hydroxymethylfurfural to 2,5-diformylfuran on manganese oxide catalysts.* Journal of Catalysis, 2014. **316**: p. 57-66.
340. Grasset, F.L., et al., *Selective oxidation of 5-hydroxymethylfurfural to 2,5-diformylfuran over intercalated vanadium phosphate oxides.* RSC Advances, 2013. **3**(25): p. 9942-9948.
341. Li, Y., et al., *Fabrication of Trifunctional Polyoxometalate-Decorated Chitosan Nanofibers for Selective Production of 2,5-Diformylfuran.* ChemSusChem, 2019. **12**(15): p. 3515-3523.
342. Ke, Q., et al., *Boosting the activity of catalytic oxidation of 5-hydroxymethylfurfural to 2,5-diformylfuran over nitrogen-doped manganese oxide catalysts.* Green Chemistry, 2019. **21**(16): p. 4313-4318.
343. Kisszekelyi, P., et al., *Selective Electrocatalytic Oxidation of Biomass-derived 5-Hydroxymethylfurfural (HMF) to 2,5-Diformylfuran (DFF): From Mechanistic Investigations to Catalyst Recovery.* ChemSusChem. **n/a**(n/a).
344. Wu, Q., et al., *Photocatalytic selective oxidation of biomass-derived 5-hydroxymethylfurfural to 2,5-diformylfuran on metal-free g-C3N4 under visible light irradiation.* Molecular Catalysis, 2017. **436**: p. 10-18.
345. Ma, B., et al., *Photocatalytic synthesis of 2,5-diformylfuran from 5-hydroxymethyfurfural or fructose over bimetallic Au-Ru nanoparticles supported on reduced graphene oxides.* Applied Catalysis A: General, 2018. **552**: p. 70-76.
346. Han, G., et al., *Visible-Light-Driven Valorization of Biomass Intermediates Integrated with H2 Production Catalyzed by Ultrathin Ni/CdS Nanosheets.* Journal of the American Chemical Society, 2017. **139**(44): p. 15584-15587.
347. Battula, V.R., A. Jaryal, and K. Kailasam, *Visible light-driven simultaneous H2 production by water splitting coupled with selective oxidation of HMF to DFF catalyzed by porous carbon nitride.* Journal of Materials Chemistry A, 2019. **7**(10): p. 5643-5649.
348. Lu, W., et al., *Porous Polymer Networks: Synthesis, Porosity, and Applications in Gas Storage/Separation.* Chemistry of Materials, 2010. **22**(21): p. 5964-5972.
349. Wu, J., et al., *Porous Polymers as Multifunctional Material Platforms toward Task-Specific Applications.* Advanced Materials, 2019. **31**(4): p. 1802922.
350. Cheng, G., et al., *Soluble Conjugated Microporous Polymers.* Angewandte Chemie International Edition, 2012. **51**(51): p. 12727-12731.
351. Zhang, P., et al., *Solution-Dispersible, Colloidal, Conjugated Porous Polymer Networks with Entrapped Palladium Nanocrystals for Heterogeneous Catalysis of the Suzuki–Miyaura Coupling Reaction.* Chemistry of Materials, 2011. **23**(23): p. 5243-5249.
352. Huang, W., et al., *Visible-Light-Promoted Selective Oxidation of Alcohols Using a Covalent Triazine Framework.* ACS Catalysis, 2017. **7**(8): p. 5438-5442.
353. Schareina, T., et al., *Copper-Catalyzed Cyanation of Heteroaryl Bromides: A Novel and Versatile Catalyst System Inspired by Nature.* Synlett, 2007. **2007**(04): p. 0555-0558.
354. Mureddu, M., et al., *MeOx/SBA-15 (Me = Zn, Fe): highly efficient nanosorbents for mid-temperature H2S removal.* Journal of Materials Chemistry A, 2014. **2**(45): p. 19396-19406.

355. Antonyraj, C.A., et al., *Selective oxidation of HMF to DFF using Ru/γ-alumina catalyst in moderate boiling solvents toward industrial production.* Journal of Industrial and Engineering Chemistry, 2013. **19**(3): p. 1056-1059.
356. Özcan, L., et al., *Selective photoelectrocatalytic oxidation of 5-(hydroxymethyl)-2-furaldehyde in water by using Pt loaded nanotube structure of TiO2 on Ti photoanodes.* Catalysis Today, 2017. **281**: p. 205-213.
357. Zhang, H., et al., *Photocatalytic Selective Oxidation of 5-Hydroxymethylfurfural to 2,5-Diformylfuran over Nb2O5 under Visible Light.* ACS Sustainable Chemistry & Engineering, 2017. **5**(4): p. 3517-3523.
358. Nardi, G., et al., *Scope and limitations of the TEMPO/EPR method for singlet oxygen detection: the misleading role of electron transfer.* Free Radical Biology and Medicine, 2014. **77**: p. 64-70.
359. Göttinger, H.A., V.E. Zubarev, and O. Brede, *Low-temperature EPR study of the reaction of the 2,2,6,6-tetramethylpiperidyl radical with molecular oxygen. Direct spectroscopic observation of an aminylperoxyl radical.* Journal of the Chemical Society, Perkin Transactions 2, 1997(11): p. 2167-2172.
360. Clément, J.-L., et al., *Assignment of the EPR Spectrum of 5,5-Dimethyl-1-pyrroline N-Oxide (DMPO) Superoxide Spin Adduct.* The Journal of Organic Chemistry, 2005. **70**(4): p. 1198-1203.
361. Ancona, A., et al., *Lipid-Coated Zinc Oxide Nanoparticles as Innovative ROS-Generators for Photodynamic Therapy in Cancer Cells.* Nanomaterials, 2018. **8**(3): p. 143.
362. Chauvin, J., et al., *Analysis of reactive oxygen and nitrogen species generated in three liquid media by low temperature helium plasma jet.* Scientific Reports, 2017. **7**(1): p. 4562.
363. Ventura, M., et al., *Selective Aerobic Oxidation of 5-Hydroxymethylfurfural to 2,5-Diformylfuran or 2-Formyl-5-furancarboxylic Acid in Water by using MgO·CeO2 Mixed Oxides as Catalysts.* ChemSusChem, 2018. **11**(8): p. 1305-1315.
364. Byun, J., K. Landfester, and K.A.I. Zhang, *Conjugated Polymer Hydrogel Photocatalysts with Expandable Photoactive Sites in Water.* Chemistry of Materials, 2019. **31**(9): p. 3381-3387.
365. Ilkaeva, M., et al., *Selective photocatalytic oxidation of 5-hydroxymethyl-2-furfural in aqueous suspension of polymeric carbon nitride and its adduct with H2O2 in a solar pilot plant.* Catalysis Today, 2018. **315**: p. 138-148.
366. Mehrabi-Kalajahi, S.S., M. Hajimohammadi, and N. Safari, *Selective photocatalytic oxidation of alcohols to corresponding aldehydes in solvent-free conditions using porphyrin sensitizers.* Journal of the Iranian Chemical Society, 2016. **13**(6): p. 1069-1076.
367. Wan, P., et al., *Photooxygenation of nitrobenzyl derivatives. Mechanisms of photogeneration and hydrolysis of α-hydroperoxy nitrobenzyl ethers.* Canadian Journal of Chemistry, 1987. **65**(8): p. 1775-1783.
368. Zhu, G., et al., *Formation of Strong Basicity on Covalent Triazine Frameworks as Catalysts for the Oxidation of Methylene Compounds.* ACS Applied Materials & Interfaces, 2018. **10**(15): p. 12612-12617.
369. Streat, M. and L.A. Sweetland, *Removal of Pesticides from Water Using Hypercrosslinked Polymer Phases: Part 2— Sorption Studies.* Process Safety and Environmental Protection, 1998. **76**(2): p. 127-134.
370. Penner, N.A., et al., *Investigation of the properties of hypercrosslinked polystyrene as a stationary phase for high-performance liquid chromatography.* Chromatographia, 1999. **50**(9): p. 611-620.
371. Kuhn, P., et al., *"Everything is surface": tunable polymer organic frameworks with ultrahigh dye sorption capacity.* Chemical Communications, 2008(44): p. 5815-5817.
372. Law, K.-Y., *Definitions for Hydrophilicity, Hydrophobicity, and Superhydrophobicity: Getting the Basics Right.* The Journal of Physical Chemistry Letters, 2014. **5**(4): p. 686-688.

373. Chen, J., et al., *Multimorphology Mesoporous Silica Nanoparticles for Dye Adsorption and Multicolor Luminescence Applications.* ACS Sustainable Chemistry & Engineering, 2018. **6**(3): p. 3533-3545.
374. Li, H., et al., *Facile Synthesis and Enhanced Visible-Light Photocatalysis of Graphitic Carbon Nitride Composite Semiconductors.* ChemSusChem, 2015. **8**(7): p. 1189-1196.
375. Ghosh, S., et al., *Conducting polymer nanostructures for photocatalysis under visible light.* Nature Materials, 2015. **14**: p. 505.
376. Yu, L., Y. Mao, and L. Qu, *Simple Voltammetric Determination of Rhodamine B by Using the Glassy Carbon Electrode in Fruit Juice and Preserved Fruit.* Food Analytical Methods, 2013. **6**(6): p. 1665-1670.
377. Huang, H.-B., et al., *Photodegradation of Rhodamine B over Biomass-Derived Activated Carbon Supported CdS Nanomaterials under Visible Irradiation.* Frontiers in Chemistry, 2017. **5**(123).
378. Mukthar Ali, M., J.S. Arya Nair, and K.Y. Sandhya, *Role of reactive oxygen species in the visible light photocatalytic mineralization of rhodamine B dye by P25–carbon dot photocatalyst.* Dyes and Pigments, 2019. **163**: p. 274-284.
379. Guo, F., et al., *Activation of peroxymonosulfate by magnetic carbon supported Prussian blue nanocomposite for the degradation of organic contaminants with singlet oxygen and superoxide radicals.* Chemosphere, 2019. **218**: p. 1071-1081.
380. Zhang, K., et al., *[small pi]-Conjugated polyHIPEs as highly efficient and reusable heterogeneous photosensitizers.* Chemical Communications, 2013. **49**(95): p. 11158-11160.
381. Wang, Z.J., et al., *Molecular Structural Design of Conjugated Microporous Poly(Benzooxadiazole) Networks for Enhanced Photocatalytic Activity with Visible Light.* Advanced Materials, 2015. **27**(40): p. 6265-6270.
382. Heeger, A.J., *25th Anniversary Article: Bulk Heterojunction Solar Cells: Understanding the Mechanism of Operation.* Advanced Materials, 2014. **26**(1): p. 10-28.
383. Dennler, G., M.C. Scharber, and C.J. Brabec, *Polymer-Fullerene Bulk-Heterojunction Solar Cells.* Advanced Materials, 2009. **21**(13): p. 1323-1338.
384. Lu, L., et al., *Recent Advances in Bulk Heterojunction Polymer Solar Cells.* Chemical Reviews, 2015. **115**(23): p. 12666-12731.
385. Huang, Y., et al., *Bulk Heterojunction Solar Cells: Morphology and Performance Relationships.* Chemical Reviews, 2014. **114**(14): p. 7006-7043.
386. Scharber, M.C. and N.S. Sariciftci, *Efficiency of bulk-heterojunction organic solar cells.* Progress in Polymer Science, 2013. **38**(12): p. 1929-1940.
387. Wang, S., et al., *Highly efficient visible light induced photocatalytic activity of a novel in situ synthesized conjugated microporous poly(benzothiadiazole)–C3N4 composite.* Catalysis Science & Technology, 2017. **7**(2): p. 418-426.
388. Wang, L., et al., *Van der Waals Heterostructures Comprised of Ultrathin Polymer Nanosheets for Efficient Z-Scheme Overall Water Splitting.* Angewandte Chemie International Edition, 2018. **57**(13): p. 3454-3458.
389. Hammedi, T., et al., *Comparative study of textural, structural and catalytic properties of xerogels and aerogels CeO2–TiO2 mixed oxides.* Journal of Porous Materials, 2015. **22**(4): p. 939-948.
390. Bagheri, S., K. Shameli, and S.B. Abd Hamid, *Synthesis and Characterization of Anatase Titanium Dioxide Nanoparticles Using Egg White Solution via Sol-Gel Method.* Journal of Chemistry, 2013. **2013**: p. 5.
391. Mugundan, S., et al., *Synthesis and characterization of undoped and cobalt-doped TiO2 nanoparticles via sol–gel technique.* Applied Nanoscience, 2015. **5**(4): p. 449-456.
392. Zhang, K., et al., *Surface Area Control and Photocatalytic Activity of Conjugated Microporous Poly(benzothiadiazole) Networks.* Angewandte Chemie, 2013. **125**(5): p. 1472-1476.
393. Raza, F., et al., *Visible-Light-Driven Oxidative Coupling Reactions of Amines by Photoactive WS2 Nanosheets.* ACS Catalysis, 2016. **6**(5): p. 2754-2759.

394. Rao, B.G., et al., *Highly efficient continuous-flow oxidative coupling of amines using promising nanoscale CeO2-M/SiO2 (M = MoO3 and WO3) solid acid catalysts.* RSC Advances, 2016. **6**(97): p. 95252-95262.
395. Lang, X., J. Zhao, and X. Chen, *Visible-Light-Induced Photoredox Catalysis of Dye-Sensitized Titanium Dioxide: Selective Aerobic Oxidation of Organic Sulfides.* Angewandte Chemie International Edition, 2016. **55**(15): p. 4697-4700.
396. Casado-Sanchez, A., et al., *Pt(ii) coordination complexes as visible light photocatalysts for the oxidation of sulfides using batch and flow processes.* Chemical Communications, 2016. **52**(58): p. 9137-9140.
397. Xu, Y., et al., *Highly selective oxidation of sulfides on a CdS/C 3 N 4 catalyst with dioxygen under visible-light irradiation.* Catalysis Science & Technology, 2017. **7**(3): p. 587-595.
398. *DIN 1054 2010-12, Baugrund - Sicherheitsnachweise im Erd- und Grundbau – Ergänzende Regelungen zu DIN EN 1997-1; Normenausschauss Bauwesen (NaBau) im DIN; Berlin* 2010.

9. List of scientific contributions

Journal publications:

C. Ayed, W. Huang, R. Li, L.C. da Silva, D. Wang, O. Suraeva, W. Najjar, K.A.I. Zhang, *Conjugated Microporous Polymers with Immobilized TiO_2 Nanoparticles for Enhanced Visible Light Photocatalysis*, Particle & Particle Systems Characterization 35(1) **(2018)** 1700234.

C. Ayed, L. Caire da Silva, D. Wang, K.A.I. Zhang, *Designing conjugated microporous polymers for visible light-promoted photocatalytic carbon–carbon double bond cleavage in aqueous medium*, Journal of Materials Chemistry A 6(44) **(2018)** 22145-22151.

R. Li, J. Byun, W. Huang, C. Ayed, L. Wang, K.A.I. Zhang, *Poly(benzothiadiazoles) and Their Derivatives as Heterogeneous Photocatalysts for Visible-Light-Driven Chemical Transformations*, ACS Catal 8(6) **(2018)** 4735-4750.

C. Ayed, W. Huang, K.A.I. Zhang, *Covalent triazine framework with efficient photocatalytic activity in aqueous and solid media*, Frontiers of Chemical Science and Engineering 14(3) **(2020)** 397-404.

C. Ayed, W. Huang, G. Kizilsavas, K. Landfester, K.A.I. Zhang, *Photocatalytic Partial Oxidation of 5-Hydroxymethylfurfural (HMF) to 2,5-Diformylfuran (DFF) Over a Covalent Triazine Framework in Water*, ChemPhotoChem 4(8) **(2020)** 571-576.

Conferences:

C. Ayed, W. Huang, R. Li, and K. A. I. Zhang, *Visible-light- induced photocatalysis using TiO_2/ Conjugated microporous polymer hybrid nanomaterials*, MAINZ student seminar (Amesterdam, Netherlands) **2017**.

C. Ayed, K. Landfester, and K. A. I. Zhang, *Visible Light-Promoted Carbon-Carbon Double Bond Cleavage over Conjugated Microporous Polymers in Aqueous Media*, European Polymer Congress EPF (Crete, Greece) **2019**.